High Pressure LOx/H_2 Rocket Engine Combustion

THE UNIVERSITY OF ADELAIDE
AUSTRALIA

Joshua J. Smith

School of Mechanical Engineering

The University of Adelaide

South Australia 5005

Australia

A thesis submitted in fulfillment of the requirements

for the degree of Ph.D in Mechanical Engineering

on the 30th of March 2007

Abstract

Increasing liquid rocket engine performance margins for re-usability and escalating payload demands requires a detailed understanding of injection and reaction of transcritical and super-critical propellants. Full scale static firing of modern day liquid rocket engines for research and development purposes is prohibitively expensive. A sub-scale combustor has been developed for fundamental liquid rocket engine research. The combustor is fitted with quartz glass windows for optical accessibility and is capable of multiple re-starts for extended periods with representative propellant temperatures, injector flow rates and combustion pressures.

A parametric study based on propellant injection conditions has been performed with a single shear coaxially injected liquid rocket engine combustor. Steady state operation has been closely examined with the thrust chamber operating at sub critical, near critical, and supercritical pressure levels with respect the thermodynamic critical pressure of oxygen. High speed optical diagnostics have been applied to the near injector field including spontaneous OH chemiluminescence to visualise the combustion zone and shadowgraph imaging to observe the propellant flowfield.

The propellant injection velocity ratio (R_v) and reduced pressure (P_r) have been identified to have a significant effect on thrust chamber operation. Interchanging injector geometries and

regulating propellant flow-rates at constant ocidiser to fuel ratio (R_{OF}) has enabled examination of the local and global influence of R_v and P_r on combustion over a range of conditions. Two hydrogen injection temperature ranges have been successfully investigated at a constant liquid oxygen injection temperature.

Analysis of measurement system data indicates a significant difference exists between thrust chamber operation at pressures below, near and above the thermodynamic critical pressure of oxygen. The combustion efficiency (η) and the peak-to-peak dynamic pressure data analysis ($P_{p\text{-}p}$) consistently highlight dissimilarities between sub- and supercritical pressure regimes. An inherent unsteadiness at reduced pressure levels less than unity is frequently observed through examination of the near injector flow-field and combustion zone images. The liquid oxygen core typically exhibits an increase in local surface perturbations and flow oscillations at reduced pressure levels less than unity ($P_r < 1$) which coincides with observations construed from the measurement data.

A range of combustor start-up transients have also been analysed. The point of ignition has been captured using high speed diagnostics with different injection conditions. The start-up process is characterised and described in detail for each of the conditions examined.

Low frequency (LF) combustion instability has been witnessed at subcritical pressure levels. Investigations indicate that unstable combustion triggered at $P_r < 1$ could not be replicated at a P_r equal to, or greater than unity under near identical injection conditions. In fact, unstable combustion could not be triggered whatsoever with LOx/H_2 propellants at near or supercritical pressure irrespective of operating conditions. Such findings illustrate that operating near or above the critical pressure of propellants (oxygen) results in inherently stable combustion process over a broad range of operating conditions.

Statement of Originality

To the best of my knowledge, except where otherwise referenced and cited, everything that is presented in this thesis is my own original work and has not been presented previously for the award of any other degree or diploma in any University. If accepted for the award of the degree of Ph.D. in Mechanical Engineering, I consent that this thesis be made available for loan and photocopying.

Joshua J. Smith

Acknowledgements

Completion of my thesis would not be possible without the support of my wife Toni. She has been there from the onset and has been supportive and positive throughout - and that is why she is my wife today!

I also with to thank my family (especially mum) and friends in Australia for being so patient and tolerant with my 'never ending story.' Airport farewells were never easy for anyone.

I would like to thank all of my fantastic friends and colleagues throughout Europe who have made the whole experience all the more enjoyable. I would like to thank Dr. Oskar Haidn for his great coffee room discussions, Dr. Michael Oschwald for providing focus and praise and Dr. Gerald Schneider for his support back in Adelaide. I am indebted to the P8 test facility staff including Andy Braun and the rest of the team.

Coming this far would have never happened without the continual, unrelenting support from the great Dr. Dmitry Suslov. The many good laughs with Francesco Cuoco and great times with Dimitri Klimenko, Alexei Vereschagin, Burny Shin and Dirk Greuel all contributed to make the whole experience worthwhile. I will always remember the great times we shared.

I would like to dedicate my thesis and my work to the late Dr. Wolfgang Mayer.

A good supervisor and a great friend. He is greatly missed.

Table of Contents

List of Figures

List of Tables

Chapter 1

Introduction

Liquid propellant rockets engines (LPRE's) have undergone continual development since the culmination of the second World War. Sustained advances made in LPRE technology has put humans into space on countless occasions and contributed to modern day luxuries such as extensive mobile communication networks and global internet and television coverage.

Despite significant progress over the last half century, LPRE development and qualification is an overwhelmingly expensive exercise. Many modern day rocket engine design philosophies are based on historical, empirically developed formulations derived from exhaustive testing regimes. Improved performance and reusability are the most challenging requirements for future development of LPRE's and further significant technical advances are required in many engineering and physical disciplines. A detailed understanding of injection and combustion phenomena at elevated pressures in liquid rocket engines is necessary to promote continual performance enhancements for existing and future propulsion applications.

Recent observations of high-pressure liquid oxygen/hydrogen (LOx/H_2) propellant injection under reacting conditions (Mayer and Tamura (1996)) and various simulants under non-reacting conditions (Chehroudi and Talley (2004), and Oschwald and Smith et al. (2006)) have highlighted the existence of significant physical disparities between sub-, trans- and supercritical injection and atomisation regimes. Strong influences are primarily owing to sharp thermodynamic gradients and non-idealities experienced at near critical, transcritical and supercritical pressure conditions.

Until recently, most LPRE research was undertaken at low chamber pressure conditions. Empirical correlations derived at low (subcritical) pressure levels cannot be extrapolated to trans- or supercritical pressure regimes where most modern day LPRE's operate (refer Mayer and Smith (2004)).

Experimental testing of liquid rocket engines at representative operating conditions however, is prohibitively expensive and will eventually be replaced or at least significantly reduced by advanced numerical modelling tools. Before this can occur, the noteworthy progresses made in theoretical and numerical studies of high-pressure LOx/H_2 injection and reaction (for example, refer Oefelein and Yang (1998)) require validation from well-defined, representative experimental databases.

1.1 Objective

All modern day LOx/H_2 main engines operate at high combustion chamber pressures in excess of the thermodynamic critical pressure of the propellants. Until recently, little was known in the field of transcritical and supercritical injection. Strong thermodynamic non-idealities occur near to the critical point, surface tension tends to zero as the critical point is exceeded and droplets

no longer exist. Until recently, comprehensive experimental studies of high pressure, LOx/H_2 combustion at representative conditions have been limited due to the high costs and the extreme physical conditions present inside the combustion chamber.

The primary objective of this work is to provide a better understanding of LPRE injection and reaction at elevated pressure conditions below, near and above the thermodynamic pressure of the propellants. Results and outcomes from previous experimental and numerical studies have motivated further investigation with the application of high-speed optical diagnostics to a windowed, single shear coaxially injected, high pressure O_2/H_2 thrust chamber with a high precision data measurement system. Unlike many other investigative studies, the thrust chamber employed is capable of operating at conditions representative of modern day rocket engines. This includes representative propellant temperatures, flow rate per injector element and combustion chamber pressure levels.

A parametric study at various points of LPRE operation will assist in understanding the dominant influences on global combustion including combustion and flame stability and efficiency. The application of time-resolved diagnostics to the near injector field will provide further information on local flame stability and flow behaviour. Examination of transient operation during start-up and unstable combustion is made possible with the application of high speed optical diagnostics and will provide further insight to LOx/H_2 combustion behaviour.

1.2 Scope

Development of a high pressure, windowed liquid rocket motor combustion chamber with a unique measurement system and hardware has enabled a range of studies in a reacting LOx/H_2 flowfield.

Dominant trends are highlighted and quantified with a focus on the influence of relative propellant velocities (R_v) and oxidiser reduced pressure (P_r) on global combustion, including near injector propellant flow and flame emission behaviour during steady-state and transient start-up operation.

A literature survey was undertaken to highlight the gaps in the existing knowledge in the field of LOx/H_2 LPRE research. This survey is presented in the subsequent chapter followed by a description of the experimental set up developed and optical diagnostic systems utilised. A discussion on the image and data processing techniques employed precludes the results component of the document which discusses observations pertaining to LPRE start-up transients, steady-state operation and low frequency combustion instability.

Conclusions summarise important observations and a direction for future research is suggested.

Chapter 2

Literature Review

2.1 Launch Vehicles and Rocket Propulsion Systems

2.1.1. Rockets and Launch Vehicles

A 'launch vehicle' or 'launcher' are terms commonly used in today's space industry to describe what is more traditionally referred to as a 'rocket.' A launcher can be employed for a variety of purposes such as commercial, research or military use. Whatever the application, the primary aims of the launcher and the basic principles of propulsion are very much the same. The ultimate function of a launch vehicle is to transport a payload above the Earth's atmosphere, imparting sufficient velocity to station the payload in an orbit around the Earth, or into outer space.

Launch vehicle technologies range from propulsion and control systems to advanced materials development. Meteorological predictions, international communication, military intelligence and space research and exploration are all owing to the development and successful application of rocket

technologies. Launch vehicle propulsion systems are the 'heart' of the vehicles themselves as overall mission success relies ultimately on the flawless operation of engine(s) and the design and construction of the entire propellant storage and feed systems.

2.1.2. Types of Propulsion

There are currently four common types of propulsion used for commercial and non-commercial launchers. These include cold gas systems, monopropellant, bi-propellant and solid rocket systems. System choice is determined by a multitude of reasons including necessary performance range (impulse), cost, and specific mission applications. Burn duration is mission dependent, with some applications requiring restarts, throttling or pulsed operation, and atmospheric or orbit insertion launches.

Smaller cold-gas and hypergolic systems are typically used for reaction control systems (RCS) for attitude control and Orbital Manoeuvring System (OMS) engines for orbital alignment of launchers and satellites. Solid rocket motors are used on commercial launch vehicles to provide added thrust during liftoff. The solid rocket motor casings are jettisoned from the launch vehicle once a specific altitude is reached. Monopropellant systems rely on the ignition of a pre-mixed combination of an oxidiser and combustible matter, or through the exothermic decomposition of a monopropellant via a catalyst bed. Bi-propellant systems employ two propellants, typically a fuel and an oxidiser. The fuel and oxidisers are stored in separate tanks and are mixed once injected into the combustion chamber. Despite their complexity, bi-propellant systems are currently used in many launch vehicle applications due to their high performance and safe operation. Large scale launch vehicles use a combination of propulsion devices such as liquid rocket engines, solid rocket motors and hypergolic bi-propellant systems as shown in Figure 2.1.

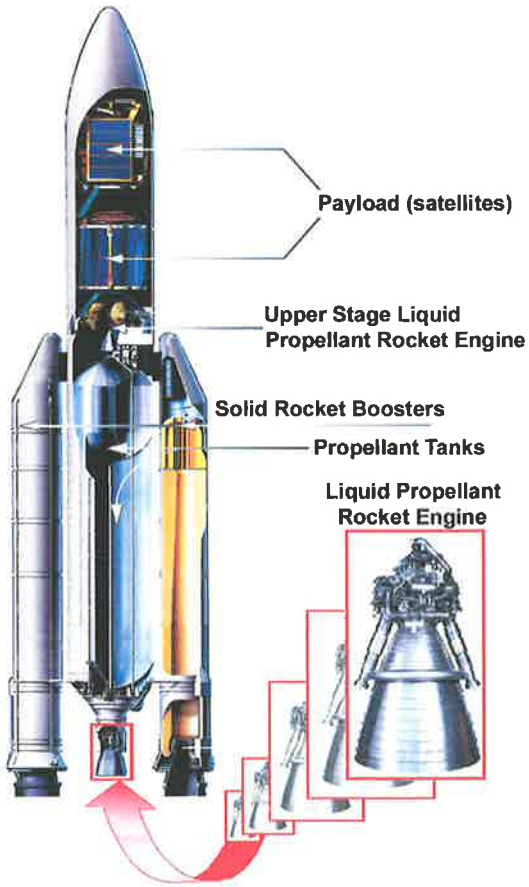

Figure 2.1 Typical commercial launcher configuration highlighting the liquid propellant main engine at the base of the vehicle.

2.1.3. Liquid Propellant Rocket Engines (LPRE's)

Griffin and French (1991) claim that no single factor constrains the design of a space vehicle and the execution of its mission more than the state of the art in propulsion technology. Liquid propellants are the most common propellants used in all heavy launch vehicle applications today, with and without the aid of solid propellant boosters. Also referred to as chemical propellants, commonly used liquid propellant fuels include the high grade kerosene 'rocket propellant-1' (RP-1), hydrogen, hydrazine, and various hydrocarbons. Oxygen is commonly used as an oxidiser with alternatives such as nitrogen tetroxide and hydrogen peroxide being less favourable today due to handling difficulties and high toxicity levels. A detailed review of rocket engine propellants is given by Kit and Evered (1960).

A liquid propellant rocket engine consists of 4 main components; a thrust chamber, one or more propellant storage tanks, a propellant feed system and a control mechanism to regulate propellant flow. The LPRE fuel and oxidiser are stored in separate tanks and are fed through a system of pipes, valves, and turbo-pumps to the propellant manifolds. Propellants are then injected, mixed and combusted generating large amounts of energy.

The injection, mixing and reaction of propellants into a combustion chamber for thrust production poses a series of complexities from an engineering and development perspective. High mass flow rates of high energy density propellants are required to develop the thrust levels necessary to elevate payloads from the earth's surface into orbit. Material selection is critical to injector and engine survivability during extended operating periods. Extreme temperature gradients exist with cryogenic propellant temperatures as low as 35K coupled with stoichiometric combustion temperatures reaching 3500K. Despite its low melting point, copper alloys are typically employed for thrust chamber liners and injector heads due to their superior heat transfer characteristics. Thermal conductivity of copper alloys are up to more than 20 times that of conventional stainless steels making them ideal for dissipating excessive heat loads such as those experienced by liquid rocket engines.

The kinetic energy in an LPRE is created by the high temperature, high pressure, propellant products being accelerated through the exhaust nozzle. The ejected mass is expelled in a direction opposite to the intended motion of the rocket. Due to the law of conservation of momentum, the rocket itself moves at a velocity proportional to the mass of the rocket and the mass and velocity of the exhausted combustion products. The ejected combustion products produce thrust, the propulsive force of the rocket (eqtn. 2.1).

$$F = \dot{m} v_{eq} \tag{2.1}$$

Thrust values in excess of 5.3 million Newtons have been achieved with liquid oxygen/liquid hydrogen (LOx/LH_2) propellants on launch systems such as the M-1 engine. Single chamber engines such as the ambitious L-6H had theoretical thrust values in excess of 122 million Newtons.

Liquid propellant engines are more complex than their solid propellant counterparts, however, they offer several advantages. The control of propellant flow to the combustion chamber means the engine can be throttled, stopped, or restarted.

2.1.4. Liquid Oxygen

Liquid oxygen (LOx) has been the most widely used oxidiser for space propulsion devices. Other oxidisers such as fluorine have a higher energy potential although handling problems, toxicity and availability has made such alternatives less popular. LOx was the first inexpensive and relatively safe oxidiser for large launch vehicles. Oxygen has a boiling point of 90K (-183°C) which creates storage difficulties, rendering it unsuitable for military purposes. The critical point of oxygen is at a pressure of 50.43 bars and a temperature of 154.62K. Liquid oxygen has a light blue, transparent colouring and is odourless.

The very low boiling point of oxygen means that LOx must be transported and used shortly after production. Storage containers and transporters require extensive insulation to minimise evaporation losses and must be fitted with pressure relief valves. Despite the handling and storage difficulties and high production costs related with liquid oxygen, handling methods have been safely developed and LOx remains inexpensive in comparison to many other rocket propellants.

2.1.5. Hydrogen

Hydrogen is the ninth most abundant element on earth and according to Lide (1997) it is the single most abundant element in the Universe. Hydrogen is readily available in water with the earths ocean estimated to have 1.7×10^{17} tons, which can be extracted by electrolysis. The boiling

point of hydrogen is very low at 20.43K. The critical temperature is only slightly higher at 33.23K and the critical pressure is 12.96 bar.

Liquid hydrogen (LH_2) is expensive in comparison to LOx (up to 45 times according to Wade (1999)). This is due to the extreme physical properties of the element and the costs associated with storage and transportation. To produce LH_2, hydrogen gas must be cooled under pressure below its very low critical temperature (33K) making it much harder to liquify than most other gases. Michael Faraday classified hydrogen as a permanent gas and it was not successfully liquified until 1898 at a temperature just below critical, requiring a pressure of approximately 90 bar. LH_2 has no odour and is completely transparent.

2.1.6. LOx/LH_2 Bi-Propellant System

Liquid oxygen and hydrogen have been used for rocket propulsion devices for many years and are still considered the best combination in many launch applications today. The cryogenic liquid oxygen (LOx) and hydrogen (GH_2 and LH_2) bi-propellant combination is used for the majority of today's heavy launch vehicles. LOx/H_2 powers the Space Shuttle Main Engine (SSME), the Japanese H-IIA upper and main-stage engines and various stages of Europe's most successful series of commercial launch vehicles in the world; the Ariane family (Figure 2.2). The cryogenic combination is the highest performer with a Specific Impulse (equation 2.2) higher than any other liquid or solid propellants flight tested to date. Specific Impulse is the most common measure of performance for rocket engines and is defined as the thrust produced per unit flow rate of propellant as follows;

$$I_{sp} = \frac{F}{\dot{m}g} = \frac{v_{exh}}{g} \tag{2.2}$$

Table 2.1 Physical properties of oxygen and hydrogen.

Property	Oxygen (O_2)	Hydrogen (H_2)
Molecular Weight M	31.9988	2.01588
Critical Temperature T_c (K)	154.62	33.23
Critical Pressure P_c (bar)	49.77	12.96
Critical Volume v_c (m^3/kg)	2.295×10^{-3}	3.184×10^{-2}
Normal Boiling Point T_{bp} (K)	90.23	20.43
Melting Point (K) T_{mp}	54.40	13.99
Critical Compressibility kr_c	0.288	0.305
Heat of Combustion h (kJ/kg)	0	-119,858.47

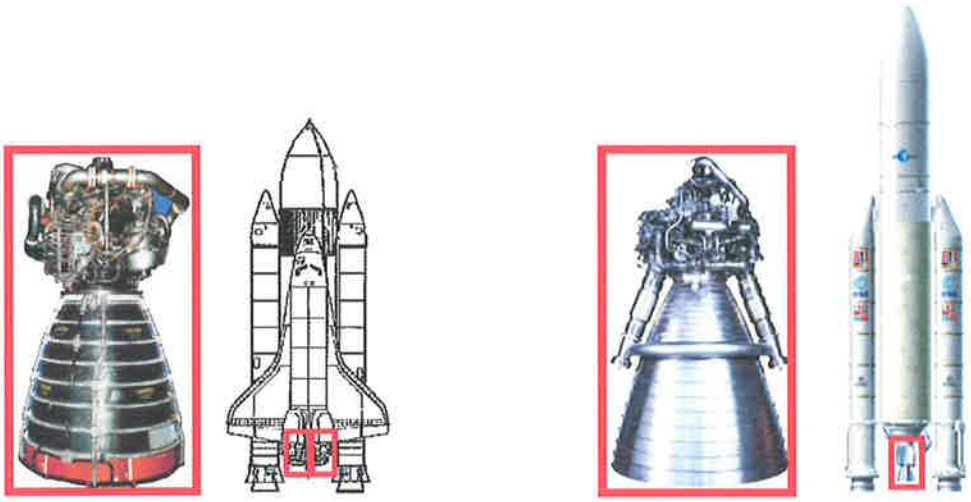

Figure 2.2 LOx/LH2 Rocket Engines: Space Shuttle Main Engine (SSME) and Space Shuttle launch vehicle (left). Ariane V launcher and VULCAIN II Engine (right).

Unlike hypergolic liquid propellants, cryogenic LOx/H_2 propellants are a non-spontaneous bi-propellant combination requiring a separate device for ignition. This generally results in more precise regulation and control of engine operation granting enhanced flexibility. The availability and relatively low cost of the propellants is complemented by the fact that they are completely non-polluting. Other high performing propellants are highly toxic, making the LOx/H_2 bi-propellant system a favourable preference.

2.2 Propellant Injection and Combustion

Liquid atomisation and spray systems have received significant interest from researchers and industry for a variety of applications ranging from irrigation systems to liquid rocket engines. Outstanding contributions to the field by those such as Lefebvre, (1988) have improved our understanding of injection and spray atomisation processes and the typical cascade of ensuing events such as jet disintegration, ligament growth and detachment and droplet vaporisation in both quiescent and reacting environments. Injection and spray systems play a fundamental role in modern liquid rocket engines which require a well distributed supply of propellants injected at optimal conditions ensuring a balance between performance, efficiency and stability.

2.2.1. Liquid Rocket Engine Injectors

A variety of injection techniques and injector designs have been employed in liquid rocket engines. Simple "shower-head" and impinging arrangement injectors are some of the simplest types with more sophisticated developments such as the coaxial pintle injector enable unique engine throttling capabilities. Porous materials were used for face plate cooling in the J-2 and RL-10 engines and advanced porous injector designs have been proposed and tested by Bazarov (1993) and more recently by Smith et al. (2003). The application of porous materials for propellant injection is beneficial as transpiration of propellants effectively cools the face plate and injection passages.

Impinging injectors have been utilised on a range of liquid rocket engines developed in the 1950's 60's and 70's such as the F-1, H-1 and Viking. Impinging injector configurations were successful, however they often proved difficult to manifold with sensitive design tolerances (Anon (1976)). Poor impinging injector head designs have led to excessive heat loads with an increased susceptibility to combustion instability in the Rocketdyne F-1 engine (see Oefelein and Yang, (1993)). Combustion instability issues with the F-1 engine haunted the Apollo program for 7

years with over 2000 full scale engine tests necessary for qualification prior to the first successful manned mission to the moon in July of 1969.

A more versatile and reliable injector type was required to reduce the formidable risks associated with manned space flights. Shear and swirl coaxial injectors had been utilised almost exclusively in all Russian booster engines until the 1970's. Pratt and Whitney had employed the coaxial injector design in the RL-10 with Rocketdyne and Aerojet following suit with development and production of the J-2 and M-1 engines. The remarkable performance of the simple yet highly effective coaxial injector design had finally been realised.

2.2.2. Coaxial Injection

Coaxial injectors in rocket engines are most commonly utilised for LOx/H_2 injection applications. As the name suggests, a coaxial injector refers to an element whereby a jet core is injected, surrounded by a concentric annulus of a secondary fluid. In the LOx/H_2 case, the core flow is liquid oxygen with an annular flow of hydrogen. A schematic of a coaxial injector is represented by Figure 2.3.

Claimed to have been developed and patented by NASA engineer Sam Stein, coaxial injectors are the most common type used in modern rocket engines. The coaxial injection element has been used in cryogenic LOx/H_2 rocket engines since the 1940's and has since become the injection element of choice for most flight vehicle engines (Hulka and Hutt (1994)). The Space Shuttle Main Engine (SSME), HM7, HM60, LE-5, LE-7, Vulcain I and II, the RD-0146 and the new European VINCI engine all employ shear coaxial injector elements. Coaxial injectors are located inside the injector head of a rocket engine and supply propellants to the combustion chamber. Typical large scale main engines employ hundreds of coaxial injectors to provide copious amounts of propellants necessary for large levels of thrust production. The SSME and Vulcain II engines for example employ 620 and 516 coaxial injectors respectively.

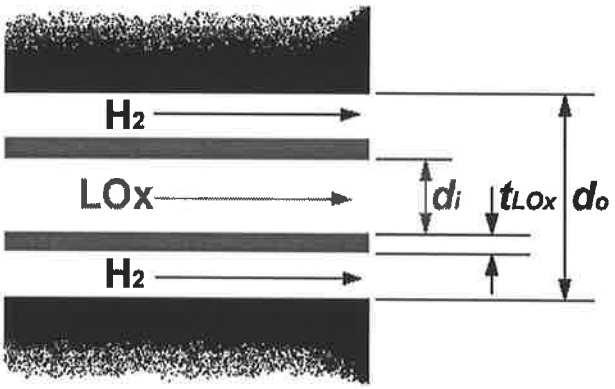

Figure 2.3 2-D representation of a typical liquid rocket engine coaxial injector configuration.

A coaxial injector is described as a 'twin fluid' atomiser and uses mainly the principal of airblast atomisation. Often, one of the jets (generally the core) is in a liquid state and is atomised by the second, high velocity (high Re. no.), annular jet. At low operating pressures, the jet break-up and atomisation process is dominated by aerodynamic (inertial) forces. Propellant atomisation is promoted by the momentum exchange through the shearing action between the propellants, associated with the high velocity annular flow.

Previously, the relative injection velocity ratio of propellants (R_v) was considered an important parameter for characterising atomisation and mixing efficiency of coaxial sprays and ultimately, the combustion stability of liquid rocket engines (see Wanhainen et al. (1966), Yang and Anderson (1995), and Harrje and Reardon, (1972)). Experimental investigations by Hopfinger and Lasheras (1994) with water and air in a coaxial arrangement indicated that primary liquid core break-up was governed by the momentum flux ratio J (eqtn. 2.3). This dimensionless value has since been adopted for defining operating regimes with coaxial injection in liquid rocket engine model combustors (Candel and Herding et al. (1998), Snyder and Herding et al. (1998), Smith and Klimenko et al. (2002), and Woodward and Pal et al. (2006)) . The relative Weber number of the injectants (*We*) is also employed for characterisation of low pressure spray

combustion (Gurliat et al. (2002) and Cuoco et al. (2004)) and represents the ratio of inertial to surface tension forces and strongly influences droplet sizes and thus vaporisation time scales.

$$R_v = \frac{v_{H_2}}{v_{O_2}} \tag{2.2}$$

$$J = \frac{(\rho v^2)_{H_2}}{(\rho v^2)_{O_2}} \tag{2.3}$$

$$We = \frac{\rho_{H_2}(v_{H_2} - v_{O_2})^2 d_{H_2}}{\sigma} \tag{2.4}$$

Although known to have poor atomisation efficiency, various derivations of the coaxial injector have proven extremely effective in mixing and atomisation of cryogenic LOx/H_2 for combustion. A series of performance enhancing features are typically incorporated with coaxial injector elements such as LOx post tapering and recessing which has been reported by Wanhainen et al. (1966) to increase performance by up to 3%. The effects of LOx post recess has been investigated experimentally by Mayer and Tamura (1996) with a hypothesis for the performance increase detailed by Kendrick et al. (1999). Typical coaxial injector configurations are presented in Figure 2.4.

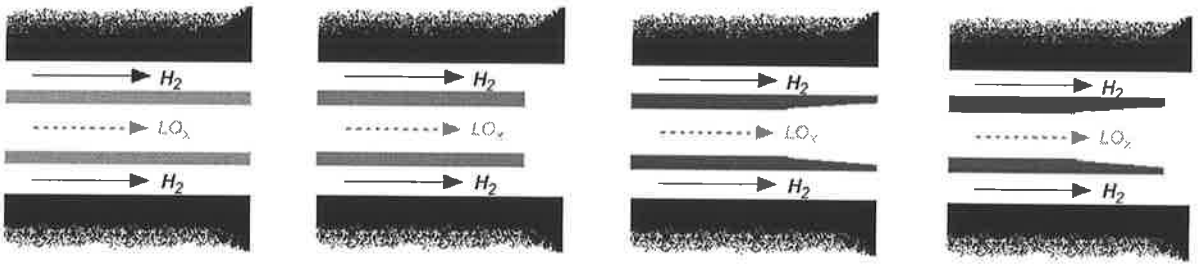

Figure 2.4 Shear coaxial injector configurations from left to right; Simple shear, recessed shear, tapered shear, and recessed tapered shear coaxial.

2.2.3. Coaxial Injection and Combustion Research.

Conceptually, coaxial injection of propellants is relatively straight-forward however, the injection of reactive propellants into a high temperature combusting environment introduces a range of complexities and ambiguities from a scientific perspective. A vast amount of research has been undertaken studying the influence of various parameters on coaxial spray and flame formation with a variety of injectants and simulants. Cold-flow, non-reacting investigations at low pressure provide precise quantitative information such as droplet sizing and spray distribution functions (Farago and Chigier (1992), Vingert and Gicquel (1995), Pal and Moser et al. (1996), Rehab and Villermaux et al. (1997)). Low pressure studies with reactants (LOx/GH_2 and GOx/GH_2) introduce the realism of combustion, coupling the effects of fluid mechanics with chemistry and heat release.

Extensive studies of coaxially injected flames at atmospheric and low pressure conditions have been performed at a range of establishments worldwide in order to understand injection of real propellants at representative injection temperatures in a combusting environment. These contributions have provided quantitative and qualitative information on flame structure, propellant flow-field distribution, flame stabilisation and emission data. Such investigations have been realised with the development and construction of combustion chambers with optical access.

Heidmann (1965) was one of the first to employ an optically accessible micro-combustor facility for observation of low frequency (LF) combustion instability. The chamber operated at low pressure with optical access via a 25mm diameter glass window.

A windowed combustion facility at Pennsylvania State University has been extensively utilised for low pressure shear coaxial and swirl coaxial injector studies by numerous researchers. Moser and Menerich (1993) developed the chamber and initiated the experimentation with low pressure GOx/GH_2 emission and velocity measurements. Woodward and Pal et al. (1996) developed jet

core length correlations for coaxial sprays under non-reacting and reacting conditions at chamber pressures of approximately 13 bar. The primary influences on intact core length were found to be the injectant density ratios, liquid Reynolds number and Weber number. As ambient pressure and co-flow velocity was increased, the jet core length decreased. Increased liquid core velocity resulted in increased length. The tests were conducted over a large range of conditions (up to 4 orders of magnitude) however limited data points were collected.

Foust and Deshpande (1996) applied Raman spectroscopy and Laser Doppler Velocimetry (LDV) to a low pressure, uni-element GOx/GH_2 combustor to measure species concentrations and velocity profiles. A nominal combustion chamber pressure of approximately 12.9 bar was achieved in the study.

Extensive research has been performed at the German Aerospace Centre (DLR) with windowed chambers employed at the "M3" test facility. Low pressure atomisation and combustion studies have been undertaken by Vogel (1994) and the application of optical diagnostics has been extensive (for example Schmidt et al. (1999)). More recently, ignition studies have been investigated with various ignition regimes being identified. Exhaustive experimental test campaigns have been dedicated to the study of ignition transients at low pressure conditions between 1.5 and 5 bar (Mayer et al. (2001), Gurliat et al. (2002) and Cuoco et al. (2004).

The French test bench "Mascotte" has been widely used in conjunction with optical diagnostics to assist in assessing the influence of different operating conditions on performance at operating pressures of up to 10 bar (see for example, Herding and Snyder et al. (1998), Candel and Herding et al. (1998) and Kendrick et al. (1999)). More recently, the test facility has been upgraded to operate at increased pressure levels. High pressure LOx/H_2 studies were brief (Juniper and Tripathi et al. (2000)) with the new generation facility now focused on transcritical hydrocarbon fuel studies (Singla and Scouflaire et al. (2004)).

2.3 High Pressure Injection and Combustion

2.3.1. Supercritical Phenomena

The study of supercritical fluids has been an active field of research since the discovery of supercritical phenomena in 1822 by French Physicist and Engineer Baron Charles Cagniard de la Tour (de la Tour, (1822). In 1875, Professor Andrews of Queens College determined the critical point of carbon dioxide (Andrews, (1875)) and shortly thereafter in 1879, Hannay and Hogarth (1879) reported that supercritical fluids have a remarkable pressure-dependent dissolving power. Supercritical fluid extraction technologies have since been utilised for a broad range of applications in the food and beverage industry. The first large-scale construction of supercritical fluid extraction facilities began in Germany and the United States in the late 1970's.

By definition, a fluid is termed supercritical when it exists at a state above the corresponding thermodynamic critical point of the fluid. The critical point of a specific medium is defined by a critical pressure (P_c) and a critical temperature (T_c) and is situated at the end of the liquid-vapour coexistence curve (see Figure 2.5). Above the critical temperature, there is no liquid phase transition irrespective of the pressure applied.

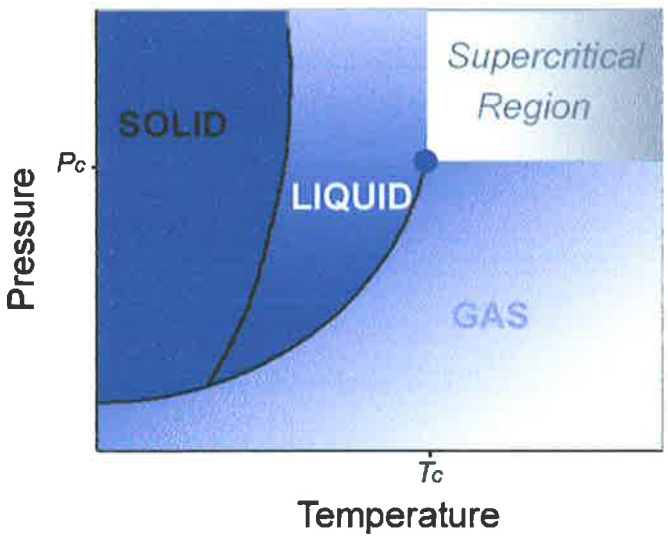

Figure 2.5 Phase diagram of a substance indicating the supercritical region

Supercritical fluids are liquid-like in that they have transport and dissolving properties resembling a liquid and are much more dense than a gas. Supercritical fluids are gas-like in respect to their very low viscosity (μ) and little to no surface tension (σ) allowing them to enter extremely small pores, making supercritical fluids appealing for applications such as cleaning, extraction, and chromatography.

As the thermodynamic critical point of a fluid is approached, thermodynamic and transport properties deviate significantly from ideal. The isothermal compressibility (k_T) increases dramatically and is infinite at the critical point. The latent heat of vaporization (l_{vap}) tends toward zero as the constant pressure specific heat (c_p) becomes infinite. As the critical point is exceeded the distinction between liquid and gas phase no longer exists and the only appropriate phase description is the substance becomes a *fluid*. In modern large-scale LPRE's. the fuel and oxidiser are typically injected in a supercritical state.

The following section describes supercritical injection phenomena from the perspective of high pressure, coaxially injected liquid rocket engines.

2.3.2. High Pressure Injection Studies

The importance of supercritical fluid injection and combustion research with regard to liquid rocket engines has recently been highlighted with unique and meritorious advances in the field both experimentally and numerically (for example, Mayer and Tamura (1996), Oefelein and Yang (1998)). Terminology practised when referring to supercritical fluids is often misleading and is defined in advance to ensure brevity. The terms subcritical and supercritical conditions are employed here in reference to the quiescent chamber pressure condition with respect to the injected propellant(s) critical point. Typically, conditions are deemed supercritical when the critical point (T_c and P_c) of all injectants are exceeded. Transcritical is a term commonly used when the operating pressure exceeds the critical pressure of the injectants but the injected

temperature of the propellants/simulants is below the critical temperature (i.e. $P_{ch}>P_c$, $T_{inj}< T_c$). The reduced pressure (P_r) is defined as the ratio of critical pressure to chamber pressure (eqtn. 2.3) and the reduced temperature (T_r) is the ratio of critical temperature to injection temperature (eqtn. 2.4).

$$P_r = \frac{P_c}{P_{ch}} \tag{2.3}$$

$$T_r = \frac{T_c}{T_{inj}} \tag{2.4}$$

In a majority of liquid rocket engine thrust chambers, propellants are coaxially injected in a transcritical state (see Table 2.2). However, with reaction and heat release within the shear layer, convective heat transfer results in thermodynamic stratification of the LOx core with a rapid transition from transcritical to the supercritical condition.

Table 2.2 Operating conditions of current coaxially injected LOx/H_2 rocket engines

	HM-7	LE-5B	LE-7	SSME	VINCI	Vulcain
Chamber Pressure (bar)	~ 31	~ 36	~ 147	~225	~ 60.8	~ 115
LOx flow rate/element (g/s)	~ 130	~ 90	~ 460	~ 670	~ 202	~ 532
H_2 flow rate/element (g/s)	~ 30	~ 20	~130	~ 110	~ 40.4	~ 87
LOx injection Temp. (K)		~ 95			~ 94	~ 95
H_2 injection Temp. (K)		~ 60			~ 225	~ 34
O/F ratio	~ 4.5	~ 5.5	~ 6	~ 6	~ 5.84	6.1
Pressure regime	subcrit.	subcrit.			transcrit	transcrit.

High pressure injection research accelerated significantly in the 1990's with the construction of optically accessible facilities for non-reacting transcritical and supercritical injection studies. Cold flow, non-reacting high pressure test facilities developed by the DLR and the US Air Force Research Lab (AFRL) have contributed significantly to the understanding of high pressure

injection phenomena. Although lacking the realism of combustion, cold-flow studies enable one to visualise fundamental processes such as atomisation, mixing and jet break-up without the complexities and optical distortions introduced by combustion. A vast amount of experimental work has been performed with sub-scale conditions capturing and characterising intricate processes at AFRL (Chehroudi & Talley et al. (2002), Chehroudi and Davis et al. (2003) and Davis and Chehroudi (2004)). These studies are complemented by full-scale cold-flow studies at the DLR M51 facility using injector geometries and flow rates similar to those experienced in actual rocket engine applications (for example Mayer, Schik and Talley et al. (1998), Mayer and Telaar (2002) and Mayer and Smith (2004)). A recent overview of high pressure cold-flow injection studies by the two research groups is presented by Oschwald and Smith et al. (2006).

Simulants used for high-pressure cold flow studies include non-reacting fluid combinations such as gaseous and liquid nitrogen (GN_2 and LN_2), helium (He) and water (H_2O). Other reactive elements such as hydrogen (H_2) and ethanol (C_2H_5OH) have been used in the absence of an oxidiser (Oschwald and Schik et al. (1999), (Branam and Mayer (2003)). The critical properties of common propellants and simulants are listed in Table 2.3.

Table 2.3 Critical properties of commonly used simulants and propellants for injection studies (National Institute of Standards and Technology)

Fluid	Symbol	Critical Pressure P_c (bar)	Critical Temperature T_c (K)	Critical Density ρ_c (kg/m³)
Ethanol	C_2H_5OH	514	63	-
Helium	He	2.2746	5.1953	69.641
Hydrogen	H_2	13.15	33.19	30.12
Nitrogen	N_2	33.958	126.192	313.3
Oxygen	O_2	50.43	154.581	436.1
Water	H_2O	220.64	647.096	322

For multi-component systems, the critical mixing temperature and pressure determine the critical point. A definitive point no longer defines the critical region of a mixture but rather, critical mixture lines represent critical regions for mixtures and examples of these lines for common binary systems are displayed in Figure 2.6. Often, this critical mixture region is dependent on relative concentrations of the injected species and is often in excess of the critical point of the individually injected components.

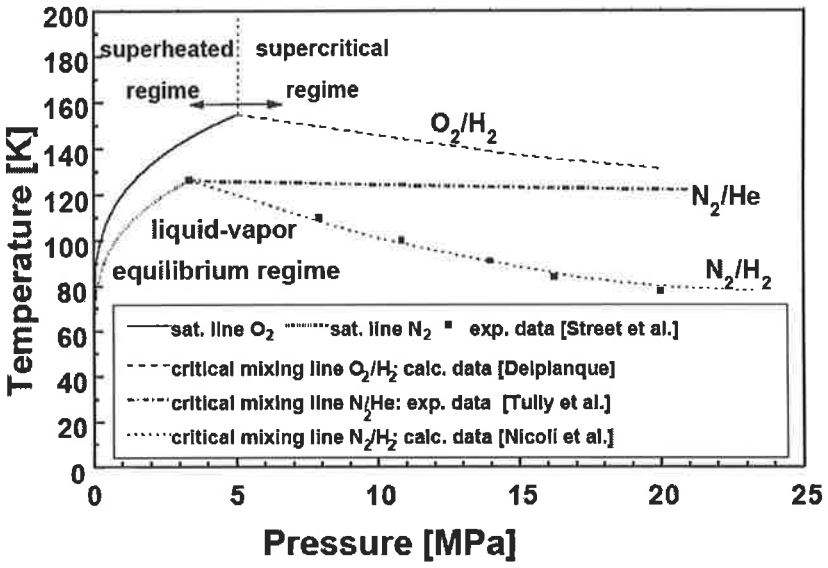

Figure 2.6 Critical mixing lines of common binary systems (Mayer & Smith (2004))

Nitrogen has been the fluid of choice for single fluid injection studies at high pressure due to its favourable physical properties, non-reactivity and high availability (low cost). For a single component system, a phase equilibrium between liquid and vapour exists when the system pressure is equal to the component vapour pressure. At the critical point, which is characterized by the critical temperature and pressure, the density of the gas and liquid phase become equal. A phase equilibrium no longer exists and the surface tension tends toward zero. Small increases in temperature near the critical point cause large expansions of the fluid and thus, at supercritical conditions the break-up process is not only influenced by lack of surface tension but also through enhanced heat transfer to the jet. Other properties such as density (Figure 2.7) also change

remarkably around the critical point. Besides the specific heat, physical properties tend to remain between the limits of pure gas and liquid properties.

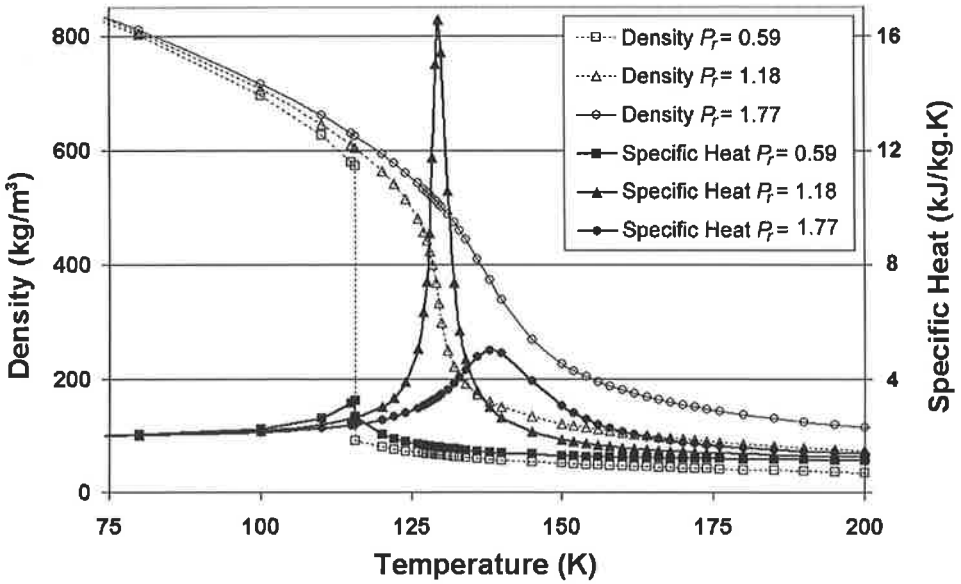

Figure 2.7 Density and specific heat of nitrogen as a function of reduced pressure and temperature.

Capillary, aerodynamic, and shear forces, as well as turbulence and expansion all contribute to atomisation, depending on injection conditions. Mayer and Telaar (2002) have shown that at near critical conditions the capillary forces are reduced considerably, but at low injection velocity droplet detachment still occurs. At the higher injection velocity shear forces exceed the capillary forces and the 'atomisation' phenomenology resembles a turbulent gas-like mixing process.

Figure 2.8 illustrates the aforementioned atomisation phenomena observed at various chamber pressures for a single, turbulent LN_2 jet with an injection temperature of 100 K into GN_2 at 300K. Injection velocity was maintained constant at v = 1m/s. The effects of P_r show significant jet expansion as the critical pressure is approached and exceeded.

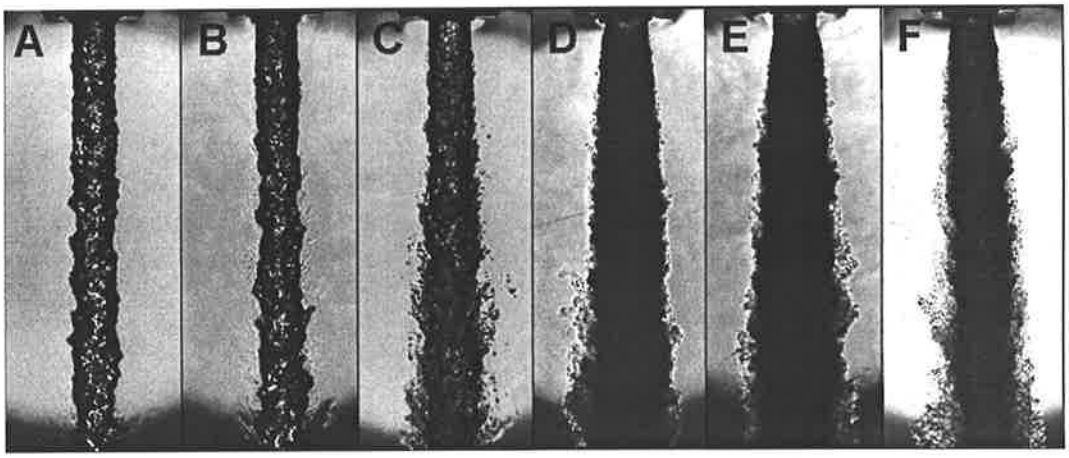

Figure 2.8 LN_2 injected into GN_2. v_{LN2} = 1m/s, d_{LN2} = 1.9mm, T_{LN2} = 100K. Image A: P_r=0.29, B: P_r=0.59, C: P_r=0.89, D: P_r=1.18, E: P_r=1.48, F: P_r=1.78 (Mayer & Smith (2004))

These observations are strongly supported by the work of Chehroudi and Talley (2002) who used high resolution shadowgraph images for fractal measurements of sub- and supercritical nitrogen jets. Their work showed significant differences in fractal dimensions in N_2 jets at sub and supercritical conditions. Fractal dimensions were comparable with those of liquid sprays at subcritical pressures and resembled dimensions representative of turbulent gaseous jets under supercritical conditions.

Examinations close to the surface of the jet highlights the effects of injection velocity and P_r on atomisation as shown in Figure 2.9 (Mayer and Smith (2004)). Droplet detachment is enhanced at higher injection velocities however the opposite trend is observed as P_r increases. Once the critical pressure is exceeded, no droplets are evident with a total loss of surface tension. Observations by Chehroudi and Talley et al. (2002) at similar pressure conditions (P_r = 1.22, Re = 66 600) revealed finger or thread-like structures emanating from the surface of the N_2 jet which appeared to coalesce with a further increase in P_r. This phenomena appears to occur within a narrow range of injection conditions and can be attributed to a reduction in surface tension and disappearance of the enthalpy of vaporisation as the critical point is exceeded.

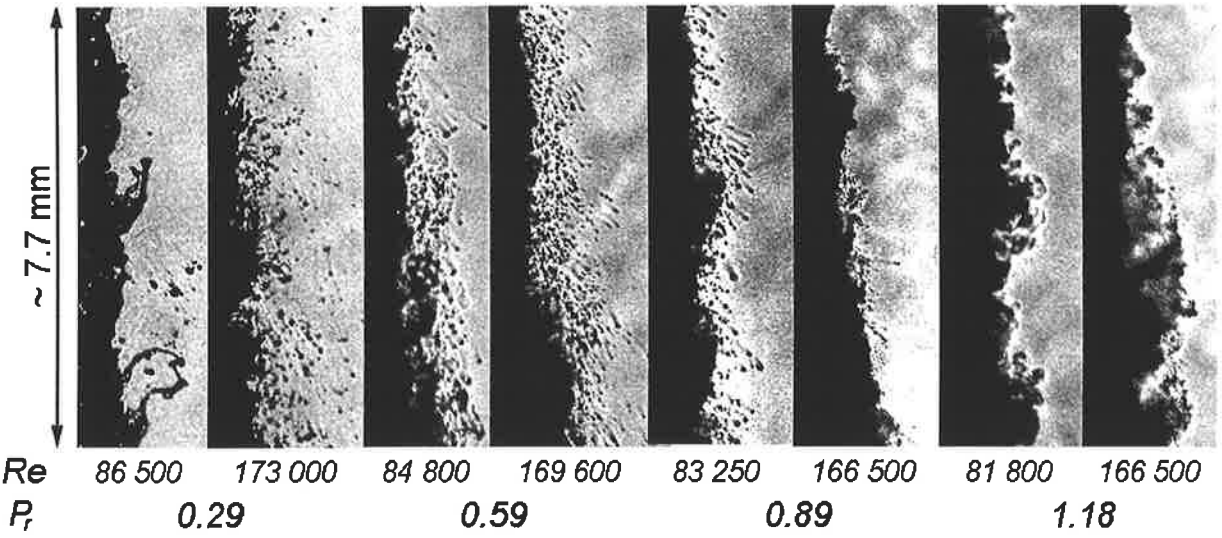

Figure 2.9 LN_2 jet surface at various injection velocities and reduced pressure; T_{LN2}=105K, d_{LN2}=1.9mm, T_{amb}=300K (Mayer & Smith (2004))

To better simulate conditions experienced in LPRE's, experimenting with binary high pressure injection systems is necessary to study the influence of a co-flowing coaxial stream in the presence of a supercritical environment. Cold-flow testing is often advantageous for fundamental studies rather than combusting environments due to reduced optical gradients and significant cost savings. A range of optical diagnostic techniques have been applied to high pressure binary component systems under non-reacting conditions with a coaxially injected configuration. Shadowgraph photography has been primarily employed to qualitatively assess the flowfield.

The change of atomisation mechanisms with reduced surface tension is clearly evident from the coaxially injected N_2/He system illustrated by Figure 2.10. (Mayer and Smith (2004)). Aerodynamic effects diminish and the flow is dominated by turbulent gas-like mixing. Such visualisation studies clearly indicate that no definitive boundary exists separating the liquid core from the coaxial flow at supercritical pressure conditions.

Spray formation is clearly evident in Figure 2.10 at low pressure (image A) and dense, light fluid turbulent mixing is apparent at supercritical pressure conditions (image B). The critical mixing

temperature of the N_2/He system is 125.7K. Within the interfacial mixing layer (between LN_2 and He), transcritical zones may exist. The visible 'surface' of the LN_2 jet is assumed to be the layer which reaches the critical mixture temperature. The effects of surface tension relative to shear forces diminishes with increasing pressure as shown in image B of Figure 2.10. Shear forces and expansion of the jet dominate and as in the single N_2 jet case, heat transfer to the jet plays an important role under supercritical pressure conditions.

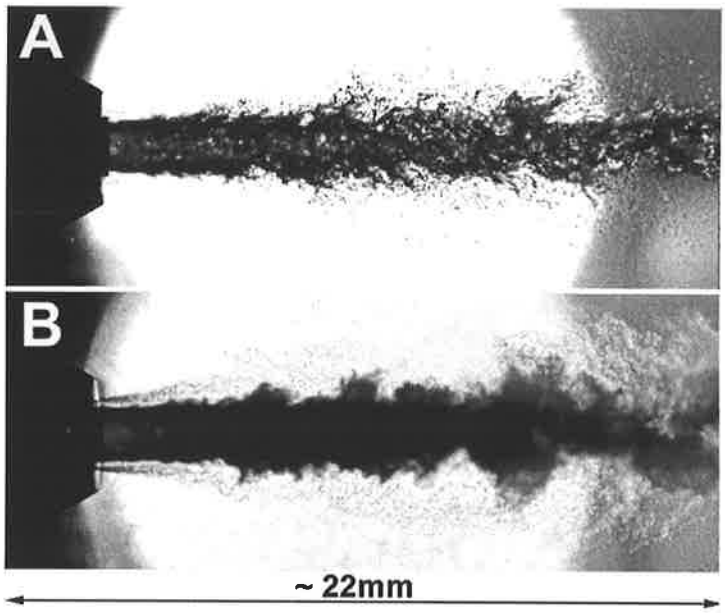

Figure 2.10 Coaxially injected binary LN_2/GHe system at A: P_r=0.29, B: P_r=1.78, d_{LN2}=1.9mm, v_{LN2}= 5m/s, v_{He} = 100m/s, T_{LN2}=97K, T_{He} = 280K (Mayer & Smith (2004))

The importance of heat transfer is supported by a recent contribution by Branam and Mayer (2003). Relatively large volumes of high resolution shadowgraph photography has enabled the measurement of visible length scales employing two point correlation methods. Reduced pressure values P_r = 1.18, 1.48 and 1.77 were studied with injection temperatures of T_{LN2} = 100, 120 and 130K. Length scales measured correspond to the Taylor micro-scale with eddies exhibiting an elliptical shape near to the injector exit. Temperature variations were apparently responsible for changes in density and flow conditions in the experiment whilst pressure and

velocity had a negligible effect.

Spontaneous Raman spectroscopy has been performed in parallel at the AFRL and the DLR with LN_2 jets at elevated pressure (Oschwald and Schik (1999), Chehroudi and Cohn et al. (2000), Mayer and Telaar et al. (2003)). Raman provides quantitative radial density measurements of the injectants and has also been used for estimating potential core lengths. Coaxial LN_2/GH_2 studies have been performed by Oschwald and Schik et al. (1999) and Mayer and Telaar et al. (2003). Substantial temperature differences between the injectants resulted in significant heat transfer between the core and annular flows. It was concluded by Oschwald and Schik (1999) that injection temperature dominated jet evolution rather than momentum flux ratio.

To better simulate LPRE injection conditions with non-reacting fluids, the AFRL group have excited single LN_2 jets with an acoustic device at subcritical and supercritical conditions (Chehroudi and Talley (2002)). The acoustic field appeared to compress the direction of acoustic wave propagation and expand the jet in the direction perpendicular to that of wave propagation. A greater impact was observed from the acoustic waves on the jet structure at sub-critical pressures conditions as opposed to supercritical pressures. An interesting point was that the most significant jet expansion was observed at low flow rates and near-critical pressure conditions ($P_r \sim 0.73$). The reduced effect of acoustics on the injected jet at elevated pressure supports hypotheses that mechanisms governing the coupling between acoustic waves and jets are significantly different for supercritical jets than for subcritical jets.

The study of jet-acoustic interactions at various reduced pressures was recently extended to coaxial jets (Chehroudi, Davis and Talley (2003), Chehroudi and Davis (2004)). The core injectant used was LN_2 surrounded by a GN_2 co-flow. The results show a sinusoidal behaviour of the core flow at both sub- and supercritical pressure conditions in the presence of an acoustic

field. This observation supports previous reports of helical flow fields under reacting, supercritical pressure conditions by Mayer and Tamura (1996) and Smith and Klimenko et al. (2002). The wavelength observed by Chehroudi, Davis and Talley (2003) coincides with transverse acoustic modes of the chamber. Further studies are planned pending an overhaul of the existing test facility. A comprehensive overview of elevated pressure injection studies undertaken at the DLR and AFRL is given by Oschwald and Smith et al. (2004).

2.3.3. Supercritical Modelling

Modelling supercritical injection phenomena requires a significant theoretical foundation coupled with complex equations of state (EOS) to accurately predict real gas properties at near critical conditions. Detailed chemistry combined complex thermodynamic and numerical theory results in comprehensive codes which are computationally demanding.

Modelling supercritical injection has generated significant interest from a number of distinguished research groups. Serious effort has been vested in developing numerical codes which incorporate complex thermodynamic-fluid theory capable of supporting supercritical H_2/O_2 injection and combustion. A landmark contribution was the achievement of Large Eddy Simulation (LES) by Oefelein and Yang (1998). The unique theoretical framework is extensive with a sub-grid-scale 2D modelling approach employing a Soave-Redlich-Kwong equation of state and a modified Benedict-Webb-Rubin EOS for near-critical conditions. This important work highlighted the significance of large density gradients, diminished mass diffusion rates and the momentum flux ratio on flame stabilisation in the near injector field.

Additional work by Oefelein (2003) has been systematic in tackling the physical and numerical challenges associated with such a complex flowfield. A 3-D geometry was constructed based on the DLR combustion chamber C, which has been utilised for the experimental work from which this thesis is based. More recently, direct numerical simulations (DNS) were employed

by Oefelein (2004) which have the advantage of resolving all scales within the flowfield. It was reported that variations in the thermophysical properties across the flame intensified respective gradients such that they approached the behaviour of a contact discontinuity. Extremely low values of density in the hot reaction zone cause a considerable reduction of aerodynamic interaction between the LOx jet and the H_2 stream. The flame holding mechanism in the near injector region was shown to be dominated by an unsteady stagnation region. Development of the flame within this region is dominated by diffusion and enhanced by convective energy transport from the back-flow of fuel-rich combustion products which sustains the ignition process and promotes vaporisation of the dense liquid-oxygen core.

Bellan (2000) has presented a comprehensive overview of supercritical fluid behaviour focusing primarily on theoretical aspects. The study probes fundamental phenomenon exposing underlying complexities associated with supercritical phenomenon. Okongo and Bellan (2000), Okongo and Harstad et al. (2002) and Miller and Bellan (2002) have performed 3-D DNS of heptane-nitrogen and oxygen-hydrogen mixing layers. Regions of large density gradients appeared to have a stabilising effect on the evolution of the mixing layer, more so than an equivalent gaseous mixing layer. Areas of high density gradients have a similar effect to a material surface by damping emerging turbulent eddies. This finding is similar in nature to that of DNS results presented more recently by Zong and Yang (2003) and Zong and Wang et al. (2003).

The DNS of O_2/H_2 mixing layers under supercritical conditions by Okongo and Harstad et al. (2002) employed conservation equations based on fluctuation-dissipation theory and employs a modified Peng-Robinson equation of state. The author(s) claim, unlike Oefelein (2003), (2004), the effects of Soret and Dufour are significant and hence were utilised in the study. Results indicate that turbulence models relating dissipation to viscous effects may not be accurate under supercritical conditions, where mass flux has shown to play a more dominant role in turbulent

dissipation. Further examination is necessary to validate and generalise these conclusions.

The group of Yang (1993),(1995),(1998),(2000) have provided a deluge of noteworthy contributions to the field of high pressure injection, combustion and droplet modelling. Reviews of earlier contributions to the field of high pressure combustion phenomenon have been presented by Givler and Abraham (1996) and more recently by Bellan (2000). Discussion here is limited to more recent contributions on the subject.

An overview of collaborative high pressure combustion modelling efforts between Oefelein and Yang (1998) and Yang and Hsiao et al. (1996) was reviewed and assembled by Yang (2000). This noteworthy article discussed modelling of supercritical droplet vaporisation and combustion in quiescent and convective environments. Droplet response to flow oscillations was briefed with supercritical spray field dynamics, mixing and combustion processes comprising a major component of the work. As part of the concluding remarks, it was stated that the current quantitative experimental database of supercritical injection and combustion was inadequate and hence the theoretical efforts were limited due to a lack of validated theories.

More recently, Zong and Yang (2003) and Zong and Wang et al. (2003) have also undertaken DNS modelling of supercritical cryogenic nitrogen jets. Moving to a non-reacting, single jet configuration avoids complexities associated with a binary, reacting mixture. A parametric study based on the variation of ambient pressure was explored to understand the dominant processes associated with supercritical jet evolution. A single jet with a diameter $d_i = 254\mu m$ was used for the investigations.

A baroclinic torque and volume dilatation was said to arise from a stratified density profile across the injected jet and ambient gas. These effects coupled with real-fluid behaviour play an influential role in flow field evolution. It was found that areas of large density gradients act as

a solid wall that apparently amplifies the turbulent fluctuations in the axial direction yet damps those in the radial direction. Increased radial damping was evident at near critical conditions where the density gradients are highest. As ambient pressure increases, the radial damping was shown to reduce due to a decreased nitrogen density gradient.

Power spectra of radial velocity oscillations exposed two dominant frequencies (harmonics) induced by the flowfield. These frequencies correspond to a theoretical vortex shedding frequency based on an empirically determined Strouhal number. At increased (supercritical) conditions, thread-like entities were described to emanate from the fluidic jet as observed experimentally by Chehroudi and Talley et al. (2002).

Continual interest from a series of research groups supports ongoing development of existing models detailing supercritical injection under reacting and non-reacting conditions. Enhanced computing technologies enable continual refinement of existing models comprising highly resolved flow fields with detailed chemistry and computationally demanding equations of state. With further validation and development of existing models, a theoretical database pertaining to supercritical injection and combustion can significantly reduce with potential to replace current methods of engine development and qualification which are both timely and highly expensive.

2.3.4. High Pressure Experimental Combustion Studies

The successes achieved from cold-flow research facilities combined with numerical advances has promoted increased interest in high pressure combustion research. A monumental experimental study by Mayer and Tamura (1996) employed an optically accessible, high pressure model combustor which produced compelling results (see Figure 2.11).

The test-rig utilised by Mayer and Tamura (1996) consisted of a single, shear coaxially injected

LOx/H_2 windowed combustion chamber. The injector element had an inner diameter d_i of 1mm and an outer diameter d_o from 2.5-3.9mm. The injector LOx post tip thickness t_{LOx} was 0.3mm. Combustion chamber pressures of 15, 45, 60 and 100 bar were investigated. LOx was injected at 100K with injection velocity ranging from 10-30m/s. H_2 injection temperature ranged from 150-300K with injection velocities from 200-300m/s. Injector LOx post configurations with and without recess were tested. The broad range of operating conditions were devised in an attempt to understand the dominating effects on global mixing and combustion efficiency.

Shadowgraph images and emission spectra were recorded during combustor operation. A noteworthy observation were the LOx jet visualisations utilising a backlit shadowgraph setup. At a combustion chamber pressure of 15 bar, non-spherical droplets and ligaments were observed. The droplet number density was significantly less than that observed under non-reacting conditions. Upon approaching and exceeding the thermodynamic critical point of O_2, droplets were no longer observed. Thread-like structures developed and grew from the LOx core which did not detach but rapidly dissolved. Several tens of diameters downstream, the LOx core broke down into large lumps which dissolved in the same manner. At an increased combustion chamber pressure of 45 bar (P_r = 0.89), "snake-like" oscillations were observed.

One of the highlights of the study was the observation of the LOx post wake, shear layer and flame interaction. The flame was described to always instantaneously attach to the LOx post upon ignition. A small but intense recirculation zone exists behind the LOx post which acts as a flame holder appearing to stabilise the flame which extends up to 15 LOx jet diameters downstream (see Figure 2.11). At 45 bar and above, the effects of diminished surface tension resulted in a liquid jet that was no longer round and a well defined surface was no longer visible. Exceeding the critical pressure of oxygen exhibited severe optical gradients which resulted in reduced image quality.

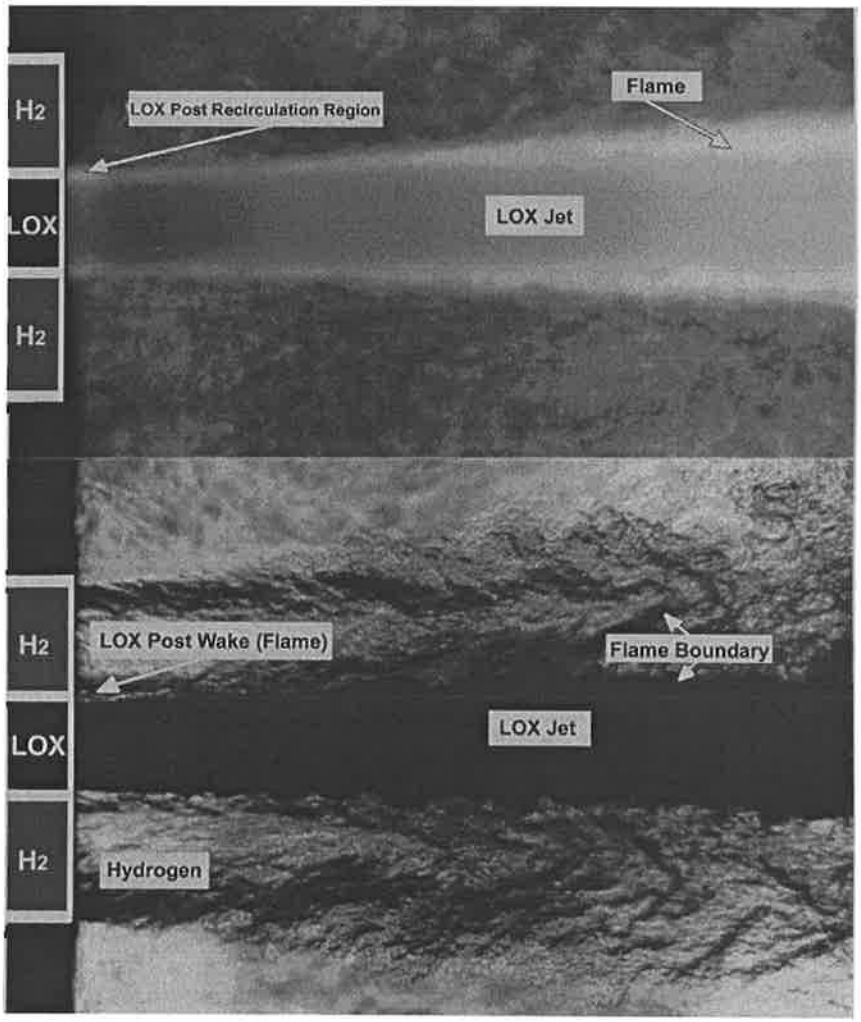

Figure 2.11 Near injector flame and flow visualisation at near-critical chamber pressure showing the LOx post wake, recirculation zone and flame residing in the shear layer. Oxygen and hydrogen velocities are 30 and 300m/s respectively with d_i=1mm and P_{ch}=45bar. (from Mayer and Tamura (1996)).

These results have provided valuable phenomenological insight of high pressure combustion processes and has provided major impetus for further research in this field including Mayer and Schik et al. (1998), Mayer and Ivancic et al (2001), Smith and Klimenko et al. (2002), Ivancic and Mayer et al. (2002) and the work presented herein.

2.3.5. Summary

Cold-flow, non reacting, trans- and supercritical injection studies remain a major field of interest for research groups from experimental and theoretical backgrounds. Experimentally, a substantial array of diagnostic techniques have been applied to high-pressure, non-reacting injection systems with single and binary simulants. These experiments have highlighted the significant

differences between sub-critical, trans-critical and supercritical injection regimes.

As the critical point of the injectants is approached, surface tension diminishes and certain thermodynamic properties deviate strongly from ideal. As the critical point is surpassed, aerodynamically dominated sprays change to a diffusion dominated jet which becomes highly influenced by internal turbulence. The supercritical jet resembles that of a high density, highly turbulent gaseous jet.

Heat transfer between injected simulants and the ambient environment has a major influence on flow evolution and jet expansion. Jet surface temperatures can rapidly increase resulting in transitions from transcritical to supercritical regimes at a similar rate. Acoustic fields have shown to have a greater influence on subcritical jets as opposed to supercritical jets resulting in the jet adopting a sinusoidal waveform consistent with the first transverse mode of the chamber.

Low pressure (subcritical) coaxial injection combustion studies have conceded positive results from a range of research groups with the successful application of diagnostic tools assisting in establishing extensive databases.

Despite a significant interest in supercritical and transcritical combustion in regard to liquid rocket engines and diesel engines, publications concerning experimental work and quantitative data is limited. Application of visualisation and measurement techniques under such high pressure, high temperature conditions are overwhelmingly challenging. Such experiments require unique, dedicated test facilities to operate at such conditions which understandably pose significant safety concerns and are financially consuming. Based on this reasoning, many published articles to date typically provide qualitative descriptions of the combustion zone and flowfield. Comprehensive characterisation of trans- and supercritical combustion with coaxially injected LOx/H_2 propellants under representative liquid propellant rocket engines has not yet

been documented.

Complex numerical models incorporating extensive theories have highlighted important physical trends inherent to supercritical mixing and reaction. Large thermophysical gradients and injection conditions within the flowfield play an important role in flowfield evolution. It remains difficult to discern which conditions play a more dominant role in localised mixing, flow-field evolution and flame stabilisation due to the limited operating points of investigation. Existing numerical models can only be validated within the confines of the limited experimental datasets currently available.

2.3.6. Gaps in Existing Knowledge

Despite the regular progress in low pressure combustion research and non-reacting high pressure studies, results can not be directly extrapolated to trans- or supercritical reacting conditions.

Non-dimensional values such as Weber number are typically used to characterise subcritical spray combustion. At supercritical conditions surface tension tends to zero and the Weber number by definition becomes infinite.

It has been shown that high relative propellant velocities R_v are imperative for efficient and stable combustion of LPRE's at combustion pressures below the critical pressure of the injectants (Wanhainen et al. (1966)). The influence of R_v (and J) on atomisation has not been verified for combustion at conditions exceeding the critical point of the injected propellants. To date, the importance of the propellant velocity ratio and momentum flux ratio on atomisation has been highlighted for non-reacting coaxial sprays at low or atmospheric pressure levels only.

Cold flow, non-reacting studies have highlighted occasional differences between research groups however results are generally consistent. Detailed studies of near critical phenomena has been limited and is yet to be explored.

Aside from the theoretical challenges faced, numerical modelling of supercritical injection continues to prove a formidable task due to the lack of experimental data crucial for comparison and model validation. Some theoretical discrepancies remain which will be overcome through continual numerical development and theoretical refinement. Understanding the intrinsic physics governing injection, mixing and reaction at trans- and supercritical conditions require parallel experimental and theoretical investigations before a unified modelling approach can be adopted and implemented for liquid rocket engine development purposes.

A parametric study of velocity ratio or momentum flux ratio effects on flame stability, combustion response, and flowfield evolution would prove beneficial in understanding global physical trends experienced at elevated pressure conditions.

Dimensionless numbers such as injection velocity ratio, momentum flux ratio, density ratio etc. can be used to characterise various operating regimes. A broad matrix of experimental data from the trans- and supercritical regime would compliment the plethora of low pressure data currently available and provide further insight into high pressure combustion processes. The effects of operating conditions and reduced pressure on combustion efficiency, flame stability and combustion response are important steps in characterising high pressure combustion and providing a valuable dataset to assist in validation of numerical models.

This work attempts to characterise high pressure LOx/H_2 combustion under conditions representative of real liquid rocket engines. Cryogenic temperatures, high mass flow rates and shear coaxial injector elements are employed in a high pressure, windowed combustion chamber operated at the P8 test facility at the DLR, Institute of Space Propulsion.

"The entire injection and combustion behaviour is fundamentally different from that experienced at low, subcritical pressures (Mayer and Smith, (2004))."

2.3.7. Experimental Characterisation of High Pressure Combustion

In retrospect to the void of high pressure combustion experiments and a lack of validation data, a series of test campaigns were planned and undertaken in the hope of filling a part of the void. A dedicated experimental thrust chamber and high pressure test facility has been employed coupled with a series of optical diagnostics techniques in order to characterise the near field of a single shear coaxially injected LOx/H_2 rocket engine thrust chamber. An elaborate measurement system was developed and implemented to ensure all operating parameters were known throughout an entire test.

A range of operating pressure and H_2 injection temperatures have been investigated with the application of ultra high speed diagnostics to investigate the combustion zone and flowfield behaviour. This series of test covered a broad matrix of conditions enabling the determination of dominant trends under different conditions. A campaign based on an advanced optical diagnostic technique termed coherent anti-Stokes Raman spectroscopy has reported a range of temperature data elucidating temperature profiles in the near injector zone at elevated pressure conditions.

Chapter 3

Experimental Approach

3.1 Introduction

Experiments outlined in this work were performed at the German Aerospace Centre (DLR), Institute of Space Propulsion. The data and results contained herein were collected over a series of extensive large scale experimental test campaigns. This section introduces the DLR Institute of Space Propulsion followed by a brief explanation of the test facility utilised for the experiments. Descriptions of the individual test campaigns follow detailing the aims of each and finally, descriptions of the hardware, measurement systems and diagnostic techniques employed are provided.

3.1.1. DLR Institute of Space Propulsion

Located in a remote forest in the area of Hardthausen, the German Aerospace Centre, Institute of Space Propulsion is the largest liquid rocket engine test facility in Western Europe. Established in

1959, the DLR has provided decades of testing for Europe's aerospace program and the 'Ariane' family of launch vehicles. The institute currently tests the main engine (Vulcain II) and the upper stage engine (Aestus) from the current European launch vehicle Ariane V. The new upper stage engine 'Vinci' is currently being qualified prior to flight testing. The DLR has numerous test facilities constructed primarily for research and development purposes. A high pressure test facility designated 'P8' was developed and erected at the DLR in cooperation with CNES, the French space agency and partners from French and German industry. The test bench was constructed primarily for O_2/H_2 liquid rocket engine research.

3.2 The P8 Test Facility

The P8 test bench claims to be one of the most sophisticated research test facilities in Europe. The facility consists of two identical test cells available for testing up to 100 days per year. The bench has a high pressure supply system for liquid oxygen (LOx) and gaseous hydrogen (GH_2) with a maximum pressure level of 360 bar at the test specimen interface. Propellant mass flow rates of up to 8kg/s of LOx and 1.5 kg/s of GH_2 are achievable. A high pressure, de-ionized cooling water system can provide a maximum mass flow rate of 50 kg/s with a 200 bar interface pressure. Nitrogen is available in gaseous or liquid form and Helium in a gaseous state for cooling and purging purposes. Test duration of up to 7 minutes have been achieved and test periods of approximately 15 seconds are possible at the highest propellant mass flow rate level.

A closed loop control system accurately regulates mass flow rates of all species with an elaborate series of calibrated regulation valves. Two laboratories are situated adjacent to each test cell, which accommodate measurement devices and diagnostic control systems.

Access to all necessary data acquisition channels and command lines of P8 is provided to the

diagnostic rooms to enable remote real-time and programmable operation of sensitive diagnostic equipment. All equipment and measurement system devices are connected to the Measurement Command and Control system (MCC) via optical data transfer lines.

The entire test bench facility and control system is monitored and controlled by the MCC which can facilitate remote operation of optical and laser diagnostic equipment. The MCC records and stores data at very high sampling rates from the test facility and user channels.

The entire system described is operated remotely from the control building D68, some 150m from the test bench itself. Due to strict safety regulations, all personnel must remain inside the control building prior to, during, and after testing.

Figure 3.1 illustrates the observation monitors and remote terminals in the test facility control room. A schematic of the test facility is shown in Figure 3.2.

Figure 3.1 Remote operations in the control building (D68) for the P8 test facility

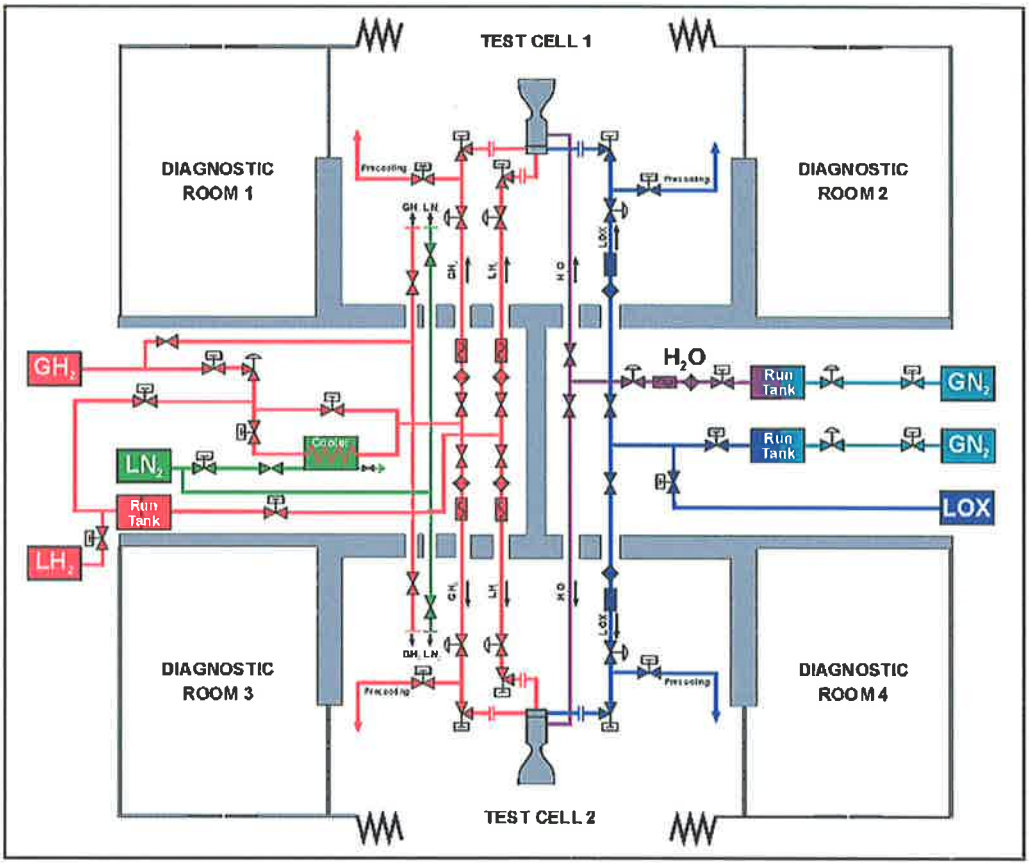

Figure 3.2 Schematic of P8 test facility illustrating opposing test cells and diagnostic rooms.

3.2.1. Test Operating Sequence

Operating sequences are programmed into the MCC to monitor, regulate and control the test specimen prior to, during and after operation. Once the MCC is set to pre-test mode, a series of "redline" limits are also set. Redlines are set for nearly all measurement devices and data transfer channels connected to the specimen. Should a particular pressure, temperature, or mass flow value fall outside of a specified range, the MCC will automatically switch to shutdown mode. The implementation of such a system is imperative to ensure maximum safety of personnel, test facility and hardware. A range of diverse operating sequences have been specifically developed and calibrated based on the aims and requirements of the individual tests and test specimens. Test duration typically ranges from approximately 7 seconds to over 7 minutes.

3.2.2. Test Campaigns

Experimental test campaigns undertaken are frequently referred to herein. A brief introduction to each test campaign is provided Table 3.1 in tabular format for convenient reference.

Table 3.1 Test campaign overview

Designation	Date	Injector	Purpose
VIS2001	2001	Single shear coaxial	High Pressure LOx/LH_2 & GH_2 visualisation, H_2 temperature effects at constant v_R and temperature mapping (CARS)
VIS2003/2004	2003/2004	Single shear coaxial	High Pressure LOx/H_2 parametric study. Effect of injection conditions on combustion. High speed flame emission and flow field imaging.

Both test campaigns listed in Table 3.1 employed the single shear coaxial injector element with LOx and H_2 in gaseous and liquid form. Test campaign designated VIS2001 utilised a generic measurement system similar to that used in VIS2003/2004 (outlined in Section 3.4). The optical diagnostics systems utilised for each campaign differed significantly and are discussed in the proceeding sections. The preliminary VIS2001 campaign provided valuable experience which resulted in substantial operational and diagnostic improvements and a highly successful VIS2003/2004 test series.

3.3 Hardware

3.3.1. Combustion Chamber C

A windowed combustion chamber designated 'Combustor C' has been developed within the DLR for research purposes. The combustion chamber shown in Figure 3.3 is of modular design with 5 main chamber segments. The thrust chamber body is constructed primarily from a copper alloy due to its favourable heat transfer properties and is cooled with de-ionized water during operation.

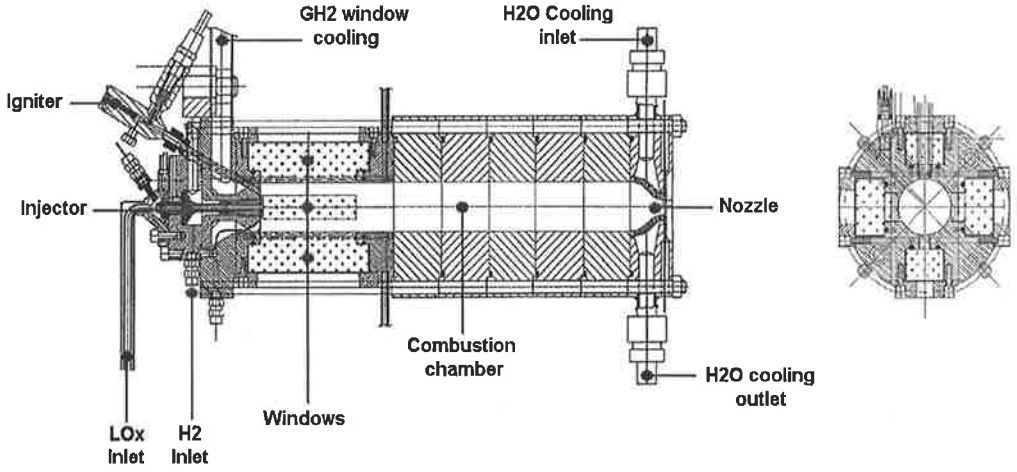

Figure 3.3 Schematic of combustion chamber C highlighting major details (from Smith and Bechle et al. (2004))

Combustor C has been designed to withstand internal combustion pressures of up to 100 bar. The first chamber segment accommodates up to 4 quartz glass windows for optical access as shown in Figure 3.3. The glass windows thickness of 40mm is necessary to withstand extreme pressure and temperature conditions during ignition transients and steady-state thrust chamber operation. Gaseous hydrogen film cooling protects the quartz glass windows and ensures they remain clean during thrust chamber operation.

As a safety measure, 'dummy' windows manufactured from steel are fitted prior to the installation of glass windows for each and every test condition. Dummy windows accommodate a series of thermocouples which monitor wall temperatures during thrust chamber operation. Once a satisfactory ignition sequence and steady operation is achieved with dummy windows they are replaced with glass windows and the optical diagnostic systems are installed.

The injection head and exhaust nozzle are interchangeable. The outlet nozzle and injector head can be replaced or modified to regulate combustion chamber pressure, injection conditions and propellant mass fluxes. Various injector head arrangements have been implemented including porous injector head designs (refer Smith and Bechle et al. (2004)) however, the standard configuration utilises a single, shear coaxial injector element.

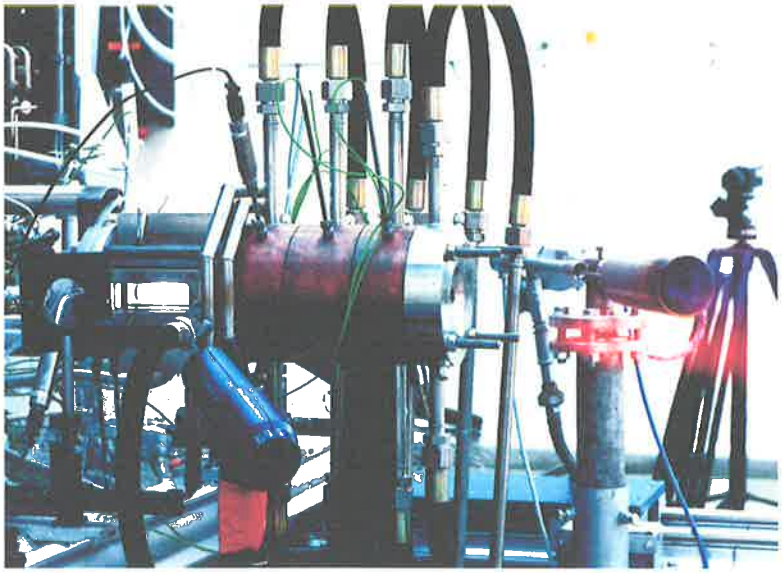

Figure 3.4 Combustion chamber C during a test at the DLR test facility P8 (from Oschwald & Smith et al. (2006))

3.3.2. Single Shear Coaxial Injector Element

The shear coaxial injection element employed for combustion studies presented here is similar to that used in modern launch vehicle main engines listed in Table 2.2. The single coaxial injector is without recess or taper in test cases detailed here. A sketch of the injector element is illustrated below in Figure 3.5.

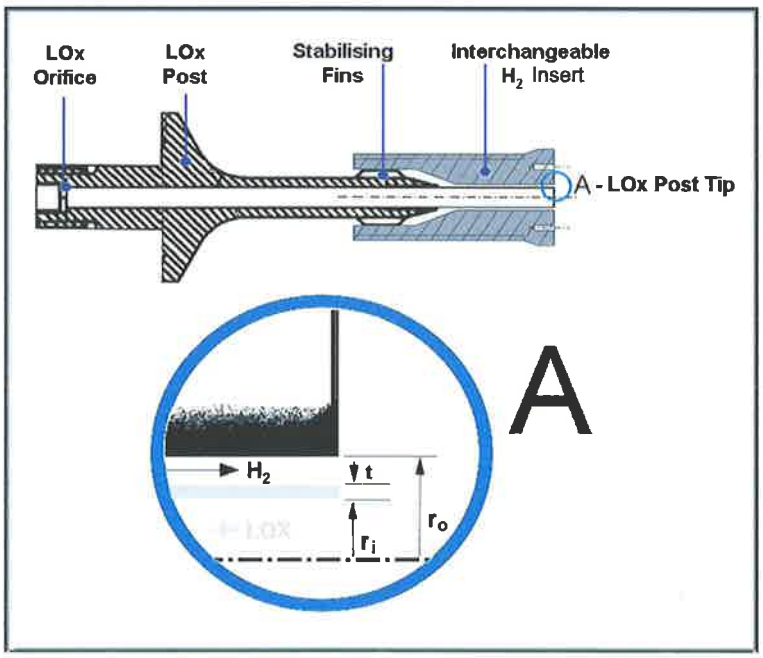

Figure 3.5 Single shear coaxial injector used in combustion chamber C (from Smith and Schneider et al. (2007))

The injector employed is a unique design as the geometry of the outer H_2 annulus is easily modified. H_2 flow rate is regulated by a threaded copper insert which fits over the LOx injector post and is secured by the LOx post stabilising fins as shown in Figure 3.5. A series of H_2 injector inserts with varying outlet geometries can be exchanged through the exhaust nozzle without having to remove any other components from the thrust chamber. Changing the internal geometry of the H_2 injection annulus enables precise adjustment of the H_2 injection velocity (at constant flow rate) as shown by continuity in equations (3.1) and (3.2) below.

$$\dot{m} = \rho v A \tag{3.1}$$

$$v_{H_2} = \left(\frac{\dot{m}}{\rho A}\right)_{H_2} \tag{3.2}$$

A sufficient pressure drop across both sides of the injector (ΔP_{H2} and ΔP_{O2}) is necessary to suppress combustion chamber and propellant feed system coupling otherwise known as low frequency combustion instability (see Chapter 9). Extra stabilising fins are added to the LOx post when large diameter H_2 inserts are fitted to ensure a satisfactory ΔP_{H2} is achieved (see Figure 3.6). A metering orifice is added to inlet of the LOx tube on all injectors to ensure sufficient pressure drop ΔP_{O2} is achieved as shown in Figure 3.5.

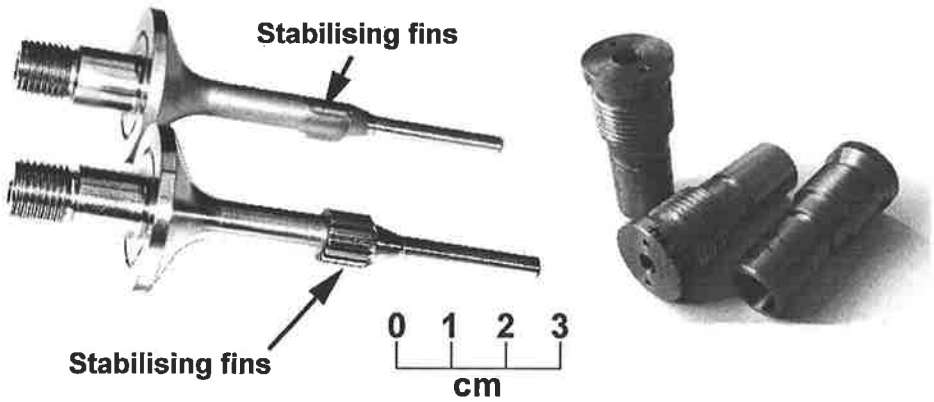

Figure 3.6 Coaxial injector LOx posts with stabilising fins and interchangeable H_2 inserts

3.4 Thrust Chamber Measurement System

An extensive measurement system fitted to the test specimen is necessary to monitor conditions inside and around the chamber prior to, during and after test firing. The measurement system incorporates a closed loop control system which was developed to ensure precise propellant properties are maintained throughout an entire test. A schematic of the measurement system is shown in Figure 3.7.

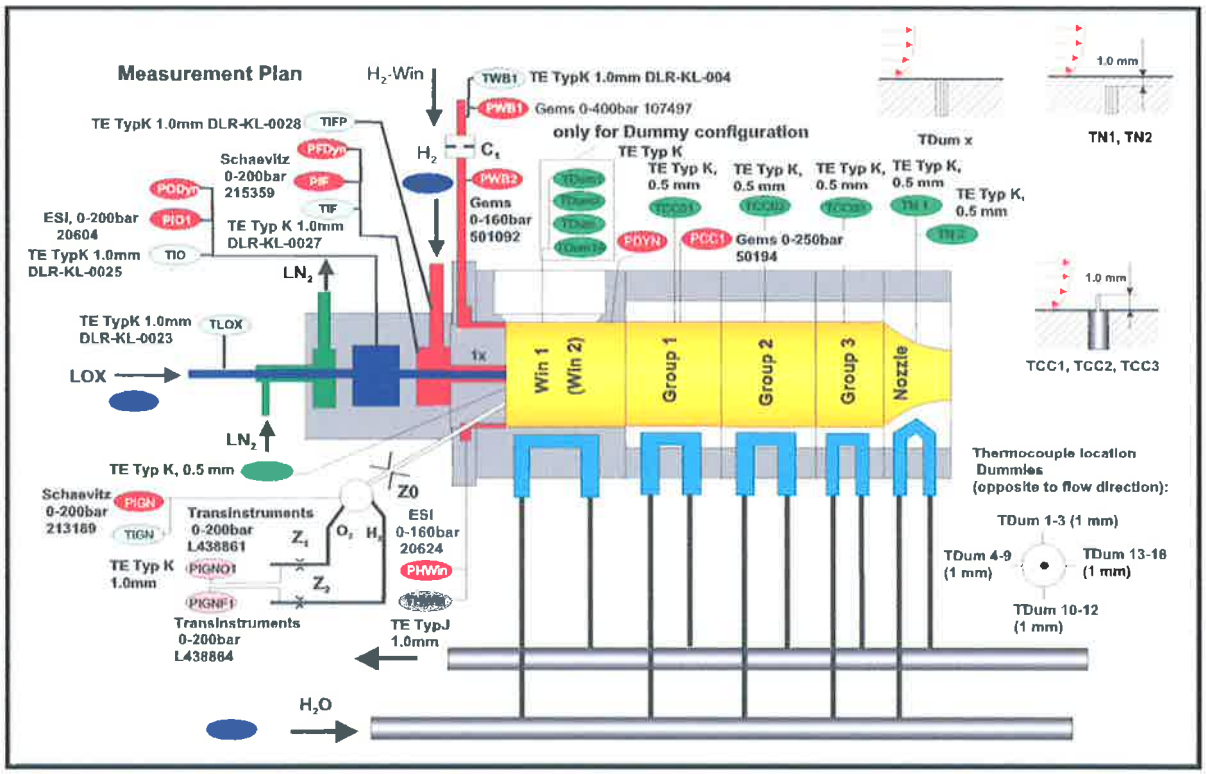

Figure 3.7 Extensive test specimen measurement system

Thermocouples are installed in the propellant feed lines and manifolds to provide accurate propellant temperature values during operation. Thermocouples are also fitted to monitor chamber wall, face plate, igniter and nozzle temperatures to ensure they remain below prescribed (redline) values. Static pressure transducers are implemented for similar reasons to ensure values remain below prescribed limits. Pressure and temperature data from the propellant manifolds provide important information on injection conditions during ignition and steady operation.

Dynamic pressure transducers are mounted within manifolds and the thrust chamber itself to capture high frequency (HF) pressure data throughout each test. The dynamic pressure data acquisition rate was typically set to 100kHz. Such high sampling frequencies are necessary to resolve the acoustic modes of the thrust chamber.

3.4.1. Temperature Measurement Errors

All propellant mass flow meters, thermocouples and pressure transducers have been individually calibrated to ensure maximum accuracy. Thermocouples mounted in the propellant feed lines and thrust chamber manifolds experience cryogenic temperatures as low as 50K. A unique method was developed and employed to calibrate conventional thermocouples to such low temperatures on site.

A dedicated cryogenic calibration laboratory at the DLR Institute of Space Propulsion employs a liquid helium (LHe) cryostat and an advanced measurement system for high accuracy, low temperature calibration. The system was utilised to calibrate a series of 'K type', class 3 thermocouples for cryogenic temperatures. Each thermocouple has been calibrated individually with polynomials prescribed for minimal measurement error at deep temperatures. Thermocouple accuracy is within +/-0.25K for the low propellant injection temperatures experienced. The measurement system accuracy at the test site P8 is estimated to be within +/-1K for conditions sustained during operation of combustion chamber C. This equates to a total propellant temperature measurement error of approximately +/-1.25K. For further detail of the thermocouple calibration technique and the level of precision achieved, refer to Suslov and Kopp et al. (2003).

3.4.2. LOx Mass Flow Meter Errors

The LOx flow meter was calibrated from 0.1 to 10 L/s. LOx mass flow rates typically range from approximately 0.15 kg/s to 0.35 kg/s (approximately 0.15 to ~0.35 L/s) throughout operation of combustor C. Under these conditions, the LOx flow meter calibration indicated a

maximum potential error of up to 2.6%. The volumetric flow rate measured by the flow meter is converted to a mass flow rate by the MCC based on real-time propellant temperatures recorded at 1000Hz. The propellant density required for the flow rate conversion is determined from precisely measured system pressure and temperature data. The corresponding density values are then extracted from a 'look-up table' which is based upon real-gas data from Younglove (1982).

The temperature measurement errors are less than 0.5K in the operational temperature region of interest. Similarly, the relevant pressure transducer has also been calibrated and shows an error of less than 0.25 bar in the area of interest (refer Figure 3.8). These low temperature and pressure inaccuracies result in a very low LOx density error in the region of interest (< 0.2%). This combined with the aforementioned potential 2.6% flow meter error gives a total LOx flow rate error of less than 3%. This value is the error in flow rate measurements through the flow meter itself. An analysis performed in Section 4.5.4 determines the LOx flow rate through the injector.

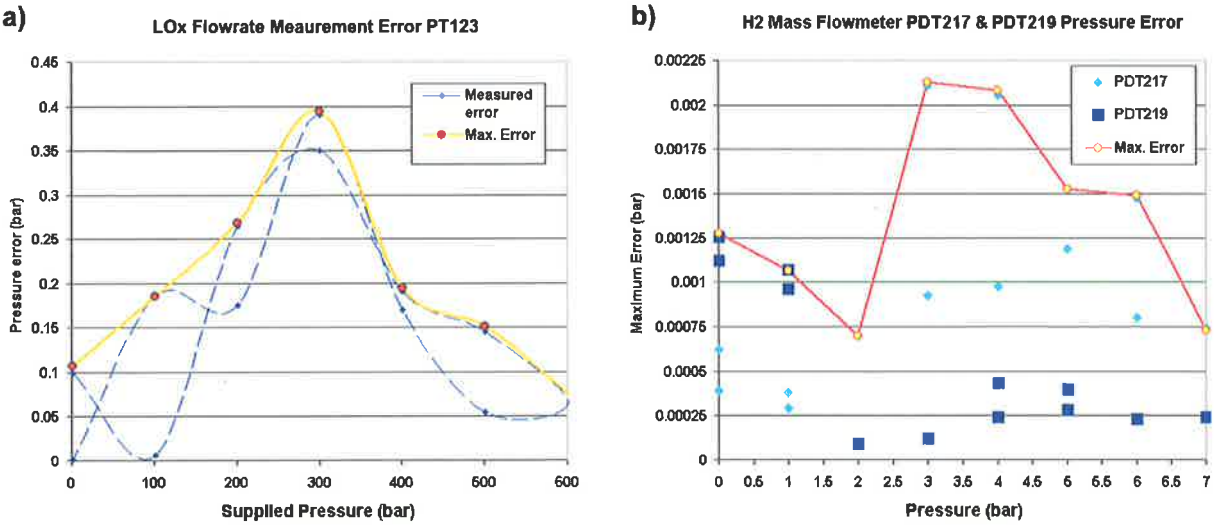

Figure 3.8 Flow meter pressure transducer calibration data showing maximum error for LOx flow meter (a) and H_2 flow meter (b)

The H_2 mass flow meter has been calibrated similarly resulting in a maximum potential error of approximately 4%. The GH_2 film cooling mass flow rate is measured using a sonic flow meter which also has an accuracy within approximately 3%.

3.5 Optical Diagnostics

A range of optical diagnostics have been employed during the test campaigns discussed herein. The optical diagnostics are implemented as a tool to assist in the understanding of high pressure injection and combustion processes through the acquisition of data which can be processed to provide quantitative and qualitative information. The techniques predominantly utilised are radical emission imaging (OH chemiluminescence and H_2O), shadow-photography, spectroscopy and coherent Anti-Stokes Raman spectroscopy (CARS). Each of these techniques is discussed briefly with references provided for further, more detailed information. Various diagnostic systems were employed for different test campaigns and thus the optical diagnostic setup for each test campaign is discussed separately.

3.5.1. Spectral Emission Imaging

Energy release through propellant reaction and combustion can be in various forms such as heat, sound and electromagnetic radiation. Sorting this radiation as a function of its wavelength is referred to as spectral analysis. This radiation is dissipated at various spectral ranges such as ultra-violet (UV), visible, and infra-red (IR). Major species such as H_2, O_2 and H_2O are transparent in the visible and UV range according to Pungor and Cornides (1969). From the intermediate species such as OH, H, and O, OH is the only combustion product which has an appreciable equilibrium concentration which gives a relatively strong signal in the near UV region between approximately 306 and 320nm (Gaydon (1974)). Formation of excited OH (OH*), can be formed in the primary reaction zone by the following chemiluminescent reactions;

$$O + H \rightarrow OH^* \tag{3.3}$$

$$H + O_2 \rightarrow OH^* + H_2O \tag{3.4}$$

Spontaneous emission of OH chemiluminescence provides an indication of the reaction zone in

an O_2/H_2 flame. Through analysis of relative spectral emission of radicals such as OH and H_2O the combustion intensity and concentration of mixed propellants within the chamber can be estimated. OH emission bands are typically well separated from those of O_2 and H_2O enabling emission spectroscopy with narrow band filtering of image intensified CCD cameras in a line of sight arrangement.

The nature of the combustion experiments (high pressure, turbulent diffusion flames with high vibration levels), makes quantification of OH LIF (laser induced fluorescence) intensity not possible and high speed line of sight imaging is considered superior option for this application.

3.5.2. Shadowgraph Photography

The shadowgraph imaging technique is relatively straight forward in terms of necessary equipment and setup and provides a non-intrusive, informative representation of a flow field in 2D (refer Settles (2006)). The principle of the shadowgraph is based upon the concept of light passing through media with differing refractive indices. The technique basically comprises of a flash lamp located behind the flow being investigated and a camera mounted on the opposite side of the flow.

The simplicity and effectiveness makes shadowgraph photography ideal for application in a liquid rocket engine due to significant density gradients. The effect of density variations is compounded by the occurrence of combustion and the introduction of high temperatures and local composition non-uniformities.

3.5.3. Coherent Anti-Stokes Raman Spectroscopy (CARS)

Coherent Anti-Stokes Raman spectroscopy (CARS) is a complex diagnostic technique which provides precise point-wise temperature and concentration measurements of major flame species. Druet and Taran (1981) provide a good overview of CARS spectroscopy.

Three lasers (2 pump and 1 Stokes) of frequencies $\omega_{p,}$ ω_p and ω_s are focused into a small probe volume at the point of interest. If the frequency difference $\Delta\omega = \omega_p - \omega_s$ is equal to a Raman-active molecular transition of a specific molecule, the molecular vibrations of this key molecule are coherently and resonantly driven by the waves ω_p and ω_s. From within this probe medium, a fourth signal ω_{CARS} is generated which has a resonantly enhanced intensity.

Experimentally, a CARS spectrum results from the interaction of the single laser pulses from the pump laser w_p and the Stokes laser ω_s exciting the molecules of the resonant and non-resonant species within the gas mixture. Application of a Stokes-laser with a broad spectral bandwidth creates a spectra over the frequency difference $\omega_p - \omega_s$ in a single laser shot. Detection and recording of the CARS signal is achieved with a multi channel CCD detector attached to the output of a conventional optical spectrometer. Collected spectra are compared to a library of spectra to deduce local temperatures and specie concentrations. Adaptation and implementation of CARS in high pressure environments has been a continual field of research within the DLR. For example, see Clauss and Il'ukhin et al. (1996), Clauss and Kozlov et al. (1997), Klimenko and Clauss et al. (2002) and Vereschagin and Vereschagin et al. (2006).

For investigations of LOx/H_2 combustion, H_2 would typically be the target probe molecule. CARS at high pressure poses difficulties due to H_2 spectral line broadening due to collisions between H_2 and H_2O. The precision of deducing temperature values from the recorded spectra is critically dependent on the reliability of line broadening coefficients together with their dependencies on temperature and concentration of collision partners. To overcome this, H_2/H_2O line broadening coefficients were measured extensively using a Fabry-Perot interferometer in conjunction with a variable pressure, pulsed hydrogen-oxygen burner by Clauss and Klimenko et al. (2002). The spectral library developed was utilised here to deduce local the temperature values from the spectral data collected the experimental campaign outlined here in Section 3.6.4.

3.6 Initial Experimental Setup VIS2001

3.6.1. Aims

The primary aim of the initial experimental campaign was to develop a reliable operating sequence for the thrust chamber. The secondary aim was to implement a range of diagnostic equipment in an attempt to visualise and characterise the high pressure combusting flow field both qualitatively and quantitatively at different H_2 injection temperatures. Diagnostics implemented would provide information on the combustion zone, flame emission intensity, and propellant flow field. Combustion response was also a point of interest with information deduced from dynamic pressure data.

3.6.2. Operating Conditions

The nominal target operating pressure for the initial test campaign VIS2001 was approximately 60 bar. This would provide a transcritical/supercritical injection condition. Propellant injection velocity ratio R_v and momentum flux ratio J were maintained relatively constant throughout the test campaign as shown in Table 3.2.

Table 3.2 VIS2001 test conditions

	Test Case 1 (VIS03A)	**Test Case 2 (VIS04B)**
Chamber pressure P_{ch} (bar)	59.4	63.1
H_2 temperature T_{H2} (K)	117	~ 55
H_2 mass flow rate m_{H2} (kg/s)	0.06	0.08
H_2 density ρ_{H2} (kg/m³)	11.94	34.7
O_2 temperature T_{O2} (K)	115.5	95.7
O_2 mass flow rate m_{O2} (kg/s)	0.29	0.3
O_2 density ρ_{O2} (kg/m³)	1024.4	1128.2
Injection velocity ratio R_v	13.47	11.12
Momentum flux ratio J	2.11	3.80

The H_2 injection temperature was adjusted and the H_2 injector insert was exchanged between tests. Injection conditions initially reported by Smith and Klimenko et al. (2002) are now believed to be slightly incorrect due to the application of a polynomial which results in slightly

inaccurate thermocouple measurements at very low temperatures. Test case 1 is dubbed the GH_2 (gaseous hydrogen) condition whilst test case 2 is termed the LH_2 (liquid hydrogen) scenario. Table 3.2 provides an overview of test conditions examined with corrected temperature values. Test measurement and image data is divided into regimes based on combustor operating phases. A transient period exists upon start-up which involves opening of the main propellant run valves and ignition of the propellant mixture. During this period, propellant mass flow rates and injection temperatures fluctuate. This period of operation is referred to as the ignition transient. Once the combustion chamber reaches nominal pressure, mass flow rates and propellant temperatures are typically steady. From this point forward, the thrust chamber is said to be in steady state operation until the shutdown phase. Figure 3.9 presents the ignition transient and steady state operation phases relative to combustion chamber operating conditions.

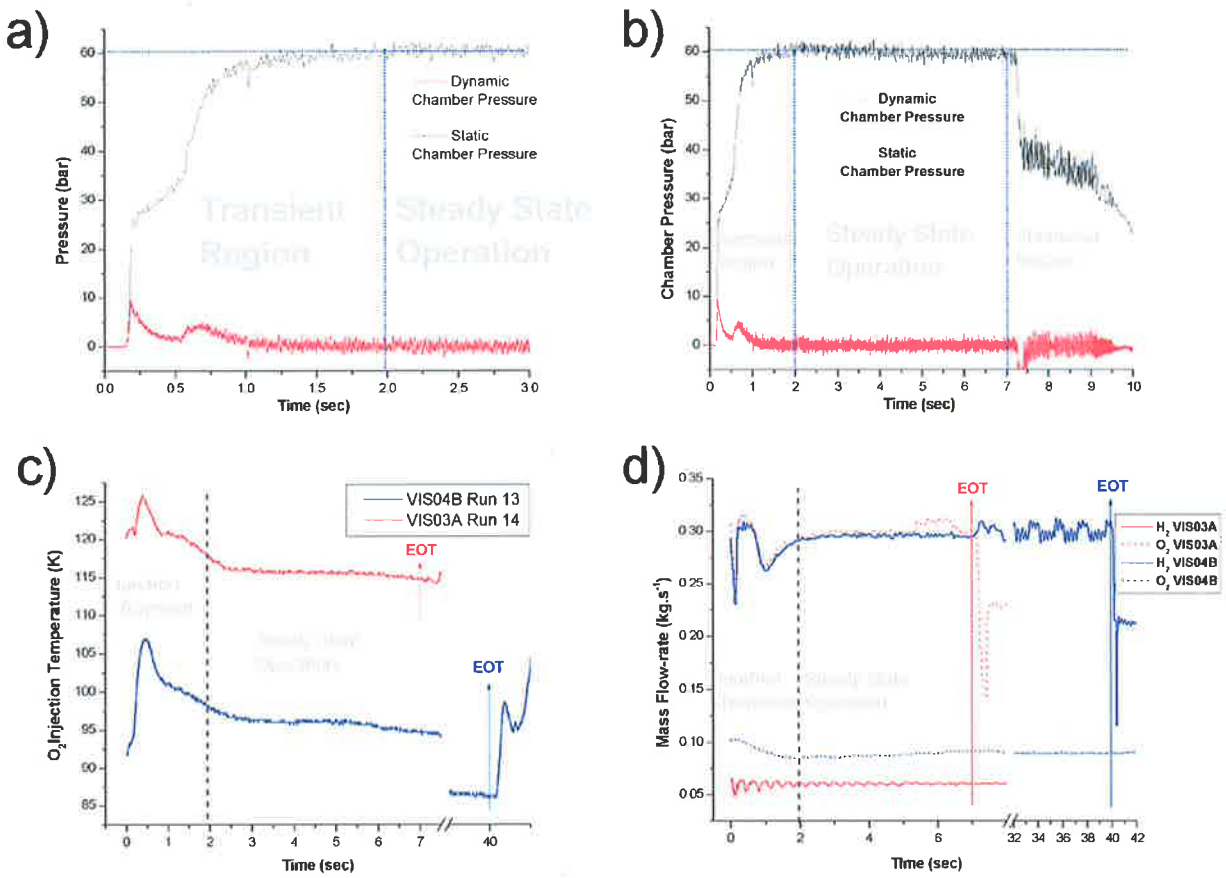

Figure 3.9 Ignition transient and steady state operation. Combustion chamber pressure a) and b), O_2 injection temperature c), and propellant mass flow rates d).

3.6.3. Simultaneous Flame and Flow field Visualisation Setup

To capture flame emission of the OH radical, an intensified, gated CCD camera (PCO DiCAM II) was employed to capture line of sight (LOS) images. The DiCAM CCD camera employed a fixed focal length 105mm 1:4.5 Nikon Nikkor lens fitted with an OH bandwidth optical filter (Schott). A second, high resolution 12 bit ($2K^2$) CCD camera (Kodak Flowmaster II) was used to perform simultaneous shadowgraph imagery of the flow field. A series of initial tests were necessary to determine the dynamic range of the CCD cameras.

A pulse generator supplied the OH imaging DiCAM amplifier with a low voltage TTL trigger pulse at a frequency of 25Hz. The OH images were recorded directly to a video cassette from the DiCAM camera at 25 frames per second. The images acquired were then digitised from the magnetic tape and transferred to a PC for further analysis. The DiCAM amplifier settings maintain the OH image exposure time (width) at 20ns with a delay of 4 μsec and a gain of 6.5.

A second cable runs parallel from the TTL pulse generator and passes through a frequency splitter that moderates the 25Hz trigger pulse by a factor of 4 to a frequency of 6.25Hz. This frequency can be further reduced to 3.125Hz if necessary. This lower frequency trigger pulse is connected externally to the shadowgraph photography system comprising a nanolite driver, computer system and Flow Master camera. The shadowgraph system dictates the acquisition frequency which is a compromise between image quality (resolution) and total test (acquisition) duration. The computer system is a specialised LAVision dual processor unit equipped with DaVis 6.0 operating software. Figure 3.10 represents a schematic of the optical diagnostic setup.

The OH image acquisition and shadowgraph system images are generated from the same TTL pulse generator to ensure simultaneity. With this system, every 4th LOS OH emission image corresponds to a shadowgraph image.

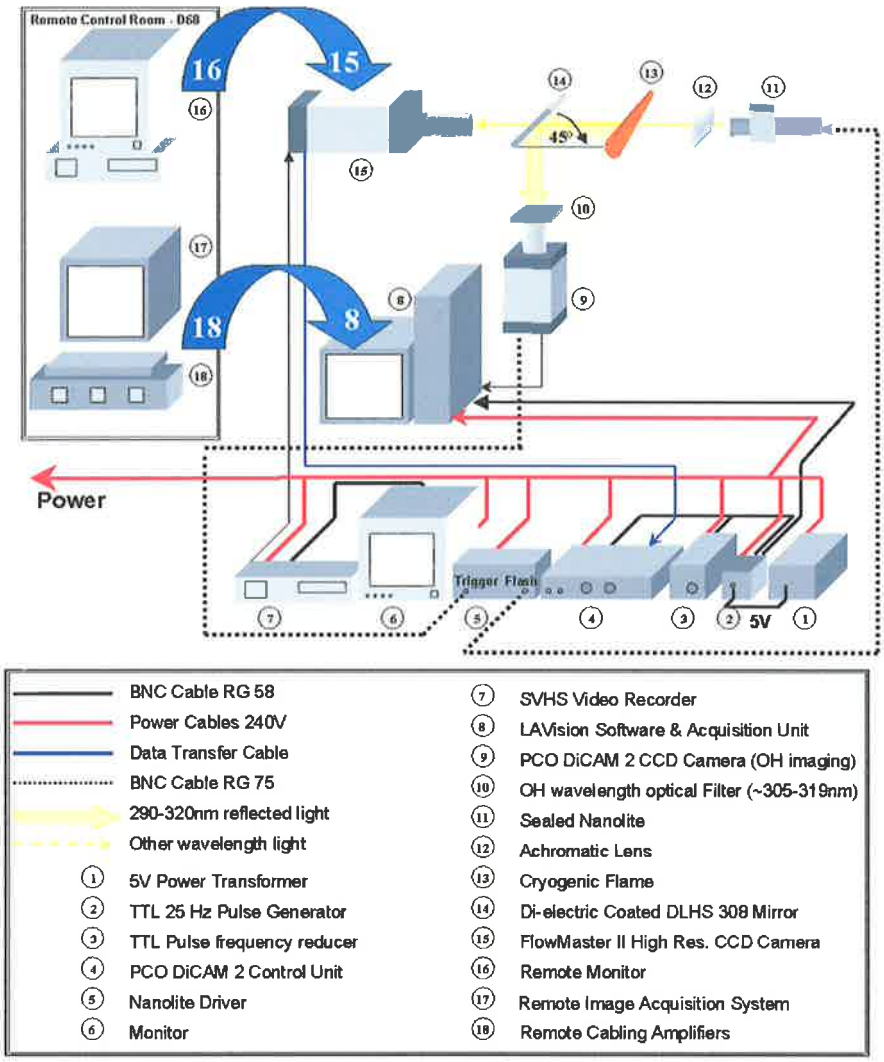

Figure 3.10 Optical diagnostic setup for initial flame and flow field visualisation experiments VIS2001

With limited confines at the test bench, it was necessary to devise an apparatus whereby both cameras achieved sufficient optical access to the near injector region to visualise the near injector region. The solution was to use a 'light splitter' and position the two CCD cameras orthogonally as shown in Figure 3.11. Flame Emission with a wavelength of λ = 290-330nm (OH radical) is reflected via a custom 'DLHS 308' Di-electric coated mirror from Linos Photonics. This light is reflected at 90 degrees, directly into the intensified DiCAM CCD camera. Further light outside of this OH bandwidth passes through the mirror and into the LA-Vision CCD camera for shadowgraph imagery. This solution proved successful with limited access at the facility

A high-speed 'nanolite' is necessary for shadowgraph imaging of high-speed flows such as those experienced within the liquid rocket engine thrust chamber. The nanolite used is a sealed unit from Impuls-Physik with a flash duration of 100ns which ensures excellent temporal resolution. The Kodak 2K²-camera exposure time of 91msec is admissible with such a short flash duration. The optical diagnostic setup for simultaneous flame and flow field visualisation is shown in Figure 3.11 mounted at the P8 test facility. Controllers, PC's and amplifiers used to operate the camera systems are situated in the diagnostic room adjacent to the test cell and operated remotely from the control building D68.

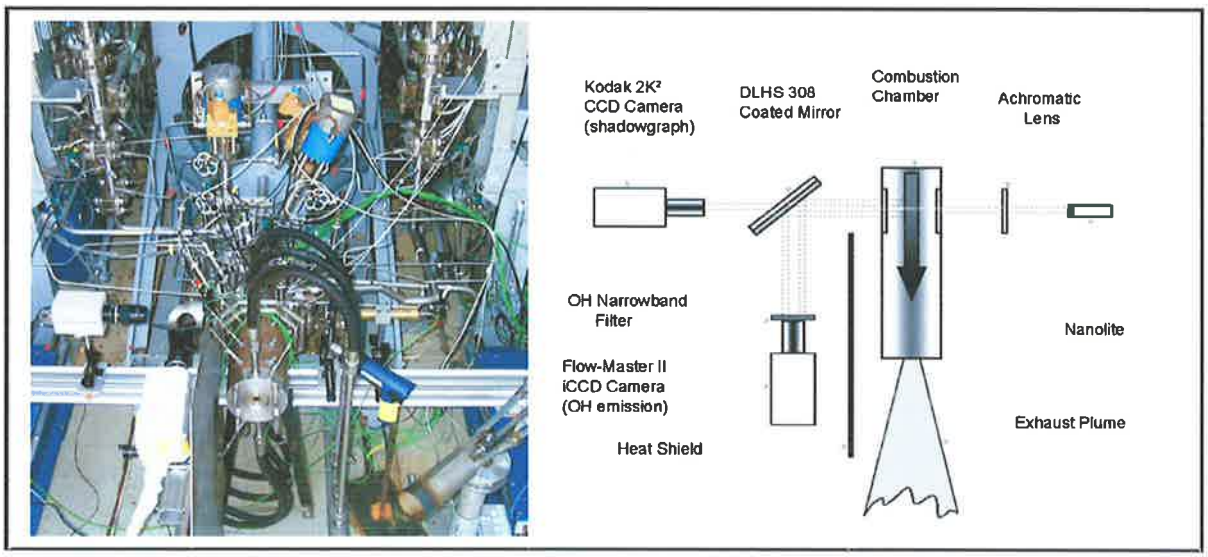

Figure 3.11 VIS2001 optical diagnostic setup at the test facility P8

3.6.4. Temperature Probing Optical Setup

The camera systems are removed to effectively install and operate the CARS system for temperature measurements. The CARS system consists of a Coherent "Infinity" frequency doubled single mode Nd:YAG laser which is used to pump modeless dye lasers. A degenerate CARS setup with a single dye laser was applied as well as Dual-Broadband-CARS (see Eckbreth (1996)). The CARS system employed was developed by the group of Smirnov et al. (1999) and the layout of the experimental setup is shown schematically in Figure 3.12.

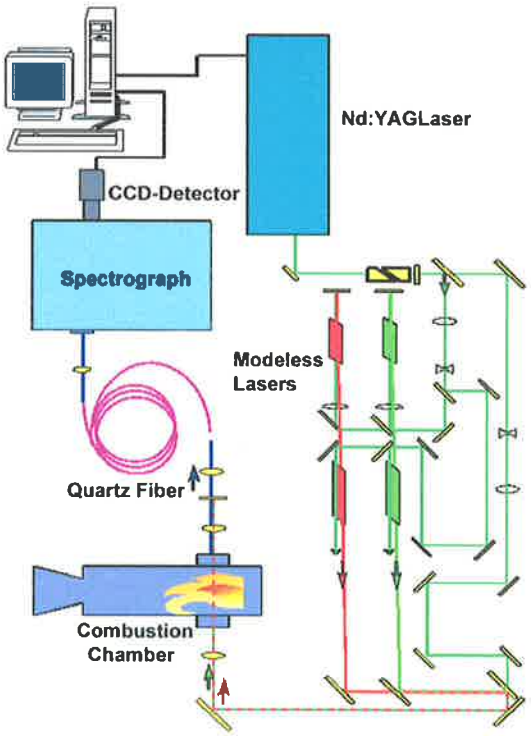

Figure 3.12 Coherent anti-Stokes Raman spectroscopy setup (from Klimenko and Clauss et al. (2002))

The CARS system was initially set up for simultaneous probing of H_2 and H_2O molecules using a mixture of Pyridin and DCM dyes. A CARS signal is only measured when sufficient concentration of the target molecule enters the probe volume. Therefore probing for a reactant (H_2) and a product (H_2O) essentially increases the chance of a signal by a factor of 2. The laser beams were combined either in planar BOXCARS or angle geometry and focused into the probe volume resulting in a measured longitudinal and spatial resolution of about 2mm and 2.5 mm respectively. The CARS beam was delivered to the detection system via a 6m long 600μm diameter fused silica fiber in order to avoid vibration problems typically experienced with conventional mirror optics. A 46-cm HR460 (1200 grooves/mm) Jobin Yvon spectrograph was used with an acquisition system consisting of a back illuminated 256x1024 CCD detector, an ISI138 16 bit 430kHz controller and the PI Winspec data acquisition software.

Due to the strong vibration levels at the test site, the laser system was situated in a diagnostic room adjacent to the test cell. The beam guiding optics and focusing lens' were mounted to a specially designed heavy duty translation stage and platform system shown in Figure 3.13. This platform was constructed from heavy duty linear stages, welded steel brackets and X95 optical profiles. All guiding lens' and optical components could be traversed along three axes to enable accurate mapping of the flame. Further details regarding the CARS setup is given in Smith and Klimenko et al. (2002) and Klimenko and Clauss et al. (2002).

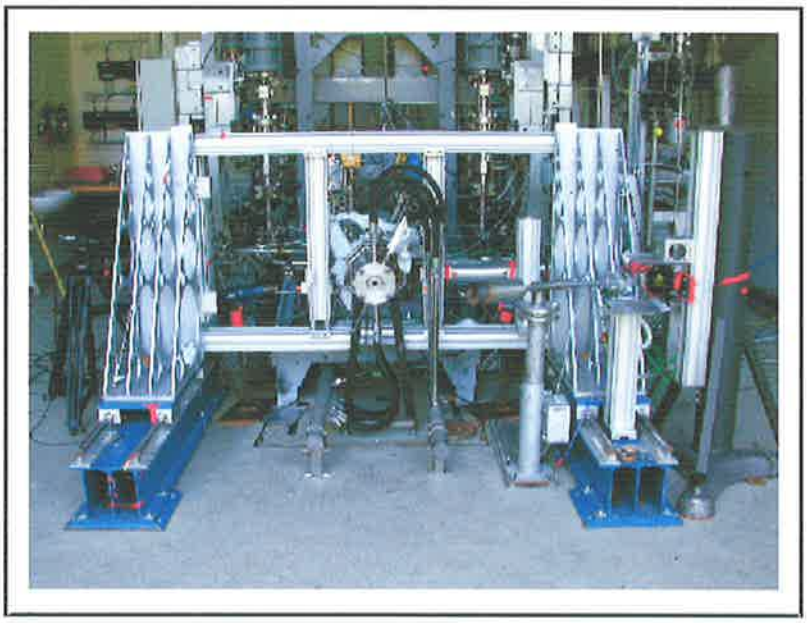

Figure 3.13 Heavy duty optical translation stage with axial traverse mounted with the rocket engine test chamber (from Klimenko and Clauss et al. (2002))

3.7 Evolved Optical Diagnostic Setup

Experimental complexities arise with the application of optics in highly turbulent, reacting flows with large density gradients, extreme thermophysical properties and stoichiometric temperatures approaching 3500K. This coupled with stringent and rigorous safety guidelines associated with high pressure test-facilities make the availability of large sets of reliable data challenging. Although fundamentally valuable, quantitative information gained through the successful application of advanced optical and laser diagnostics in high pressure thrust chambers has been limited in previous experimental studies. (i.e. Smith and Klimenko et al. (2002), Ivancic and Mayer (2002)).

Typically, low data acquisition rates have produced results with reduced statistical confidence. Temporal resolution of previous investigations have been limited to around 25Hz which have provided no information on the evolution of the flame and flow field and transient phenomena such as ignition. Ultra high speed diagnostics not only provide temporally resolved events but provide a significant increase in the number of images from a single test and hence increase the statistical confidence of the data and results. Advances in state-of-the-art camera systems, software and hardware has extended the capabilities enabling the resolution of diminutive time scales.

High sound pressure and vibration levels combined with space restrictions required the development of a unique optical diagnostics setup for observation of the near injector flow field and combustion zone at high acquisition rates.

An evolved optical diagnostics setup, comprising a series of high-speed camera systems and heavy duty mounting arrangements were implemented at the test facility. Diagnostics systems could be fine-tuned and interchanged depending on the test condition under investigation.

The primary purpose of the optical diagnostics systems employed was to observe the OH chemiluminescence, and the propellant flow field at the near injector field. A parametric study of a variety of test conditions would assist in characterisation of the near injector one at representative operating conditions. High sampling rates of diagnostics would ensure non-stationary and transient behaviour would be captured and resolved.

3.7.1. Proposed Operating Conditions and Test Matrix

The thrust chamber operating conditions investigated covers sub-critical, near-critical and super-critical pressure conditions. The operating sequence will realise 3 combustion chamber pressure levels (approximately 60, 50.5 and 40 bar) in a single test through modulation of the propellant mass flow rates. The proposed pressure levels represent reduced pressure values of $P_r > 1$, $P_r \sim 1$, and $P_r < 1$. An example of the proposed combustion chamber pressure trace is illustrated in Figure 3.14.

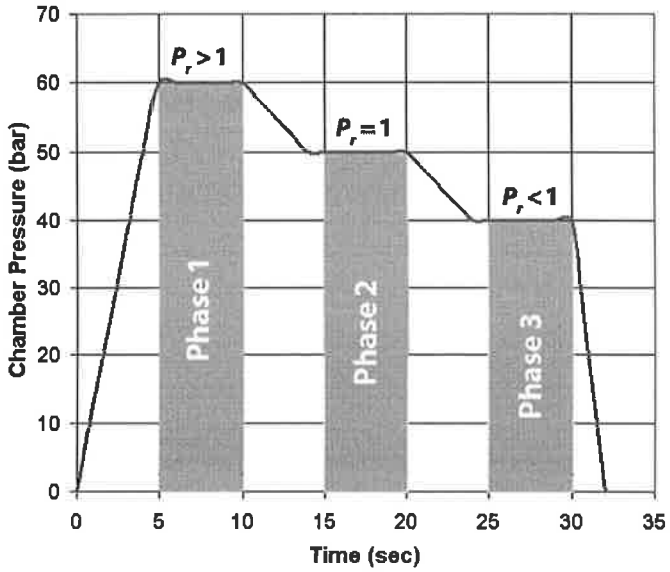

Figure 3.14 Proposed combustion chamber pressure trace highlighting pressure steps at approximately P_{ch} = 60, 50.5 and 40 bar.

A broad range of test conditions is covered in terms of propellant injection velocity ratio R_v and momentum flux ratio J (eqtn. 2.2 and 2.3 respectively). Proposed J values span 4 orders of magnitude and the velocity ratio ranges from $80 > R_v > 5$. The relationship between R_v and J is

almost linear over the conditions examined and the two values can be interchanged. As both dimensionless terms are commonly used throughout the references, a proposed test matrix is presented here for both R_v and J for completeness.

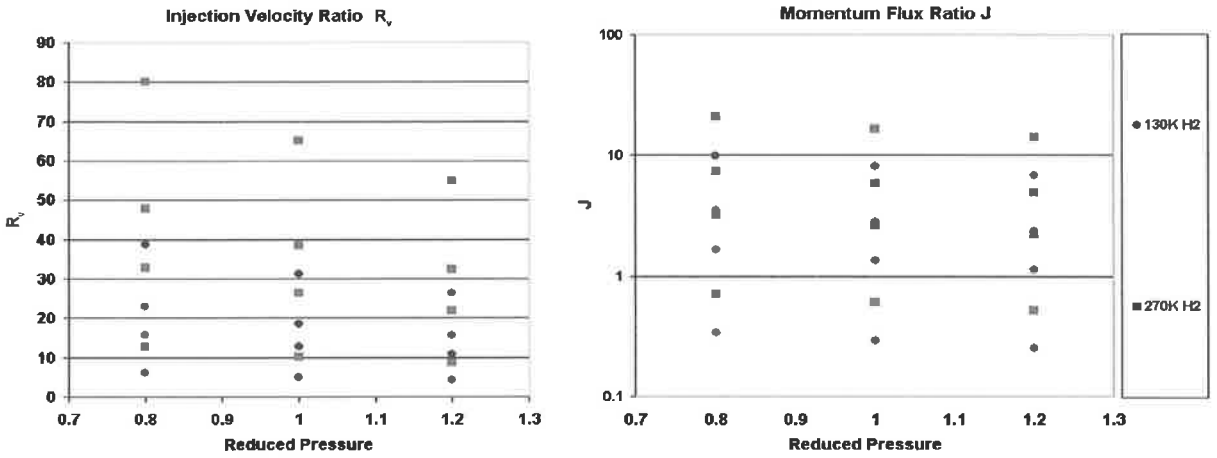

Figure 3.15 Proposed test matrix in terms of propellant injection velocity ratio (left) and propellant momentum flux ratio (right).

3.7.2. Steady State Combustion Optical Diagnostics Setup

Spontaneous OH radical emission is recorded at up to 9kHz with 128 x 256 pixel image resolution. The system used is a Photron Ultima i² SE fastcam with a shutter gated to as low as 4 ms. The image intensifier enables receptivity of low level OH emission well into the UV range (λ ~306nm - 309nm). The Ultima i² SE camera head is fitted with a fixed focal length 105mm 1:4.5 Nikon UV lens fitted with an OH narrow bandwidth optical filter (Schott) to capture spontaneous line of sight OH emission images. The narrow band filter used transmits 100% of light at λ~298-325nm as shown in Figure 3.16. The OH radical is reflected from a Linos Photonics light splitter mounted at a 45° angle to the chamber. The Photron Ultima SE camera system captures up to 16382 images at a frequency of 9kHz and thus for steady state analysis, the system is operated in a burst mode capturing 256 images every 0.5 seconds.

H_2O emission is recorded with a high speed, Photron Ultima 1024 8 bit CMOS camera unit. Image acquisition is up to 4kHz with a typical image resolution of 512x128 pixels. The camera

is fitted with an optical filter transmitting wavelengths characteristic of H_2O emission as determined from high pressure H_2/O_2 spectroscopic data from Mayer and Tamura (1996). Both Photron camera systems are operated remotely from a single PC. Control units are connected to the camera heads via dual firewire cables for a maximum data transfer rate resulting in minimised down-time at the test facility.

The high speed camera used for capturing OH emission and the associated cabling were wrapped in heat-proof material and mounted in an aluminium cases where possible positioned parallel to the thrust chamber which is further isolated from the exhaust plume by a heat shield. Running both high-speed camera systems in a burst mode avoids any biased time-averaged images which could occur should steady state images be recorded consecutively at high frequency.

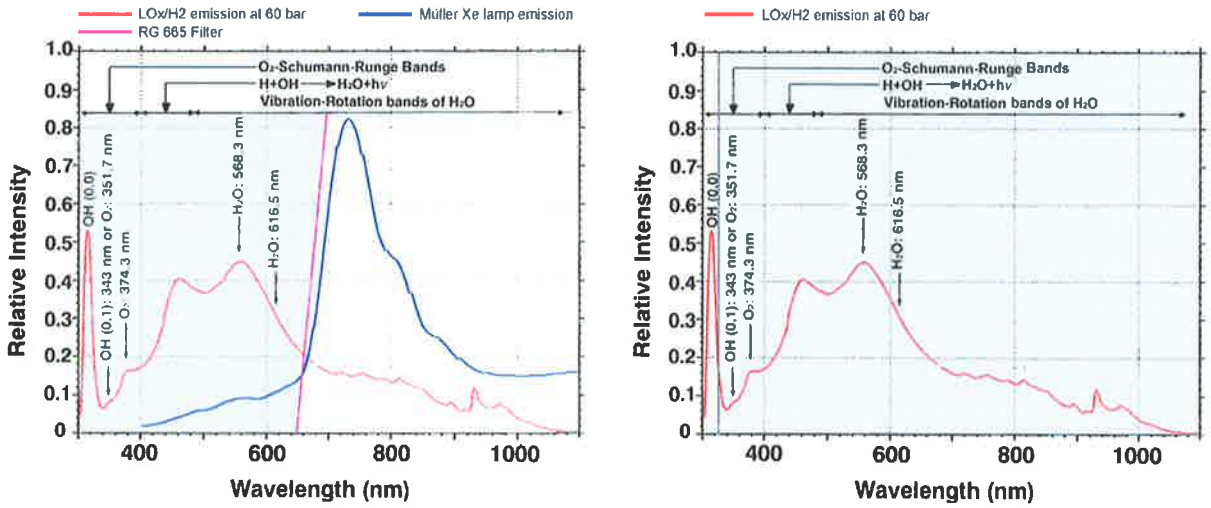

Figure 3.16 Emission spectra at P_{ch} = 60 bar and filter characteristics for shadowgraph (left) and OH emission imaging (right). LOx/H_2 emission spectra data adapted from Mayer and Tamura (1996).

A high resolution, low frequency (7Hz) shadowgraph setup was utilised to observe LOx jet stability during different operating phases. A Kodak Flowmaster $2k^2$ camera was coupled with a ultra-high speed flashlight system to ensure satisfactory temporal resolution. A high-speed nanolite lamp was focused into the aperture of the Flowmaster camera which was filtered using a Schott RG665 optical filter to suppress a majority of the flame emission while transmitting the

high intensity lamp. A significant quantity of the flame emission is suppressed through appropriate filtering as illustrated in Figure 3.16.

A nanolite flash duration of approximately 100ns provides a temporal resolution of 0.1mm with a flow velocity of 1000m/s. A backup camera was mounted (LAVision Flamestar II) and filtered for OH emission at low frequency in the case of failure of the high speed unit. A colour CCD camera was also installed for flame observation within the visual range and was fitted with a very small aperture to avoid saturation from the high intensity LOx/H_2 flame experienced at high pressure. The optical diagnostic systems were installed around the thrust chamber in various arrangements depending on the type of test. A generic configuration is shown in Figure 3.17 where 3 of the 4 available optical access quartz glass windows are utilised for optical access.

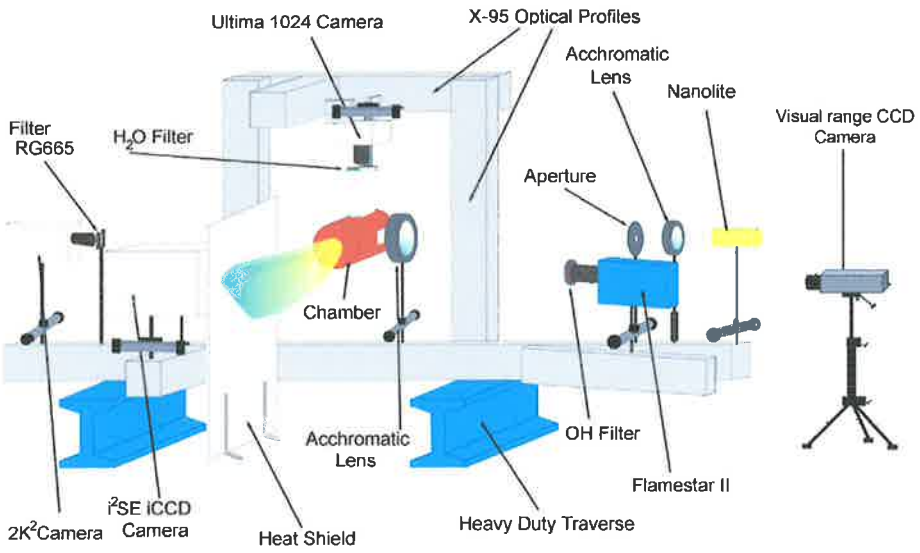

Figure 3.17 Enhanced optical diagnostics setup employed for steady state operation (from Smith and Bechle et al. (2004))

3.7.3. Ignition Transients Optical Setup

High speed shadowgraph imaging was also implemented during a series of ignition tests using the Photron Ultima 1024 in an alternative arrangement to that shown in Figure 3.17. A continuous emission Xenon lamp was used as the light source in conjunction with a high speed gated shutter from the Ultima 1024 camera. Filters were used to suppress the dominant flame emission and

transmit the Xenon lamp as shown in Figure 3.16. Frame rates up to 4000Hz provide sufficient temporal resolution and insight into transient ignition behaviour.

3.7.4. Flame Emission Spectral Measurements

Flame emission spectra were recorded from combustor C using a spectrograph and CCD detector. The investigation is undertaken to better understand the local combustion behaviour in the chamber in the near injector region. Measuring spectra and comparing relative line peaks provide an indication of dominant processes under varying operating conditions.

O_2/H_2 spectral data were recorded by Mayer and Tamura (1996) at approximately 60 bar at the former National Aerospace Laboratory of Japan (NAL). Precise operating and corresponding boundary conditions of these former tests are not known and thus performing independent test is warranted. To perform a quantitative analysis of the spectra, the transmission of the detection system must be considered. The experimental setup consists of a detection unit, optical fiber and spectroscopic system as shown in Figure 3.18.

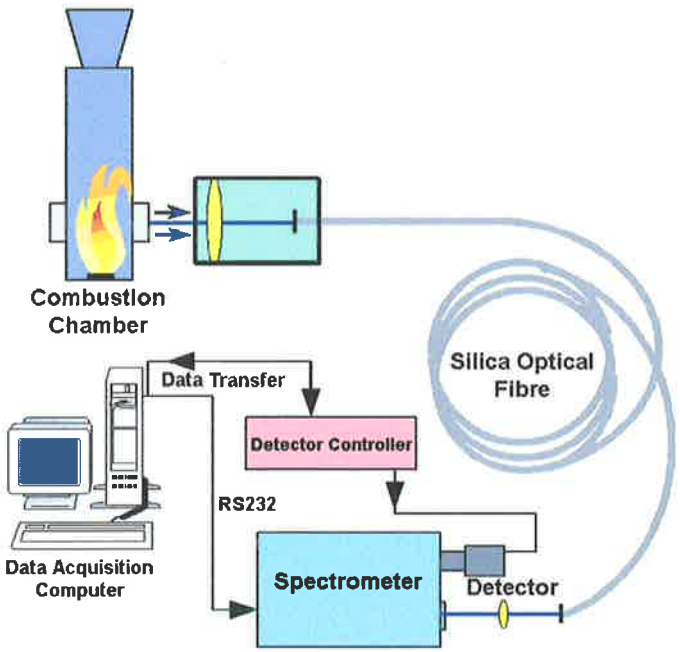

Figure 3.18 Spectrometer and detection system setup for flame emission spectral measurements

The flame emission signal was focused into a 10m long, 600-mm-diameter fused silica fiber and delivered to the spectrometer, which was positioned in an adjacent diagnostic cell. The spectrometer utilised was a 46-cm HR460 (100 grooves/mm) Jobin Yvon type. The spectral range was set for 300-700nm or 600-1100nm depending on the test. This setup was used in conjunction with a detection system consisting of a back illuminated 600x1752 CCD detector, an ISI138, 16 bit, 430kHz controller, and PI Winspec data acquisition software.

Spectra acquisition rate was 12.5Hz and with a 30 second test duration, 375 flame emission spectra were recorded during a single test. The detection system was aligned using a Ne-He laser prior to tests as shown in Figure 3.19. The spatial resolution is estimated to be 1.5 mm and 2.5mm in the axial and radial directions respectively.

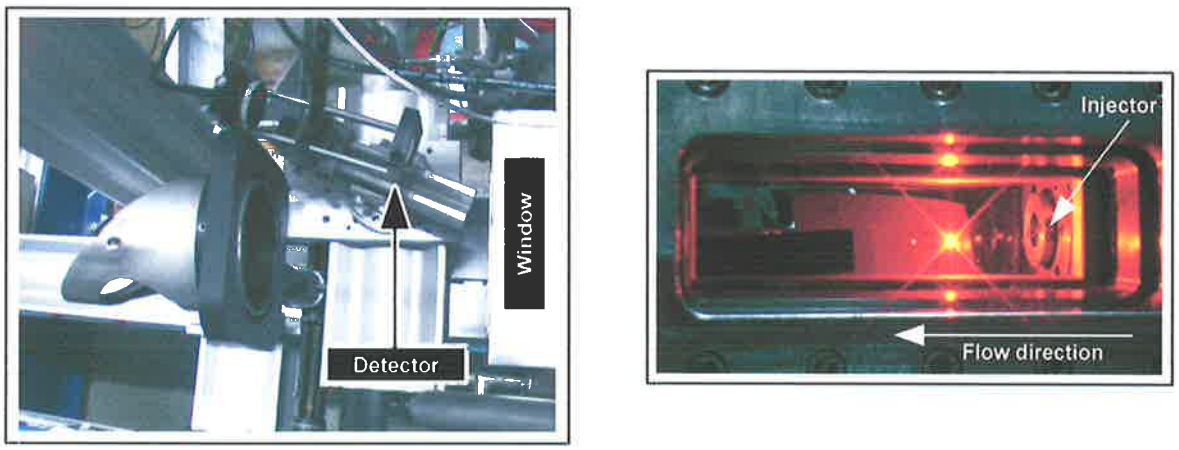

Figure 3.19 Detection system focused into window (left) and laser shot produced from the Ne-He laser used for detection system alignment

3.7.5. Precautionary Measures

Due to extreme vibration levels, all diagnostics systems were solid-mounted to X-95 optical profiles which were fixed upon a heavy duty traverse (refer Figure 3.18). Camera operating systems were arranged in the diagnostic rooms adjacent to the test cell and were further operated remotely from the control building D68.

A propane torch burner was employed to burn excess propellants exiting the exhaust nozzle

preventing any accumulation. All camera systems and cabling were wrapped with fire-resistant material as a preventative measure. The cameras and cabling were further shrouded with aluminium foil to suppress electromagnetic radiation from the ignition system, propane burner and surrounding electronic equipment. Where possible, cameras were enclosed in steel boxes to limit the potential damage in the case of an unforeseen explosion or fire. Heat shields and covers were fabricated to protect the diagnostics from the exhaust plume and the elements when the roof opens during thrust chamber operation.

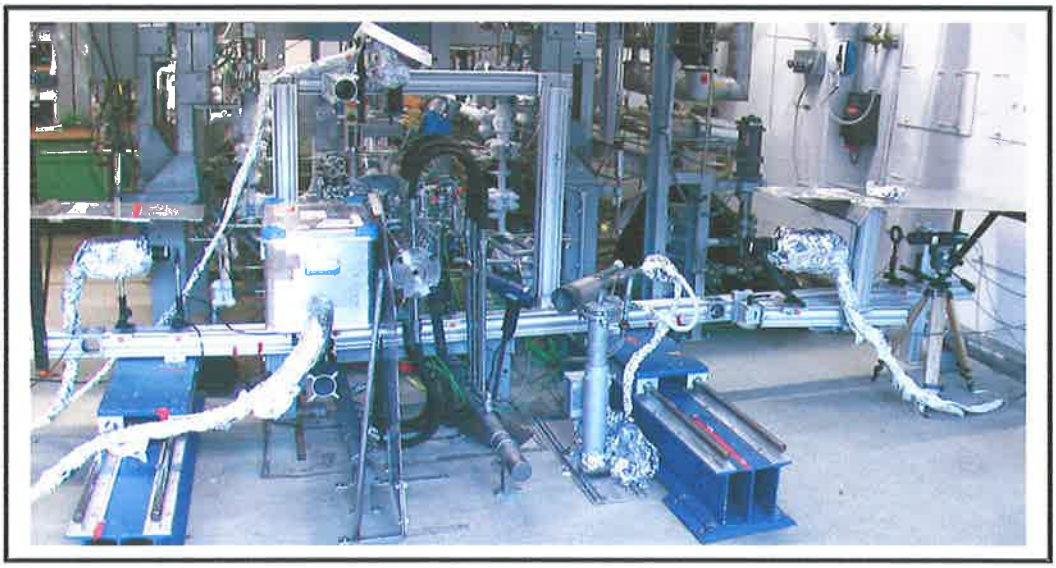

Figure 3.20 Enhanced optical diagnostics and thrust chamber setup at the test facility P8

Chapter 4

Analysis Techniques

4.1 Image and Data Processing

4.1.1. Data Processing

Processing data recorded prior to, during, and after thrust chamber operation is necessary to reveal physical phenomena and highlight common trends. Large data sets require efficient reduction techniques to minimise analysis time whilst retrieving the maximum amount of information possible. Various temperature, pressure and propellant mass flow rate values recorded throughout the individual rocket engine test firing require manipulation and analysis to accurately predict operating and injection conditions. Results from data reduction and analysis techniques are typically represented in graphical format. Spectral analysis techniques are applied to HF measurement data to reveal periodic behaviour in the thrust chamber and propellant feed systems. Unique data reduction and analysis techniques employed are discussed and detailed throughout this chapter.

4.1.2. Image Processing

Like data processing, image processing involves enhancement or manipulation of images to reveal useful information and enables extraction of data for further analysis and post processing. Operating optical diagnostics and camera systems under hostile conditions can introduce noise and distortions which can be reduced through the application of image processing techniques. Development and application of image processing methodologies coupled with measurement system data analysis techniques can be complimentary in resolving physical phenomena and dominant trends.

High speed optical diagnostic systems result in large image sets requiring batch processing to adequately cope with the volume of information. Development and implementation of various computer programs and scripts is necessary to assist in the qualitative and quantitative analysis of excessively large sets of data. Various image processing and analysis techniques performed herein are detailed in the following sections of this chapter.

4.2 Initial Test Campaign Analysis Techniques

The initial test campaign (VIS2001) provides insight to the near injector region with emission imaging, shadowgraph imaging, combustor response and propellant temperature measurements. The data obtained is assessed through the application of various image processing and data reduction techniques described here. A secondary test campaign was performed on the basis of the results from the initial test series. Significant improvements were made to the diagnostics, measurement system and hardware as outlined in the previous chapter. The secondary test campaign employed ultra-high speed diagnostics to assist in providing further insight to the flame and flowfield behaviour and the combustor response over a broad range of operating

conditions. Excessive quantities of time resolved measurement and image data warranted the development and implementation of enhanced data and image processing techniques. These additional techniques are only valid for the high speed diagnostic data from test campaign VIS2003/2004. These techniques are introduced in section 4.4 of this chapter.

4.2.1. Time Averaged OH Emission Images

The primary aim of applying this technique is to produce a mean representation of the combustion zone. Various sets of spontaneous OH emission images acquired at specific operating conditions are temporally averaged to provide a qualitative representation of the combustion zone in the near injector field. Temporal averaging of a large image series is essentially a filtering technique which 'de-speckles' images without loss of spatial resolution. In this case, fluctuations of OH emission intensity induced by transient behaviour and unsteady turbulence effects are filtered - resulting in a temporally averaged, qualitative representation of the flame emission and combustion zone.

Mean flame OH emission images and corresponding operating regimes and conditions can be compared qualitatively and quantitatively to deduce dominant trends and influential variables. Spontaneous OH emission images are initially recorded in 8-bit grey-scale format (256 levels of black and white) where white pixels represent zones of high emission intensity and black designates the low intensity regions.

A series of digitised grey-scale images corresponding to specific operating regimes are selected for averaging. The grey images recorded are typically identical in size and position which simplifies the averaging process. Each image is treated as a matrix of pixels where each pixel has a value assigned (from 0 to 255) based on the grey level intensity. The grey level intensity value of each individual pixel is averaged based upon the number of images selected.

The mean intensity value for pixel i at position $[x,y]$ for a series of N images is represented by $\bar{i}\,(x,y)$ as shown in equation (4.1).

$$\bar{i}\,[x,y] = \frac{1}{N}\sum_{n=1}^{N} i_n[x,y] \qquad (4.1)$$

The human eye has difficulty distinguishing between low intensity grey levels and thus artificial colouring is applied primarily for presentation purposes. An 8-bit, 256 red-green-blue (RGB) colour scale is applied and is represented by Figure 4.1.

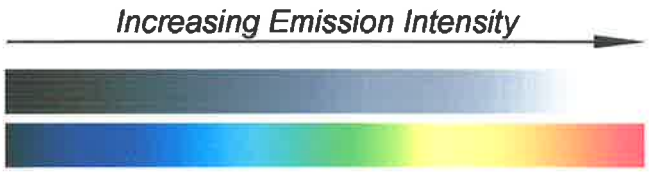

Figure 4.1 8-bit RGB colour scale applied to emission images

4.2.2. Tomographic Reconstruction Method Utilising Abel's Transform

Two dimensional (2D) OH emission images are acquired from the line of sight (LOS) optical diagnostic configuration described in Chapter 3. The 2D images represent the total radical emission from a 3-D combustion zone. The precise location of the OH radical cannot be distinguished directly from the 2-D images obtained and thus the application of an image de-convolution is necessary. The deconvolution is a mathematical technique based on Abel's transform and provides a 2D 'slice' of the combustion zone from a LOS image (Ostrovski and Butusov et al. (1977)).

The following theory describes the process for achieving the 2D representation of OH emission from the time-averaged line-of-sight images described in Section 4.2.1. Also known as the 'onion-peeling' method, the deconvolution technique assumes a rotationally symmetric flame which is treated as a set of semi-transparent layers. These assumptions are valid when applying

the technique to a series of axially symmetric, time averaged emission images. The advantage of using the time-averaged images is localised turbulence, emission absorption and scattering effects are minimised. Such a technique has been successfully applied previously by Herding and Snyder et al. (1998) to cryogenic flames.

The light intensity signal from the flame to a single pixel via the CCD detection system is summed over the radial distance through the flame and can be described by:

$$I_p(x,y) = \int_0^X \gamma(x,y,z)\, dx \qquad (4.2)$$

where X is the maximum distance which emission can be radiated and $\gamma(x,y,z)$ is the volumetric intensity assumed to be perpendicular to the camera and symmetric about the z axis where $x=y$ is the pixel dimensions. With the assumption of rotational symmetry about the orthogonal LOS axis, the variable of integration can be written:

$$r = \sqrt{y^2+x^2} \qquad (4.3)$$

which, when substituted into equation (4.2) gives an expression representative of an Abel Integral:

$$I_p(y,z) = 2\int_y^R \frac{r\gamma(z,r)}{\sqrt{r^2-y^2}}\, dr \qquad (4.4)$$

where r is the radial distance to the axis of symmetry and R is the maximum possible distance for emission transmission.

The purpose of the emission image reconstruction is to obtain $\gamma(z,r)$ from $I(y,z)$ which is achieved through application of the Inverse Abel Integral equation which can be written as:

$$\gamma(z, r) = -\frac{1}{\pi} \int_{r}^{R} \frac{\partial I_p(y, z)}{\partial y} \frac{1}{\sqrt{y^2 - r^2}} \, dy \qquad (4.5)$$

Abel's transform is the basis for reconstruction of axis-symmetric objects such as the flame emission images obtained here experimentally. An optical efficiency factor could be included however, it is assumed constant between all test cases in accordance with Herding and Snyder et al. (1998)). Emission radiation is attenuated exponentially through each flame layer and has been neglected for this analysis as this would require the inclusion of a local emission absorption coefficient for the test conditions realised (Correia and Ferrao et al. (1999)). A practical method for determining the volumetric intensity signal for pixel (y, z) is outlined in Figure 4.2 which resolves to the discrete sum:

$$I_p(j\Delta y, k\Delta z) = \sum_{i=1}^{k} A_{ik} \, \gamma(i\Delta r, k\Delta z) \qquad (4.6)$$

where $\Delta y = \Delta z$ indicates the pixel size and A_{ik} $(k\Delta z, i\Delta r)$ is the volume where $\gamma(i\Delta r, k\Delta z)$ occurs and determines the matrix of pixels with $I_p(j\Delta y, k\Delta z)$.

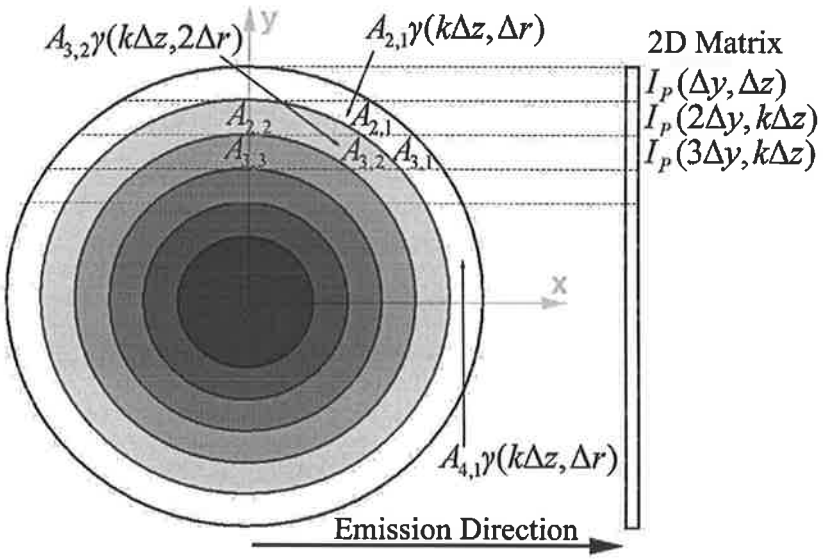

Figure 4.2 Schematic of image reconstruction principle where I(p,z) is inverted to enable calculation of γ (r,z).

4.3 Combustor Response

Analysis of HF dynamic pressure data provides information on the influence of injection and operating conditions on combustion response and stability. Combustion stability of liquid rocket engines remains today a major field of practical and theoretical research with background information found in Harrje and Reardon (1966), and more recently, Yang and Anderson (1995). Analysis of frequency spectra deduced from HF pressure data recorded from the combustion chamber and propellant manifolds provides insight to chamber acoustics and potential combustion coupling. Resonant modes of the combustion chamber can be derived analytically once an accurate approximation of the propellant mixture sound speed is obtained.

4.3.1. Propellant Mixture Sound Speed

An important consideration for accurately deriving chamber acoustic modes is a precise estimation of sound velocity in the propellant mixture (c_s) where;

$$c_s = \sqrt{nRT\gamma_s} \tag{4.7}$$

where γ_s is the isentropic exponent, given as;

$$\gamma_s = -\frac{\gamma}{\left(\frac{\partial \ln V}{\partial \ln P}\right)_T} \tag{4.8}$$

A computer program (Gordon and McBride (1994)) was used to approximate the complex chemical equilibrium composition of the injected propellants and also the specific heat ratio γ, number of moles n, and finally, the sound velocity inside the chamber c_s.

4.3.2. Combustion Chamber Acoustic Modes

Acoustic modes of the chamber are calculated based on fundamental acoustic theory. The first longitudinal acoustic mode of a cylindrical chamber with a high velocity flow is represented by equation (4.9).

$$f = \frac{c_s}{2L_c}(1 - Ma^2) \tag{4.9}$$

The propellant mixture sonic velocity values are used in conjunction with equation (4.9) to determine the longitudinal modes of the combustor. The Mach number *Ma* should be considered with high speed flows and is included in the calculations. The average chamber flow velocity has been calculated based on propellant injection velocities and continuity.

Tangential and radial mode frequencies are calculated for the combustion chamber using equation (4.10). The radial, tangential and combined modes are shown to be in excess of 20kHz due to the chamber geometry and propellant injection conditions experienced in this study (see Table 4.1).

$$f_{nm} = \frac{\beta_{nm} c_s}{2\pi r_c} \tag{4.10}$$

where β_{nm} is the value of the m^{th} zero of the n^{th} Bessel function derivative.

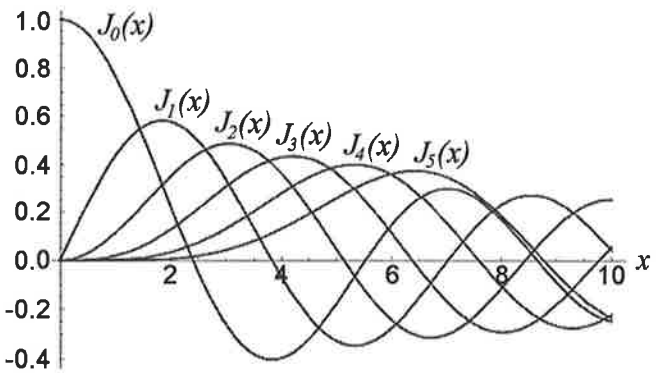

Figure 4.3 Bessel functions of the first kind $J_n(x)$

Table 4.1 Theoretical acoustic modes of the combustion chamber (dependent on injection conditions)

Mode	*f* (kHz)
1L	1.8-2.0
2L	3.6-4.0
3L	5.4-6.0
4L	7.2-8.0
1T	19-21
2T	32-35
1R	40-43
2R	73-78
1T1R	55-60
1T2R	88-95.0

4.3.3. Spectral Analysis

The HF dynamic pressure data recorded in the combustion chamber and propellant manifolds is processed to provide combustion response spectra. Transforming large amounts of stationary data from the time domain to the frequency domain is performed through the application of the Fourier Transform (FT).

The HF pressure data is sampled at a constant time interval throughout the test with sample rates ranging from 25-100kHz ($\Delta t = 4 \times 10^{-5}$ to 1×10^{-5} seconds) depending on the particular test. The measured pressure amplitudes are presented as a function of time *h(t)*;

$$h(t) = \int_{-\infty}^{\infty} H(f) e^{-2\pi i f t} df \qquad (4.11)$$

In the frequency domain, the data is presented as amplitude *H* as a function of frequency *UHF)*;

$$H(f) = \int_{-\infty}^{\infty} h(t) e^{2\pi i f t} dt \qquad (4.12)$$

The total power in a signal is calculated in either the time or the frequency domain and is also known as Parseval's Theorem;

$$Total\ Power = \int_{-\infty}^{\infty} |h(t)|^2 dt = \int_{-\infty}^{\infty} |H(f)|^2 df \qquad (4.13)$$

The power contained in a frequency interval $f + df$ (usually considered as frequency 0 to $+\infty$) is known as the one-sided Power Spectral Density (PSD) of the function h and is given by

$$P_h(f) = (|H(f)|^2 + |H(-f)|^2) \qquad 0 < f < \infty \qquad (4.14)$$

and with real $h(t)$, the two terms in equation (4.14) are equal and the PSD becomes;

$$P_h(f) = 2|H(f)|^2 \qquad (4.15)$$

The valuable range of data is determined by the Nyquist Critical Frequency;

$$f_c = \frac{1}{2\Delta} \qquad (4.16)$$

The dynamic pressure data sampled must be bandwidth limited to less than the Nyquist critical frequency as there is a large (theoretically infinite) amount of data which lies outside the domain $f_c < f < f_c$. The power spectra outside of this range can be aliased into the lower frequency range and obscure results. Spectral analysis of measurement data has been performed employing both the PSD and amplitude FT techniques throughout this study.

Various FT techniques are also employed to assess image data to reveal periodic behaviour. Further details regarding spectral analysis techniques employed can be found in Bendat and Piersol (1980).

4.3.4. CARS Spectra Fitting

Despite the relatively widespread use of CARS, the application of the technique in a high-pressure environment with a H_2 probe molecule is not a direct extension of the diagnostic technique. The small line width of H_2 make the CARS signal very sensitive to the mode structures of the exciting lasers. Typically under ambient conditions, pressure broadening of H_2 lines is not a point of concern, however this phenomenon must be taken into account in the analysis of high-pressure CARS spectra. Line broadening coefficients of the Q-branch for H_2-H_2O mixtures were adopted from Rahn and Farrow et al. (1991) and Michant and Berger et al. (2001) for H_2-H_2O and H_2-H_2 coefficients respectively. Further details are on line broadening and the coefficients used for spectral correction in this case are presented in Klimenko and Clauss et al. (2002).

To ensure accurate temperature evaluation from the CARS spectra recorded, a fitting approach was applied. After background subtraction, the CARS spectra were normalised to the appropriate spectral correction curve prior to further processing. Specialised software was employed to fit the experimentally recorded spectra to theoretically calculated spectra to obtain gas temperature values as described in Klimenko and Clauss et al. (2002).

4.4 Additional Image Processing Techniques

The sampling rate(s) of the high frequency diagnostics employed in the secondary test campaign VIS2003/2004 enables a significant extension to the image processing techniques outlined in previous sections. Enhanced data and image processing techniques take full advantage of the high temporal resolution and large number of image samples to provide additional information with increased levels of confidence.

4.4.1. Shadowgraph Image Temporal Averaging

Temporally averaged shadowgraph images depict a mean flowfield over a period of time Δt. Each pixel intensity value $i(x,y)$ from a series of images is averaged to provide a mean image as described in Section 4.2.1. It is important that the combustion chamber and optical system are free from vibration to ensure an accurate mean image is successfully constructed. Unlike the emission images, shadowgraph images are presented in grey-scale format without the application of colour. Temporally averaged images provide a mean representation of the flowfield removing unsteady phenomena such as turbulence and flowfield perturbations induced by propellant feed system or chamber pressure oscillations.

4.4.2. Time Resolved Radial and Axial Flame Emission Intensity Tracking

Near injector flame dynamics is investigated by tracking pixel intensities over a continuous series of flame OH emission images radially and axially (x and y directions). This technique is predominantly applied in the axial direction extending downstream from the injector LOx post tip. A script was developed to execute the series of commands comprising this image processing technique.

The program reads a series of specified OH emission, 8 bit grey-scale images in tagged image format (TIF). The images are converted to 2-bit or *binary* format based on a prescribed radical emission intensity value $\overline{I_{OH}}$ that is relative to the maximum pixel intensity ($I_{OH_{max}}$) value in each image. Once the 2-bit image is created based on the mean position of such values, an edge detection routine is performed to create an outline of the flame. The images are scanned in the axial and radial directions for a 'high' (white) intensity value until an edge is detected. The pixel location is recorded and the pixel number converted to a distance in mm based on image size. Each consecutive image is processed identically with the result being a list of images and corresponding position data based on the initial threshold intensity value chosen.

The resultant coordinate data is highly sensitive to the image quality and thus a the prescribed intensity threshold value is altered and the process repeated to produce a series of axial and radial positions for a range of intensity threshold values. (i.e. $0.1I_{OH_{max}}$, $0.15I_{OH_{max}}$, $0.2I_{OH_{max}}$ ...etc.). Each dataset is assessed and spectral analysis techniques are applied in an attempt to resolve any dominant frequencies or apparent flame oscillations. The technique is illustrated schematically in Figure 4.4.

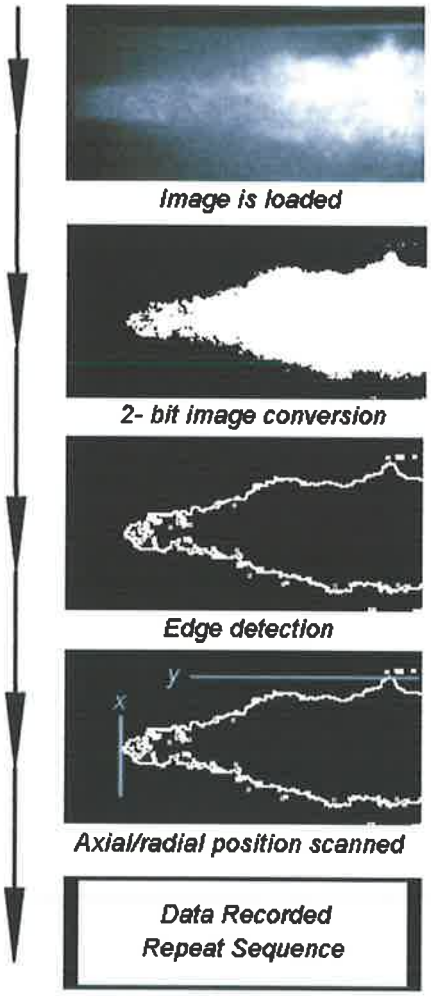

Figure 4.4 Schematic description of flame emission intensity tracking technique

4.4.3. Centre of Emission Intensity

This technique was developed to track the centre of intensity of the flame. Unlike the flame tracking technique, this script calculates the 'centroid' of intensity as a position $(\bar{x}, \bar{y})$ based on the intensity values of each individual pixel and its respective position. An image 'mask' based on the mean flame image constructed from an image series that is calculated prior to the intensity centroid routine. The pre-defined mask defines the boundaries of the flame and the centre of intensity coordinates are determined for each image in the series with dimensions set equal to the mask.

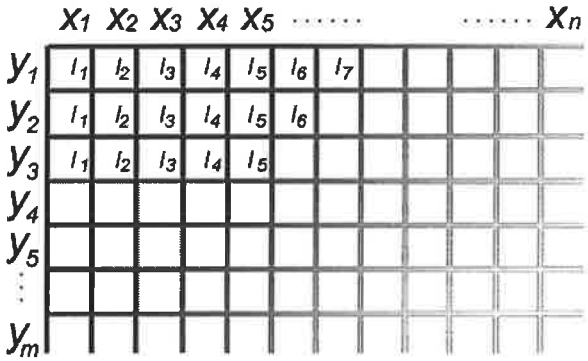

Figure 4.5 Matrix representation of a single OH emission image

Consider the intensity values of each pixel p_{xy} defined by and x and y coordinates and denoted by $\Delta I_1, \Delta I_2, \ldots \Delta I_z$. The total intensity I_{tot} is obtained by summing each individual pixel intensity value from the entire image.

$$I_{tot} = \Delta I_1 + \Delta I_2 + \ldots + \Delta I_z \tag{4.17}$$

The centre of emission intensity in the x-direction is given by the sum of each individual pixel intensity value ΔI_z multiplied by its relative position in the axial or x-direction x_n.

$$\bar{x} I_{tot} = x_1 \Delta I_1 + x_2 \Delta I_2 + \ldots + x_n \Delta I_n \tag{4.18}$$

$$\bar{x} I_{tot} = \sum_{i=1}^{n} x_i \Delta I_i \tag{4.19}$$

and similarly for the radial or y-direction y_m;

$$\bar{y}\, I_{tot} = y_1 \Delta I_1 + y_2 \Delta I_2 + \ldots + y_m \Delta I_m \qquad (4.20)$$

$$\bar{y} I_{tot} = \sum_{i=1}^{m} y_i \Delta I_i \qquad (4.21)$$

Solving equations (4.19) and (4.21) provide the centre of emission intensity coordinates $\bar{x}$ and $\bar{y}$ respectively. The centre of emission intensity technique has proven successful. Detailed results and examples are outlined in Chapter 6.

4.4.4. Flame Front Tracking

This technique was developed to track the flame front during combustor start-up and combustion instability. During steady state operation, the flame front typically extends beyond the range of the quartz glass windows and the technique cannot be applied.

The technique requires the designation of an emission intensity value which is used to trace the flame by creating a 2-bit image similar to that displayed in Figure 4.4. A prescribed region is tracked until a white or 'high' value is observed and the downstream position is recorded. This process is repeated for as many images as desired and is very similar to the process employed for the time resolved radial and axial flame emission intensity tracking technique outlined in Section 4.4.2.

The limitation of the flame front analysis is that the data is highly sensitive to the threshold value chosen for the analysis of the image series. Various threshold values are prescribed and multiple data sets created and scrutinised to provide axial flame front position as a function of time.

4.4.5. Mean OH Emission Intensity

A mean emission intensity value is calculated for each individual flame image based on the intensity value of each pixel in the image. This technique is relatively straight-forward and treats each image as a matrix where each entry denotes the emission intensity value from 0 to 255. The averaging process for each pixel is represented by equation (4.1) where N represents the total number of pixels in the image. Performing this analysis for each image recorded during a single test is useful in identifying trends in emission intensity as a function of pressure.

To simplify the analysis process, the mean emission values are calculated based on the mean images constructed during steady state operation from a series of 256 images (i.e. t = 1/9000sec). The data obtained is then normalised based on the maximum intensity value recorded during a single test. Normalising enables direct comparison between independent tests to identify common trends. This process is important as various tests have slightly different camera positions with differing fields of view and image sizes. The technique assumes the flame shape is consistent in shape and size between operating phases.

To better examine relative emission intensity during start-up, a mean flame OH emission intensity value is determined for each consecutive image based on the flame size. The resulting data is termed the relative mean flame OH emission intensity.

4.4.6. Relative Mean Flame OH Emission Intensity

A mean flame intensity value is determined for each image similar to that described in Section 4.4.5. However, a straight-forward mean emission intensity calculation does not account for changes in flame size/area which can be significant during ignition transients. This technique creates a 'trace' of the flame based on a user-defined threshold value and calculates the mean emission intensity value based on the flame size (i.e. the number of pixels encompassed by the flame 'trace'). This technique is described with the assistance of Figure 4.6.

This technique was also applied to steady state images. As the near injector flame shape does not alter significantly, little difference was observed between this technique and the mean OH emission intensity technique previously described. This technique was applied only during ignition where flame shape and length is typically highly unsteady.

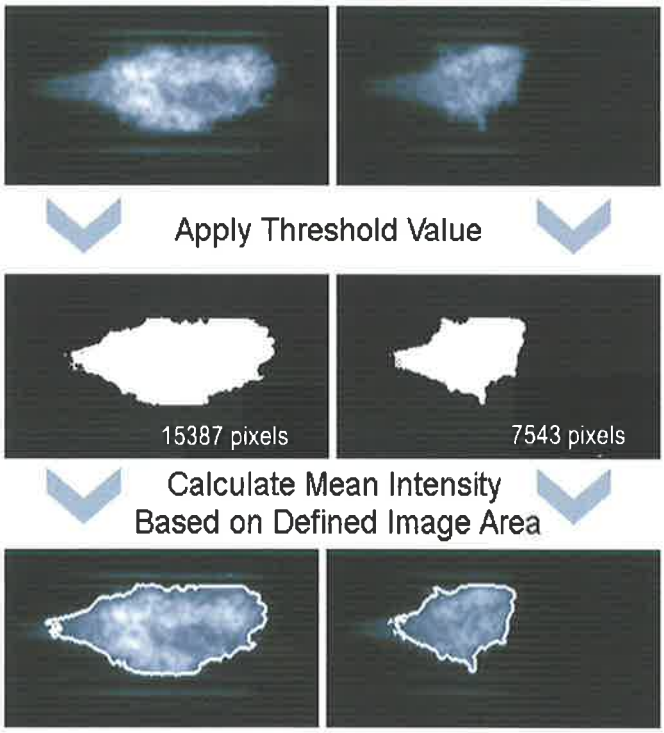

Figure 4.6 Schematic description of mean relative OH emission intensity scheme

4.4.7. Batch Crop and Re-Position

Specific operating conditions exhibited LF combustion instability. The camera and optics systems are unaffected by the unstable combustor operation and associated high vibration levels as they are fixed to a heavy duty traverse as shown in Figure 3.13. The entire thrust chamber assembly however moves significantly as depicted by Figure 4.7 which illustrates the chamber movement observed by the high-speed OH emission camera system. Movement of the thrust chamber is detrimental to image processing techniques and the images recorded require re-positioning and re-alignment prior to further processing. Details of LF combustion instability phenomena are outlined are in Chapter 9 with the image processing technique described here.

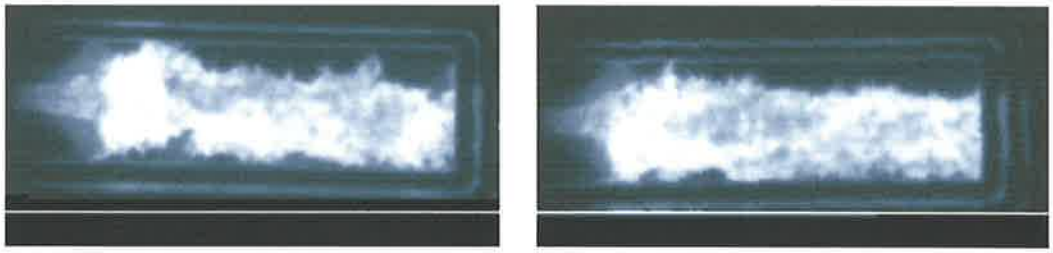

Figure 4.7 Spontaneous OH emission images captured during LF combustion instability. The image pair highlights the extent of chamber movement experienced during a single test.

In order to accurately construct the mean emission image and apply further image processing techniques, the oscillating image series is re-aligned (straightened) and cropped at a reference point common to all images. The window edge is chosen as a point of reference. The entire image re-position and crop routine is described with the assistance of Figure 4.8. Image 1 in Figure 4.8 represents a standard OH emission image rotated 90 degrees whilst image 2 is the same image which has been aligned with the window edge. The third step involves conversion to a 2-bit black and white format (image 3). Next, a predetermined area is prescribed as shown in image 4 as a red rectangle. Each column of pixels within the rectangular area is scanned from left to right until a white (high-value) pixel is found. The location is recorded and the pixel scanning process is moved 5 pixel columns to the right and re-commences scanning for a black (low-value) pixel. Once located, the second position is recorded and the image is cropped through the centre of the two values recorded with the final result illustrated by image 5 in Figure 4.8.

The sequence is repeated for all images in the image series. Various image processing techniques described in this chapter can then be applied to the series of cropped images which are free from fluctuation or oscillation.

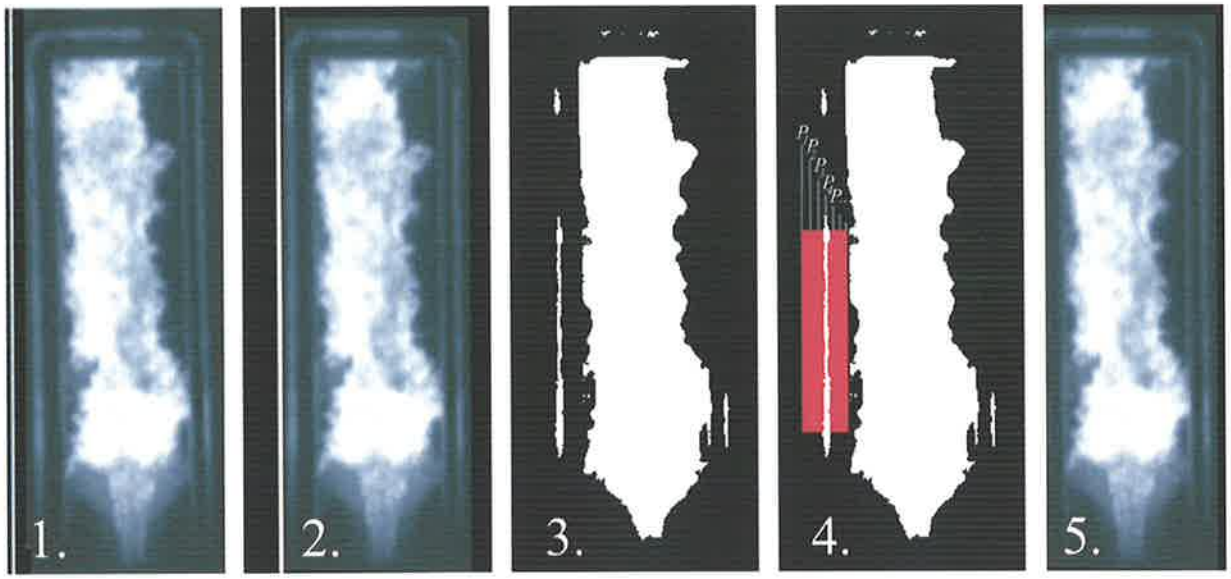

Figure 4.8 Re-position, alignment and cropping procedure for images recorded during LF combustion instability using the window frame as a reference point.

4.5 Calculating Precise Propellant Injection Conditions

Injection conditions are typically represented by non-dimensional that are strongly dependent on the thermodynamic properties of the propellant(s) which are extremely sensitive under certain operating conditions. For example, injection velocity ratio v_R is proportional to the propellant density ρ and thus an accurate estimation of density is important for all thrust chamber operating points. Accurate prediction of propellant sonic velocities and choked injector flow conditions are important in deducing injection conditions during ignition and start-up transients. Precise measurement and thermodynamic property data is mandatory in order to understand the physical processes taking place with rapid reaction and steep pressure gradients experienced during ignition. Equations of state are employed to accurately predict the thermodynamic properties with each propellant treated separately as thermodynamic properties are significantly disparate.

4.5.1. Thermodynamic Properties of Oxygen

Oxygen is typically injected as a liquid and thus cannot be modelled as an ideal gas under the conditions experienced in a liquid rocket engine. As an example, Figure 4.9 shows that below temperatures of approximately 190K, the error in estimating the sonic velocity of oxygen using the ideal gas equation becomes significant over a range of pressures. Such inaccuracies are also evident in many other thermodynamic properties at elevated pressure. Near the critical point of O_2, (~150K and 50.45 bar), errors can be up to 2 orders of magnitude! A 32 equation, modified Benedict-Webb-Rubin (MBWR) equation of state developed by Schmidt and Wagner (1985) has proven to be extremely accurate in predicting thermodynamic properties of O_2 and is employed here for maximum accuracy. Precision is high with the MBWR equation of state but is limited near the critical point.

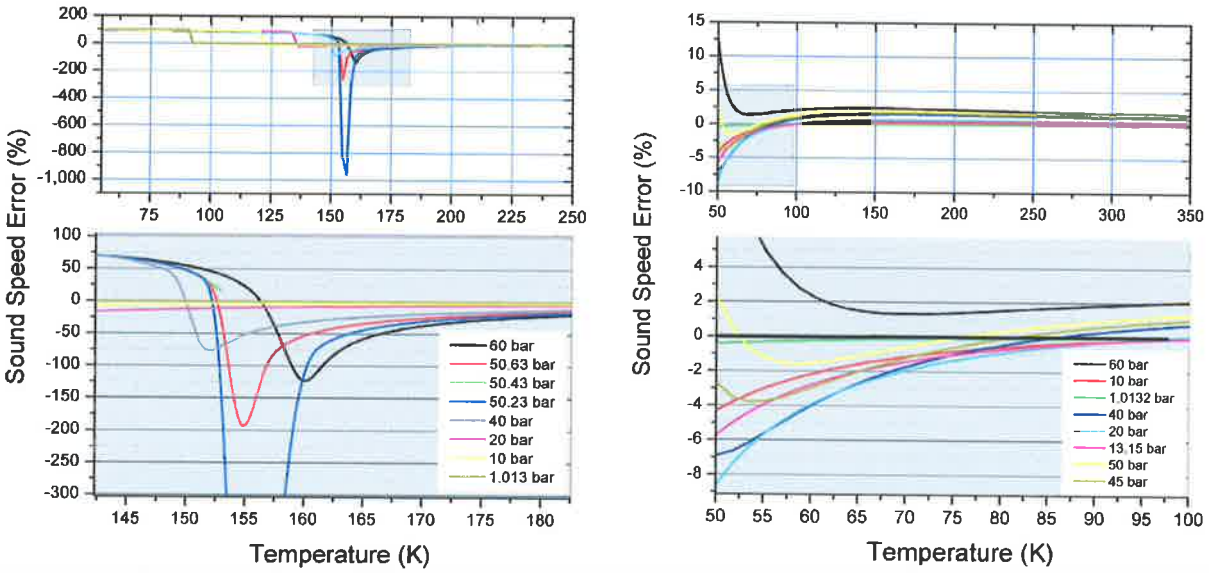

Figure 4.9 Sound speed error for oxygen (left) and hydrogen (right) comparing ideal gas to real fluid data obtained using a MBWR equation of state.

This equation of state has been endorsed by other researchers in the field of high pressure combustion to achieve the most accurate estimation of thermodynamic properties of oxygen (Yang, (2000)). Figure 4.10 illustrates various thermodynamic property data for oxygen over a

broad pressure and temperature range. Note the sensitivity of properties such as specific heat and isothermal compressibility near the critical point of oxygen with specific heat and isothermal compressibility which peak dramatically near the critical point of O_2.

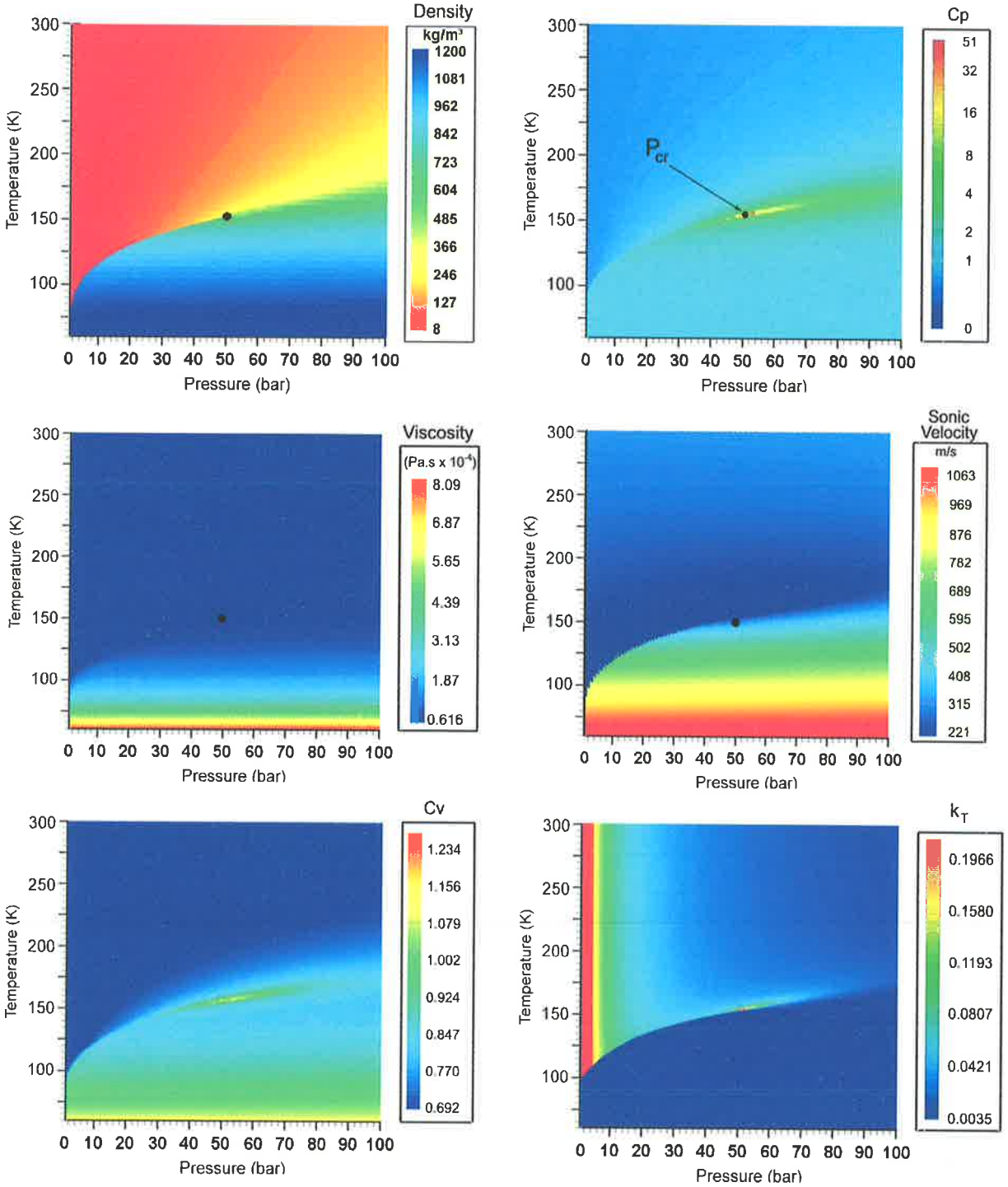

Figure 4.10 Thermodynamic properties of oxygen highlighting near critical non-idealities based on a MBWR equation of state.

4.5.2. Thermodynamic Properties of Hydrogen

For the experimental conditions investigated, it is also unacceptable to assume hydrogen behaves as an ideal gas although errors are significantly less than those associated with O_2. Figure 4.9 highlights the differences between real and ideal gas sonic velocity values of H_2 over a range of pressure conditions to be less that 2%. Below approximately 60K real gas effects dominate and errors become more significant.

H_2 density error becomes relatively high at elevated pressure levels. Figure 4.11 illustrates that an error of up to nearly 5% is possible with inaccuracies becoming more dramatic below ~90K. For the calculation of density and other thermodynamic properties (c_p, c_v, h etc.) a modified Benedict Webb Rubin (MBWR) equation of state is employed with coefficients from Younglove (1982). The steady state test matrix investigated is at conditions well above the critical point of H_2 and thus the near critical inaccuracies are not an issue.

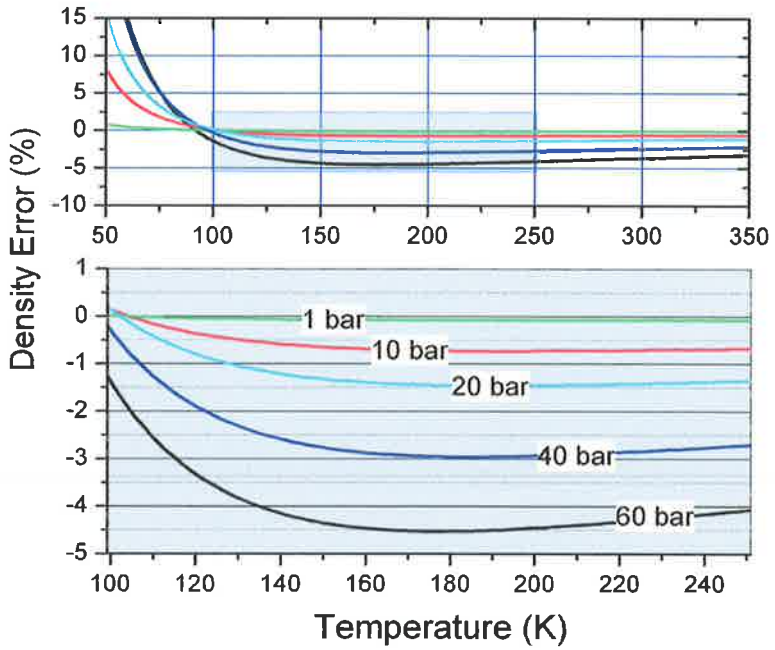

Figure 4.11 Density error for H_2 ideal gas vs. real fluid data based on a MBWR equation of state

4.5.3. H_2-Injector Flow Rate Data Correction

The mass flow meters are located a significant distance upstream from the chamber propellant manifolds and thus fluctuations experienced in the thrust chamber/manifold region are not transmitted. The mass flow meters therefore provide an inaccurate representation of mass flow rates, injection velocities and operating conditions during the start-up transient.

Propellant mass flow-rate measurements must be precise to ensure accurate injection conditions are calculated. Errors exist in the low hydrogen mass flow rate measurements recorded from the H_2 flow meters necessary to achieve the low pressure combustion operating phase ($\dot{m}$~40g/s at P_{ch}=40 bar). The low flow rate is below the minimum flow rate specification of the test facilities' H_2 supply system regulation valve an thus accuracy is not guaranteed. To minimise potential inaccuracy, a flow rate correction is made providing the actual flow rate through the injector based on the pressure difference and a discharge coefficient (C_d) derived the hydrogen side of the injector. The discharge coefficient is derived for each injector configuration based on the higher propellant mass flow rates experienced at increased chamber pressure conditions which are proven to be accurate within 4%. Using the injector pressure difference, C_dA is calculated based on the following relation;

$$\frac{\dot{m}_{H_2}}{\sqrt{2\Delta p\rho}} = C_dA \qquad (4.23)$$

The discharge coefficient C_d derived for each injector configuration is based on multiple test data and is re-substituted at the lower flow rate condition to calculate the actual H_2 mass flow rates through the injector (eqtn. 4.23).

$$\dot{m}_{H_2} = C_dA\sqrt{2\Delta p\rho} \qquad (4.23)$$

Under all conditions investigated, the discharge coefficient C_d appears relatively independent

of Reynolds number as $Re > 8 \times 10^5$. C_d values for multiple injector arrangements are plotted in Figure 4.12 with data based upon multiple tests.

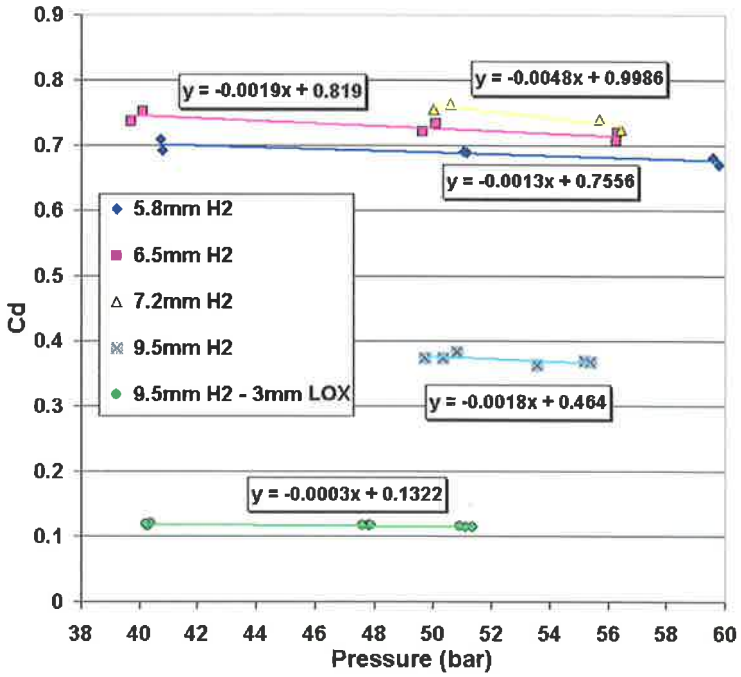

Figure 4.12 H_2 injector discharge coefficients as a function of operating pressure

Figure 4.13 provides an example of the effectiveness of applying this propellant flow rate correction technique. Figure 4.13 (a) shows the hydrogen flow rate during rough and unstable combustion as measured through the flow meter (MPH1) and the actual flow rate through the injector. Figure 4.13 (b) highlights the effectiveness of the correction technique during steady state operation. The fluctuations experienced by the mass flow meter are not transmitted to the injector flow and vice versa. A similar analysis is performed to determine the LOx flow rate through the injector for ignition transients and start-up.

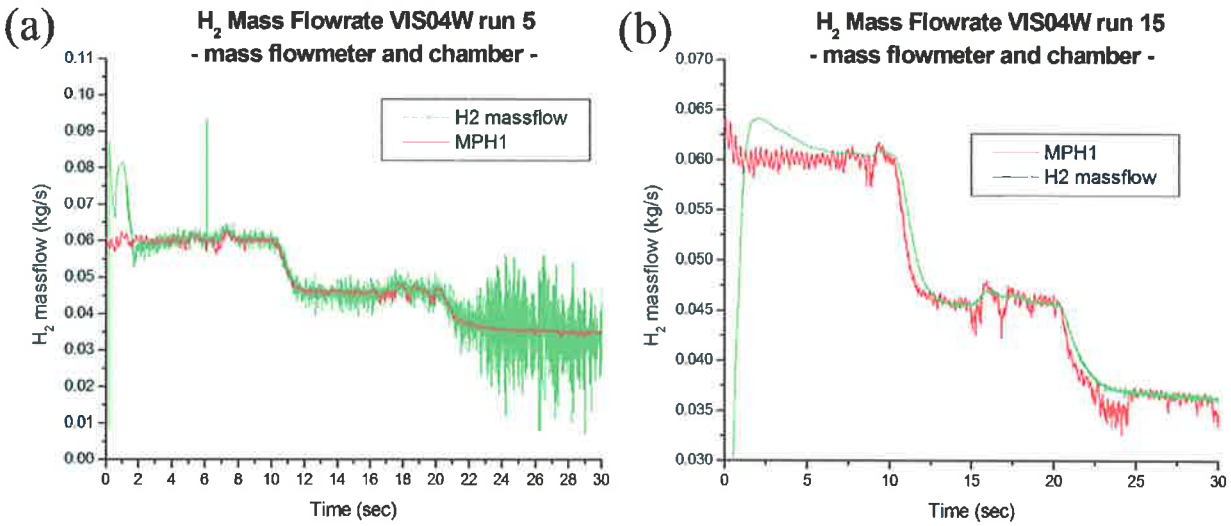

Figure 4.13 Corrected H_2 mass flow rates for (a) rough and unstable combustion and (b) steady combustion

4.5.4. LOx-Injector Flow Rate Data Correction

Discharge coefficients C_d are calculated for the oxygen component of the injector similar to the technique described in Section 4.5.3. Figure 4.14 illustrates the discharge coefficient for the oxygen component of 3 different injectors used throughout the test campaign. A linear fit is made to the data to provide an estimation of C_d as a function of reduced pressure P_r for the start-up transient period (from time $t = 0$ to $t = 2.0$ seconds).

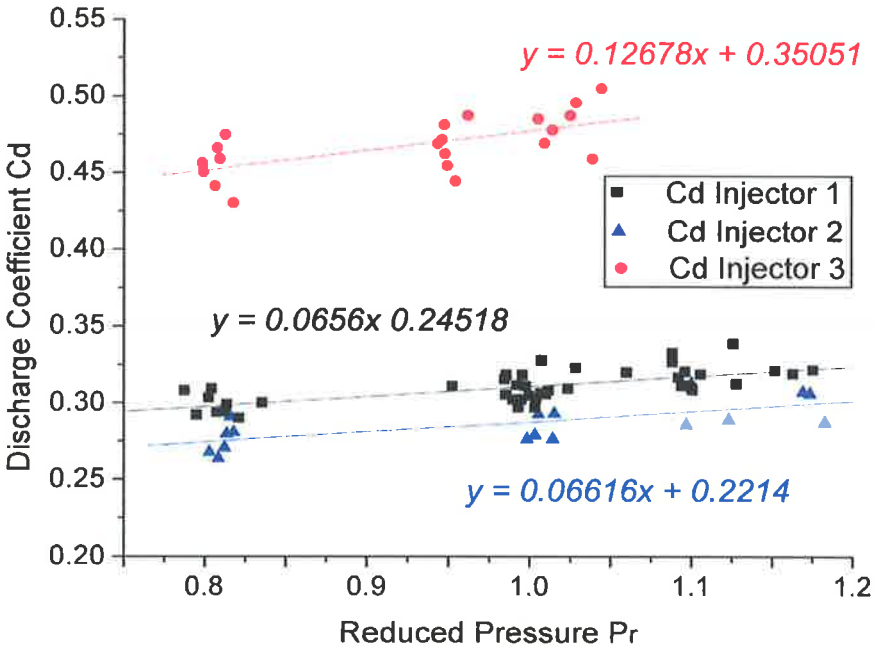

Figure 4.14 Discharge coefficients for 3 oxygen injector configurations. Injectors 1 and 2 are 4mm in diameter whilst injector 3, has a 3mm diameter.

4.6 Summary

Image data obtained through implementation of optical diagnostics are processed utilising a variety of processing techniques. Such techniques are applied to a plethora of images captured at various operating conditions in order to understand the influence on combustion and flowfield behaviour. The corrected measurement system data combined with a modified Benedict-Webb-Rubin equation of state enables accurate thermodynamic property evaluation resulting in a precise, well defined test matrix represented in terms of various non-dimensional values defined in Chapter 2.

Flame dynamics is assessed through axial flame intensity tracking in the near injector zone during ignition transients and steady state operation. During combustor start-up, the flame front position is examined and the mean OH emission intensity is calculated based on flame size. The position of the OH emission intensity centroid is also tracked axially during thrust chamber start-up and steady operation. The application of Fourier Transform techniques to HF dynamic pressure data provides an informative depiction of the combustor response, relative pressure amplitudes and dominant frequencies over the operating range examined.

Flame structure is assessed qualitatively and quantitatively based on mean images constructed from multiple image series at various operating conditions. Where combustion instability is experienced, an alignment routine enables large image sets to be a repositioned prior to the application of further image processing techniques.

With image processing successfully undertaken, post-processing and spectral methods are applied to image data sets in an attempt to highlight periodic behaviour. Identification of common trends and observations assist in the characterisation of the near injector combustion zone under various operating conditions in a coaxially injected, H_2/O_2 liquid rocket engine.

Chapter 5

Preliminary Visualisation Results

5.1 Flame and Flow Visualisation

Development and implementation of operational test sequences has resulted in a series of successful preliminary combustion tests. The two operating conditions examined (designated condition 1 and 2 in test campaign VIS2001) were focused primarily on a large hydrogen temperature differential (gaseous and liquid hydrogen) as indicated in Table 3.2. The test campaign was successful at qualifying the thrust chamber, operating sequence and the diagnostics system.

5.1.1. Simultaneous Flame and Flowfield Visualisation

Shadowgraph and spontaneous OH chemiluminescence imaging have proven challenging under the initial test operating conditions. Image quality fluctuates dramatically during transient combustor operation as density gradients change with temperature and pressure. Figure 5.1 exhibits a shadowgraph image pair recorded during ignition and steady state operation at test condition 1.

Injection of hydrogen at very low temperatures (T_{H2}~ 55K) results in a significant density increase in the near injector field. Shadowgraph images under such conditions appeared completely black with limited penetration of the flowfield by the backlit nano-light setup.

OH emission images exhibited a similar trend with low hydrogen injection temperatures. Reduced H_2 temperatures promote a significant decrease in localised emission intensity due to absorption and scattering effects. Increased near-field density gradients, thought to be attributed to low temperature H_2 and water vapour, contributes to scattering of the emitted hydroxyl radical in the near injector field. During ignition, propellants are injected at lower pressure with temperatures typically higher than steady state conditions resulting in improved emission images with greater intensity during the start-up process. Reduced OH emission intensity may also be attributed to reduced reaction rates associated with lower H_2 injection temperatures.

The shadowgraph imaging setup is highly sensitive to change in H_2 injection temperature. Propellant injection temperature can vary by up to 250K during a single test which makes optimisation of the shadowgraph arrangement difficult. Obtaining satisfactory images from ignition and steady state operating phases require adjustment of the systems between tests.

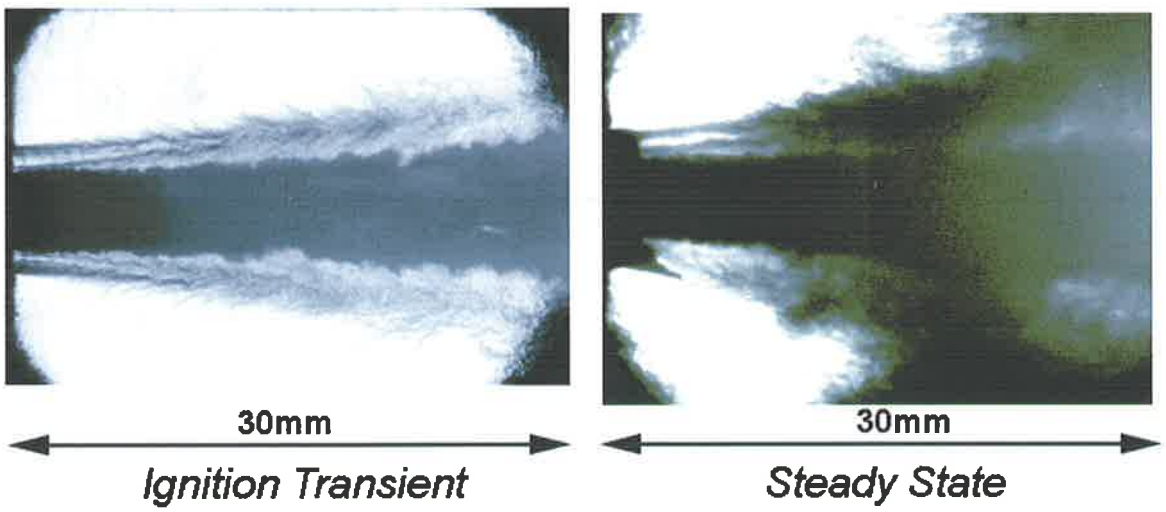

Figure 5.1 Shadowgraph images captured during start-up transient and steady state at operating condition 1. Ignition P_{ch} ~ 15 bar and steady state P_{ch} ~ 63 bar. Note ice formation around injector during steady state.

Figure 5.2 illustrates typical single shot OH emission images captured during operating condition 1 ignition and steady state operating phases. The OH emission image pair correspond to the flowfield images depicted in Figure 5.1 and represent operation at chamber pressures of approximately 15 and 62 bar for left and right images respectively.

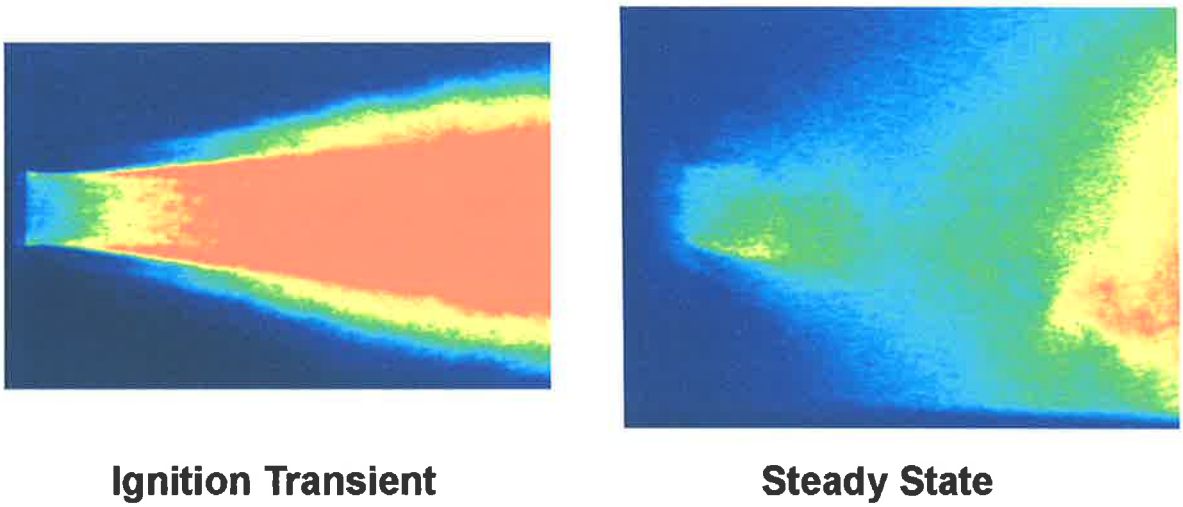

Figure 5.2 Spontaneous OH chemiluminiscence images captured during start-up and steady state at test condition 1. Ignition P_{ch} ~ 15 bar and steady state P_{ch} ~ 63 bar.

5.1.2. Time Averaged OH Emission Images

Averaged OH emission images provide a quantitative depiction of the combustion zone during start-up, steady-state operation and thrust chamber shut down as illustrated in Figure 5.3. During start-up, the flame appears to be relatively narrow due to significantly high propellant injection velocities (approaching sonic velocity). Emission intensity is lowest during steady state operation at a chamber pressure of P_{ch} = 62 bar. As chamber pressure increases and propellant injection velocities reach nominal levels, the flame spreads dramatically to fill the chamber. The recirculation zone between the main injector flow and the film cooling at the chamber boundary may also influence the flame spread angle.

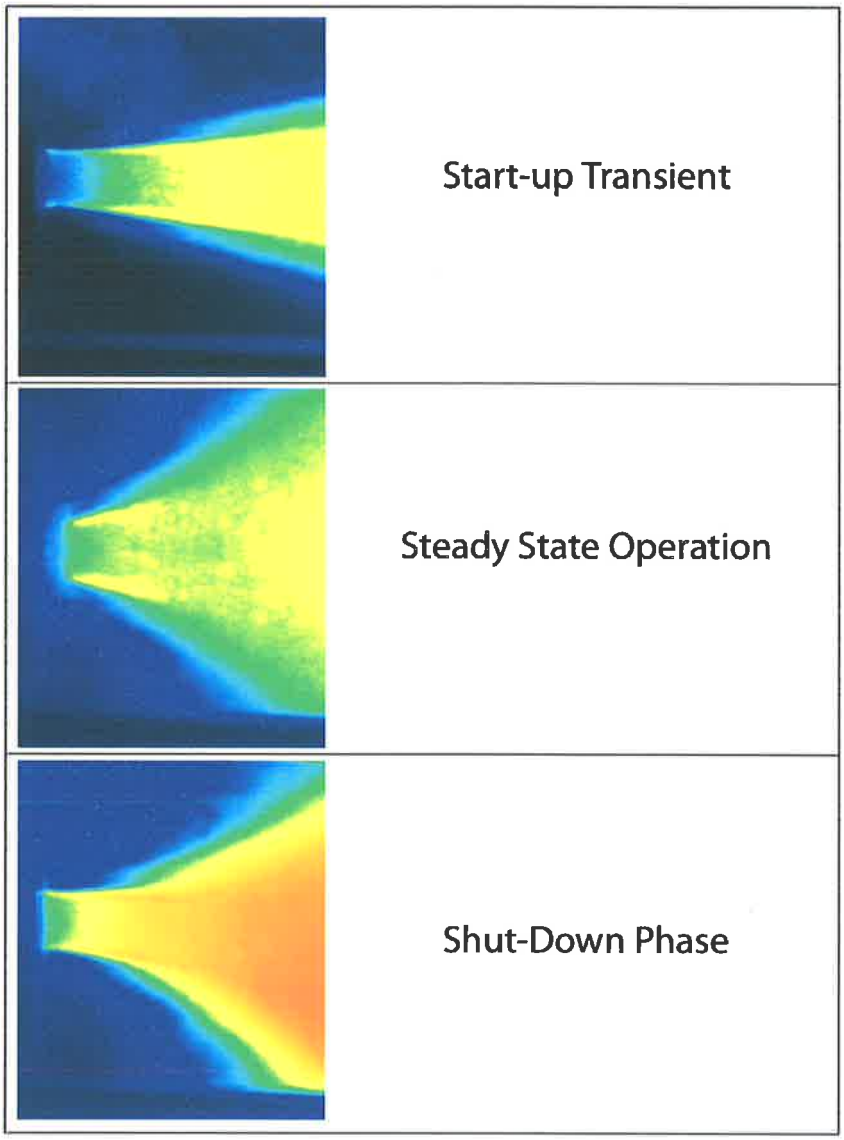

Figure 5.3 Time-averaged OH emission images of near injector zone constructed from image series' recorded during start-up, steady-state and thrust chamber shut down.

5.2 Discussion

5.2.1. Flame and Flowfield Characterisation

Identification of the localised combustion zone is made possible through the application of Abel's transform to a series of time averaged emission images (refer Section 4.2.2). Figure 5.4 illustrates deconvoluted time averaged images from operating condition 1 during ignition and steady state operation. The images represent a 2-D slice of the combustion zone and provide evidence that the flame resides in the shear layer initially between the oxygen and hydrogen streams attached to the LOx injector post.

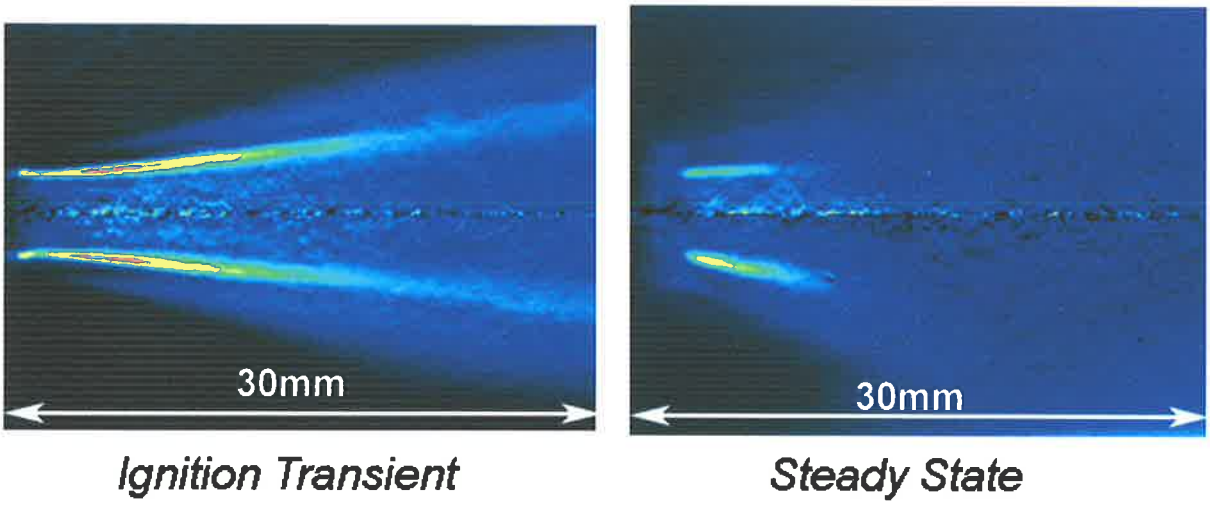

Figure 5.4 Deconvoluted time averaged spontaneous OH chemiluminescence images from start-up and steady state operating phases at test condition 1. Ignition P_{ch} ~ 15 bar and steady stateP_{ch} ~ 63 bar.

The flame appears to attach itself to the LOx post upon ignition and extends downstream as reported by Mayer and Tamura (1996). Near injector OH emission intensity appears significantly greater during the ignition transient than during steady state at high pressure. Emission intensity has also appeared greater for higher H_2 injection temperature test cases (i.e. test case 1) which may be associated to an increased rate of reaction. Combustion products are recirculated toward the face plate which results in clouding of the near injector field. Conditions consistently appear to worsen with a reduction in H_2 injection temperature.

At a pressure of 60 bar, water condenses at approximately 594K and has been observed in liquid form during transient operation (Smith and Klimenko et al. (2002)). Figure 5.5 highlights water accumulation at the outer extremities of the chamber during thrust chamber start-up.

Figure 5.5 Condensed water at chamber perimeter during combustor operation at approximately time $t \sim 0.7$ seconds after ignition. $P_{ch} \sim 45$ bar.

Below a H_2 injection temperature of approximately 80K, recirculation of combustion products and apparent condensation of water strongly contributes to a reduction in optical clarity due to an increase in density gradients. Satisfactory images could not be obtained for test case 2 whereby H_2 injection temperature was consistently below 60K (refer Table 3.2).

During test cases 1 and 2, ice has been observed to form around the injector for $T_{H2} < 120$K. This is attributed to the recirculation and solidification of combustion products (water) on the face plate. The recirculation is sustained by the H_2 film cooling transporting water vapour and combustion products toward the low temperature face plate. A face plate mounted thermocouple indicates the face plate is typically at a temperature of around 150K. The low temperature surface allows water vapour to rapidly solidify around the injector exit as shown phenomenologically by Figure 5.6.

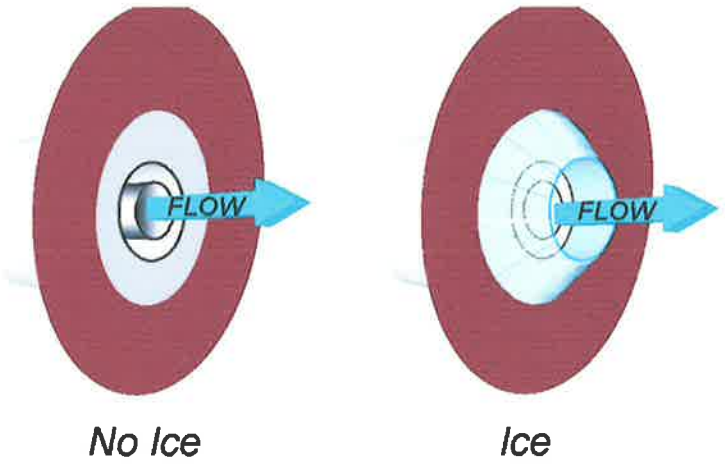

Figure 5.6 Phenomenological sketch of ice surrounding injector during steady state operation (From Mayer and Smith, (2004)).

The simultaneity of the shadowgraph and OH emission imaging systems enables the superposition of images to provide a qualitative representation of the near injector field. Figure 5.7 represents the near injector field with a deconvoluted OH emission image superimposed with a shadowgraph image. The images were captured during the ignition transient at a chamber pressure of 45 bar at approximately 0.48 seconds into the thrust chamber start-up phase.

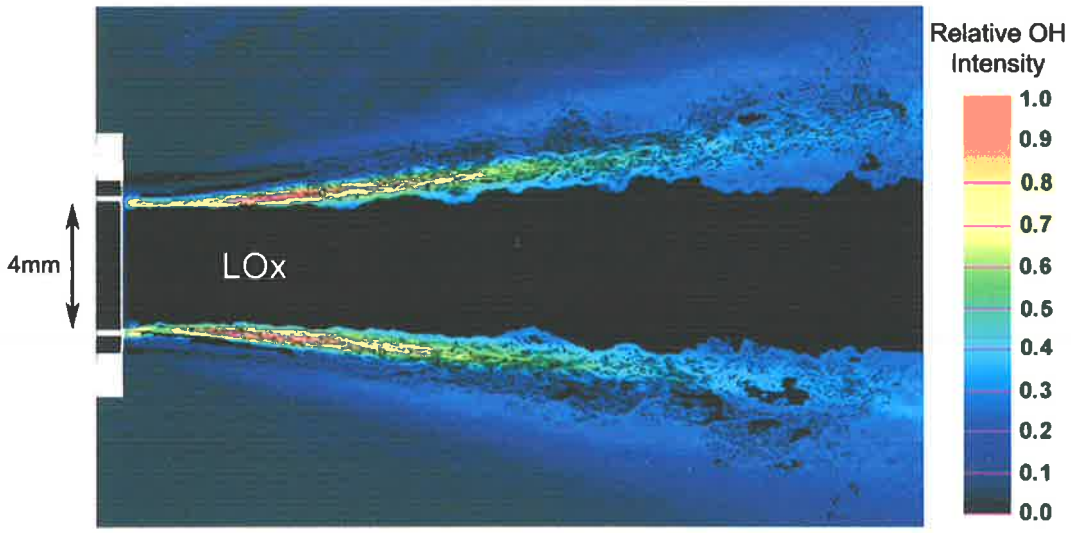

Figure 5.7 Superposition of deconvoluted mean OH emission image and shadowgraph image of near injector region. The image corresponds to ignition transient t=0.48 seconds. P_{ch}=45 bar, T_{H2} ~160K.

5.2.2. Combustor Response

A change in hydrogen injection temperature of approximately 50K has shown to increase resonant pressure amplitudes by up to one order of magnitude (refer Figure 5.8). Wanhainen (1966) has illustrated that propellant injection velocity ratio based on propellant properties prior to injection has a marked affect engine stability at subcritical operating conditions. Velocity ratio has been maintained relatively constant for this investigation (within 5%).

An FFT analysis has been performed on the raw dynamic pressure data measured at a frequency of f = 25kHz. The 1st longitudinal mode (1L) is evident in the power spectra at approximately 1800Hz as illustrated in Figure 5.8. The 1L mode corresponds well with theoretical estimations based on standardised theory outlined in Section 4.3.2.

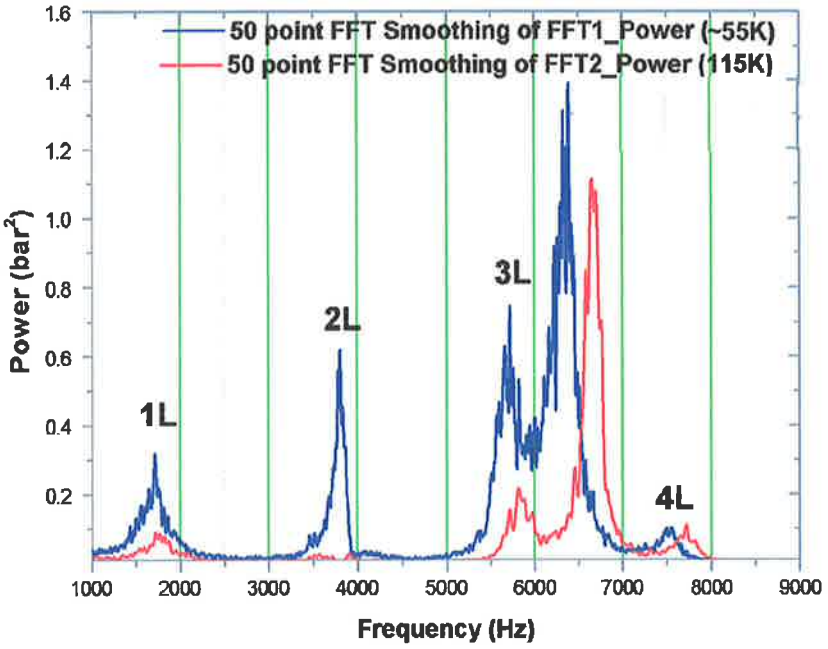

Figure 5.8 Power spectra of dynamic chamber pressure for two test cases with T_{H2} = 115K and ~55K.

The peak chamber pressure amplitudes illustrated in the power spectra (Figure 5.8) are significantly lower for the warmer H_2 test case. The first longitudinal mode (1L) pressure amplitude increases by approximately 300% with the reduced H_2 temperature conditions. Furthermore,

test case 2 (T_{H2} ~55K) exhibits a notable amplitude increase in the longitudinal mode harmonics when compared to the warmer hydrogen test case. However, amplitude rapidly diminishes above the 3L mode in both cases.

The acoustic behaviour of the combustion chamber environment is notably different with a change in hydrogen temperature. Besides the change in pressure amplitudes, there is also a frequency shift between the two test cases due to the temperature difference. Further examination with more operating points and constant boundary conditions would prove useful in verifying the effects of H_2 injection temperature on combustor response.

Excitation of radial and tangential modes are rarely observed. The dimensions of the combustion chamber results in very high radial, tangential, and combined mode frequencies with relatively low amplitudes.

5.2.3. Hydrogen Film Cooling

A high amplitude oscillation present near f = 6300 - 6800Hz is believed to be vortex shedding at the film cooling inlet (refer Figure 5.8). Consider the equation for the classical Strouhal number, given as:

$$St = \frac{fL}{v} \tag{5.1}$$

The film cooling inlet area has an equivalent length of L = 0.014, and the mean film cooling velocity is calculated as v = 222m/s for the warmer H_2 test case presented in Figure 5.8. Using an empirically derived St = 0.4 for an annular jet (Chan & Ko, (1978)) a characteristic vortex shedding frequency f ~ 6350Hz is obtained. This frequency corresponds with that seen illustrated in Figure 5.8. This frequency shifts slightly depending on pressure and injection conditions which are typically maintained constant (within 10%).

5.2.4. Temperature Field

Coherent Anti-Stokes Raman scattering was applied for point-wise temperature measurements in the near injector field of the combustion chamber. Two axial positions were probed at 50mm and 80mm downstream from the injection plane, corresponding to x/d = 12.5 and 20 respectively. A series of radial points were probed at each axial position in an attempt to resolve a temperature distribution profile. The thrust chamber was consistently operated at conditions corresponding to test case 1 in Table 3.2. Figure 5.9 indicates the positions investigated in the study.

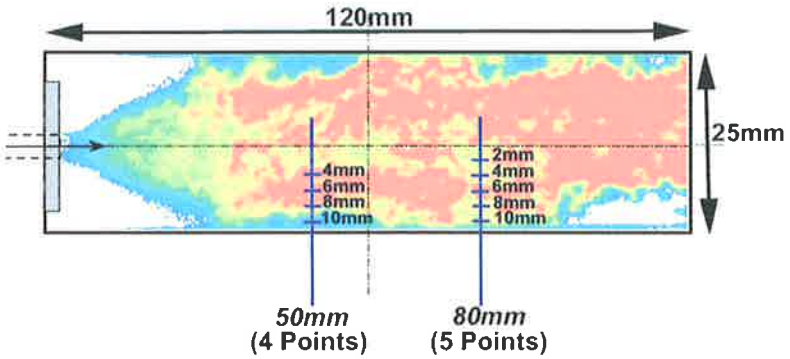

Figure 5.9 Near injector CARS Temperature probing locations relative to the injection plane (from Smith and Klimenko et al. (2002))

Limited H_2O spectra were recorded due to the low energy of the dye laser in this spectral range. The validation rate of H_2 spectra acquired at axial positions less than approximately 50mm downstream was extremely low. No signal could be measured with low H_2 injection temperatures (~55K) due to the increased density gradients in the near injector field. The temperature field in the near injector region proves difficult to characterise with a limited dataset. At warmer H_2 conditions (T_{H2} ~ 117K), spectra were successfully recorded and temperature values deduced. The validation rate of spectra acquisition was typically between 50 and 75%. A test duration of 20 seconds with 18 seconds of steady state operation and a laser pulse

frequency of 10Hz results in approximately 100 spectra samples per test per point.

At x/d=12.5 (50mm), recurring measurements of relatively low temperatures were recorded in the order of 400-500K with a low variance for all radial positions probed. Occasional high temperature values (1000-1200K) were observed at x/d=12.5. The occurrence of such a strong low temperature bias indicates limited fluctuation of the flowfield combustion zone at this axial location. This is supported by shadowgraph images which indicate the propellant flow (in particular the LOx core) remains unimpeded for up to 10-15 LOx diameters downstream (i.e. 40-60mm) as illustrated in Figure 5.10. The stability of the LOx core and the oxidiser/fuel propellant interface at x = 50mm results in a very thin, localised combustion region which may not have been regularly probed by the CARS laser shots.

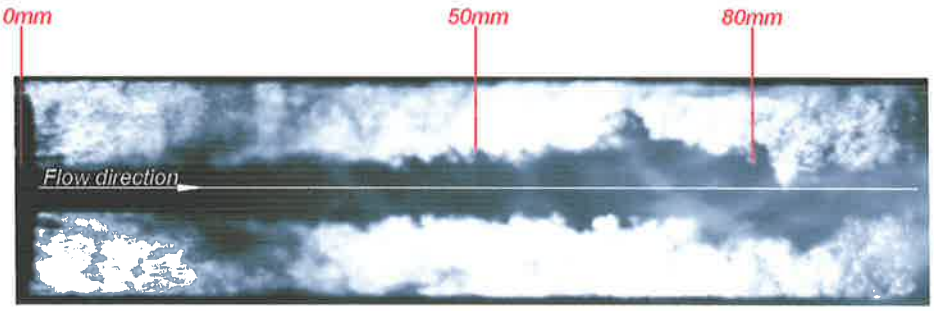

Figure 5.10 Shadowgraph image at P_{ch}=60 bar indicating CARS axial measurement locations and LOx core stability as a function of downstream position

As the propellants advance downstream, axial momentum is lost and shadowgraph images indicate that large coherent structures continually appear and coalesce, occupying and escaping the probe volume. The LOx core has also been observed to exhibit a corkscrew or helical type instability as discussed by Smith and Klimenko et al. (2002). This instability distributes the LOx core and combustion zone over a greater radial distance resulting in a fluctuating shear layer and reaction zone and thus an increased variance in captured spectra and derived temperature values. The result is coherent bimodal temperature distributions as reported by Smith and

Klimenko et al. (2002) The significant variance in temperature values support the fact that a highly fluctuating, turbulence dominated flowfield exists at axial distances exceeding approximately 15 LOx jet diameters ($x/d > 15$).

The broad temperature data ranges presented by Smith and Klimenko et al. (2002) are represented by normal (Gaussian) distributions. Temperature data are normalised here are displayed in histograms for each radial position with constant bin sizes of 100K. The resulting temperature probability distributions are fitted with exponentially modified Gaussian equations (EGM) with coefficients calculated using the Levenburg Marquardt non-linear curve fitting algorithm (refer Gill and Murray, (1978)). The resulting temperature probability distribution function $\Im$ is described by equation (5.2).

$$\Im = \frac{ac\sqrt{2\pi}}{2d} exp\left(\frac{b-x}{d} + \frac{c^2}{2d^2}\right)\left(\frac{d}{|d|} - erf\left(\frac{b-x}{c\sqrt{2}} + \frac{c}{d\sqrt{2}}\right)\right) \qquad (5.2)$$

Coefficients a, b, c, d, and e can be found in table A1 in appendix A. For radial positions 2, 4, and 10mm, the EMG function fits the data well with a strong low temperature bias. However, for radial positions 6 and 8mm, a bi-modal temperature distribution exists and the temperature probability distributions are best represented by a pair of EMG functions as shown in Figure 5.11.

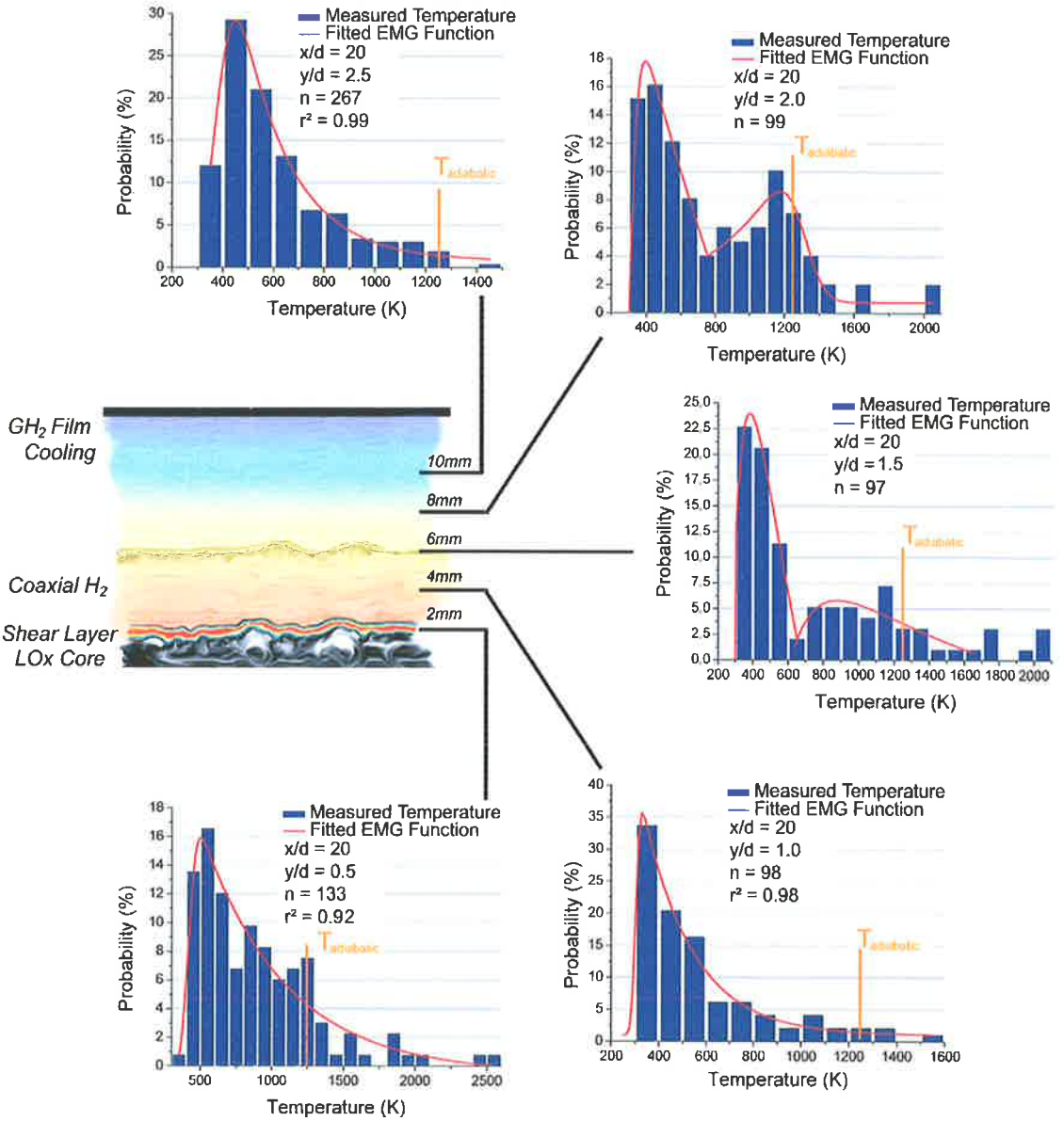

Figure 5.11 Temperature probability density profiles for radial positions 2, 4, 6, 8 and 10mm (y/d = 0.5, 1.0, 1.5, 2.0 and 2.5) at an axial position of 80mm (x/d=20).

For radial positions 2, 4 and 10mm, a quality of fit factor (r^2) is included with the plots in Figure 5.11. This value is the square of the correlation between the measured temperature and the predicted values whereby the numerator represents the sum of squared residuals (errors) and the denominator is the sum of squares about the mean. A value of $r^2 = 1$ defines a curve that

fits an entire dataset without error. The statistical measure r^2 is given by equation (5.3)

$$r^2 = 1 - \frac{\sum_{i=1}^{n} (y_i - \hat{y}_i)^2}{\sum_{i=1}^{n} (y_i - \bar{y}_i)^2} \qquad (5.3)$$

5.2.5. Statistical Confidence

To test the statistical confidence of the limited CARS dataset, results from two consecutive tests performed at identical operating conditions were compared. CARS temperature measurements were recorded 80mm downstream of the injector at the 10mm radial position (x/d = 20, y/d=2.5). Two independent test firings of the thrust chamber ensured two separate data sets were produced.

Figure 5.12 compares the pair of test data at y/d=2.5 and clearly illustrates the similarities between the two resulting temperature probability distribution profiles. The strong low temperature bias is evident in both cases and the general profile shapes are in agreement. A maximum probability difference of approximately 18% exists at the peak of the curve. The repeatability of deduced temperature values and the corresponding probability distributions indicate the average number of samples recorded for each radial position (n = 116) is valid for constructing representative temperature profiles presented herein.

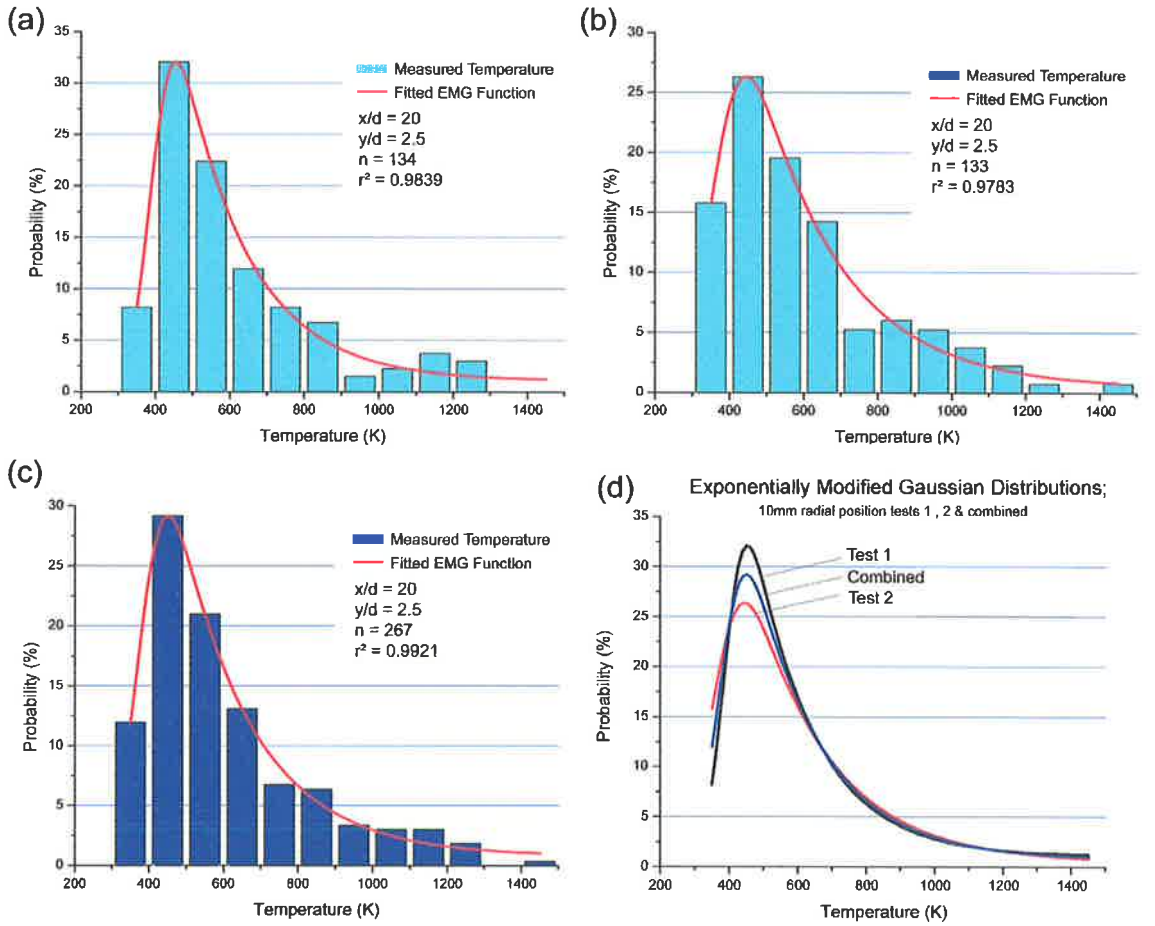

Figure 5.12 Temperature probability distributions at 80mm axial position (x/d=20) and radial position 10mm (y/d=2.5). Images (a) and (b) represent consecutive tests. Image (c) represents the combined data and image (d) compares the EMG curves fitted for each case.

5.2.6. Local Mixture Ratio Approximation

Estimates of local oxidiser-fuel mixture ratio (R_{OF}) can be derived based on measured temperature and the assumption of equilibrium chemistry. Calculating R_{OF} based on adiabatic flame temperature has been shown successful by Yeralan and Pat et al. (2000).

Yeralan and Pal et al. (2000) engaged a similar investigation through comparison of theoretical adiabatic flame temperatures with temperature measurements recorded with a LOx/H_2 thrust chamber employing a swirl-coaxial injector. At $x/d = 35.7$, the adiabatic estimation of 1257K proved very accurate at the chamber centre-line with an $R_{OF} = 1$ (within < 1%). Measured

temperature increased slightly with radial distance from the centre-line. Little variance in the measurement data indicated a very well mixed flowfield with the swirl injector configuration at $x/d = 35.7$. Data from other axial positions were not reported.

Here however, a strong bias exists toward low temperatures as shown in Figure 5.11. The consistency of the low temperature values witnessed indicate that coaxially injected propellants in a co-flowing, shear configuration results in poorly mixed propellants at x/d=20. Such observations are also evident in the shadowgraph images where a majority of the liquid oxidiser core is unreacted. This is in direct contrast to observations made with a swirl-coaxial injector (Yeralan and Pal et al. (2000)) whereby the swirl component promotes mixing through high levels of vorticity and turbulence.

Local R_{OF} probability density functions can be constructed based on the measured temperature data. An approximation of R_{OF} is made here at a pressure of 62.8 bar and is based on standard equilibrium chemistry theory (i.e. Hill and Peterson, (1992)).

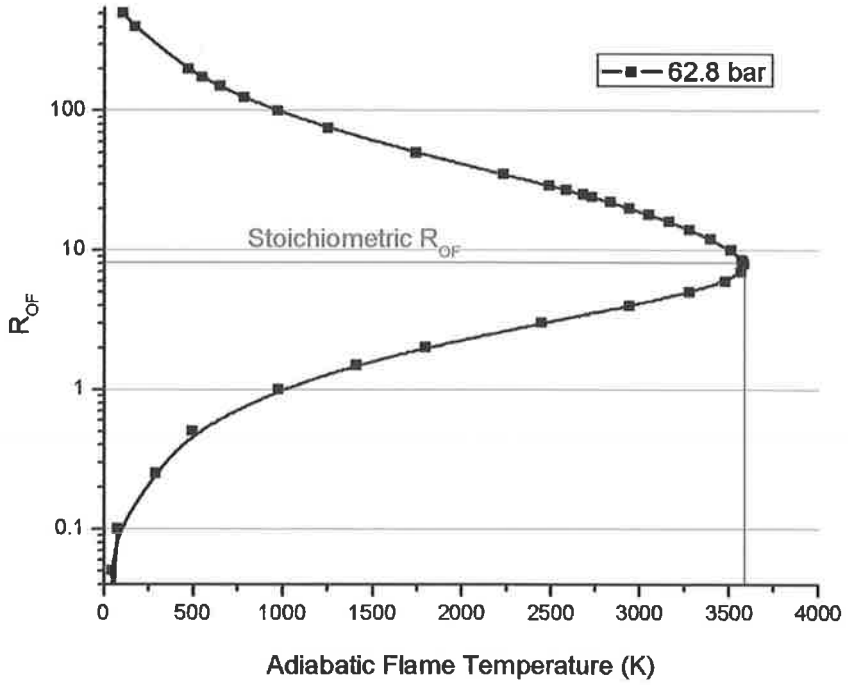

Figure 5.13 Ratio of oxidiser to fuel vs. adiabatic flame temperature at a pressure of 62.8 bar.

The temperature data presented in Figure 5.11 illustrates the local oxidiser-fuel ratio is far from stoichiometric. Near the chamber boundary (y = 10mm) the H_2 film cooling may have a major influence on the R_{OF} and local temperatures values. Approximately 240g/s of ambient temperature hydrogen is injected as film cooling to protect the windows and thrust chamber walls resulting in a total fuel rich mixture ratio of approximately 1.

As the probe volume moves toward the centre line of the chamber, an oxidiser rich environment may exist resulting again in lower temperature values. Figure 5.13 shows the effect of R_{OF} on adiabatic flame temperature and illustrates that low temperature values may exist in both fuel-rich and oxidiser rich environments. In this case however, it appears most likely that the lower temperature bias is due to a fuel rich environment. The bimodal temperature distribution are likely to be a unction of the oscillating flowfield (helical instability).

Probability density functions are calculated at various R_{OF} conditions and radial positions and is shown in Figure 5.14. The low temperature measurements indicate a low local R_{OF} value typically between 0.5 and 1.5. The R_{OF} data presented in Figure 5.14 are derived from measured temperature values and therefore reflect the plots illustrated in Figure 5.11.

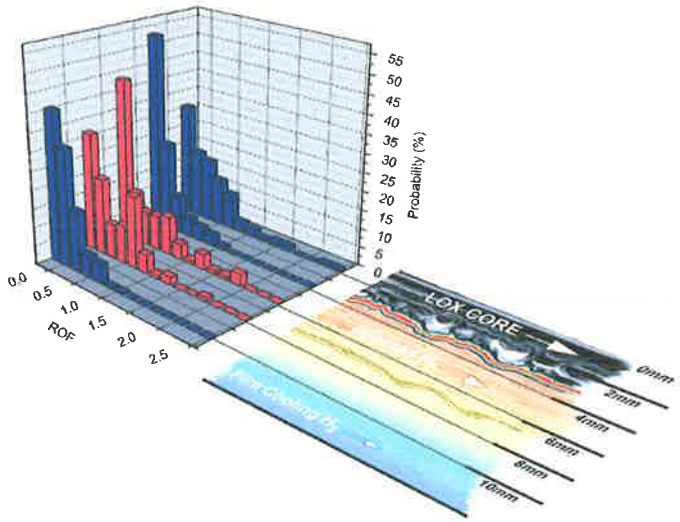

Figure 5.14 Probability density function of R_{OF} based on equilibrium chemistry at x/d = 20 for radial positions 2, 4, 6, 8 and 10mm. R_{OF} bin size of 0.5.

5.2.7. Conclusions and Discussion from Initial Experiments

Optical diagnostics has been applied to a windowed liquid rocket engine thrust chamber. Simultaneous flame and flow visualisation has been achieved using shadowgraph photography and OH emission imaging.

The shadowgraph imaging technique has proven highly sensitive to changes in propellant density gradients (temperature). Condensed water and water vapour appears to impede the optical access at reduced propellant injection temperatures (<100K) and ice has been observed to form at the injector exit. Below a hydrogen injection temperature of 80K, shadowgraph imaging was not possible with the setup employed.

OH emission imaging and deconvolution techniques have proven successful in providing a quantitative representation of the combustion zone. During thrust chamber start-up the warmer propellant combination and high injection velocities results in an elongated, high intensity flame which appears strongly anchored at the injector LOx post tip. The flame extends downstream and resides within the shear layer between the two propellant streams.

As combustion chamber pressure increases, the flame spreads radially and the emission intensity appears more scattered. At steady state operation at high pressure (above the critical pressure), deconvoluted time averaged OH images indicate that flame intensity is localised at the LOx post tip. The emission intensity downstream is relatively low.

Hydrogen injection temperature has shown to have an effect on combustor response under the conditions examined. Lower H_2 injection temperature appears to promote higher combustion pressure amplitudes at the resonant frequencies of the chamber. Further assessment of this phenomena would be useful to better understand the global effects of significant changes in hydrogen injection temperature to combustor response.

CARS has been successfully implemented to measure the local temperature values in the near injector field of a liquid rocket engine. Results have illustrated strong variations in temperature measurements which is indicative of a fluctuating flowfield and combustion zone at the radial positions examined. Low H_2 temperatures (~55K) result in very low validation rates. Increasing hydrogen temperature (~117K) results in acceptable validation rates in the order of 50-70%. Temperature probability distributions are constructed based on the results obtained. The temperature probability distributions are represented by exponentially modified Gaussian (EMG) curves.

Local mixture ratio approximations based on equilibrium chemistry indicate that very low oxidiser-fuel ratios are present in the region probed with the CARS lasers ($R_{OF} < 1.0$). This could be attributed to the high levels of H_2 film cooling present in the chamber at the locations examined (i.e. up to $x/d = 20$). The bimodal temperature distributions indicate that a flame certainly resides in a very narrow shear layer which continually occupies and escapes the probe volume of the lasers.

The application of such an advanced diagnostic technique has limitations under conditions experienced. High levels of vibration have been overcome through the implementation of heavy duty foundations and traverses for mounting the optics. Low numbers of tests and significant delays between consecutive tests reduces the size of the results data sets and hence the statistical confidence of the results is diminished.

Modifying the existing CARS setup to incorporate an automated traversing system combined with extended operation of the thrust chamber would be highly advantageous in acquiring significant data sets.

Extended thrust chamber operation is achieved and combined with the application of high

speed camera systems to capture large data sets of shadowgraph and OH emission images at various operating conditions during thrust chamber start-up and steady state operation. The large image sets are processed and results presented in the proceeding sections.

Chapter 6

Start-up Transients and Ignition

6.1 Ignition in Liquid Rocket Engines

Ignition phenomena and start-up transient processes remain a major point of interest within the liquid propellant rocket engine research and development community. Unstable ignition transients were considered a serious threat in the ground testing and qualification of HM7 engines for Europe's Ariane family of launchers (see Preclik and Spagna (1988)). The loss of Ariane V flight 142 was also linked to the ignition failure of the Aestus engine in July 2001 (Dauptain (2002)). Literature regarding non-pre-mixed ignition is sparse. Dedicated research and exhaustive ignition tests are currently being undertaken by researchers and industrial partners to obtain a better understanding of ignition phenomena (for example refer Barensky (2001), Schmidt and Sender (2001)).

The transient start-up process of liquid rocket engines is a complex series of events which proves

difficult to characterise due to the diminutive time scales associated with ignition of injected propellants. Physical and theoretical observations generated through investigation of transient ignition behaviour may often be unique to the specific hardware and operating conditions examined. Fundamental ignition phenomena and dominant trends are presented here in an attempt to discern the underlying sequence of events surrounding ignition in LOx/H_2 LPRE's.

One must remain mindful of the terminology employed herein. The point of *ignition* is defined here as the point when the flame emission intensity increases dramatically indicating establishment of a stable flame. Combustor *start-up* represents the entire process from time $t = 0$ seconds until nominal, steady state operating conditions are achieved. This time period is typically around 2.0 seconds in total with the hardware and injection conditions employed here.

6.1.1. Gaseous O_2/H_2 Torch Igniter

The ignition system employed by combustion chamber C utilises is a gaseous hydrogen/oxygen (GH_2/GOx) spark torch igniter which is relatively simple in principle. A continuous spark operates in a small chamber filled with an approximate 1:1 mixture of gaseous hydrogen and oxygen. A flame exits the torch igniter tube and impinges directly upon the non-pre-mixed main injector flow at an angle of approximately 45 degrees as illustrated by Figure 6.1.

The torch igniter is enabled at time $t = -0.5$ seconds and operates continuously until it is disabled once nominal operating conditions are achieved at time $t = +2.0$ seconds. The torch igniter utilised here is similar to that employed by the latest Ariane V expander cycle upper-stage engine "VINCI." The VINCI ignition system functions independent of engine operating conditions with a separate supply system enabling multiple ignitions for restartability.

Ignition of the main propellant flow occurs upon opening of the propellant manifold run valves and flash-over between the torch-igniter flame and the primary propellant flow. A flame

propagates downstream and develops steadily with increased propellant flow rate.

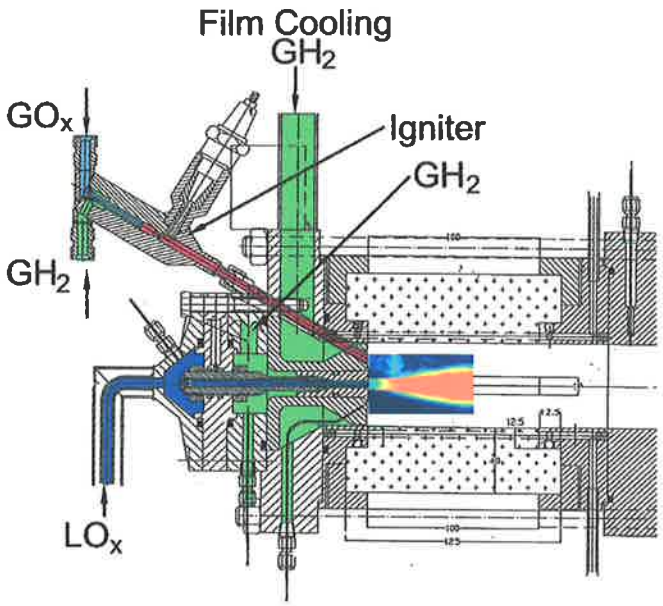

Figure 6.1 Detail of igniter, propellant supply and manifold system

Correct ignition timing is critical in order to avoid 'hard-starts' and achieve a safe ignition. A hard start or explosive ignition is typically due to an ignition delay resulting in propellant accumulation and large peaks in the combustion chamber pressure. Ignition delay has potentially explosive results as shown in Figure 6.2.

In the case of a liquid rocket engine employing cryogenic propellants, igniter design and ignition timing and are especially critical to ensure sufficient activation energy is provided in a low temperature environment. The start-up operating sequence employed for the test firing presented herein has been developed and optimised to achieve a very smooth start-up transient without undesirable pressure peaks in the thrust chamber. These are detailed in Sections 6.2 - 6.4.

The entire start-up and ignition transient period experienced in a liquid rocket engine with conventional spark-torch ignition systems is a highly transient process with non-stationary injection conditions.

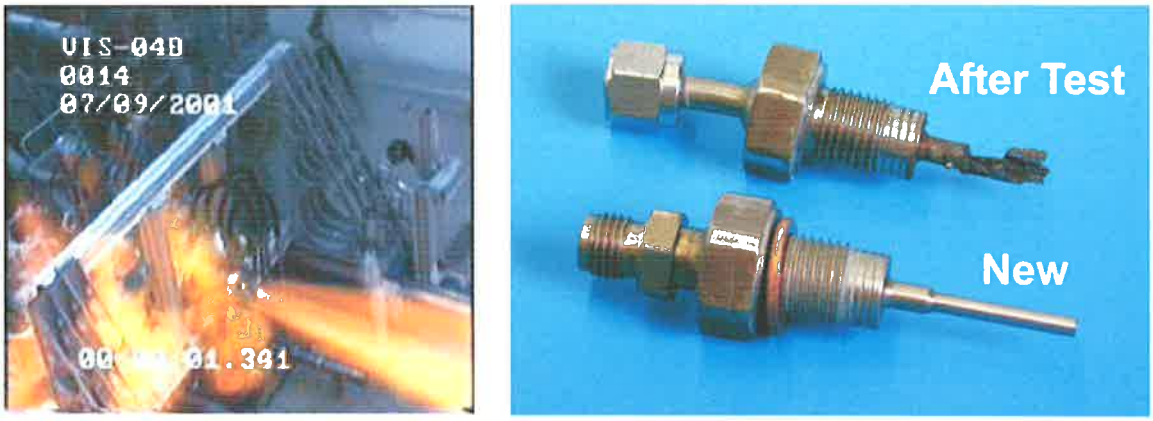

Figure 6.2 Catastrophic failure due to explosive ignition (delayed) caused by a faulty igniter. Test campaign VIS2001, t = +1.341 seconds.

6.1.2. Propellant Flow Rate Correction During Ignition

Applying the propellant mass flow rate correction technique described in Section 4.5.3 is imperative for transient data recorded during start-up. Figure 6.3 illustrates the difference between the oxygen mass flow rate measured by the upstream flow meter and the corrected oxidiser flow rate. Hydrogen mass flow rate and chamber pressure are also included in Figure 6.3 for comparisons sake.

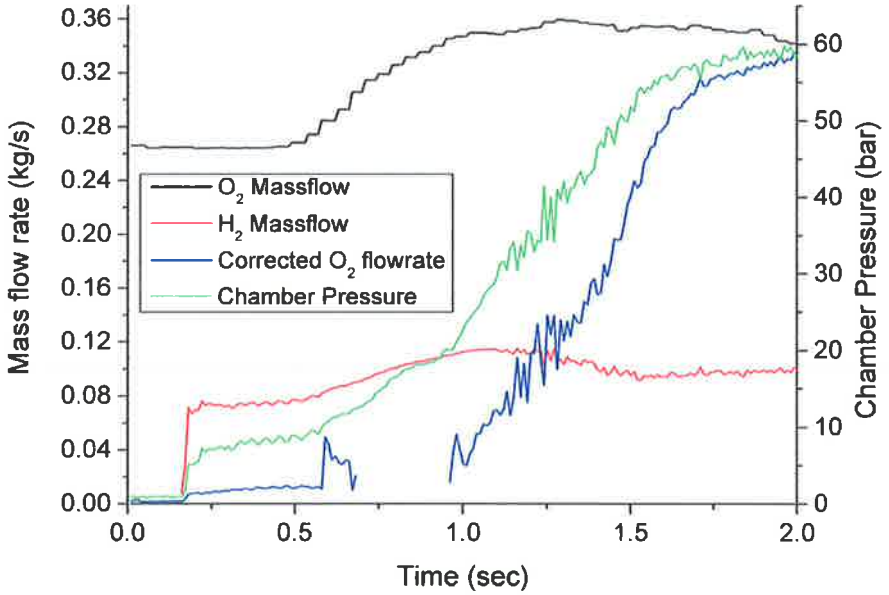

Figure 6.3 Corrected oxygen mass flow rate showing strong synchronous oscillations with chamber pressure. Data from test VIS05WA run 2.

6.1.3. Ignition Test Series - General Observations

Results from a parametric study of start-up and ignition transients is presented in the following sections of this chapter. Ignition characteristics are illustrated based on the combustion response and near injector flame behaviour observed.

During all tests the igniter is operational from $t = 0.09$ seconds prior to the activation of the main run valves (at $t = 0.0$ seconds). The torch igniter flame ignites the main propellant flow and the flame has a very low intensity. At this point, flow rates are very low and in some cases, the flame does not appear to be stable. This observation is seen in the emission images from approximately time $t = 0.4$ to 0.8 seconds. During this period it is difficult to characterise the flame and ignition process due to the very low emission intensity.

Increasing chamber pressure and H_2 film cooling flow rate results in a loss of positive pressure across the injector and a momentary void in oxidiser flow through the injector. This results in a loss of flame which consistently occurs anywhere between approximately 0.7 and 1.1 seconds. This observation is clearly visible in the corrected oxygen flow rate data presented in Figure 6.3. Once a positive pressure difference is established across the injector, the main propellant flow appears to re-ignite and a sharp, almost instantaneous increase in emission intensity signifies a stable flame has been established. This point of increased emission intensity defines the point of ignition. This point has been observed to vary somewhat depending on the injection conditions experienced.

The sequence of events mentioned are relatively consistent in each test and are understood to be directly related to the start-up sequence programmed into the test facility's master control system. The ignition sequence is acceptable due to the absence of excessive pressure peaks in the chamber or manifolds.

Table 6.1 details a series of ignition tests and lists the various operating conditions at the point of ignition defined by an instantaneous increase of emission intensity indicating flame stabilisation. Optical diagnostics were applied in the near injector field for each test condition listed. The thrust chamber was operated to nominal pressure (P_{ch} ~ 60bar) in each case presented.

Table 6.1 Injection conditions at point of ignition for three startup test cases

Parameter	Ignition Case 1	Ignition Case 2	Ignition Case 3
Actual Test Designation	VIS06WA run 2	VIS04WA run 12	VIS03WA run 20
Description	Stable. Definitive point of flame stabilisation.	Stable. Apparent flame oscillation at 1L chamber mode	Stable. Apparent flame re-ignition
Time of ignition t (sec)	1.17	1.17	1.25
Chamber pressure P_{ch} (bar)	35.76	29.7	31.1
Hydrogen temperature T_{H2} (K)	231.3	266.8	162.4
Oxygen temperature T_{O2} (K)	199.9	195.8	124.6
Oxidiser-fuel ratio R_{OF}	0.19	0.24	1.42
Velocity ratio R_v	25.85	38.7	144.8
Momentum flux ratio J	31.59	84.7	99.9
Hydrogen velocity v_{H2} (m/s)	711.96	1089*	976*
Oxygen velocity v_{O2} (m/s)	27.54	28.2	6.73
Oxygen density ρ_{O2} (kg/m³)	77.4	51.6	954.3
Hydrogen density ρ_{H2} (kg/m³)	3.66	2.92	4.55
O_2 injector pressure drop ΔP_{O2} (%P_{ch})	13.25	10.14	8.53
H_2 injector pressure drop ΔP_{H2} (%P_{ch})	114.5	44.3	16

*. Indicates sonic velocity

6.2 Characterisation of Smooth Start-up - Ignition Test Case 1

6.2.1. The Start-up Process

The ignition sequence implemented for the test series consistently results in a relatively stable, smooth start-up transient. Characterisation of the entire start-up process encompasses the time period from $t = 0$ seconds to $t = 2.0$ seconds and includes details regarding the point of ignition and the flame, flow and combustion response throughout the entire transient period. In all test cases examined, the observations made are unique to the hardware employed and the conditions examined.

Despite the transient being 'smooth,' the start-up phase of a liquid propellant rocket engine as a whole is an inherently unstable process regardless of injection conditions. Injection conditions favourable for ignition exhibit rapidly decaying, low pressure oscillations resulting in stable thrust chamber operation. Unfavourable conditions can result in pressure peaks upon ignition and large scale pressure oscillations which can cause hardware damage and/or performance losses (Figure 6.2).

Any instability experienced during combustor start-up is typically reflected in the thrust chamber and manifold dynamic pressure data. Unsteadiness experienced at start-up is related to unfavourable injection conditions. Observations presented here indicate that various forms of unsteadiness typically occur after the point of ignition of the injected propellants.

6.2.2. Flame Stability in the Near Injector Field

Ignition test case 1 listed in Table 6.1 represents conditions which result in a typical 'stable' start-up based on combustion response and flame dynamics. From $t \sim 1.12$ until $t \sim 1.17$, injection conditions are extremely unfavourable for the establishment of a stable flame. An extremely low R_{OF} exists at the point of ignition (see Table 6.1). The point of ignition is clearly visible with a definitive change in flame behaviour as illustrated in Figure 6.4.

Figure 6.4 represents a series of consecutive OH emission images recorded during the start-up period from time t = 1.1629 to t = 1.1752 seconds from ignition test case 1 (Δt = 0.0123 sec.). The images originally captured at 9kHz are represented by each third image for convenience (i.e. 3kHz). The flame exhibits a very low intensity and appears somewhat unsteady from frames 1 through 19 in Figure 6.4. Frame 20 in Figure 6.4 represents the point of ignition and a high intensity stable flame exists from frame 20 to 38.

Throughout the start-up transient, the igniter flame exhibits a periodic behaviour and appears to have a direct influence on the main propellant flow. This is a noteworthy observation clearly illustrated by Figure 6.4. The igniter flame impinges upon the main propellant flow which promotes reaction and a momentary increase in flame emission intensity (i.e. frames 2-5). This increased emission then diminishes in the absence of the igniter flame (frames 6-9) until flash-over from the igniter flame occurs once more (frames 10-12). This process continues repeatedly until conditions become favourable for a stable flame.

At approximately t = 1.17 seconds, a dramatic instantaneous increase in emission intensity defines the true point of ignition and a stable flame results (frame 20 in Figure 6.4). Upon ignition, the flame appears to immediately decrease in length and a 'fist' like shape is formed at the front of the flame.

The increase in emission intensity cannot be attributed to an increase in pressure as the pressure difference between frames 19 and 20 in Figure 6.4 is very low (< 0.5 bar). The increase in flame emission intensity is a direct result of an ignition or flame stabilisation process. Once ignition occurs in this case, the flame remains stable and a steady increase in length and emission intensity is observed until nominal operating conditions are achieved.

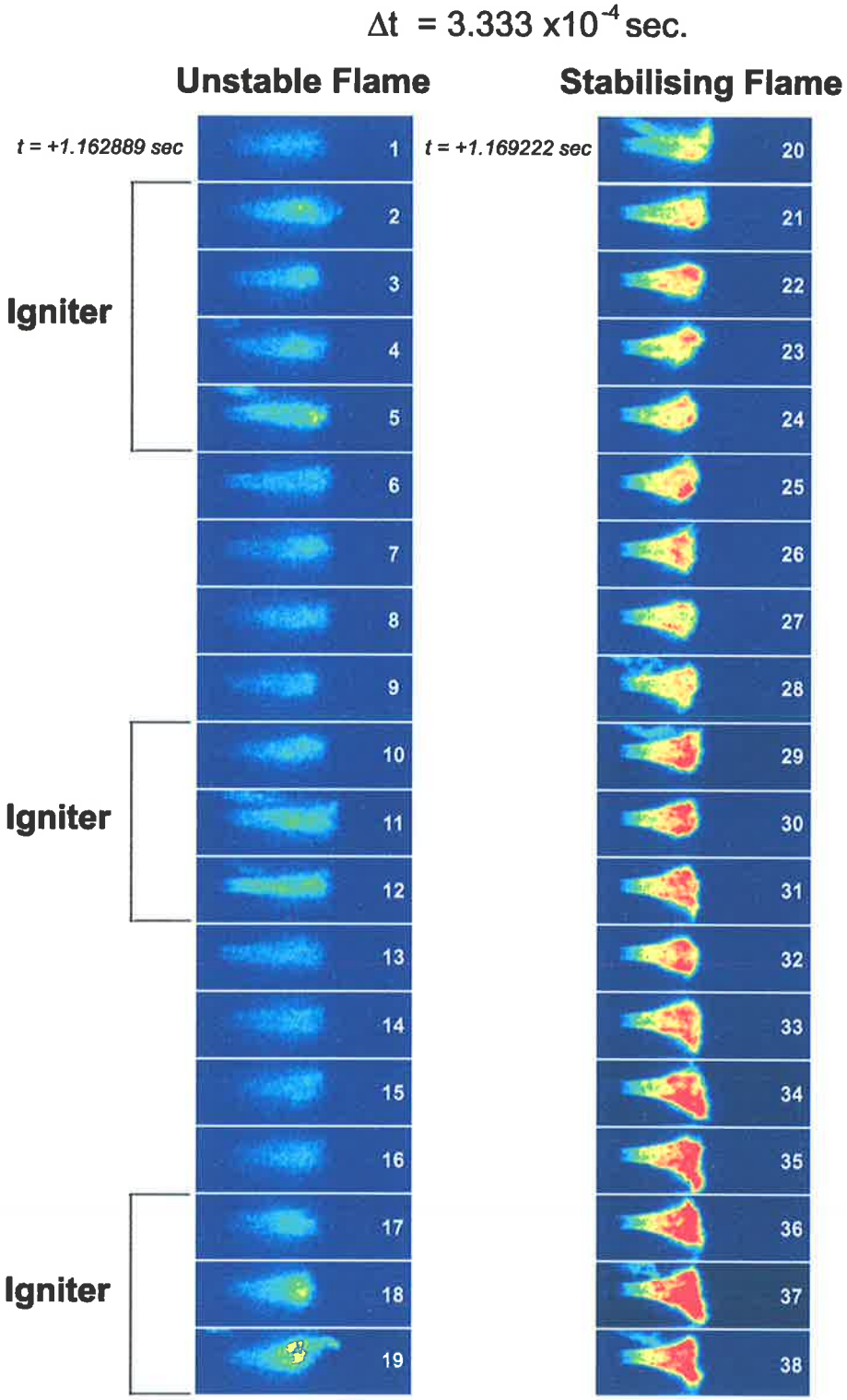

Figure 6.4 Near injector field illustrating smooth ignition process. Frame series 1-19 denote an unsteady, low intensity flame and frames 20-30 represent a stable flame. Frame 20 depicts the point of ignition. Data from Ignition Case 1. Note strong retraction of flame front upon ignition.

6.2.3. Dynamic Pressure Data

Filtered dynamic pressure data recorded during thrust chamber operation is examined to understand the dominating phenomena taking place during combustor start-up. Figure 6.5 represents the dynamic pressure data measured in the thrust chamber and the propellant manifolds during test case 1. The static combustion chamber pressure is also included.

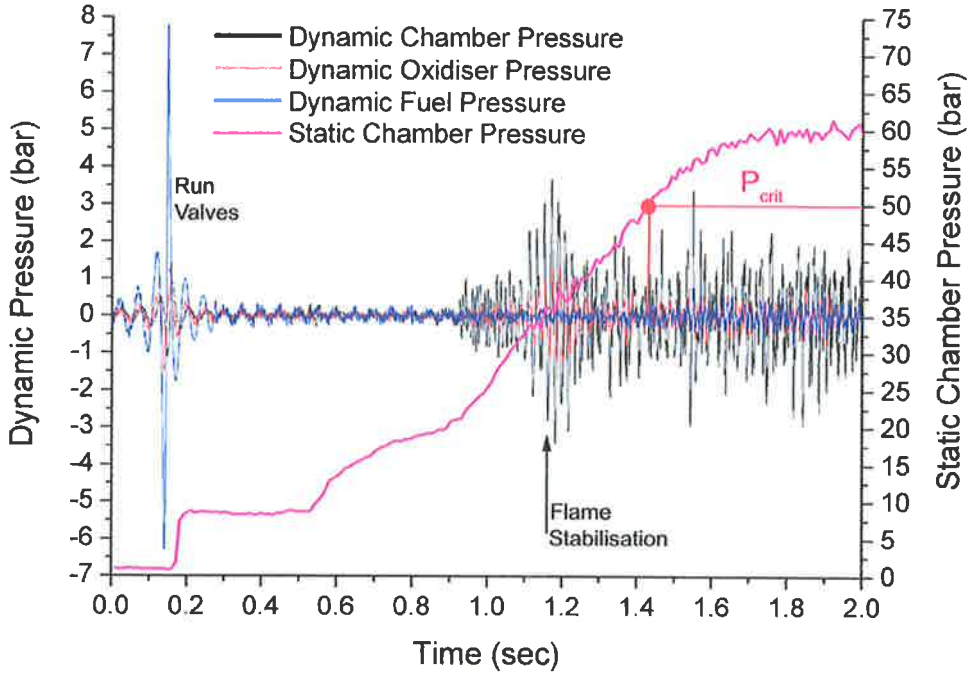

Figure 6.5 Dynamic chamber pressure, oxidiser manifold pressure, fuel manifold pressure and static chamber pressure as a function of time. 500Hz low pass filtered data from ignition case 1.

The spontaneous OH emission and shadowgraph images recorded during the start-up transient period exhibit oscillations and unsteadiness which correspond strongly with the pressure data recorded and presented in Figure 6.5.

Figure 6.6 represents a segment of filtered dynamic pressure data from Figure 6.5 recorded from approximately $t = 1.0$ to 1.2 seconds. The dynamic chamber pressure oscillations appear to lead the oxidiser manifold pressure by approximately $\Delta t = 0.004$ seconds. The combustion chamber pressure amplitudes begin to increase steadily at approximately $t = 1.1$ seconds followed by

coherent fluctuations in the oxidiser manifold. The initial unsteadiness in the chamber pressure is effectively driven by modulation of the oxidiser resulting in an apparent self sustaining (injector coupled) instability. The fuel manifold is unaffected by the large amplitude pressure oscillations in both the chamber and the oxidiser manifold.

Chamber and oxidiser manifold pressures continue to increase from $t = 1.1$ seconds and reach a maximum peak-to-peak value at approximately $t = 1.17$ seconds. Inspection of the OH emission images indicate the true point of ignition (stabilisation) occurs at this point. Once ignition occurs, the pressure oscillations appear to decay.

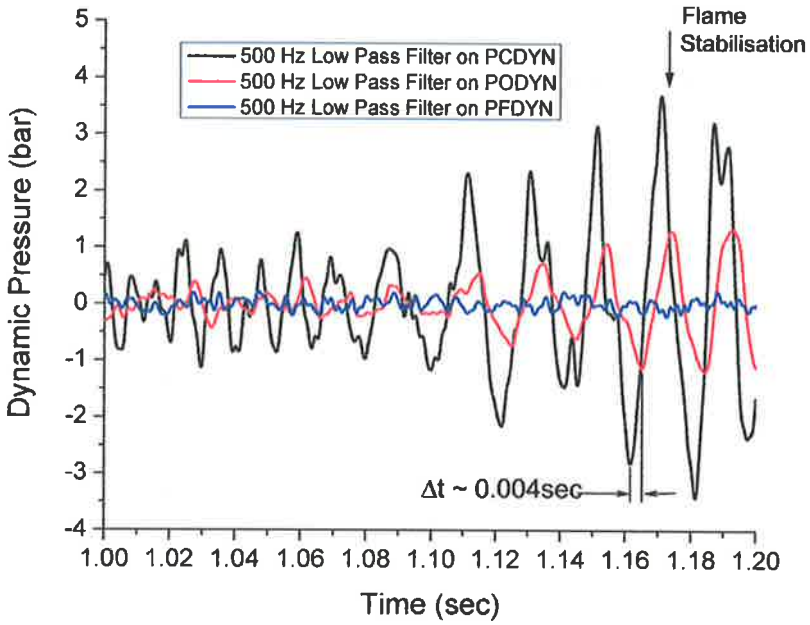

Figure 6.6 Filtered dynamic pressure data from chamber (PCDYN) and oxidiser and fuel manifolds (PODYN and PFDYN). Pressure trace illustrates increase in chamber pressure amplitudes leading oxidiser manifold pressure by t ~ 0.004 seconds. Data from ignition case 1.

6.2.4. Low Frequency Injection Coupled Ignition Instability

A dominant LF oscillation is clearly visible in the dynamic pressure trace.The oscillation frequency changes with time (injection conditions) and ranges from $f \sim$ 50 to 100Hz. A Fourier analysis indicates the frequency is coherent from approximately $t = 1.0$ seconds and it decays completely by $t \sim 1.25$ seconds. The phenomena observed resembles a classical low frequency

(LF) injector coupled combustion instability which is triggered during the start-up transient. The LF instability is clearly evident in the image series captured by the optical systems. It is apparent that ignition (stabilisation) of the flame coincides with attenuation of the injector coupled instability in this case. Figure 6.7 illustrates simultaneous OH emission and shadowgraph images captured during the decay of the unstable phase of the ignition transient. Frames displayed in Figure 6.7 represent an acquisition rate of 500Hz from $t \sim 1.238$ to $t \sim 1.284$ seconds ($\Delta t = 0.046$ seconds).

6.2.5. Dynamic Pressure Fluctuation

Further analysis of the dynamic pressure data is performed by normalising the peak-to-peak dynamic chamber pressure values relative to static combustion chamber pressure.

$$\hat{P}_{dyn_{pp}} = \frac{\Delta P_{ch_{dyn}}}{P_{ch}} \tag{4.1}$$

This analysis is similar to that performed at steady state conditions to assess levels of combustion stability. Figure 6.8 illustrates $\hat{P}_{dyn_{pp}}$ as a function of time and reduced pressure, with static chamber pressure superimposed. A minimum peak-to-peak dynamic pressure value exists at a reduced pressure equal to 1. The normalised values decrease steadily as the critical pressure is approached from approximately 1.1 seconds. A minimum is experienced at approximately 1.43 seconds followed by a steady increase and a plateau at approximately 1.7 seconds once the nominal operating pressure is achieved. It is interesting to note the minimum peak-to-peak pressure value occurs at $P_r = 1$.

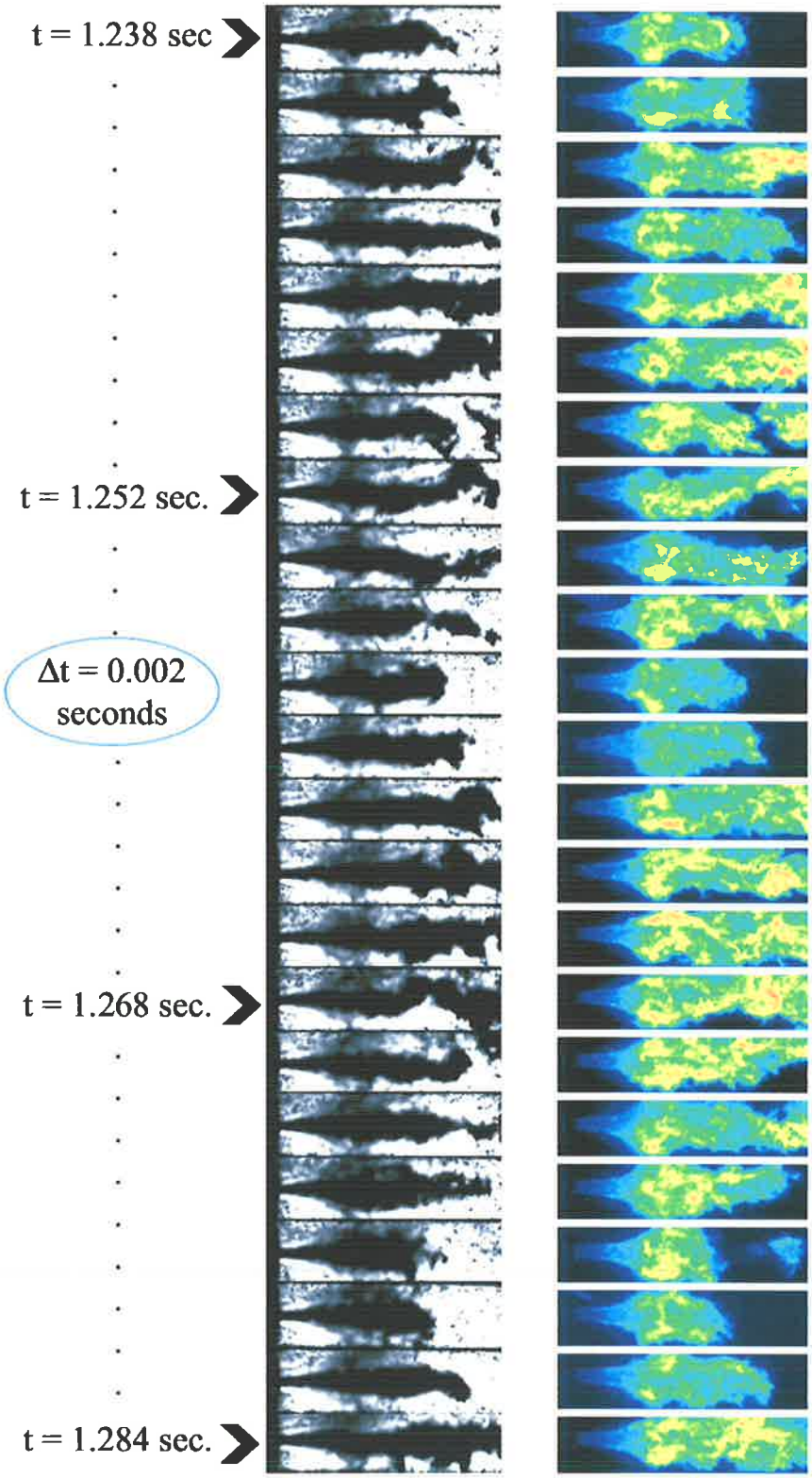

Figure 6.7 Simultaneous shadowgraph and spontaneous OH emission frames illustrating LF instability during start-up. Images shown here were captured at a frequency of 500Hz (Δt = 0.002) seconds. Strong correlations exist between the 2 image sets. Data from ignition case 1.

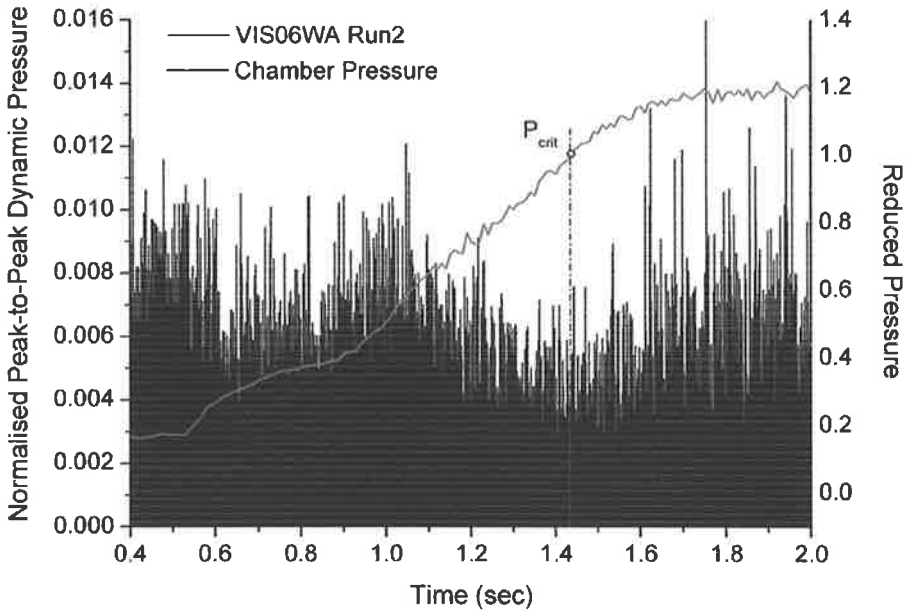

Figure 6.8 Normalised peak-to-peak dynamic combustion chamber pressure and static chamber pressure plotted against time. Data from ignition case 1.

6.2.6. Flamefront Analysis

The flame front is tracked axially during the start-up transient in order to accurately quantify any fluctuation and potentially reveal any dominant flame oscillation. Figure 6.9 demonstrates the flame front behaviour during start-up from ignition test case 1.

At low pressure, the main propellant flow field appears to ignite with relatively low flow rates from time $t = 0.42$ - 0.8 seconds and the flame has a very low emission intensity (refer to area 1 in Figure 6.9 (a)). The low intensity flame is observed to retract strongly toward the injector face plate from $t = 0.8$ - 0.9 seconds and appears to extinguish at approximately $t = 0.9$ seconds due to a lack of oxygen caused by a negative pressure difference across the oxygen side of the injector (refer area 2 of Figure 6.9 (a). As the flame moves back, the torch igniter appears to strongly influence the position of the flame front. A coherent frequency at $f \sim 380$Hz exists from approximately $t = 0.75$ seconds. Close inspection of the OH emission images reveals the frequency corresponds to the operation of the torch igniter (refer Figure 6.9 (b)). The signal is

stronger once the main propellant flow has disappeared at $t = 0.9$ seconds indicating the torch igniter continues to operate until approximately $t = 1.12$ seconds (refer area 3, Figure 6.9 (a)).

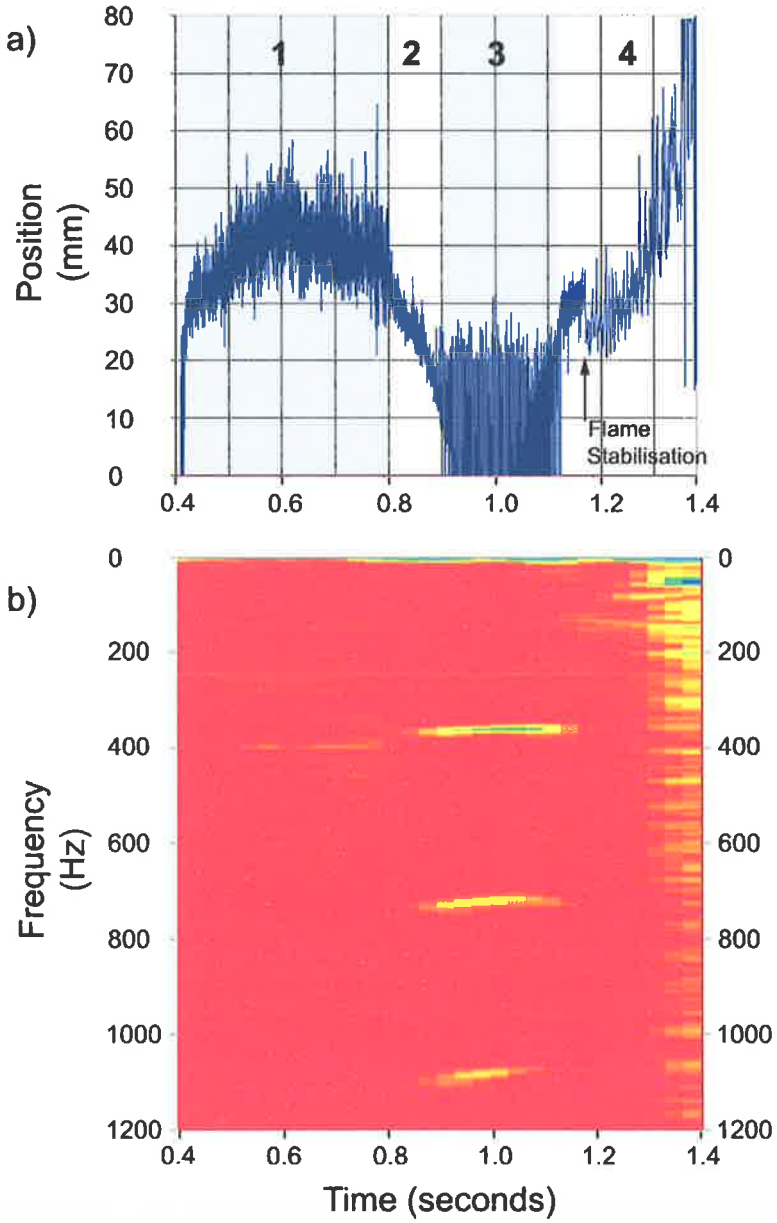

Figure 6.9 Axial flame front position (a) and corresponding FFT spectrogram (b) during combustion chamber start-up. Spectrogram indicates a coherent frequency at ~380Hz from ~ 0.9 to ~1.17 seconds and strong LF oscillation of approximately 50Hz from t ~1.27 seconds. Data from ignition case 1.

With a positive injector pressure differential, propellant flow rates and combustion chamber pressure tend toward nominal conditions. The unstable, low intensity flame described previously

Figure 6.4, Section 6.2.2) becomes apparent at approximately $t = 1.12$ seconds in Figure 6.9 (a).

The flame undergoes a significant transformation at $t = 1.17$ seconds. The apparent point of ignition (flame stabilisation) is clearly observed by the dramatic step in Figure 6.9. The flame front position data clearly indicate an immediate retraction of the flame front in a direction toward the face plate at $t = 1.17$ seconds. This observation corresponds well with the flame emission images presented in Figure 6.4.

Upon stabilisation of the flame, a coherent low frequency flame front oscillation becomes immediately apparent at approximately $t = 1.27$ seconds and is observed until the flame front extends beyond view of the window. The low frequency injector coupled instability undoubtedly corresponds with the oscillating flame and flow field illustrated in Figure 6.7.

6.2.7. Relative Flame Emission Intensity

The relative mean OH emission is calculated for the image series and the result is presented in Figure 6.10. The technique calculates the mean emission intensity based on the flame area as described in Section 4.4.6. The point of ignition (stabilisation) is obvious at $t = 1.17$ which corresponds with images and flame front analyses. Upon stabilisation, coherent OH emission fluctuations exist from around $t = 1.17$ - 1.45 seconds at a steadily decreasing frequency range from $f \sim 150$ to 54Hz in accordance with dynamic pressure data.

The normalised emission intensity exhibits an unstable behaviour as intensity amplitudes steadily increase with time as emission oscillation frequency decreases. From time $t \sim 1.37$ to $t \sim 1.43$ seconds, the frequency has reduced to around $f \sim 54$Hz before tapering off completely by $t \sim 1.45$ seconds. Oscillations are no longer coherent and all periodicity is lost.

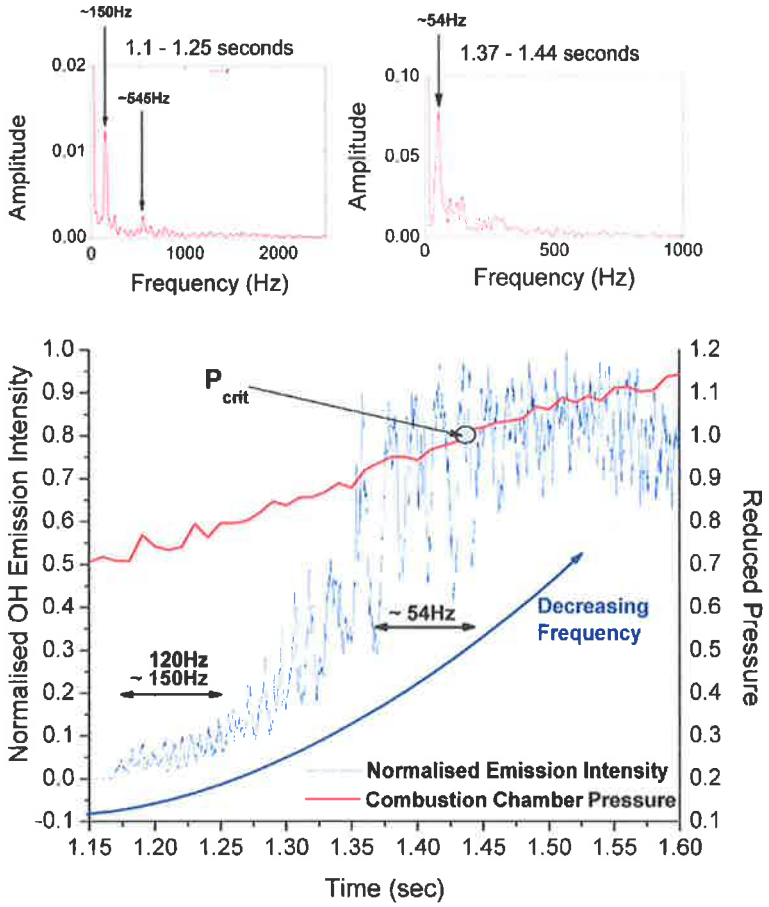

Figure 6.10 Normalised mean OH emission intensity and combustion chamber pressure recorded during combustor start-up. Data from test ignition case 1.

6.2.8. Centroid of Emission Intensity

The centre of emission intensity is investigated in an attempt to supplement previous observations of flame behaviour. Different regions of the flame are analysed independently to account for the sensitivity of the technique. The entire image (full window width of 100mm) is assessed here with a smaller area close to the injection plane subsequently investigated in Section. 6.2.6.

Figure 6.11 illustrates the flame emission intensity centroid as a function of time and strongly resembles Figure 6.9 (a) which represents the flame front position with time. Figure 6.11 indicates the igniter flame exists for a period of time prior to retracting between approximately

t = 0.8 to 1.0 second. At $t \sim 1.05$ seconds, the main propellant flow re-ignites and the flame centroid of emission extends downstream of the injection plane. Once more, a step is observed at $t \sim 1.17$ seconds indicating stabilisation of the flame at the LOx injector post. The flame centroid then steadily moves back toward the injection plane and steadies at a downstream distance of approximately 24mm. Radial position data are not included as they provide no value.

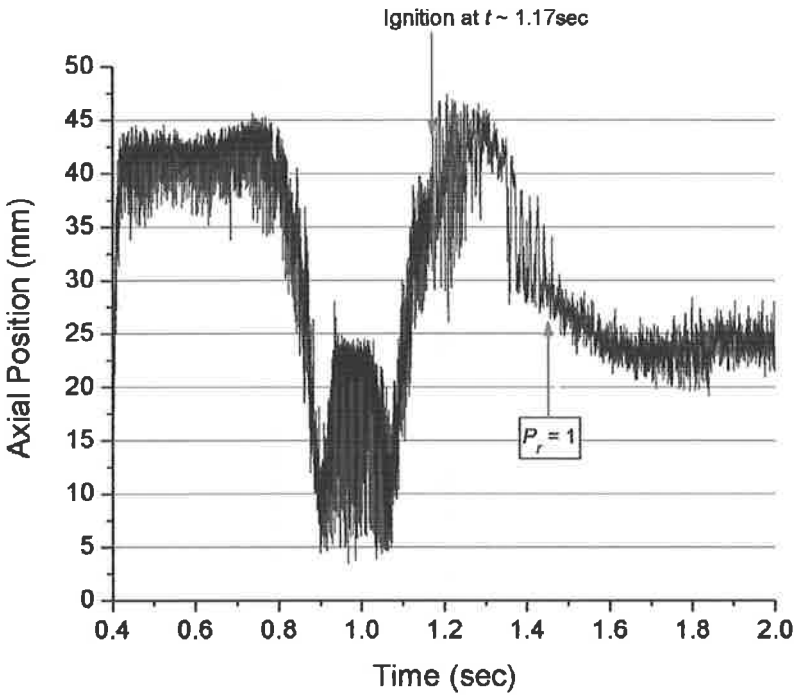

Figure 6.11 Axial position of emission intensity centroid as a function of time for full flame image during combustor start-up. Data from ignition test case 1. Axial position is measured from left edge of window.

The apparent extension of the flame during start-up may be attributed to the injection conditions during this period. Injection velocity of H_2 ranges from sonic (~1170m/s) down to as low as approximately 430m/s. As H_2 temperature decreases, density increases, and injection velocity decreases and the centre of emission intensity retracts. The presence of water vapour in the near injector field at the steady state conditions may potentially falsify the centroid position results beyond approximately $t \sim 1.8$ seconds.

The centroid of emission intensity position resembles that of the emission intensity plot illustrated by Figure 6.9. A difference is observed when comparing the axial position of the flame front and the centroid of emission intensity. A definitive step exists at the point of flame stabilisation (i.e. at $t \sim 1.17$ seconds) but unlike the flame front position, the intensity centroid does not move immediately toward the injector. At $t \sim 1.17$ seconds the centroid position moves away from the injector and exhibits a relative unsteadiness until approximately $t \sim 1.3$ seconds where the centroid position moves back toward the injector.

Upon ignition, the flame shape changes significantly and takes the form of a 'fist' with the stabilised flame amassing a far greater area near the flame front. Figure 6.4 illustrates high OH emission intensity in the 'fist' of the flame. This change in flame shape and corresponding increase in area explains the positive downstream translation of the emission intensity centroid observed in this case.

A spectral analysis performed on the centroid position data presented in Figure 6.11 results in the spectral plot presented in Figure 6.12. From approximately $t = 0.82$ to $t = 1.15$, strong coherent oscillations exist in the combustion zone at a frequency $f \sim$ 380-400Hz. The periodic behaviour observed in Figure 6.12 resemble the oscillations observed in the flame front analysis and represent the flame emanating and retracting from the torch igniter in the absence of a main injector flame. The 380-400Hz is also visible prior to $t = 0.82$ seconds with lower amplitudes as the torch igniter starts at $t = 0.2$ seconds.

As in the flame front analysis, the emission intensity centre tends to oscillate violently upon ignition at $t \sim 1.17$ seconds. A period of strong fluctuation follows resembling a typical LF unstable mode of combustion with a steady decrease in frequency and an increase in amplitude. This flame oscillation is attenuated once the critical pressure of O_2 is reached (refer Figure 6.11).

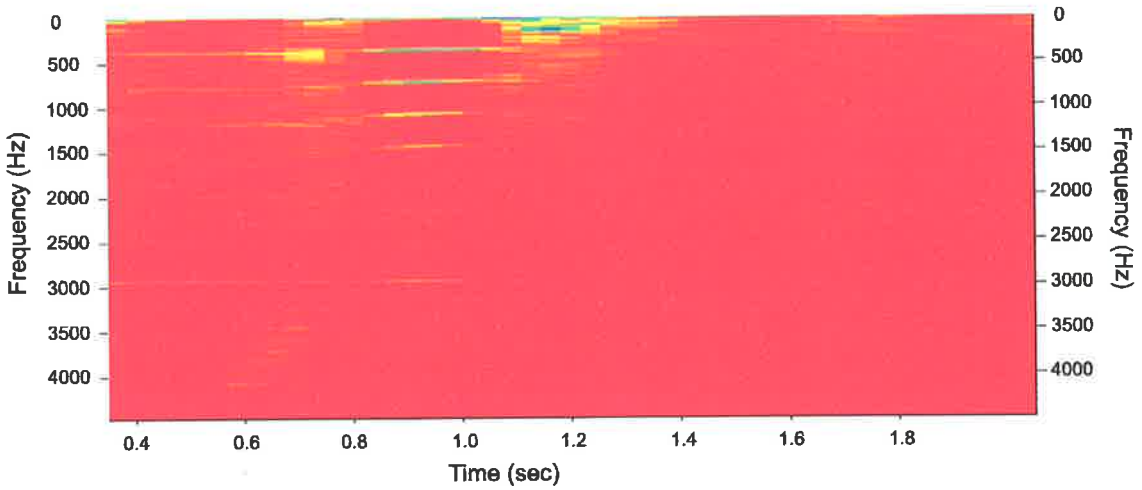

Figure 6.12 Spectrogram of centroid of OH emission intensity (axial direction) for full window illustrating torch igniter oscillations at f ~ 380-400Hz. Data from ignition test case 1.

The relative change in centroid position between frames (peak-to-peak analysis) can provide further information on flame steadiness. Peak-to-peak values presented in Figure 6.13 are calculated based on the data presented in Figure 6.11. The data is normalised based on the maximum axial position of the centroid of emission intensity. Large peaks exist from $t \sim 0.8$ to $t \sim 1.1$ seconds as the igniter operates continuously in the absence of an ignited main propellant flow.

Figure 6.13 indicates a flame unsteadiness exists until approximately $t = 1.1$ seconds. As chamber pressure increases, the fluctuation of emission intensity centroid decreases significantly. The change in axial position of the emission centroid is a minimum near the critical pressure of O_2. Once the critical pressure of oxygen is surpassed, the fluctuations tend to increase slightly once more. This observation for ignition test case 1 is in agreement with the dynamic pressure peak-to-peak pressure analysis. There appears a strong correlation between the flame and combustion steadiness and the critical pressure of oxygen. This phenomenon is consistent with other ignition tests studied.

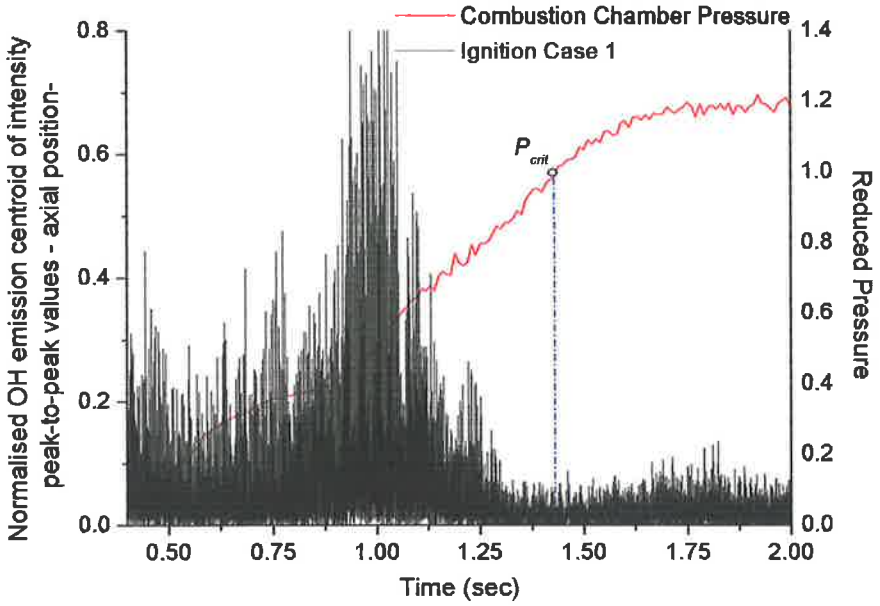

Figure 6.13 Normalised peak-to-peak centroid of intensity values with reduced combustion chamber pressure highlighting the critical pressure of oxygen. Data from ignition test case 1.

6.2.9. Near Injector Centroid of Emission Intensity

The near injector zone is studied closely by cropping the series of OH emission images assessed in previous sections to provide a small region extending from the face plate to approximately 21mm downstream of the injection plane (refer Figure 6.14). Examination near to the injector is necessary to identify whether trends exist common to those observed using other techniques.

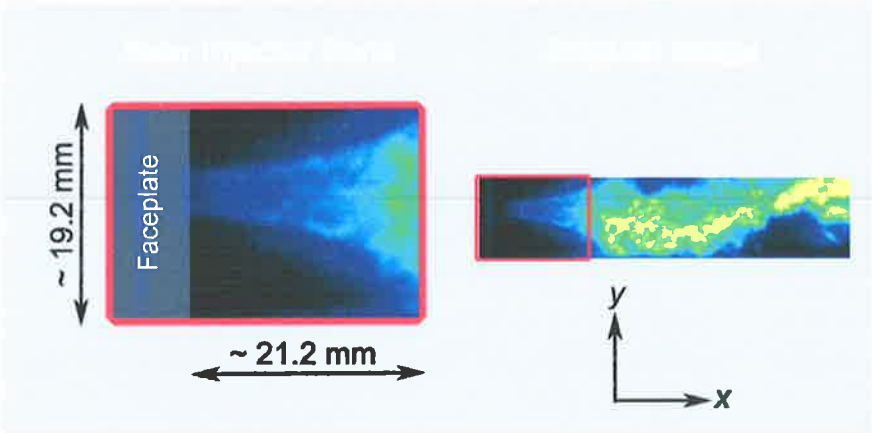

Figure 6.14 Near injector zone used for calculating the centroid of emission intensity during start-up

The near injector centroid position is presented as a function of time during the start-up period in Figure 6.15 in the axial direction. The results exhibit similarities once again to both the full flame centroid intensity analysis and the flame front position investigation.

A large "step" in intensity centroid position clearly visible in Figure 6.15 at around time $t \sim 1.17$ seconds. This step represents the stabilisation of the flame as discussed previously and is especially obvious in the near injector zone.

A major difference between examination of the full window and near injector field appears to be a more distinct influence from the torch igniter and far greater coherence in periodic fluctuations throughout the transient period. Figure 6.16(a) and Figure 6.17 highlight this observation and clearly shows the increased near injector emission intensity due to the addition of localised energy to the main propellant flow from the torch igniter.

From approximately $t = 1.2$ seconds, low frequency oscillations are observed in the centroid position data. From t=1.3 to t=1.47 seconds the igniter frequency of $f \sim$ 380-400Hz is dominated by a coherent oscillation at approximately f = 54Hz in the near injector field as illustrated by Figure 6.16(b). The frequency of unsteadiness appears to decrease with time and amplitudes tend to steadily increase as observed previously in the mean flame OH emission intensity and emission centroid plots (i.e. Figure 6.10 and Figure 6.11). The near injector field appears to influence the downstream flame front position through amplification of the low frequency fluctuations.

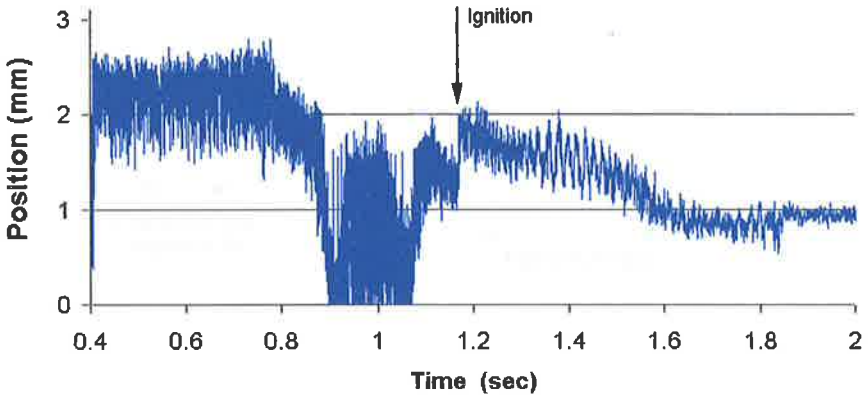

Figure 6.15 Near injector axial centroid of emission intensity position as a function of time during combustor start-up. Data from ignition test case 1.

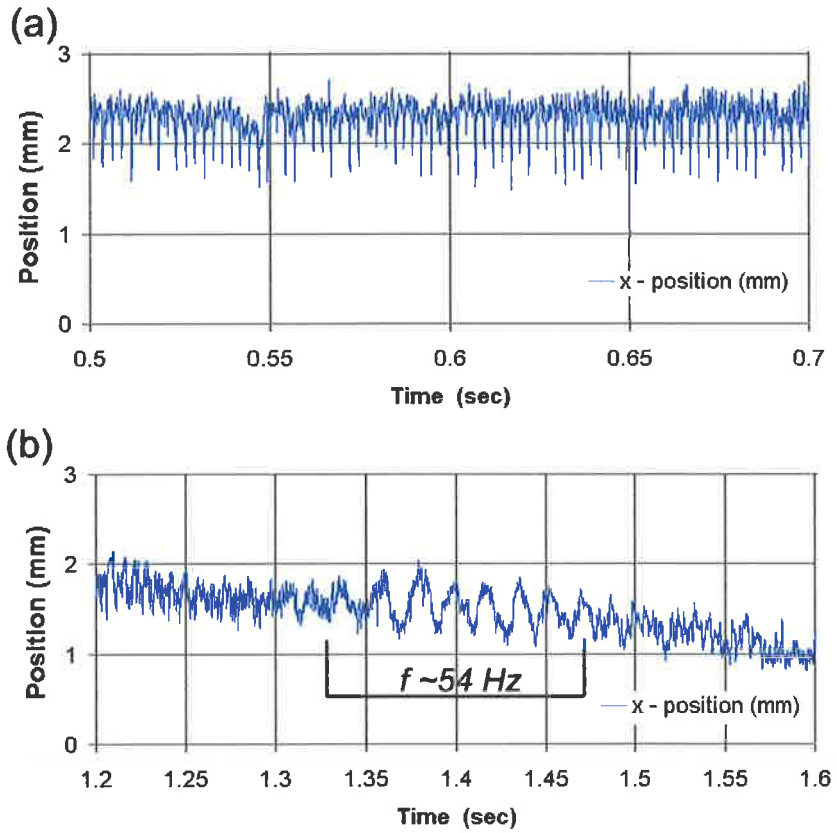

Figure 6.16 Near injector axial centroid position of emission intensity exhibiting strong periodic behaviour at time t = 0.5 - 0.7 sec (a) and t = 1.33 - 1.47 sec (b). Data from ignition test case 1.

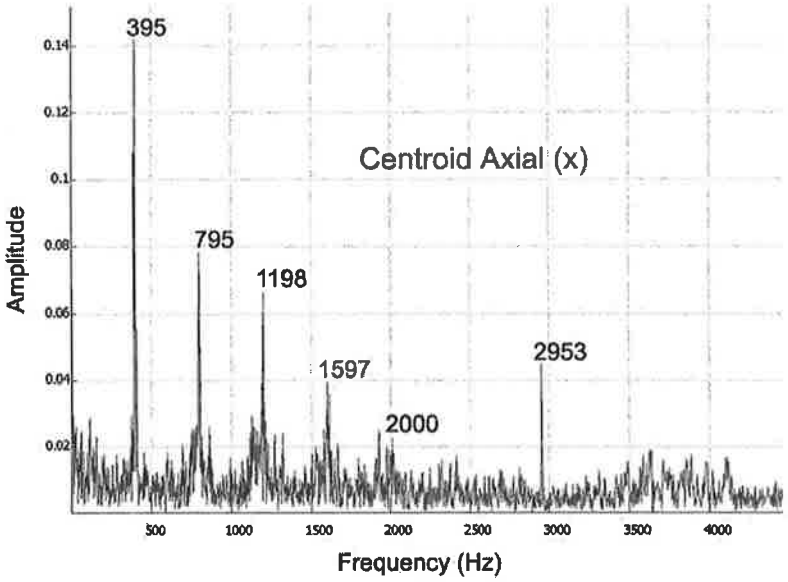

Figure 6.17 Spectra resulting from near injector axial centroid position during start-up at time t = 0.5 to 0.7 seconds indicating a coherent frequency at f ~ 395 Hz with harmonics. Data from ignition case 1.

6.2.10. Summary of Smooth Start-up - Test Case 1

Conditions listed as ignition case 1 in Table 6.1 result in a relatively smooth start-up transient and ignition of the injected propellants. The torch igniter is analogous to the VINCI igniter and is thought to provide a continuous flame to the main propellant flow. In this case the torch igniter however has been observed to operate periodically. Prior to ignition (stable flame), the periodic operation of the igniter flame is observed to influence the emission intensity of the main propellant flow. The imaging systems and image processing methodologies employed indicate the torch igniter flame enters the chamber for a short period (~90ms) and fluctuates at approximately f = 380-400Hz.

A fuel rich, gaseous propellant mixture with an injection velocity ratio of around R_v = 25.9 results in ignition with an instantaneous increase in emission intensity at t = 1.17 seconds. An obvious feature of ignition is the strong retraction of the flame front toward the injection plane. A positive axial movement of the emission centroid results from the flame front amassing to form a 'fist' of high emission intensity. Upon ignition, the flame exhibits an unsteadiness which is consist-

ently visible in various forms and is analogous to an injector coupled (LF) instability. Injector coupled instability is typically related to the pressure differential across the injector.

A coherent oscillation exists in the normalised emission intensity analysis from $t = 1.17$ seconds at approximately $f \sim 150$Hz. This flame front oscillation frequency rapidly decreases with a steady increase in amplitude until a frequency of $f \sim 54$Hz is achieved at $t \sim 1.3$ seconds. At this point, the LF oscillation is also observed in the OH emission images and emission centroid position corresponding to the full flame (full window) and near injector field close to the injection plane. The LF phenomenon is also observed in the flame front analysis. Although the pressure difference across the O_2 injector exceeds 13% of chamber pressure at ignition, the oscillation represents an injector coupled instability which is also evident in the dynamic pressure spectra.

At this point in time, the static chamber pressure increases at a rate of approximately 54 bar/sec. Upon reaching the critical pressure of oxygen (50.4 bar) the coherence is lost in the fluctuations and no periodicity exists. The flame appears to steady rapidly near to the critical pressure. Normalised peak-to-peak fluctuations in dynamic pressure, and centroid position indicate a minimum near a reduced pressure equal to unity. As chamber pressure increases to the nominal level, the aforementioned peak-to-peak values slightly increase and stabilise.

Whilst LF fluctuations exist, the thrust chamber exhibits stable characteristics throughout start-up with injection conditions listed under test case 1 (Table 6.1). At no point does any image data exhibit fluctuation or oscillations which coincide with the acoustic modes of the combustion chamber. The start up transient process for test case 1 is relatively smooth and stable. During the start-up phase of liquid rocket engines, the fluid and injection system may be exposed to unfavourable conditions at some point during the transient process. The key to stable ignition is to operate at a point whereby the effects and duration of the threatening condition are minimised.

6.3 Stable Start-up - Ignition Test Case 2

Data relating to ignition test case 2 based on conditions listed in Table 6.1 reveal significantly different behaviour to that described for stable ignition in the previous section. The primary difference between the two test cases is the geometry of the injectors utilised which affects the propellant injection velocities and the local R_{OF} at the point of ignition. Both tests ignite with gaseous propellants as shown in Table 6.1.

The near injector combustion zone for ignition case 2 is depicted by Figure 6.18 and undergoes a different ignition process in comparison to ignition case 1. The oxidiser flow is suppressed until approximately $t = 0.9$ seconds when the low flow rate, low R_{OF}, main propellant flow field is ignited. The point of ignition is not as obvious as in ignition test case 1 but occurs nonetheless at 1.17 seconds - identical to that of test case 1. The point of ignition is apparent due to a sudden increase of flame emission intensity.

The OH emission intensity and flame length increase steadily with pressure and propellant flow rate. The flame develops and the emission intensity appears relatively consistent along the length of the flame. From approximately $t = 0.9$ seconds until approximately $t = 1.18$ seconds, an occasional yet coherent flame oscillation is observed. This oscillation is clearly evident in Figure 6.18 which displays an image series from time t =1.1747 to t = 1.1773 seconds. The flame length appears to oscillate at a frequency between approximately f = 1500 -1700Hz which corresponds to the 1L mode of the thrust chamber. This observation, clearly evident from the image series presented in Figure 6.18 is illustrated further by the flame front analysis data presented in Figure 6.19.

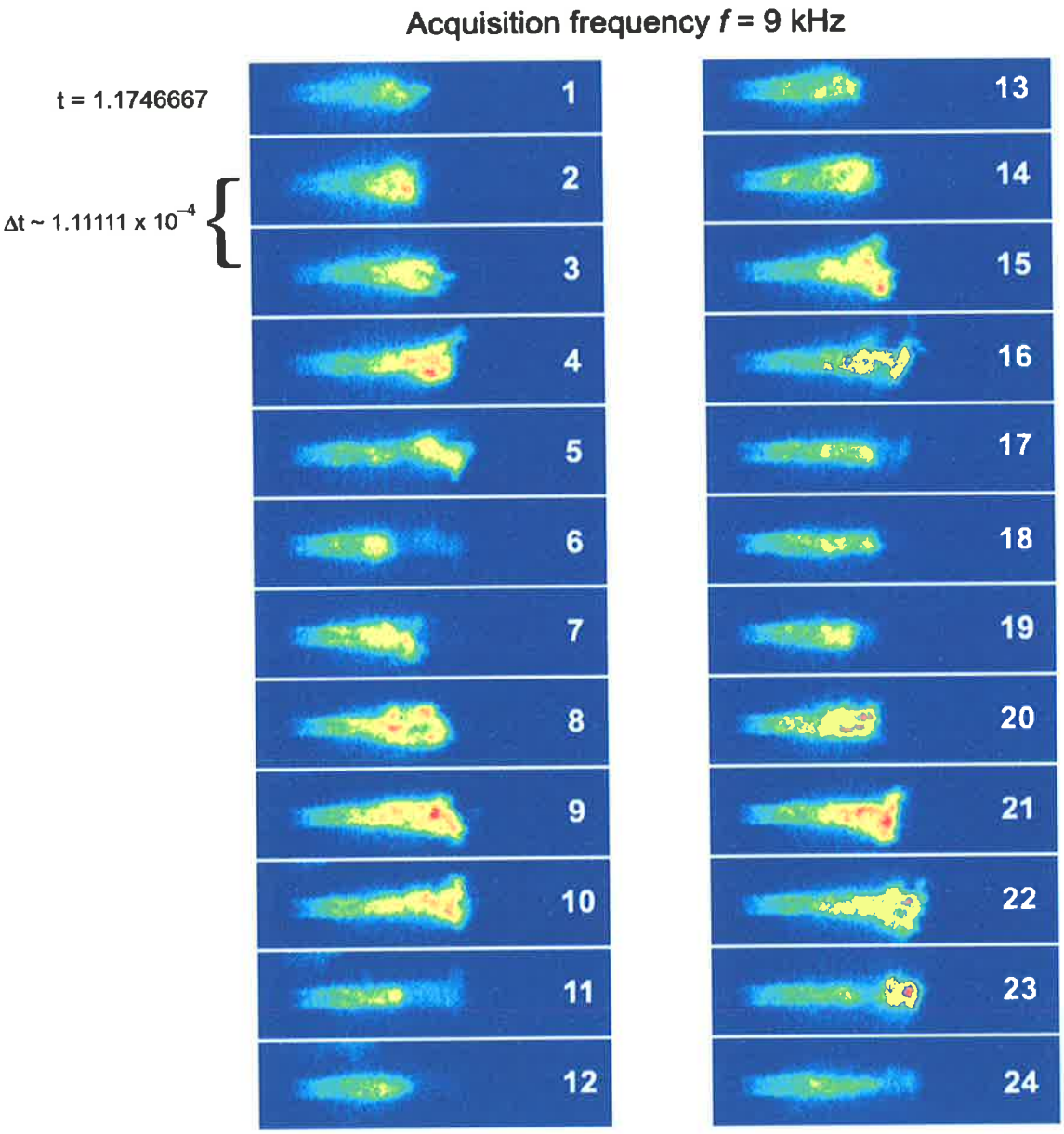

Figure 6.18 Strong flame front oscillations at a frequency near to the 1st longitudinal acoustic mode of the combustion chamber (f~ 1500-1700Hz). Data from ignition test case 2.

By approximately $t = 1.198$ seconds, the oscillations have decayed and periodicity is lost. In comparison to ignition test case 1, the flame appears relatively stable during the start-up transient. This may be attributed to the greater R_v experienced during ignition test case 2 however this cannot be confirmed. All other parameters listed in Table 6.1 are very similar in magnitude.

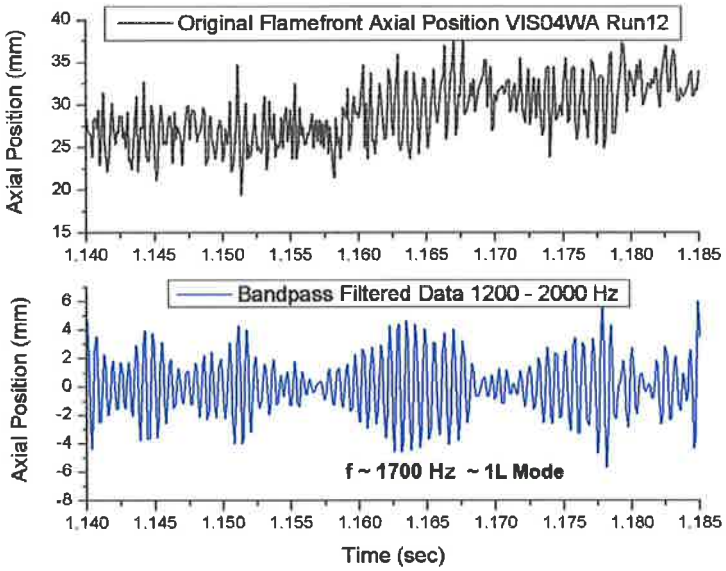

Figure 6.19 Flame front position data (raw top, filtered bottom) highlighting strong interaction of flame front with combustion chamber 1L mode at f ~ 1500-1700 Hz. Data from ignition test case 2.

A noteworthy observation is the correlation between mean relative flame emission intensity and axial flame front position depicted by Figure 6.20. The technique described in Section 4.4.6 accounts for relative flame size and results here indicate that mean flame emission intensity increases with flame front position. This is somewhat noticeable by inspection of image series' such as those presented in Figure 6.18.

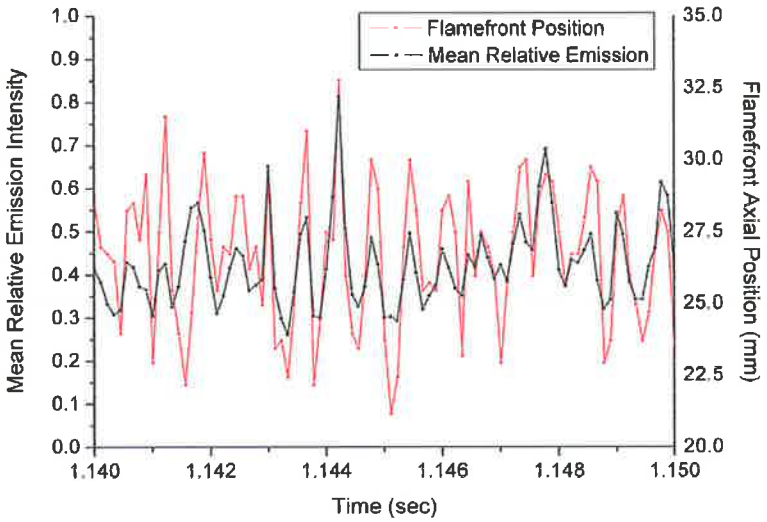

Figure 6.20 Segment of mean relative OH emission intensity and flame front axial position with time highlighting the strong correlation between flame front position and emission intensity. Data from ignition test case 2.

6.4 Stable Start-up - Ignition Test Case 3

A third ignition test designated ignition test case 3 (Table 6.1) exhibits further ignition phenomenon not experienced during the other test cases. Unlike ignition test cases 1 and 2, liquid oxygen is injected as opposed to gaseous oxygen as during the start-up transient. As a result, the R_v and the R_{OF} are significantly greater than that experienced by the previous two test cases. The introduction of two-phase flow during start-up further complicates the ignition process. Under such conditions, the evaporation rate of LOx core may be of a greater influence than R_v or R_{OF}.

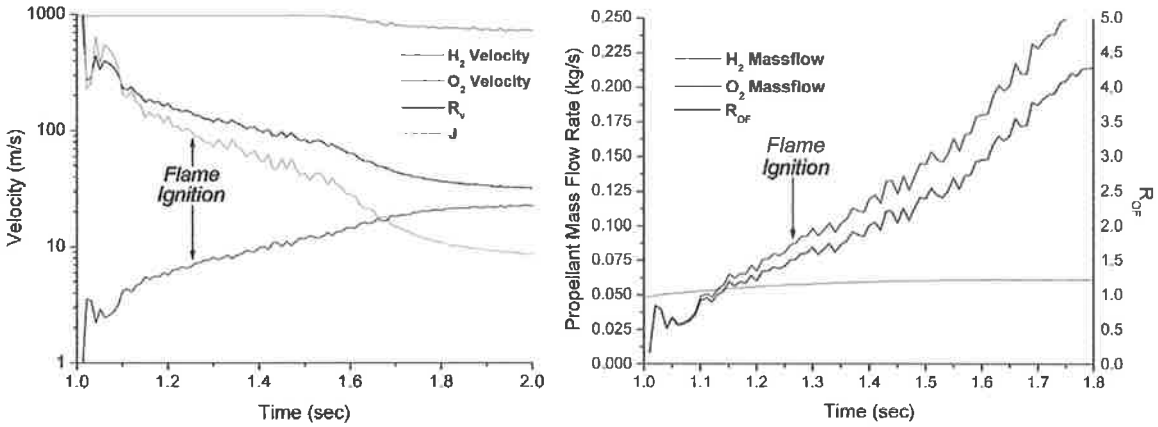

Figure 6.21 Injection conditions during start-up transient of ignition test case 3 highlighting the point of flame stabilisation at t = 1.25 seconds.

At the point of ignition, the injection velocity ratio is of the order $R_v = 144$. The high relative propellant velocity creates a highly unstable flame and flame front which is clearly evident from the emission images obtained throughout the start-up transient.

From the point of flame stabilisation through to nominal operating conditions, the flame appears relatively unsteady until $t \sim 1.7$ seconds. The flame length continuously extends beyond the field of view and retracts to within view until approximately $t = 1.78$ seconds.

At one point during the start-up transient, the flame appears established before it is observed to "blow-out" for a short moment before re-igniting. This observation is clearly illustrated by the

image series 1 - 27 listed in Figure 6.22. The total time period represented is 8.66msec from time t = 1.2665 to t = 1.2752 seconds. The main propellant flow initially ignites and stabilises momentarily at approximately t = 1.266 seconds and appears established until t = 1.2686 seconds which is represented by frames 1-8 in Figure 6.22. This phenomenon may be attributed to a very high relative injection velocity of propellants which fluctuate between R_v = 120 - 145 during this period. High relative velocities create a region of significant strain between flows which may facilitate localised flame extinction. High strain rates coupled with low temperature (liquid) oxygen may appear to temporarily prohibit reaction and flame stabilisation. At this point in time, hydrogen flow rates are nominal and the R_{OF} is relatively high in comparison to other ignition tests. The evaporation rate of the liquid oxidiser may be a controlling mechanism during start-up and may contribute to the observations witnessed here.

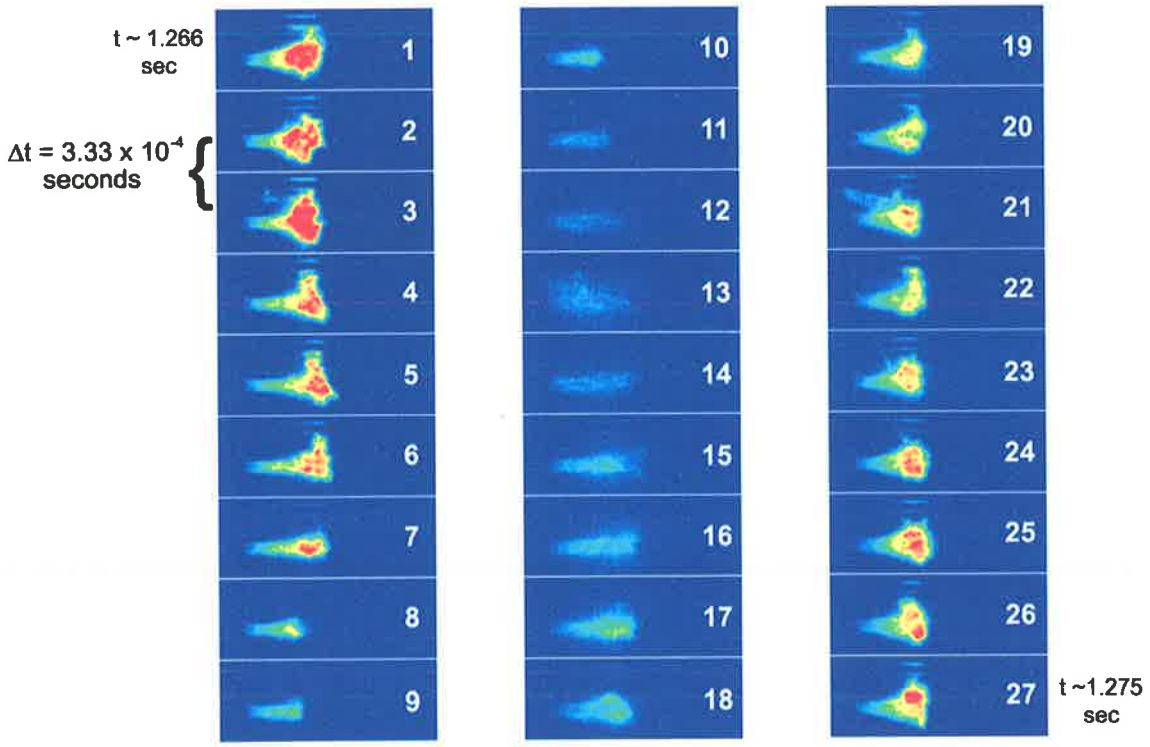

Figure 6.22 Blow out and re-ignition of the main propellant flow during ignition with liquid oxygen and high relative propellant injection velocities (R_v ~ 140). Data from ignition test case 3.

6.5 Flame Emission Spectra During Ignition

Spectra were acquired for 2 axial positions - 20mm and 70mm downstream from the injection plane during ignition. Accurate positioning of the detection unit was achieved by measuring a signal maximum from a reference point produced by a He-Ne laser focused on the chamber centre line at the aforementioned axial distances from injector. In order to obtain a spectral range of 300-900nm, the central wavelength of the spectrograph was set to 550nm for both axial positions.

Mean flame emission spectra were constructed from a series of spectra recorded during the ignition transient at 20mm and 70mm as shown in Figure 6.23. In order obtain a correct ratio of line intensities, the transmission function of the detection system was measured using a tungsten lamp. The spectra recorded have been adjusted to account for the transmission function.

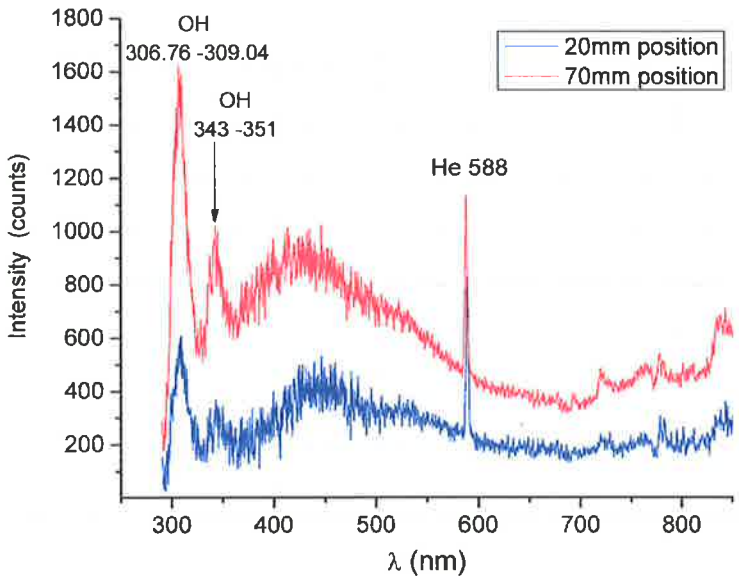

Figure 6.23 Mean emission spectra recorded during ignition at axial positions of 20mm and 70mm downstream of the injection plane.

Spectra obtained consist of OH bands at λ = 306-309nm and λ = 343-351nm with strong broadened Schumann-Runge bands of O_2 at 337nm < λ < 450nm and vibrational-rotational bands

of H_2O at 500nm < λ < 1000nm. The peaks of emission bands are well defined and correspond well to those assigned by Gaydon (1974). A peak at λ = 588nm depicts a strong Helium (He) signal. A post ignition He purge of the igniter is responsible for this signal which is evident only during the ignition transient.

The downstream position (70mm) exhibits a significantly greater emission intensity typically 2-3 times greater than that of the near injector position (20mm). The near injector field typically experiences a lower emission intensity due to a poorly mixed, flow field in comparison to the downstream position.

In general, greater emission intensity has been observed during the combustor start-up transient. This may be due to less water vapour in the near injector field which inhibits flame visualisation and spectral measurements. This observation corresponds with those made through visualisation and flame imaging techniques.

6.6 Discussion

6.6.1. LPRE Start-up Transients

The start-up and ignition phase of a liquid propellant rocket engine is an inherently unstable process regardless of injection conditions. Unfavourable conditions can cause pressure peaks upon ignition (hard-starts) and large scale pressure oscillations which can result in hardware damage and/or performance losses.

Propellants can be injected in a liquid or gaseous state. Low pressure differentials across the fuel and oxidiser side of the injector elements may result in LF (chugging) instability which in some cases, may trigger higher (HF) instability modes. The transient nature of LPRE start sequences will almost always result in unfavourable operating conditions at some point. The role of the engine designer is to minimise a) the duration (period) of the unfavourable operation and b) the effects of the unfavourable operating conditions. This is not a trivial exercise and often requires exhaustive testing late in the LPRE development/qualification phase.

Implementation of high speed optical diagnostic systems with a windowed LPRE thrust chamber enable close examination of the flame and flow field to reveal correlations between operating conditions and flame and flow-field behaviour.

Large volumes of image data (16384 images per test) and high acquisition frequencies (typically 9000Hz) make it possible to successfully apply the various image processing techniques outlined in Chapter 4 with a high degree of confidence. Detailed, time resolved analysis of the near injector field assists in characterisation of the start-up and ignition processes in LPRE's. Detailed experimental studies at representative conditions provide insight to the highly non-stationary processes taking place during thrust chamber start-up. During each transient phase, gaseous hydrogen is consistently introduced at the chamber boundaries to provide film cooling for the

quartz glass windows. The run valve opening times and flow rates are consistent throughout chamber start-up tests as is igniter operation and propellant flow rates.

6.6.2. Thrust Chamber Start-up, Ignition and Flame Stability

Three separate combustor start-up cases have been examined, each with different injection conditions. Each test case investigated undergoes a stable ignition without hard starts or detrimental combustion instability. Examination of the near injector field reveals very different behaviour in terms of flame and flow field in each test case.

In all start-up test cases, two distinct, coherent fluctuations are consistently observed during combustor start-up and witnessed through the various image processing and data reduction techniques employed. Firstly, a coherent frequency at $f \sim 380$Hz is typically seen in the early phase of the start-up process. This frequency corresponds to the torch igniter and it clearly affects the main propellant flame and flow until the point of ignition. A second frequency represents a LF injector coupled unstable mode which varies from $f \sim 50$Hz to 100Hz. This LF phenomenon is typically witnessed around the point of ignition and is completely damped as reduced pressure approaches unity. Often, the LF fluctuation is only witnessed momentarily. Injection conditions (and ΔP across the injector) either promote or attenuate the magnitude and duration of the coupling mechanism.

During ignition test case 1, fuel and oxidiser are both injected in gaseous form and with a relative propellant velocity ratio of R_v=26. The chamber pressure steadily increases with propellant flow rate. A LF phenomena is clearly visible in the thrust chamber and oxidiser manifold pressure trace and increases in amplitude until approximately $t = 1.17$ seconds. Examination of the flame emission images illustrate a flame which appears unstable until approximately $t = 1.17$ seconds whereby an instantaneous increase in emission intensity is clearly observed indicating the point of ignition.

At this point, (ignition) the flame front position retracts strongly toward the face plate and the flame appears to form a fist-like shape in which emission intensity increases significantly resulting in a downstream translation of the centroid of emission intensity. The LF oscillations remain present in the pressure data but decay in amplitude by approximately t = 1.3 seconds. The flame emission intensity also exhibits coherent LF fluctuations which decrease in frequency from f~ 150Hz to 54Hz between t~ 1.17 and t~ 1.42 seconds. The flame and flow field fluctuate strongly in the axial direction at a frequency corresponding to that observed in the chamber and manifold pressure data. By approximately t = 1.42 seconds, the fluctuations have decayed significantly and no periodic behaviour is observed.

Interesting to note is the static chamber pressure reaches the critical pressure of oxygen near to t = 1.43 seconds. Assessment of normalised peak-to-peak pressure data and centroid position indicate that approaching the critical pressure of oxygen tends to have a stabilising effect on the near injector flame.

The dynamic chamber pressure does not indicate any hard-starts or excessive pressure amplitudes through the start-up process for ignition test case 1. Despite LF fluctuations the entire process is considered stable.

Ignition test case 2 exhibits similar behaviour to ignition case 1 in that an instantaneous increase in emission intensity occurs at t = 1.17 seconds defining the point of ignition. Unlike test case 1, the emission intensity increase is not as dramatic for test case 2 but nonetheless takes place. The propellants are injected in a gaseous state as in test case 1 but the propellant velocity ratio is somewhat higher at R_v = 38.7. Upon ignition, the flame front is observed to oscillate at a frequency which coincides strongly with the 1L mode of the combustion chamber (at t ~ 1.175 seconds). The downstream movement of the flame front coincides with an increase in mean

flame emission intensity creating a 'pulsating' type effect. The unsteadiness does not result in increased dynamic pressure amplitudes however. Despite a low pressure differential across the injector upon ignition ($\Delta P \sim 0.1 P_{ch}$), the dynamic pressure amplitudes are relatively low and a detailed flow and flame response analysis exhibits a low sensitivity to LF oscillations when compared to ignition test case 1. This may be attributed to the increased propellant velocity ratio.

Ignition test case 3 is significantly different in that the oxidiser is injected in a liquid state resulting in very high relative propellant velocities throughout start-up ($R_v \sim 145$). From the three examples, test case 3 has the lowest pressure differential across the oxidiser side of the injector during start-up ($\Delta P \sim 0.085 P_{ch}$). Despite this, the process is relatively stable with very little LF unsteadiness in the dynamic pressure trace or flame emission data. Again, this enhanced steadiness may be attributed to the very high R_v. The high R_v may also be responsible for localised extinction of the flame during the start-up process however this is somewhat speculative.

Low injector pressure differential results in increased risk of injector coupled instability. Despite this, ignition case 1 is injected with the largest pressure differential across the injector, but dynamic pressure and flame stability data exhibit a greater susceptibility to LF oscillations. Further investigation of injector-coupled (LF) instabilities has been undertaken as a result of the observations presented here. For further detail, refer Chapter 8.

Results from the tests undertaken indicate increased relative propellant velocities appear to have a more positive influence on general combustion steadiness during thrust chamber start-up. In all start-up tests, the effect of the torch igniter is evident in the near injector field. The emission intensity fluctuates strongly with the operating frequency of the torch igniter (f = 380 - 400Hz).

6.6.3. Flame Emission Spectra

Emission spectra were measured for an O_2/H_2 flame during the thrust chamber start-up transient

at two axial positions, 20mm and 70mm downstream of the injection plane. Results indicate the flame emission intensity is approximately 2-3 times greater at the 70mm position when compared to 20mm downstream. This would indicate enhanced mixing and reaction at the downstream position. The emission spectra observations correspond with OH emission images captured during the start-up transients.

6.6.4. Critical Pressure

Operating near to the critical pressure of oxygen appears to have a stabilising effect on the flame in the near injector field. Flame oscillations and fluctuations tend to decay as the critical pressure is approached. This observation has been consistently observed through analysis of peak-to-peak steadiness of emission intensity centroid and dynamic chamber pressure data. This observation is more prevalent during steady state operation (Chapter 7) and ramping tests (Chapter 8) but is nonetheless also observed during thrust chamber start-up.

Chapter 7

Steady State Combustion

7.1 Test Matrix and Operating Conditions

A broad test matrix has been established for steady state operation in terms of non-dimensional numbers and injection conditions. Unlike combustion at low pressure, the influence of various dimensionless parameters such as relative propellant injection velocities R_v and momentum flux ratio J (equations (2.2) and (2.3)) are not clearly known at elevated pressures. Hydrogen injection temperature effects have also been a point of interest in the past (Wanhainen and Parish et al. (1966) and Smith and Klimenko et al. (2002)) and are also investigated here to an extent. Hydrogen injection temperature is adjusted significantly during steady-state operation and range from T_{H2} ~ 130K to 150K and T_{H2} ~ 240K to 270K. Liquid oxidiser injection temperature is maintained relatively constant between T_{O2} ~ 110K and 130K.

A test matrix representing steady state operating conditions is provided in terms of propellant momentum flux ratio and propellant injection velocity ratio in Figure 7.3 and Figure 7.4 respectively. These dimensionless parameters have been commonly employed for characterisation of coaxial sprays and jets in the past and are therefore both presented here (for example, Wanhainen and Parish et al. (1966) and Woodward, and Pal et al. (2006)). Throughout a test period, the thrust chamber pressure (and reduced pressure P_r) is adjusted through regulation of the propellant mass flow rates at a constant oxidiser-to-fuel ratio (R_{OF}). Each pressure level experienced throughout a test sequence is designated a "phase" to avoid any ambiguities.

The start-up transient combined with three operating phases defines a test sequence whereby combustion chamber pressure is adjusted in steps as illustrated in Figure 7.1. Target operating pressures are: above the critical pressure of the oxidiser (phase 1), very near to the critical pressure (phase 2) and below the critical pressure (phase 3). Chamber pressures of 52 - 60bar ($P_r > 1$), 49-51 ($P_r \sim 1$) bar and 39-41bar ($P_r < 1$) correspond to phases 1, 2 and 3 respectively. Each phase is followed by a transient period as illustrated by the combustion chamber pressure trace shown in Figure 7.1.

The ignition transient period varies slightly between each test condition investigated and is detailed in Chapter 6. Figure 7.1 suggests a transient period of approximately 6 seconds however only the first 2 seconds are generally considered as the ignition or "start-up" phase. Following start-up, the first steady state period is designated "phase 1." Conditions are deemed as steady when there is no observable variation of propellant injection temperatures, combustion chamber pressure or propellant mass flow rates (see Figure 7.1 and Figure 7.2). The second and third steady-state phases are designated accordingly and represent steady conditions at different operating pressure levels both near and below the critical pressure of O_2.

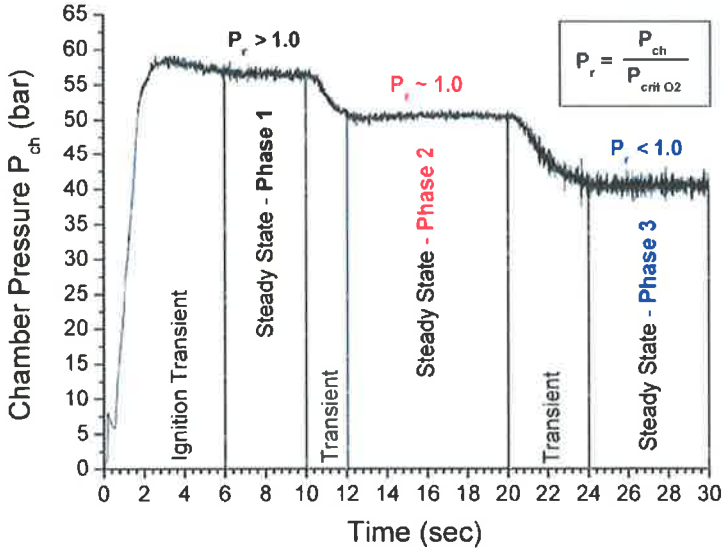

Figure 7.1 Combustion chamber pressure trace illustrating three operating phases in terms of operating pressure and reduced pressure. Data from test VIS04WA Run 12.

The test matrix demonstrated graphically in Figure 7.3 and Figure 7.4 spans two and four orders of magnitude of R_v and J respectively. All conditions presented are determined based on thermophysical properties derived using the MBWR equation of state outlined in Schmidt and Wagner (1985)).

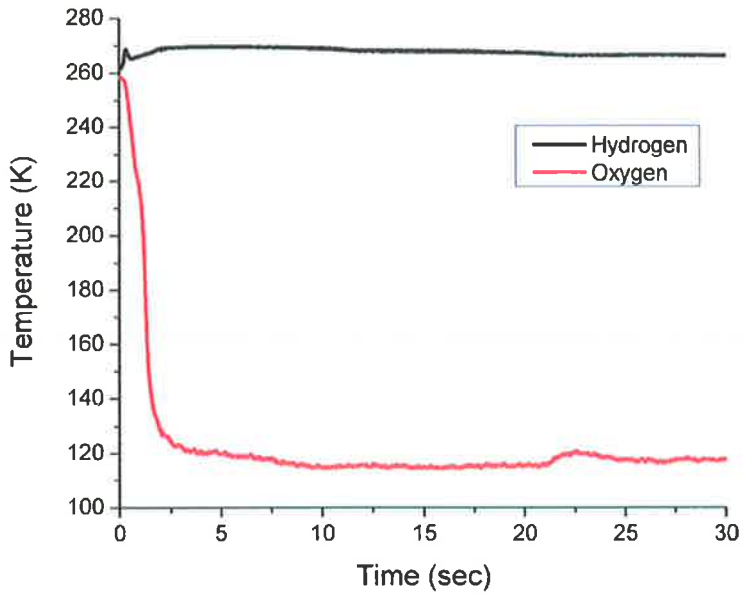

Figure 7.2 Propellant injection temperature traces highlighting constant temperature conditions throughout an entire test. Data from test VIS04WA Run 12.

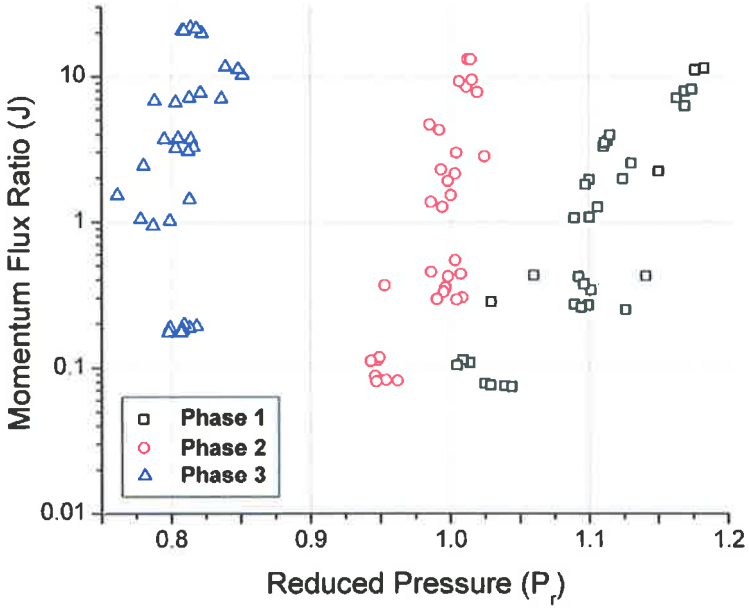

Figure 7.3 Steady state test matrix in terms of propellant momentum flux ratio J and reduced pressure P_r.

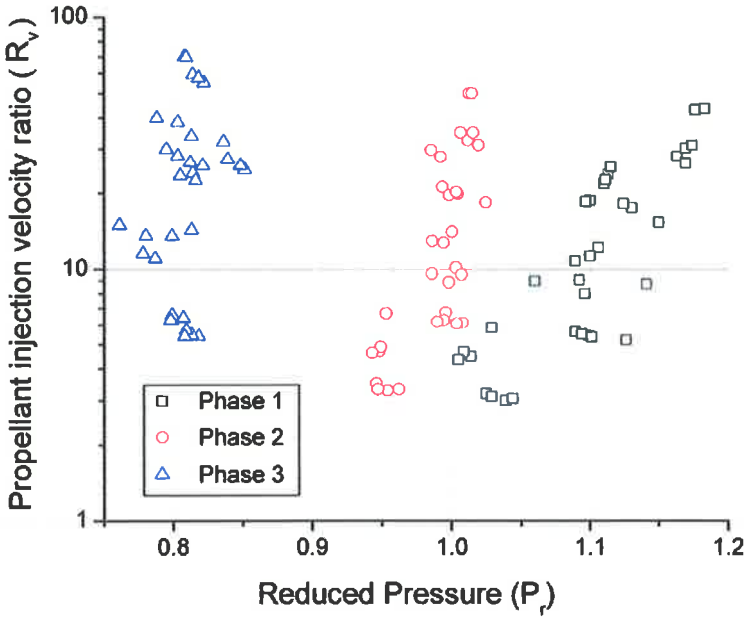

Figure 7.4 Steady state test matrix in terms of propellant velocity ratio R_v and reduced pressure P_r.

7.2 Steady State Operation

7.2.1. Combustion Response

As previously mentioned, steady state is defined here as the operating period where all conditions are maintained constant. Typically, steady state is achieved for approximately 5 seconds for each of the three phases during a test. The level of pressure amplitudes experienced in the combustion chamber classifies the combustion regime through assessment of dynamic pressure peak-to-peak ($P_{p\text{-}p}$) values relative to the mean combustion chamber operating pressure $\bar{P}_{ch}$. Comparison of $P_{p\text{-}p}$ values relative to $\bar{P}_{ch}$ is a standardised approach for classifying stable, "rough" or unstable combustion and is discussed by Harrje and Reardon (1972).

The dynamic chamber pressure data often exhibits a distinct change in combustion behaviour between phases. As phase 2 is reached and the chamber pressure approaches the critical point of oxygen, the peak-to-peak pressure ($P_{p\text{-}p}$) values have been observed to decrease significantly relative to the mean combustion chamber pressure ($\bar{P}_{ch}$). The combustion process remains inherently stable until phase 3 where peak-to-peak values increase once more (relative to $\bar{P}_{ch}$).

The peak-to-peak pressure amplitude values are given by;

$$P^{2}_{p\text{-}p} = \frac{1}{N-1}\sum_{i=1}^{N}(P_i - \bar{P}_{ch})^2 \qquad (6.1)$$

where $\bar{P}_{ch}$ is the mean static combustion chamber pressure calculated on a running average basis from three pressure measurement values ($\Delta t = 3 \times 10^{-5}$ sec) recorded immediately prior to P_i as illustrated by equation (6.2). This approach has proven to work effectively.

$$\bar{P}_{ch} = \frac{1}{3}\sum_{i=j\angle 2}^{j} P_j \qquad (6.2)$$

Peak to peak amplitudes of static chamber pressure data are calculated and manipulated to provide a graphical representation of the probability of such peak-to-peak values for each operating phase. This process has been repeated for a number of steady state operating conditions and indicates a common trend. In all test cases, the peak to peak pressure values relative to mean combustion chamber pressure are significantly higher at conditions below the critical point of oxygen. Figure 7.5 illustrates a typical example of this observation. All data is fitted with curves which represent a Gaussian fit.

Phase 3 exhibits a broad range of $P_{p\text{-}p}$ values whereas phases 1 and 2 show a rather steep curve with a majority of the peak-to-peak pressure amplitudes being very low. Interesting to note is the fact that the conditions experienced during operating Phase 3 are more favourable for stable combustion in terms of the classical non-dimensional R_v and J values. Despite this, the consistent observation indicates there exists a significant level of relative unsteadiness at operating pressures below the critical point of oxygen.

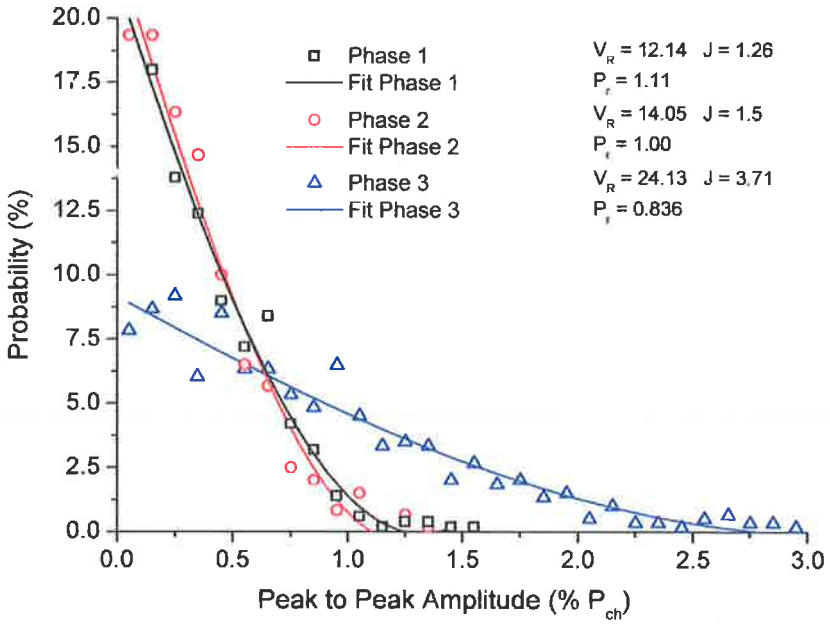

Figure 7.5 Typical plot of peak-to-peak chamber pressure amplitudes recorded during steady state operation indicating a significant difference in behaviour at conditions below the critical pressure of oxygen. Data from test VIS03WA Run 6.

7.2.2. Propellant Injection Velocity Ratio vs. Momentum Flux Ratio

Characterisation of coaxial sprays under non-reacting and reacting conditions has received mixed treatment with different research groups employing various non-dimensional values such as Weber no. (*We*), injection velocity ratio (R_v), density ratio (R_ρ) and injector exit area ratio (R_A).

$$R_A = \frac{A_{H2}}{A_{O2}} \tag{6.3}$$

Here the focus is primarily on the classical R_v and J for the following reasons. The range of R_ρ experienced in this test campaign is relatively small with almost constant O_2 temperature. Furthermore, *We* is only valid for a system where an interfacial surface tension exists which is not the case for $P_r > 1$ and area ratio R_A does not account for the dramatic change in hydrogen injection temperature. Momentum flux ratio is a popular choice and is shown by Figure 7.6 to scale almost linearly with R_v over the broad range of conditions examined in this study - particularly where $R_v > 20$ (refer Figure 7.6). .

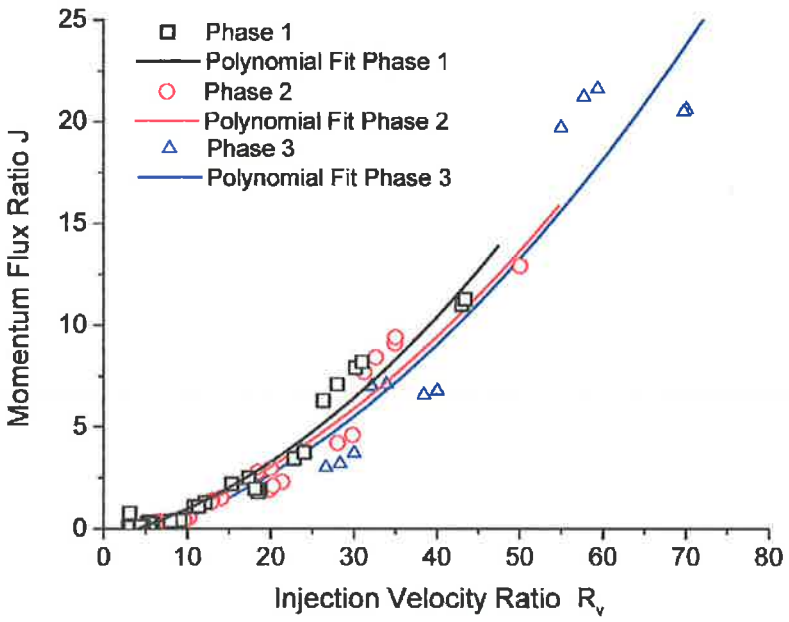

Figure 7.6 Injection velocity ratio R_v as a function of momentum flux ratio J for all steady state conditions examined.

Therefore, R_v and J are commonly referred to here for characterisation purposes combined with reduced pressure P_r. When one of the dimensionless terms is mentioned, Figure 7.6 can be utilised to cross-reference the other value.

7.2.3. Combustion Efficiency

Another noteworthy difference between phases is clearly seen in the combustion efficiency defined by equation (6.4). With decreasing R_v and J, combustion efficiency η is dramatically affected during phases 1 and 2.

Phase 1 indicates injection conditions significantly influence η with $R_v < 20$ and $J < 4$. A similar trend is observed during phase 2 at conditions where $R_v < 10$ and $J < 2$. The influence of injection conditions appears less evident during phase 3. With $P_r < 1$, the effect of R_v and J on η appears almost negligible. Figure 7.7 and Figure 7.8 clearly illustrate this observation.

Combustion efficiency η is defined as:

$$\eta = \frac{c^*_{actual}}{c^*_{theor}} \tag{6.4}$$

where

$$c^*_{actual} = \frac{(P_{ch})_{actual} A}{\dot{m}_{total}} \tag{6.5}$$

and c^*_{theor} is a theoretical based approximation of the characteristic velocity c^* with further details found in Gordon and McBride (1994).

The theoretical combustion efficiency calculation employed does not account for heat losses to the cooling fluid, kinetic energy of the exhaust gas, boundary layer corrections etc. The intent here however is not to provide a precise theoretical efficiency estimation, but rather, to employ a idealised formulation in order to make a relative assessment of all conditions examined in an attempt to reveal common trends. For this purpose, the analysis approach is very effective.

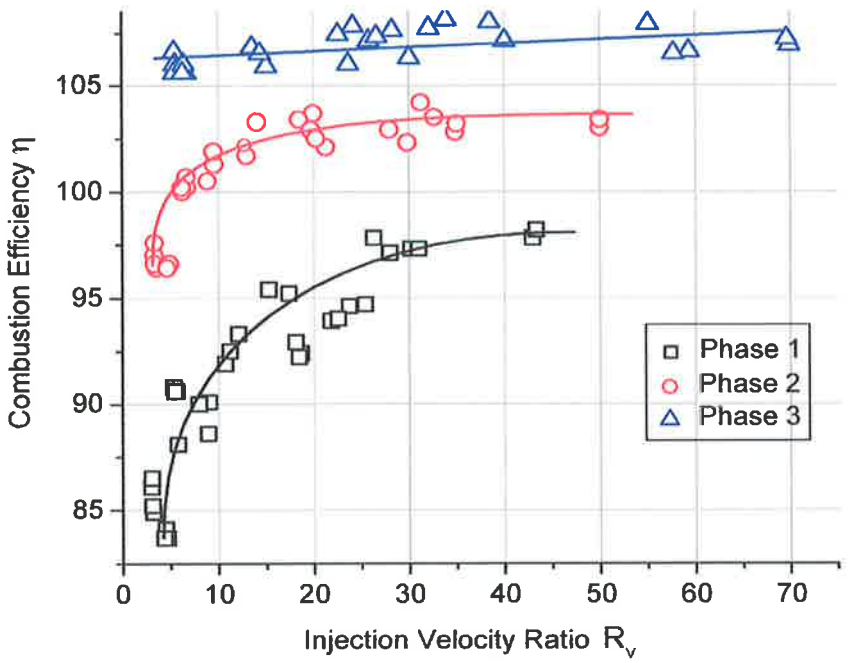

Figure 7.7 Combustion efficiency as a function of velocity ratio for each operating phase. Data from all steady state test conditions.

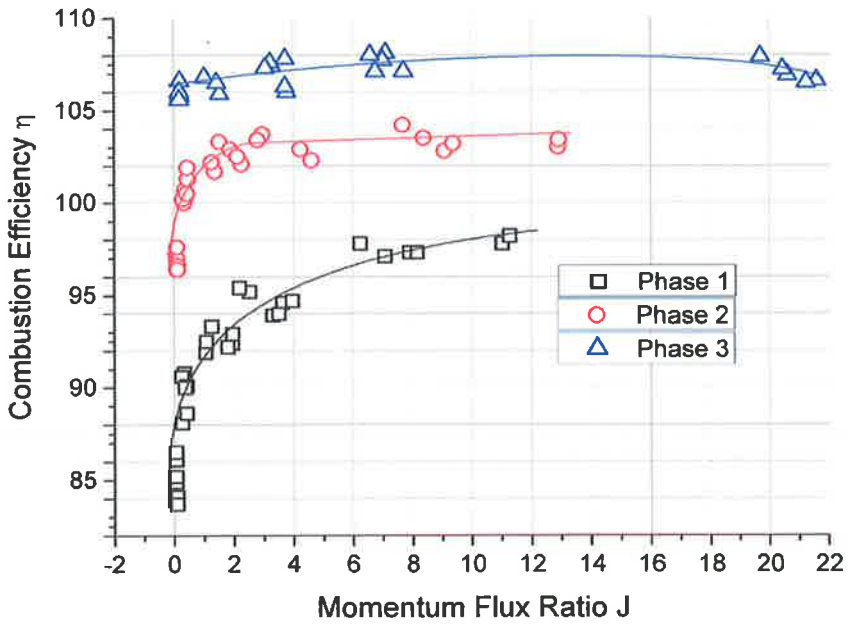

Figure 7.8 Combustion efficiency as a function of momentum flux ratio for each operating phase. Data from all steady state test conditions.

The reduction in combustion efficiency with decreasing injection velocity ratio has been reflected in the observation of the combustion zone and more specifically the intensity of the near injector field of the OH emission images recorded. The low relative flow between propellants results in diminished stripping and atomisation of the liquid oxygen core. This further results in reduced reaction and a reduction in emission in the near injector field. Under such conditions, propellants may exit the exhaust nozzle un-reacted.

7.2.4. Flow-field Observations

Observing flow field behaviour with shadowgraph techniques is highly qualitative. Calculating jet core break-up lengths and measuring various phenomena is practically impossible over a range of operating conditions. Slight changes in injection temperatures or propellant mass flow rates significantly alters the optically accessible field of view due to changes in density and refractive index gradients. These effects are especially obvious at elevated pressure conditions. The shadowgraph setup utilised here has proven to be extremely sensitive to injection conditions. It must therefore be stressed that no quantitative data is presented based on the shadowgraph imaging technique. The diagnostic technique has proven valuable however in providing a qualitative insight to the flow field behaviour under various operating regimes which is discussed herein.

During steady state operation, H_2 injection temperature has a major influence on shadowgraph image quality. As previously reported by Smith and Klimenko et al. (2002), injection of H_2 at temperatures below 80K results in heavy restrictions in optical accessibility due to an increase in density gradients. The warmer hydrogen test conditions however, (T_{H2} ~220K to 250K) have provided improved quality images such as those shown in Figure 7.9. Single shot and time averaged flow field images are presented from all three test phases captured during steady, stable operating conditions from test VIS04WA run 12.

Comparing steady state images for phases 1, 2 and 3, reveals a significant difference in the appearance of the liquid oxygen core. The major influence on the LOx jet shape and stability in the near injector field appears to be P_r rather than injection conditions (R_v and J). Above and near the critical point of oxygen (phase 1 and 2) the oxygen core flow appears very steady with surface perturbations reducing as P_r approaches 1. Below the critical point of oxygen, the LOx jet experiences increased expansion, oscillation and general unsteadiness. The initially undisturbed flow appears to become unsteady at approximately 15-20 LOx jet diameters downstream as seen in Figure 7.9. This observation is common and has been observed under multiple test conditions. The nature of the unsteadiness and the influence of reduced pressure P_r is in agreement with the peak to peak dynamic pressure oscillations discussed in the previous section.

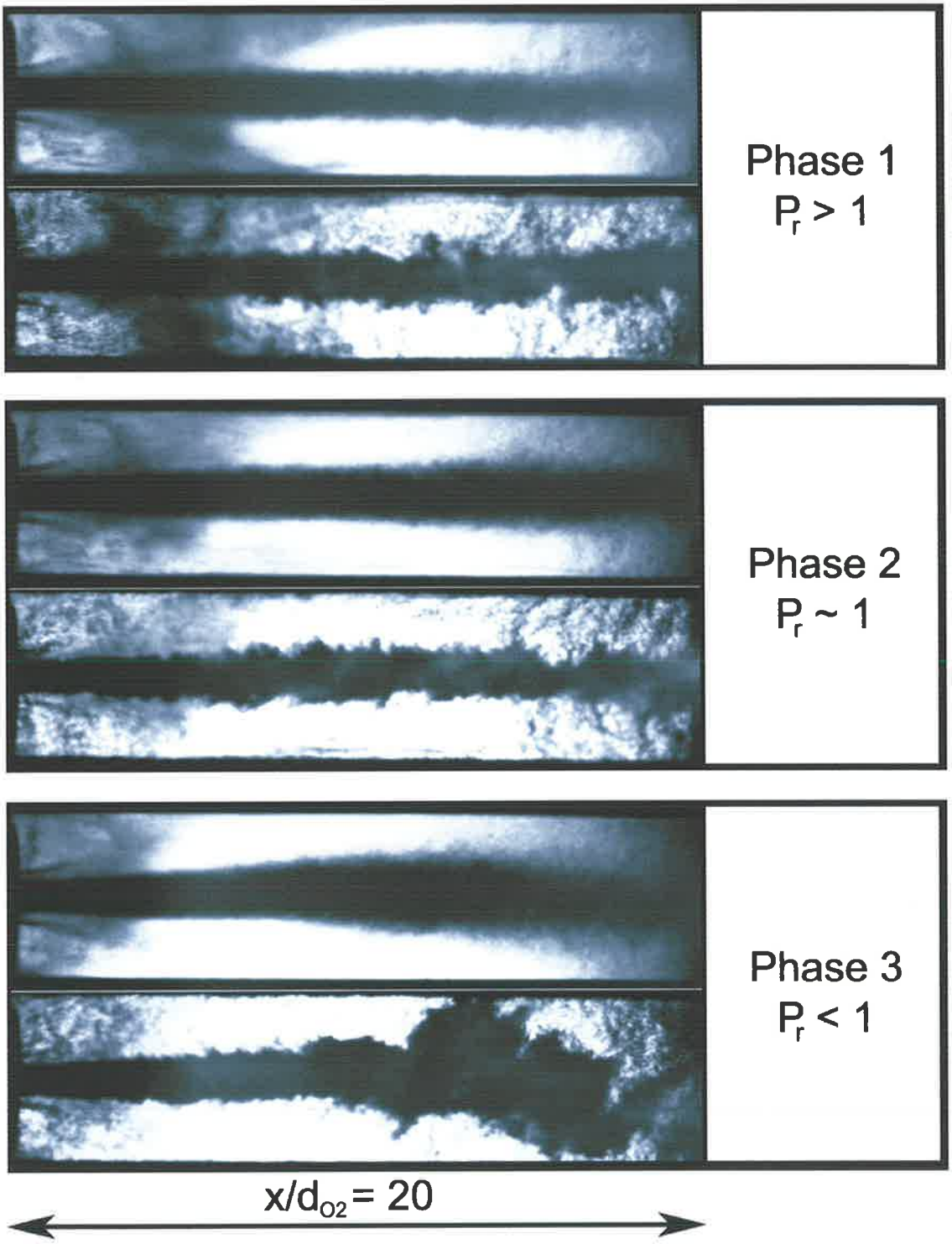

Figure 7.9 Single shot and time averaged shadowgraph images recorded during each test phase (and reduced pressure) of steady state operation. Image data from test VIS04W Run12.

7.3 Steady State Combustion Zone

7.3.1. Flame Emission Spectral Measurements

Spectral measurements during steady-state operation illustrate flame emission intensity over the entire emission spectrum from λ=300-1100nm (see Figure 7.11 and Figure 7.12). Two axial positions were probed at the chamber centre-line, at 20mm and 70mm downstream from the injection plane. Spectral measurements were taken at thrust chamber operating conditions whereby combustion efficiency was low and low levels of near injector emission intensity was observed. Note corresponding reduced pressure values listed in Table 7.1.

Table 7.1 Operating conditions during spectral measurements

Test Condition	Measurement Position (mm)	Chamber Pressure (bar)	Velocity Ratio R_V	Average T_{H2} (K)	Average T_{LOx} (K)	Spectral Range (nm)
1	20	51.7	3.21	152	110	300-800
2	20	47.7	3.52	153	110	300-800
3	20	40.8	5.73	154	112	300-800
4	20	50.9	4.67	226	115	600-1100
5	20	47.9	4.92	226	115	600-1100
6	20	40.7	6.42	227	117	600-1100
7	70	51.9	3.12	152	110	300-800
8	70	47.8	3.34	153	110	300-800
9	70	40.7	5.42	154	112	300-800
10	70	50.7	4.35	226	115	600-1100
11	70	47.7	4.66	226	115	600-1100
12	70	40.3	6.31	227	117	600-1100

Nearest to the injector at the 20mm downstream position (Figure 7.11), the greatest emission intensity was observed at the lower pressure condition (phase 3) with the lowest intensity recorded at the highest combustion chamber pressure level (phase 1). This observation is counter-intuitive and is the result of recirculated combustion products shrouding the near field which is most prevalent at elevated pressure with low H_2 injection temperature.

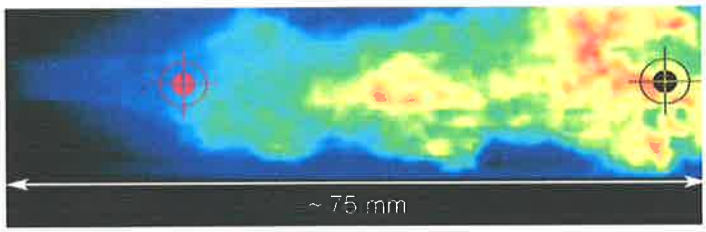

Figure 7.10 Flame OH emission image indicating the x/d = 5 (20mm) and x/d = 17.5 (70mm) positions probed with the spectrometer.

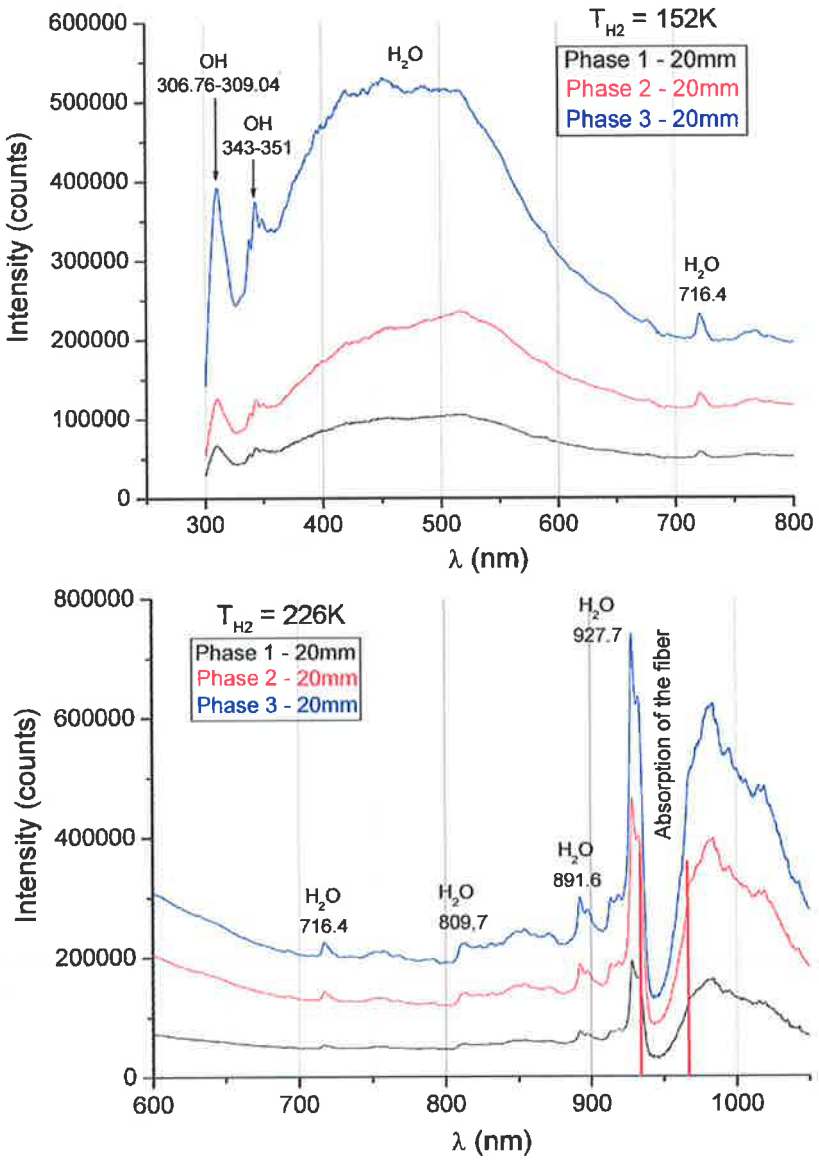

Figure 7.11 LOx/H_2 flame emission spectra from λ = 300-1100nm measured at an axial position of 20mm (x/d = 5) downstream from the injection plane for 3 steady state operating phases.

At the 70mm downstream location, the highest pressure level (phase 1) radiates with the highest levels of emission across the entire spectrum as shown in Figure 7.12. At the lower pressure case (phase 3) the LOx/H_2 flame emits the lowest intensity levels across the entire spectrum from UV through to IR.

At the 70mm position, a significant increase in H_2O emission is also observed at the highest pressure level (phase 1) as seen between $\lambda \sim$ 400-550nm in Figure 7.12.

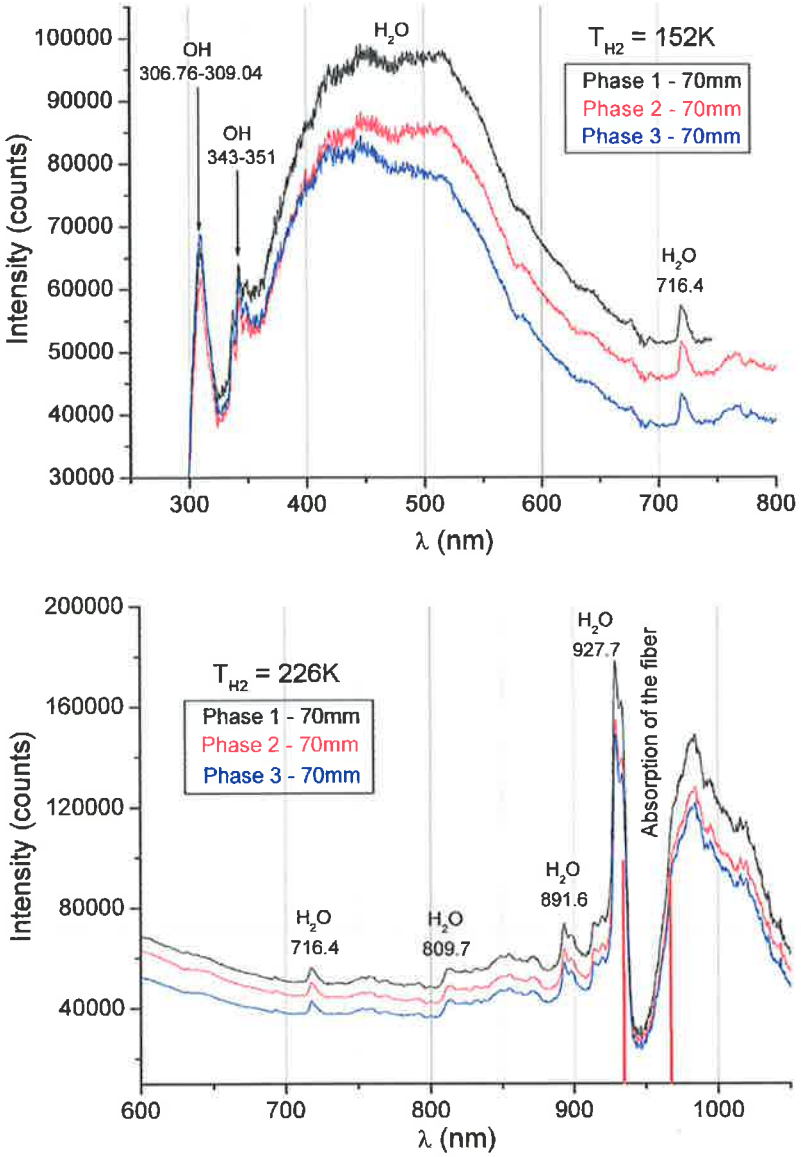

Figure 7.12 LOx/H_2 flame emission spectra from λ = 300-1100nm measured at an axial position of 70mm downstream from the injection plane for 3 steady state operating phases.

Typically, one would expect a greater level of emission intensity at elevated pressure regardless of hydrogen injection temperature. This is indeed the case at the 70mm downstream position (i.e. $x/d = 17.5$) as expected. At this position, the propellants are relatively well mixed compared to the 20mm ($x/d = 5$) case. Another cause of reduced emission intensity in the near injector region could be the accumulation of combustion products and condensed water shrouding the near injector field. Further literature on H_2/O_2 spectral measurements can be found in Burrows and Povinelli (1964).

7.3.2. Combustion Zone Visualisation

Throughout thrust chamber operation, the near injector combustion zone is observed at high sample rates to reveal dominant trends under various operating regimes with a high degree of statistical confidence. During steady state operation, the flame appears to be constantly attached to the injector LOx post under all conditions examined. At supercritical pressure conditions ($P_r > 1$), condensed water continuously inhibits visualisation of the near injector region. The lower H_2 injection temperatures investigated have also proven detrimental to the quality of optical accessibility with an apparent increase in water production and condensation in the flow field and combustion zone.

7.3.3. Time Averaged and De-convoluted OH Emission Images

Time averaging and deconvolution of the OH emission images recorded during steady state provides an indication of the near injector flame structure and mean combustion zone. An example is given in Figure 7.13 whereby 3 operating phases are presented in both time averaged and deconvoluted format. The images provide a qualitative insight into flame structure at similar values of R_v and P_r.

In general, the lower pressure (phase 3) test cases appear to exhibit the greatest emission intensity very near to the injector (see Section 7.3.1). Typically, the flame appears to amass a greater

volume at lower pressure (phase 3) in the optically accessible near injector region which is clearly observed in Figure 7.13. The images presented are at similar injection velocity ratios and constant R_{OF}. At higher pressure conditions, the injection velocity ratio of propellants appears to have a greater influence on the near injector flame structure than at lower pressure. The flame is attached to the LOx post under all conditions however at near-critical and supercritical pressure conditions, the flame appears elongated or stretched when compared to the mean images constructed at lower pressure.

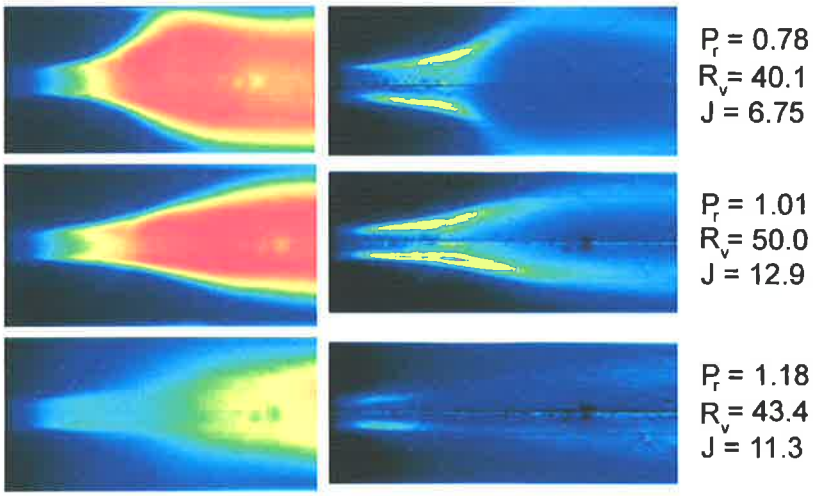

Figure 7.13 Time averaged and deconvoluted OH emission images from three steady state operating phases. Injection velocity ratio is relatively constant for the three test cases. Reduced pressure is increasing from top to bottom.

Gaseous hydrogen window cooling has an effect on flame shape but is maintained relatively constant for conditions presented in Figure 7.13. The change in flame shape may be a direct result of the atomisation and mixing at conditions whereby the reduced pressure is greater than, or equal to unity. At increased pressure conditions, it appears that the heavy mixing and combustion zone occurs further downstream. This observation is further supported by the combustion efficiency data presented in Figure 7.7. The mixing and atomisation mechanisms at elevated pressure conditions may result in unburned propellants leaving the thrust chamber at low R_v values.

Furthermore, the emission intensity is clearly much lower at supercritical pressure conditions due to an apparent increase in water condensation and scattering of emission. This observation is seen not only in flame emission images but also in within the visual range as illustrated by photographic images presented in Figure 7.14. The near critical pressure case exhibits a more uniform and symmetrical flame structure which corresponds with earlier discussion.

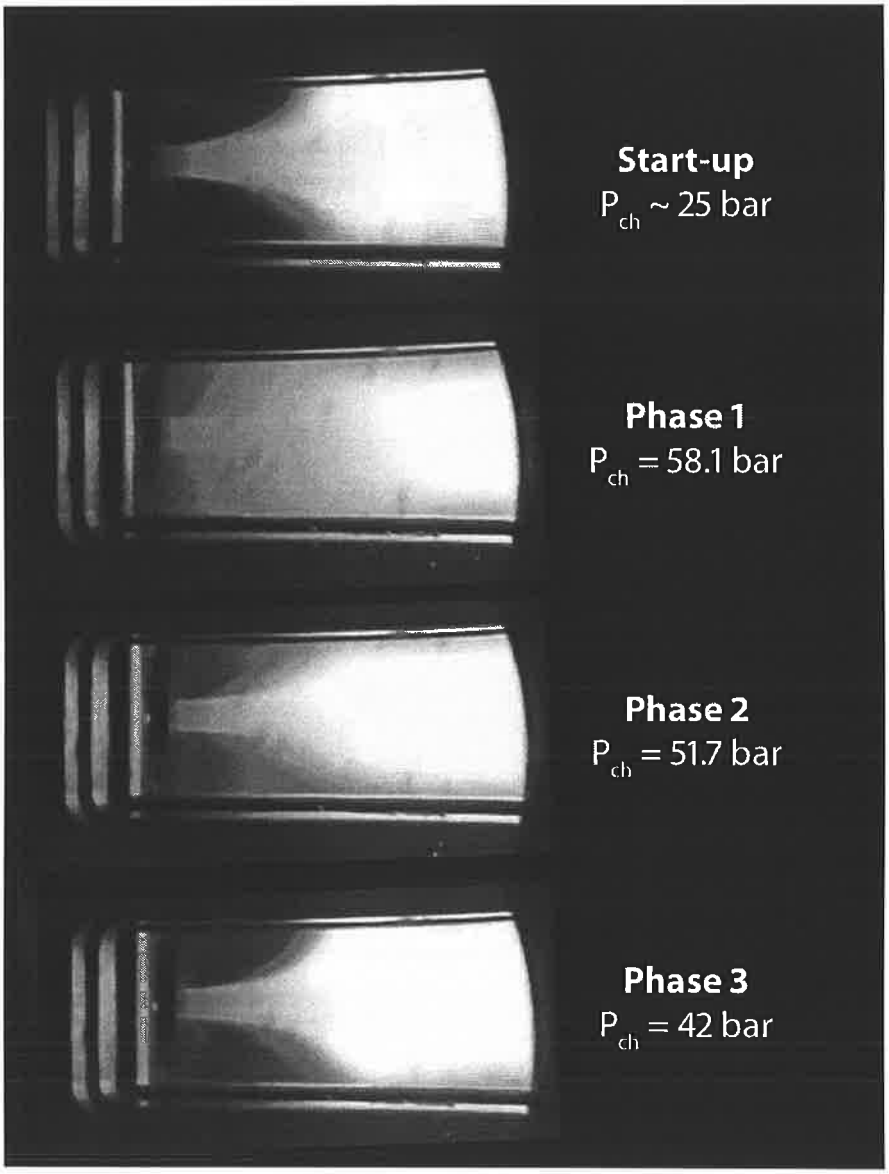

Figure 7.14 Photographic images of the near injector field captured during all phases of steady state operation and ignition

7.3.4. Mean OH Emission Intensity

A series of mean OH emission intensity values are determined for each operating point based on the plethora of images obtained at various steady state operating conditions. OH emission images captured in batch mode are time averaged to provide a mean intensity image as outlined in Section 4.2.1. The average emission intensity value of each time-averaged image is then calculated to provide a set of intensity values each representing a different point in time. Figure 7.15 represents the mean OH emission intensity values recorded throughout an entire test. Each intensity value plotted in Figure 7.15 represents the mean of 256 emission images from each image set recorded at 0.5 second intervals throughout an entire 30 seconds of chamber operation.

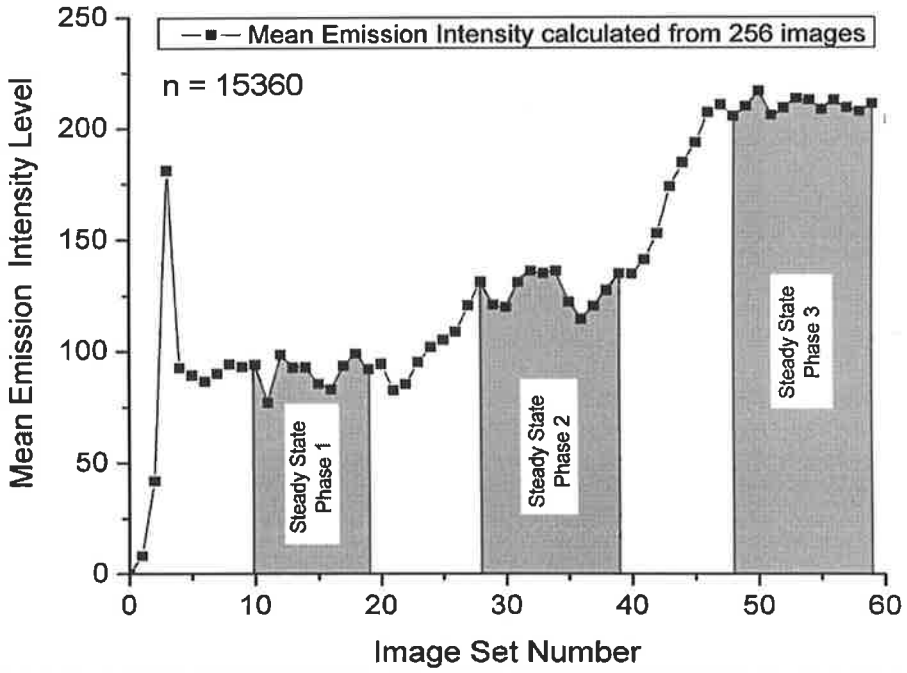

Figure 7.15 Mean OH emission intensity calculated throughout an entire test highlighting regions of steady state operation. Each point represents a mean emission intensity value derived from 256 individual images. Data from test VIS03WA run 15. Total number of samples n = 15360.

The OH emission intensity is normalised based on the maximum value recorded during each test. Normalising the image series from each test is necessary due to the effects of various camera positions, image sizes and propellant injection temperatures between tests. Figure 7.16 repre-

sents the normalised OH emission intensity I_{OH} as a function of injection velocity ratio R_v for a series of tests with a hydrogen injection temperature from $T_{H2} \sim$ 222K - 251K at steady state operating conditions.

Start-up and ignition periods are ignored due to the transient behaviour and varying flame size and lengths typically observed in start-up transients. An alternative approach is utilised for the ignition process as described in Section 4.4.6.

Each point in Figure 7.16 represents relative emission intensity values calculated once again from time-averaged images constructed from 256 separate images recorded during stationary conditions. A decrease in relative OH emission intensity with increasing pressure is consistently obvious with the maximum normalised emission intensity always occurring at the lowest pressure condition (i.e. phase 3). It is also apparent that the flame OH emission intensity is strongly influenced by the injection velocity ratio at reduced pressures greater than or equal to unity. The influence of R_v on I_{OH} is significant at $R_v < \sim 9$ for phases 1 and 2 ($P_r > 1$ and $P_r \sim 1$). This observation exhibits a similar trend to the combustion efficiency results and leads us to the intuitive fact that the near injector flame emission intensity I_{OH} is related to the combustion efficiency η. Similar results are observed for lower H_2 injection temperatures (i.e. $T_{H2} \sim$ 146K - 164K) with data presented in Figure 7.18.

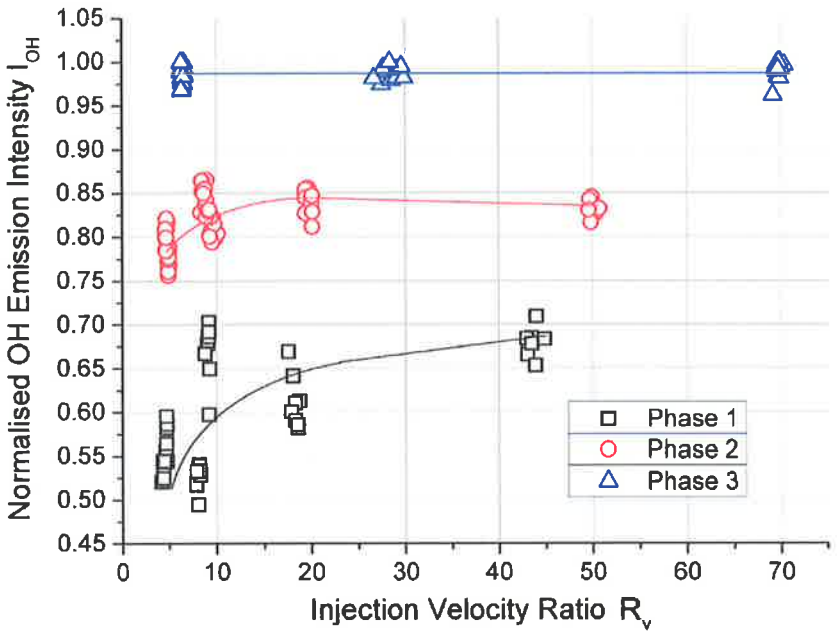

Figure 7.16 Normalised OH emission intensity vs. injection velocity ratio for 222< T_{H2} <251K. Each point represents a mean value from 256 samples.

7.3.5. Influence of H_2 Injection Temperature

As previously mentioned, the H_2 injection temperature appears to have a major influence on the near injector optical accessibility. Decreased injection temperature results in reduced optical clarity in the near injector field. Below approximately 80K, the entire field of view is completely inhibited by an apparent recirculation and accumulation of condensed water.

Combustion efficiency is plotted as a function of velocity ratio and hydrogen injection temperature in Figure 7.17. There appears to be no influence of hydrogen temperature on efficiency at subcritical or near critical pressure conditions (phase 3 and phase 2 respectively). During operating phase 1 however, an influence of H_2 injection temperature is more apparent.

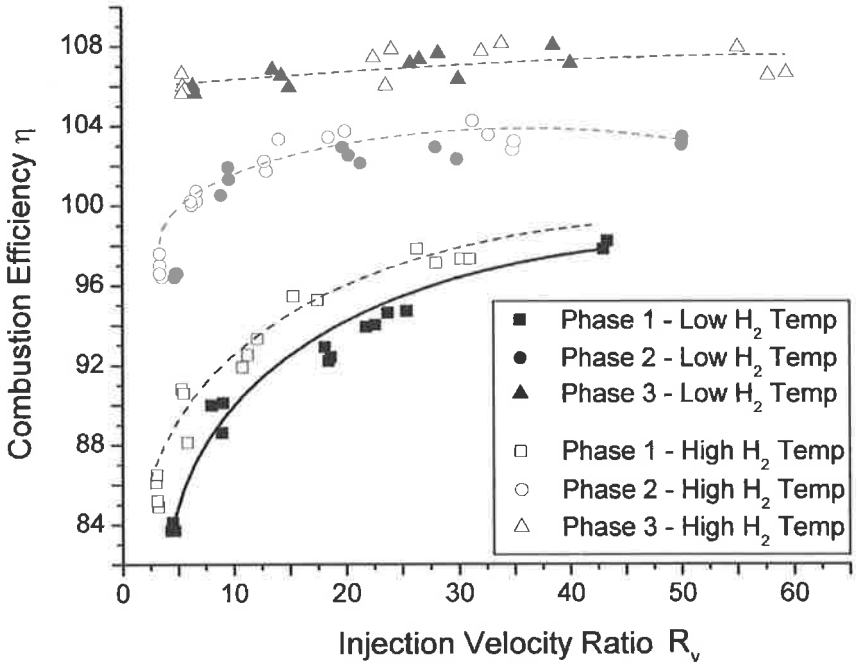

Figure 7.17 Influence of hydrogen injection temperature T_{H2} on combustion efficiency η. Low temperature hydrogen is injected from 146K < T_{H2} <164K whilst high temperature hydrogen is 222< T_{H2} <251K.

An increase in combustion efficiency of approximately 3% is evident due to warmer H_2 injection temperatures at $P_r > 1$. This observation of H_2 temperature influencing combustion at $P_r > 1$ is in accordance with previous observations reported by Smith and Klimenko et al. (2002).

Furthermore, this observation is in accordance with previous studies at subcritical pressure conditions where H_2 injection temperature was not observed to have a direct effect on thrust chamber operation or combustion stability (Wanhainen et al. (1966)).

Examination of the relative OH emission intensity in the near injector field with low H_2 temperature (T_{H2} ~ 146K -164K). illustrates a similar trend to the warmer test results (refer Figure 7.16). The emission intensity at near critical conditions decays rapidly below $R_v = 13$. During phase 1 ($P_r > 1$), the OH emission intensity scales almost linearly with R_v. The phase 1 and phase 2 results may be affected by the recirculation of combustion products in the near

injector field. Nonetheless, the trend is in accordance with the warmer H_2 test case and the combustion efficiency data which is independent of the imaging techniques. The low pressure test case exhibits an increased level of emission intensity relative to the other operating pressure conditions.

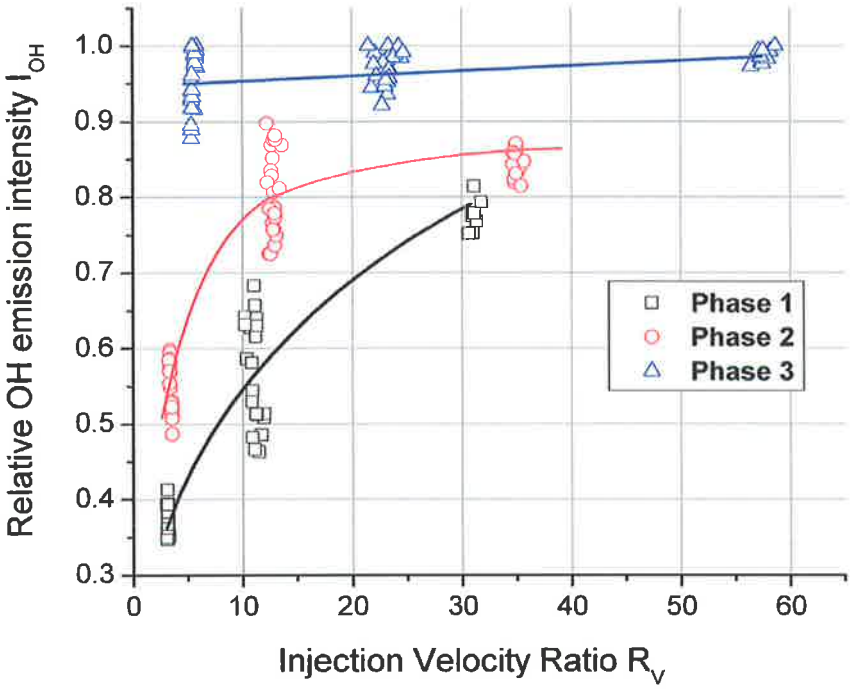

Figure 7.18 Normalised OH emission intensity as a function of injection velocity ratio for low H_2 temperature ($146K < T_{H2} < 164K$). Liquid oxygen temperature is constant ($110K < T_{O2} < 125K$). Each point represents a mean value from 256 samples.

The inhibition of the near injector field by recirculated combustion products was also evident in the emission spectra measurements. Despite this, it must be noted that the reduced pressure P_r was barely greater than unity for the spectral measurement tests due to the very low R_v.

7.3.6. Near Injector Flame Emission Intensity Tracking

The near injector OH emission intensity is assessed as a function of injection conditions by applying a mean emission intensity thresholding and tracking technique as described in Section 4.4.2. The technique identifies the axial (x_I) and radial (y_I) positions of mean emission intensity gradient based on prescribed threshold values. The pixel position is recorded and converted to

a distance in millimetres based on the image size. This techniques is applied to an array of time averaged images constructed from 256 single shot images.

Comparison of the mean emission intensity axial position (x_f) between operating phases is portrayed by Figure 7.19 which clearly illustrates the effect of injection velocity ratio on the mean axial flame threshold position (x_f). The mean flame threshold position tends to move further downstream with reduced relative propellant velocities. Once again, a distinct difference is observed between operating regimes. A linear relation is obvious between mean flame threshold position and propellant velocity ratio for $P_r < 1$. However, a very strong influence of R_v on x_f is visible for $R_v < 10$ at near critical pressure conditions ($P_r \sim 1$). Data from phase 1 ($P_r > 1$) is omitted due to the sensitivity of the technique to the condensation of water which apparently falsifies results. Selected low pressure test data (phase 3) is also not included due to the occurrence of rough combustion and combustion instability under specific operating conditions (see Chapter 8).

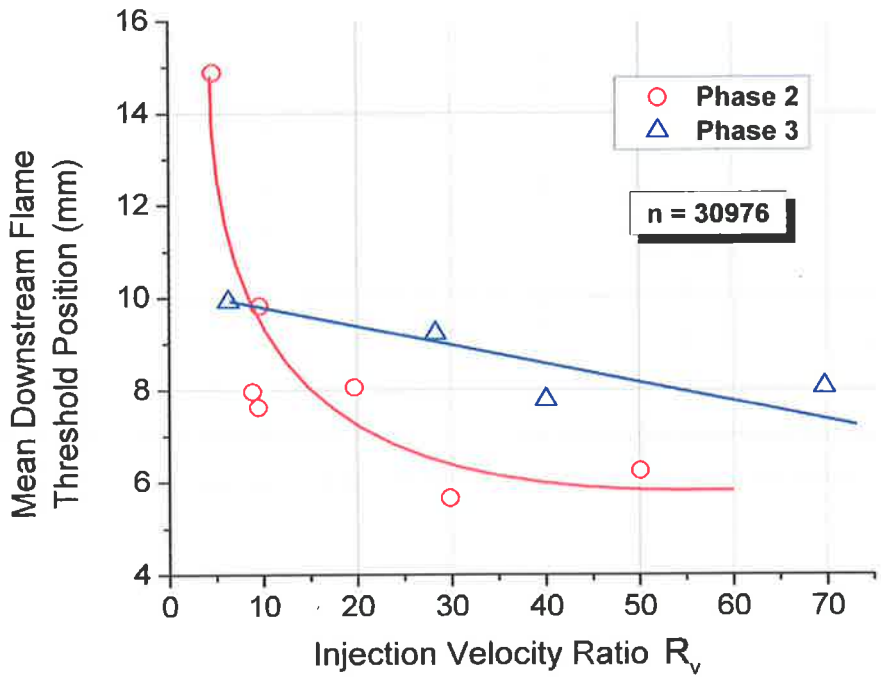

Figure 7.19 Mean axial flame threshold position x_f as a function of injection velocity ratio R_v. Data from tests with 222K < T_{H2} < 251K. Data from 30976 image samples.

The data presented in Figure 7.19 indicates the near injector emission intensity decreases with reduced injection velocity ratio. The influence of R_v is significantly greater during operating phase 2 ($P_r \sim 1$) for $R_v < \sim 9$. This result coincides strongly with those obtained from the mean OH emission intensity analysis and combustion efficiency analysis presented in Sections 7.3.4 and 7.2.3.

At higher R_v values, the mean flame threshold position is nearer to the injector during phase 2 ($P_r \sim 1$) than phase 1 ($P_r < 1$) indicating a more efficient primary mixing and reaction under the near critical pressure conditions.

7.3.7. Centroid of Flame Emission

The centroid of emission intensity is tracked as outlined in Section 4.4.3. The results presented here are obtained from steady state operation of the thrust chamber. Tests whereby LF injector coupled combustion instability occurred have been omitted. The centroid of emission intensity is sensitive to injection velocity ratio and has been observed to fluctuate between x/d = 9 - 15 and x/d = 14 - 23 the cold and warm H_2 test cases respectively. Typically, higher pressure operating conditions (phase 1) results in the centroid of emission to fluctuate furthest from the injection plane relative to the lower phase 1 and 2 operating pressure data (refer Figure 7.20). Furthermore, as R_v decreases at near critical and supercritical pressure conditions, the centroid of emission intensity moves further downstream relative to the subcritical pressure case ($P_r \sim 1$).

This trend is in accordance with all other comparisons made between operating phases. The lower relative velocities results in reduced near field mixing and reaction. The heavy mixing and reaction zone is driven further downstream resulting in diminished local flame emission and a reduction in overall combustion efficiency.

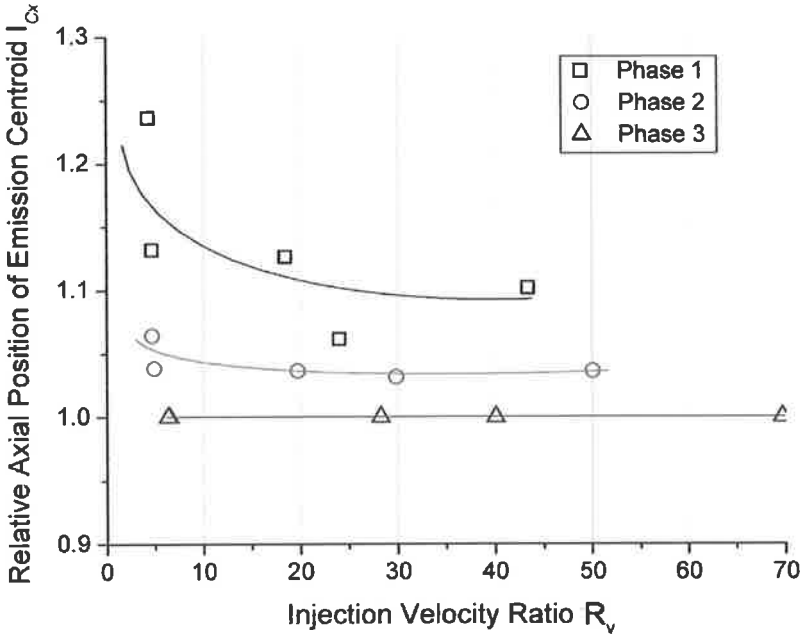

Figure 7.20 Normalised emission intensity centroid position relative to operating phase 3 ($P_r < 1$). Data from VIS04W tests.

A peak-to-peak analysis is performed on the centroid of intensity data to provide insight to the comparative level of flame "steadiness" between the 3 operating phases (see Figure 7.21).

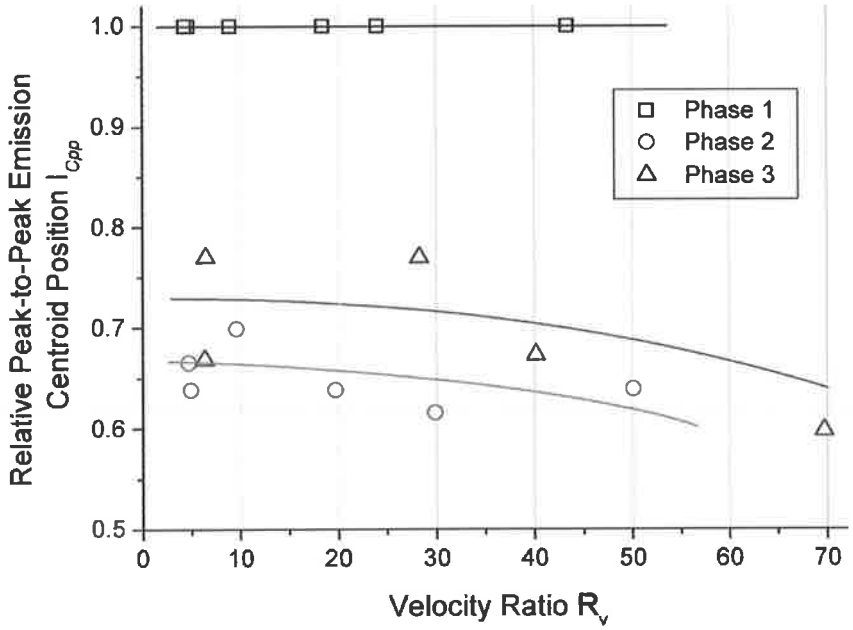

Figure 7.21 Peak to peak examination of flame emission intensity centroid relative to Phase 1 data. Data from VIS04W tests.

Data presented in Figure 7.21 indicate that the emission intensity centroid position fluctuates most at operating phase 1 relative to other operating phases ($P_r > 1$). Note however, the peak-to-peak (dynamic) data from phase 1 ($P_r > 1$) is not representative due to the significant combustion product recirculation which appears to falsify results and is included in this case as a reference for comparison only.

The near critical test condition ($P_r \sim 1$) results in a more "steady" flame with fluctuation between consecutive images in the order of 60 - 65% of that experienced at operating phase 1. Operating phase 3 ($P_r < 1$) results in fluctuations between phase 1 and 2 corresponding to 65 - 75% of that of operating phase 1.

7.3.8. Summary

A coaxially injected LO_X/H_2 model combustor with optical access has been operated over a range of steady-state conditions representative of real liquid rocket engines. Interchanging injector geometries and regulating propellant flow-rates at constant R_{OF} has enabled examination of the local and global influence of injection velocity ratio R_v and reduced pressure P_r on near injector combustion zone and general thrust chamber response over a range of conditions. Two H_2 temperature ranges were successfully investigated at a constant LOx injection temperature.

Propellant velocity ratio and momentum flux ratio values investigated span 2 and 4 orders of magnitude respectively. It must also be noted that these non-dimensional values scale almost linearly over the conditions examined here and thus the results are presented with a focus on injection velocity ratio R_v only.

At steady state conditions where $P_r < 1$, increased relative flow field and flame unsteadiness has been consistently observed using various diagnostic techniques. A peak-to-peak analysis of dynamic chamber pressure has indicated an increased level of relative unsteadiness at $P_r < 1$

when compared to $P_r \sim 1$ and $P_r > 1$ test conditions. Examination of the flow field (shadowgraph images) has also indicated an apparent increase in core flow unsteadiness at subcritical pressure relative to the near critical and super critical pressure conditions. A peak-to-peak assessment of the axial emission centroid position also indicates a relative unsteadiness at $P_r < 1$ over a range of operating conditions. Such observations are experienced over a range of injection and operating conditions.

Despite this, thrust chamber operation at $P_r < 1$ consistently results in greatest combustion efficiency over *all* conditions examined. Subcritical pressure operation appears relatively insensitive to injection velocity ratio in comparison to near critical and super critical pressure conditions. This phenomenon is reflected in the mean relative emission intensity analysis. The maximum emission intensity derived by averaging emission over the *entire* window area observed occurs at the lower pressure conditions ($P_r < 1$). At $P_r > 1$, near injector emission intensity appears to be relatively low, independent of propellant injection temperature.This observation is consistent across all operating conditions however is only truly valid for the near injector field. Further downstream however at $x/d > 15$, emission intensity is greatest at $P_r > 1$. In general, near injector emission decreases with low relative propellant velocities at constant propellant injection temperature. Flame emission intensity appears to move axially downstream with reduced velocity ratio, which is common to all pressure regimes.

At near-critical and supercritical pressure conditions combustion efficiency decreases at propellant velocity ratios of less than $R_v \sim 20$ and $R_v \sim 30$ respectively. At $P_r \sim 1$ and $P_r > 1$, the efficiency is extremely sensitive to injection velocity ratios of $R_v < 10$ and $R_v < 20$ respectively. A reduction of H_2 injection temperature does not appear to affect combustion efficiency over the conditions examined except for where $P_r > 1$ where a distinct decrease of efficiency is seen.

Classical atomisation and mixing regimes tend to dominate sub-critical injection, which is evidently dissimilar to high-pressure phenomenon as illustrated by Mayer and Tamura (1996) and Mayer and Smith (2005). Ligament formation and droplet detachment govern core flow break-up at $P_r < 1$ which, when combined with highly perturbed flow oscillation, results in increased reaction due to greater interfacial surface area and enhanced mixing of propellants. The outcome is improved combustion efficiency, which appears to be comparatively insensitive to relative propellant velocities over a broad range from $R_v = 5 - 60$.

As the critical pressure of oxygen is approached, surface tension diminishes and certain thermodynamic properties deviate strongly from ideal. Isothermal compressibility and specific heat peak dramatically at the critical pressure making the jet far less sensitive to temperature and pressure fluctuations resulting in an increase in combustion "steadiness". As the critical pressure is exceeded, the aerodynamic dominated flow field changes to a diffusion dominated jet. The supercritical jet resembles that of a high density, highly turbulent gaseous jet. Mechanisms which control mixing and reaction are relatively inefficient in comparison to those at subcritical pressure and therefore low relative propellant velocities (and momentum) have a significant detriment on combustion efficiency.

Chapter 8

Combustion Instability

8.1 Introduction

Combustion instability in liquid rocket engines remains one of the most critical design and development issues facing engine manufacturers of today and tomorrow. The physical mechanism of combustion instability in liquid rocket engines is coupling between the combustion process and the acoustic modes of the chamber or the propellant feed system. Whilst the combustion instability categories are widely known (for example see Harrje and Reardon (1972)), a detailed understanding of physical causes and preventative measures continue to elude researchers and engine developers. Experimentally validated contributions to the field are presently uncommon due to the extreme costs associated with test facilities, hardware and propellants. Research in the area with modern measurement devices and optical diagnostics systems can assist in elucidating some of the details which may have not been previously presented.

8.1.1. Characterisation of Unstable Combustion Modes

Analysis of dynamic combustion chamber pressure data indicate the longitudinal modes of the combustion chamber appear dominant as illustrated in the FT spectra in Figure 8.1. The first longitudinal (1L) mode is typically around $f \sim 1750$Hz and varies depending on operating conditions. Harmonics of the 1L mode are clearly seen in the dynamic chamber pressure frequency spectra illustrated in Figure 8.1. Triggering of HF unstable combustion modes is unlikely with the thrust chamber utilised here due to its small chamber diameter resulting in the first tangential (1T) mode at $f \sim 22$ kHz.

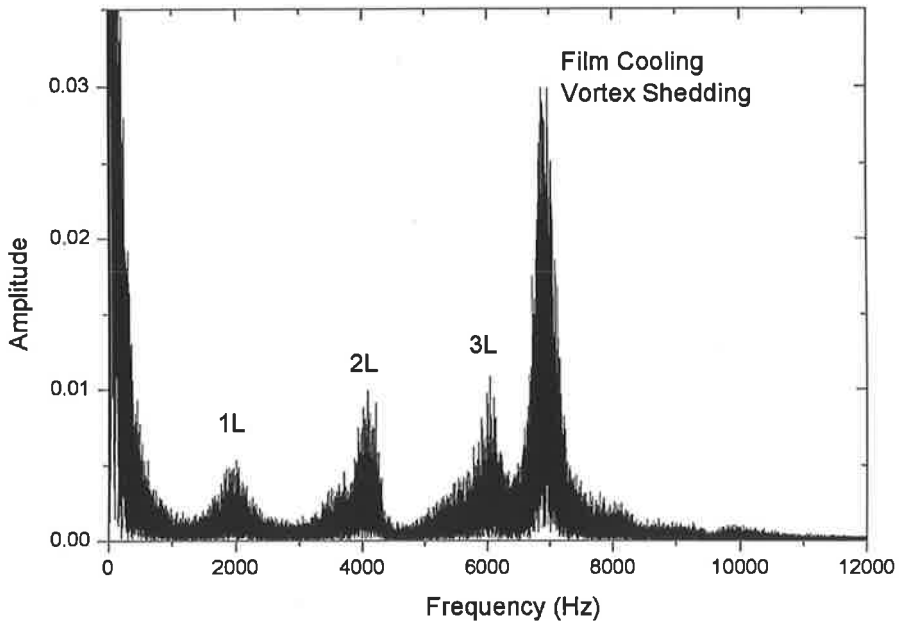

Figure 8.1 Typical frequency spectrum of dynamic chamber pressure

A dominant frequency of $f \sim 6800$Hz is be attributed to vortex shedding from the film cooling inlet. This observation is consistent and has been observed over a range of injection devices including a porous injector head design (Smith and Suslov et al. (2003)). Further detail can be found in Section 5.2.3.

Typically, dynamic chamber pressure and/or accelerometer data recorded during combustor operation is sufficient to reveal the occurrence of unstable combustion. Combustion instability is generally represented by large peak-to-peak values in the dynamic pressure data. Values in

excess of 3% of mean chamber pressure ($P_{p\text{-}p} > 0.03\bar{P}_{ch}$) constitute rough combustion whilst values greater than 5% represent combustion instability. Values in excess of 10% can be highly detrimental to performance and can lead to serious hardware failure (Harrje & Reardon (1972)).

8.1.2. Low Frequency (LF) Combustion Instability

Low frequency (LF) combustion instability, also known as "chugging" has received less attention recently due to the belief that the causes and preventative methods are widely known. LF instabilities are most often coupled to the propellant feed system whereby the pressure oscillations in the combustion chamber modulate propellant flow rates resulting in axial non-uniformities of propellants in the chamber. This in turn promotes inhomogeneous combustion and the ultimate result can be a self-sustaining periodic oscillation. In many cases, large amplitude LF instabilities can trigger high frequency (HF) instabilities whereby the combustion process couples with the acoustic modes of the combustion chamber. This latter case is highly detrimental to performance and can lead to total failure of an engine and loss of a launch vehicle. HF instability is characterised by coupling between the combustion process and higher frequency acoustic modes of the chamber such as tangential and radial modes.

8.1.3. Experimental LF Combustion Instability Observations

A pressure differential of 12-15% of mean combustion chamber pressure ($0.12\text{-}0.15\bar{P}_{ch}$) across the H_2 side of the injector has resulted in a continuous injection-coupled combustion instability with a low frequency dominance ($f \sim$ 40-60Hz). Such LF phenomenon is typically linked to the fluid system and/or test facility structure. In most cases, the LF oscillations have contained lower amplitude HF oscillations (primarily chamber longitudinal modes). Figure 8.2 demonstrates a typical combustion chamber pressure trace recorded during instability.

The LF unstable mode is triggered in the third phase of operation which corresponds to the low pressure period of the operating sequence ($P_r < 1$). The LF instability has been found to be

strongly related to the pressure differential across the hydrogen side of the injector element (ΔP_{H2}). This observation was consistent over a series of tests. In no instances was LF instability observed at $P_r \sim 1$ or $P_r > 1$ under any conditions.

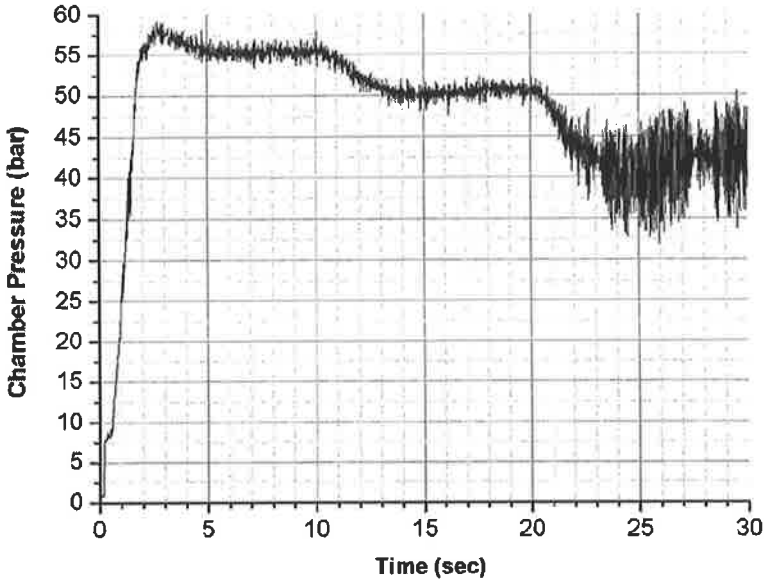

Figure 8.2 Combustion chamber pressure trace illustrating strong LF combustion instability during steady state operation during operating phase 3 ($P_r < 1$). Data from test VIS04WA Run 8.

In this particular test series, the pressure difference across the oxidiser (ΔP_{O2}) was maintained relatively constant during each operating phase. However, by enlarging the hydrogen annulus, the hydrogen pressure drop (ΔP_{H2}) varies from test to test. Shadowgraph, OH emission images were recorded throughout unstable operation. Figure 8.3 shows a series of shadowgraph images recorded during combustion instability.

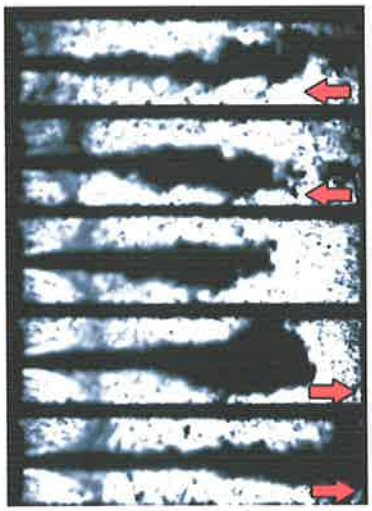

Figure 8.3 Shadowgraph images recorded during unstable combustion illustrating modulation of oxygen flow. Acquisition rate f = 500Hz. Data from VIS04WA Run 8.

8.1.4. Investigating the Stability Threshold

Interesting to note from the test conditions examined, is that combustion stability thresholds vary significantly depending on reduced pressure. At steady state conditions, a pressure drop across the H_2 side of the injector equal to 10% of chamber pressure (ΔP_{H2}=0.1$\bar{P}_{ch}$) consistently results in unstable combustion at subcritical pressures ($P_r < 1$) However, at near and supercritical conditions ($P_r \sim 1$ and $P_r < 1$), ΔP_{H2} values as low as 6.6% and 8.9% of $\bar{P}_{ch}$ respectively do not resulted in unstable combustion whatsoever. In fact, under all test conditions investigated, no instability could be triggered whilst operating above or very near to the critical point of oxygen. At reduced pressure values less than unity, intermediate LF instability has been observed with $\Delta P_{H2} \sim 11.25\% \bar{P}_{ch}$. The effect of ΔP_{H2} on stability is illustrated by Figure 8.4.

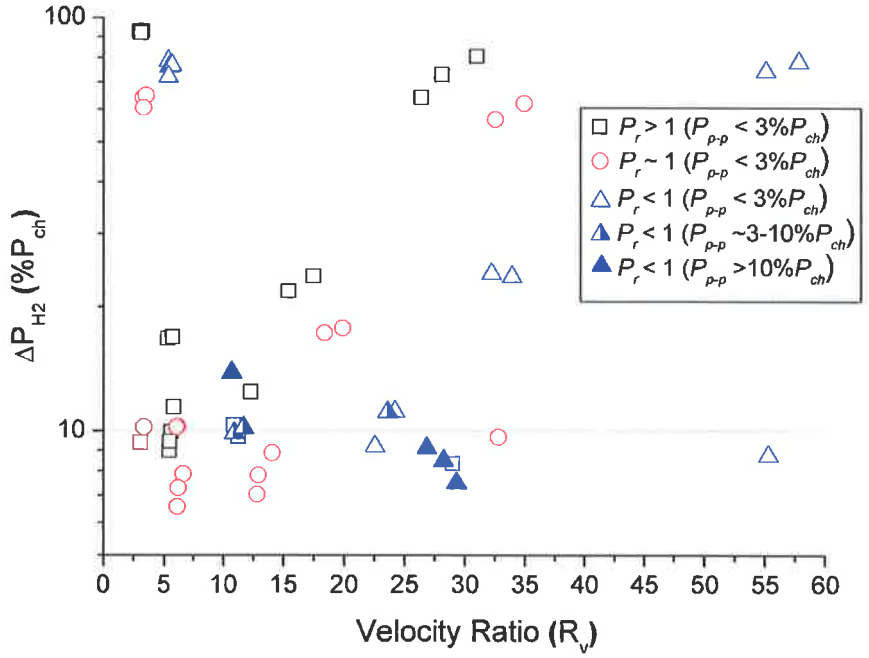

Figure 8.4 Hydrogen injector pressure drop ΔP_{H2} as a function of momentum flux ratio J and reduced pressure P_r. Data markers are assigned based on reduced pressure and dynamic pressure peak-to-peak oscillation values.

Low pressure amplitude (stable) combustion is designated for tests where peak-to-peak pressure values are less than 3% of $\bar{P}_{ch}$. Intermediate amplitudes are from 5-10% of $\bar{P}_{ch}$ and high amplitude (unstable) for $P_{p\text{-}p} > 10\%$ of $\bar{P}_{ch}$. All intermediate and high amplitude oscillations occur at a frequency of approximately $f \sim 40\text{-}60$Hz depending on injection conditions. Interesting to note from Figure 8.4 is the fact that the stability threshold based on ΔP_{H2} is apparently non-existent at near and supercritical pressure conditions. Under no circumstances was LF combustion instability observed at chamber pressures above the critical point of oxygen for the range of operating conditions examined here.

8.1.5. Chamber Pressure Ramping

A series of tests were undertaken to examine the point at where combustion instability is triggered. The propellant mass flow rates and thus combustion chamber pressure were ramped simultaneously (i.e. at constant R_{OF}) whilst continuously recording measurement and image data. The aim of this test sequence was to determine precisely where the transition from a stable to an unstable combustion mode would occur. The purpose of this study is to better understand the nature of combustion and examine the effect of reduced pressure on combustion stability. A typical combustion chamber pressure trace at constant R_{OF} is presented in Figure 8.5.

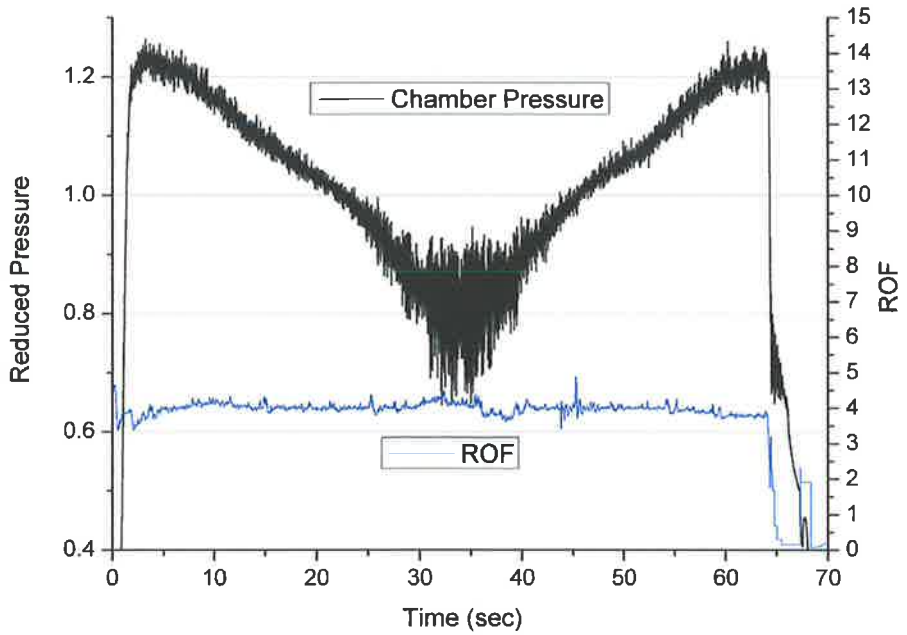

Figure 8.5 Combustion chamber reduced pressure and oxidiser/fuel ratio as a function of time for the chamber ramping tests.

The test duration was 64 seconds at relatively constant propellant injection temperatures and R_{OF}. Conditions were maintained relatively constant initially for approximately 4 seconds at an elevated chamber pressure of $P_{ch} \sim 61$ bar. The mass flow rates are then reduced simultaneously to steadily reduce combustion chamber pressure to 50 bar after approximately 22 seconds. A chamber pressure of approximately 40 bar was achieved by around 30 seconds. The low pressure

conditions were maintained constant for a period of 8 seconds before positively ramping the propellant mass flow and combustion chamber pressure. Chamber pressure steadily increased until the nominal pressure of approximately 61 bar was achieved once more and held constant for 4 seconds prior to shutdown.

As propellant flow rates decrease and P_{ch} approaches a reduced pressure equal to unity (P_r =1) the peak-to-peak chamber oscillations ($P_{p\text{-}p}$) approach a minima which is clearly evident from Figure 8.5. It has been observed that $P_{p\text{-}p}$ increases almost immediately once chamber pressure falls below the critical pressure of oxygen (P_r = 1). Instability follows and has been observed with a ΔP_{H2} as high as 15% $\bar{P}_{ch}$ with $P_r < 1$. Once the lower pressure domain is reached, the peak to peak values are excessive and typically exceed 10% $\bar{P}_{ch}$. The LF instability takes hold and continues to persist until the propellant flow rates and chamber pressure are increased. The peak-to-peak values decline steadily and again reach a minima as the critical pressure of oxygen is reached. As pressure continues to increase peak to peak amplitude values also increase once more and stabilise once the nominal pressure level of approximately 61 bar is achieved at $t \sim 60$ seconds as shown in Figure 8.5.

These observations are consistent and agree with standard tests where phase 2 data ($P_r \sim 1$) consistently exhibits very low $P_{p\text{-}p}$ values. The phenomenon is clearly depicted in Figure 8.6 where $P_{p\text{-}p}$ is plotted against P_r for an entire 'Ramping test' designated VIS06WA run 3.

The initiation of a LF combustion mode is reflected in the emission images and appears as soon as the critical pressure of oxygen is surpassed and P_r is less than unity. The pressure ramping tests were repeated with different H_2 injection temperatures and R_{OF} values from ~3.5 to ~6 with very similar results.

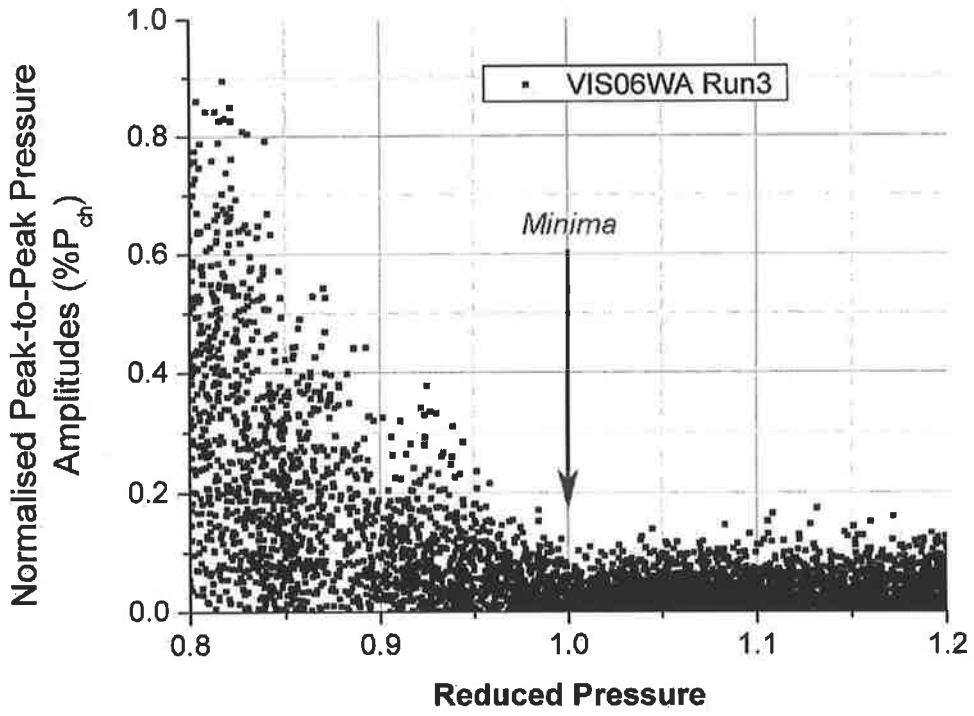

Figure 8.6 Normalised peak-to-peak combustion chamber pressure amplitudes as a function of reduced pressure. Note minima at reduced pressure P_r = 1. Data from test VIS06WA Run 3.

8.1.6. Flame and Flow Field During Combustion Instability

During ramping tests, combustion instability was not experienced whilst chamber pressure was above the critical point of oxygen under any conditions (i.e. $P_{ch} > 50.45$ bar). The effects of the low frequency combustion instability on the near injector field was examined through analysis of the images acquired under such conditions.

Analysing image data proved difficult due to significant movement of the combustion chamber during LF instability. The combustion chamber has been observed to move up to approximately 5mm during unstable combustion. A technique outlined in Section 4.4.7 was adopted to adjust and crop the images at a common point resulting in a marked reduction in the effect of the chamber movement during instability.

A series of images obtained during LF instability are presented in Figure 8.7 illustrating strong propellant and combustion zone modulation due to the occurrence of LF combustion instability.

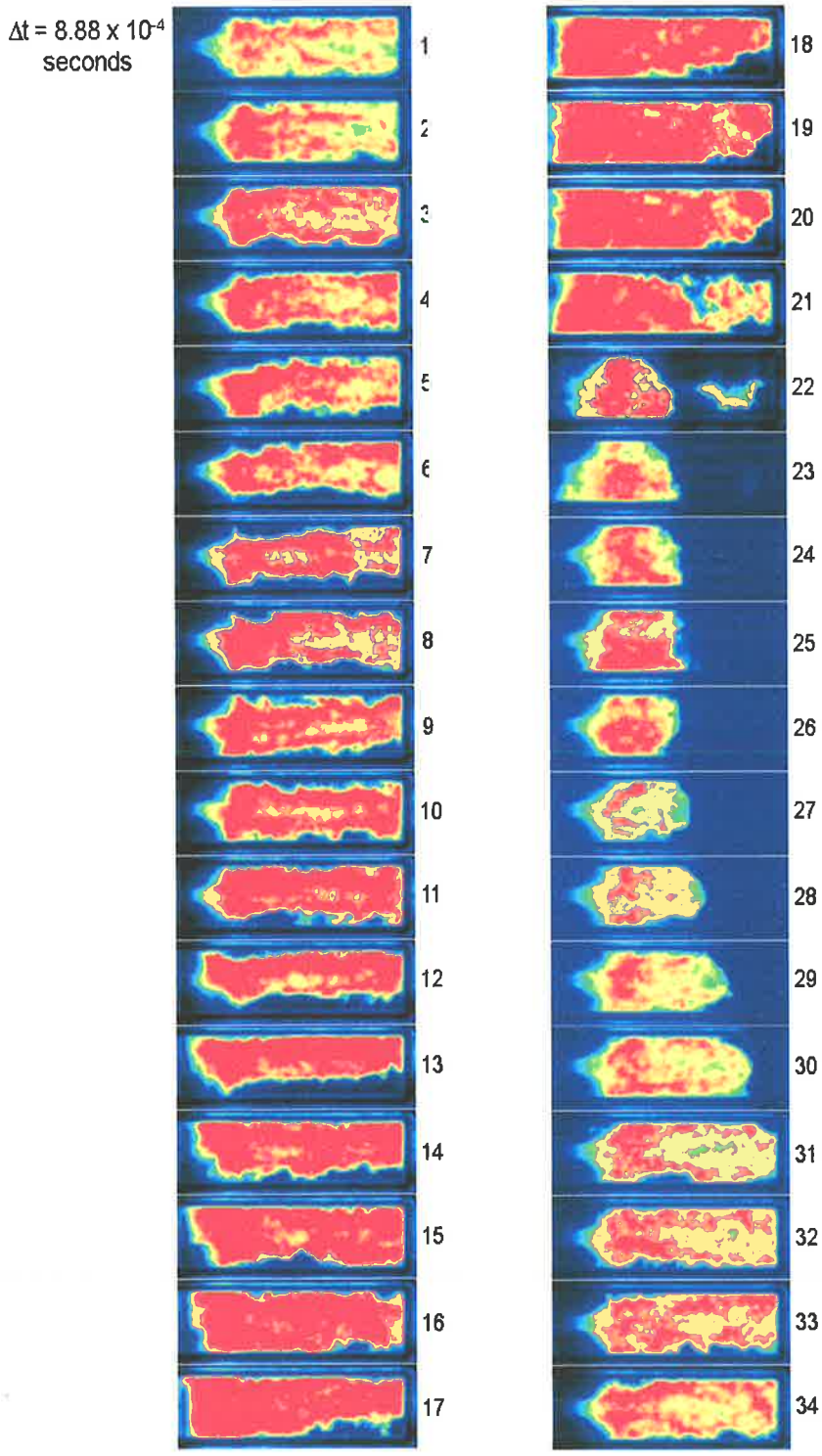

Figure 8.7 Series of OH emission image frames captured during LF instability. Acquisition frequency f = 9kHz with each 8th frame shown here. Flow from left to right. P_{ch} ~ 40 bar.

High speed shadowgraph images recorded during instability also show strong modulation of the propellants similar to that depicted by Figure 8.3. Observation of the near injector emission images shows the flame clearly oscillates from near $t = 23$ seconds, at a frequency equal to that measured by the dynamic pressure sensors during LF unstable combustion.

The occurrence of instability illustrated by Figure 8.7 was observed at a reduced pressure less than unity ($P_r < 1$). Frames 1 to 3 represent an otherwise typical OH emission image captured during steady operation. Frames 3 to 10 indicate a significant increase in emission intensity. The emission intensity tends to move toward the injection plane and the flame shape narrows. The combustion zone then appears to fill the entire injection region, with the flame shrouding the face plate region entirely (frames 10 to 20). A momentary drop in pressure across the injector results in a propellant void as illustrated in frames 21 to 26. The propellant flow then recovers and the flame appears to extend steadily once again beyond the field of view.

At the most brutal point of instability, manifold dynamic data shows a coupling effect which assists in sustaining the excessive peak to peak pressures in the chamber. Emission images show significant increase in emission intensity with the flame elongating and retreating as pressure waves propagated through the chamber. Such localised flame behaviour clearly indicates the hostile and potentially destructive nature of combustion instability. Burned injector elements and damaged face plates have resulted from the unstable operation of combustion chamber C.

Chapter 9

Conclusions

9.1 Coaxially Injected Liquid Rocket Engine Thrust Chambers

Propellants injected into liquid rocket thrust chambers at transcritical and supercritical conditions behave as dense gases with potentially liquid-like properties. Large thermodynamic gradients exist near the critical point with properties such as specific heat (c_p) developing singularities at the critical point. Exceeding the critical point shifts the thermodynamic anomalies and "pseudo-critical" lines exist.

At present, limited data-sets exist for high pressure LOx/H_2 combustion and empirically derived correlations for low-pressure (subcritical) injection and combustion phenomena cannot be directly extrapolated to transcritical or supercritical regimes. The Weber number for example (We), commonly used for characterisation of jet atomisation, is undefined above a reduced pressure of unity

due to the absence of surface tension and thus existing low pressure correlations based on *We* cannot be applied.

Exemplary sudies of high pressure, non-reacting, single and coaxial jet studies have highlighted significant disparities exist between sub- and supercritical operating regimes. However limited information is publicly available for high pressure LOx/H_2 injection and combustion. This work quantifies and characterises high-pressure, coaxially injected LOx/H_2 combustion at steady state operating conditions in a windowed, LPRE thrust chamber which is operated at conditions representative of modern-day liquid rocket engines.

9.2 Experimental Test Campaigns

A coaxially injected LO_x/H_2 combustor with optical access has been operated over a range of conditions representative of modern liquid rocket engines. Interchanging injector geometries and regulating propellant flow-rates at constant R_{OF} has enabled examination of the local and global influence of injection velocity ratio R_v, and reduced pressure P_r on thrust chamber performance and near injector flame and flow over various conditions. Two hydrogen injection temperature ranges were successfully investigated at a relatively constant liquid oxygen injection temperature. Thrust chamber operation at pressure levels below, near, and above the thermodynamic critical pressure of the oxidiser have been investigated.

Combustor start-up transients and ignition phenomena, steady-state operation and low frequency combustion instability have all been investigated as a part of this study. Throughout all operational regimes, the near injector flow-field and combustion zone have been examined using various optical diagnostics equipment and the global combustion response monitored with a series of temperature thermocouples and static and dynamic pressure transducers.

Injection velocity ratio R_v and reduced pressure P_r have both shown to influence combustion behaviour at steady and unsteady operating conditions.

9.3 Preliminary Testing

9.3.1. Background

An initial test campaign was undertaken with the primary aim of developing a reliable operating sequence for the thrust chamber. The secondary aim was to implement a range of optical diagnostics in an attempt to visualise and characterise the high pressure combusting flow field both qualitatively and quantitatively at different H_2 injection temperatures. The preliminary findings highlighted the need for temporally resolved diagnostics to better observe the near injector field combustion zone.

9.3.2. General Observations

The application of optical diagnostics including OH emission and shadowgraph imaging and CARS reveals a range of physical phenomenon. Water has been observed to accumulate near the chamber boundaries in shadowgraph images at a nominal pressure of P_{ch} = 60bar. The vapour temperature of water is approximately 594K at 60bar and the combustion products (water vapour) reaches the outer chamber boundary and rapidly condenses due to the cool hydrogen film cooling (T_{H2}~250K).

Ice formation has been observed to develop around the injector exit and grow up to 2.5mm in length. Formation of ice is exacerbated by strong recirculation of combustion products (water). The recirculated water vapour rapidly solidifies when it contacts the injector face plate which is at cryogenic temperatures.

The application of Coherent Anti-Stokes Raman Spectroscopy (CARS) has provided tempera-

ture profiles at a number of radial positions at downstream locations of 50mm (x/d = 12.5) and 80mm (x/d = 20). At the 50mm location, the temperature histograms display a uni-modal temperature distribution. The weighted average temperatures measured range between 400K and 500K. This low temperature bias indicates a strong influence of the window film cooling. At this axial location, combustion products are entrained in the recirculation zone and the combustion zone is confined to a small cone around the oxygen core. The 80mm downstream position shows a very different result.

The pronounced bi-modal temperature distributions at 2, 4, 6, and 8mm radial positions (from the centre-line) indicate that hot and cold gases constantly occupy and escape the CARS probe volume. This can be attributed to the turbulent fluctuations of the LOx jet, shear layer and surrounding reaction zone. The very low temperature component of the temperature histograms represent that of slightly heated H_2-gas representative of the film cooling flow. The higher temperatures measured are representative of heat release from the combustion zone (T>1000K).

Temperatures indicative of stoichiometric or near stoichiometric conditions were not found in the measurements (i.e. T_{st} ~ 3500K). The maximum temperature observed in this study was approximately 2000K. The consistency of the low temperature values witnessed indicate that coaxially injected propellants in a co-flowing, shear configuration results in strong temperature and flow stratification due to poorly mixed propellants at the axial positions probed (x/d =20). Such observations are also evident in the shadowgraph images where a majority of the liquid oxidiser core is unreacted at x/d > 25. The low temperatures experienced may be further exacerbated by the large volumes of hydrogen film cooling and hence a low total oxidiser-fuel ratio.

Hydrogen injection temperatures below 80K influence the optical accessibility due to increased

density gradients Low H_2 injection temperature also appears to result in diminished emission intensity in the near injector field and an increase in peak-to-peak chamber pressure amplitudes. It was highlighted that further studies are necessary to better quantify and understand the effects of H_2 injection temperature on LOx/H_2 combustion.

9.4 Combustor Start-up Phenomena

9.4.1. Background

A consistent and controlled start-up and ignition process of a liquid rocket engine is pertinent to the success of launch vehicle operation and mission execution. The rocket engine research community is working toward understanding and resolving issues pertaining to the myriad of complex physico-chemical processes which dominate the highly unsteady, start-up and ignition process. Despite this, the start-up phase of LPRE's remains a challenge in modern day space transport systems with the failed launch of Ariane V flight V-142 - attributed to an ignition problem (refer Barensky (2001)).

A revised experimental setup comprises of ultra-high-speed diagnostics including an image intensified high speed digital camera system. High temporal resolution enables a detailed examination of local combustion behaviour in the near injector field. Fundamental studies such as this provide a predominantly quantitative insight to start-up transient behaviour not previously presented.

9.4.2. Thrust Chamber Start-up and Ignition

A revised optical diagnostic setup was employed to observe the near injector field during thrust chamber start up. A torch igniter is used which has similarities to that used in modern liquid rocket motors. Correct ignition timing is paramount is avoiding pressure peaks or 'hard-starts' due to propellant accumulation. The torch igniter operates continuously prior to opening of the

main run valves and introduction of propellants to the thrust chamber. The igniter operates at a frequency of $f \sim 380$Hz and influences the primary flame and flow until the point of ignition.

Many observations are made during the start-up process which vary somewhat depending on propellant injection conditions. Propellants are typically injected in gaseous form during start-up however liquid oxidiser has been injected with the hardware employed here. It must be noted that qualitative and quantitative observations presented here may be related to the unique hardware employed. Despite this it is important that fundamental observations are documented and discussed where possible.

Throughout the series of tests undertaken, the point of ignition does not occur until the propellant flow rates and local R_{OF} are sufficient. The point of ignition is defined here as the point where the flame emission intensity increases significantly in an almost instantaneous manner. The emission intensity increase is closely followed by a steady increase in thrust chamber pressure.

9.4.3. General Ignition Observations

Upon propellant ignition, an instantaneous increase in emission intensity occurs and the flame front retracts toward the injection plane and takes the form of a 'fist' -like shape. The majority of emission intensity moves downstream and is concentrated in the flame fist. This has been verified through analysis of the centroid of emission intensity from the flame emission images.

Close examination of the very near injector field (i.e. up to x/d=5) indicates that a very sharp step exists in the axial position of the emission centroid of intensity. Upon ignition, the flame typically undergoes a brief transition to a low frequency dominated, unstable mode of combustion. This LF instability (f ~ 40Hz-100Hz) is observed in flame emission intensity, centroid of emission and flame front tracking analyses.

The pressure differential across the H_2 side of the injector element has shown to have a

significant effect on thrust chamber and flame stability. Low frequency injector coupled instability is easily triggered during the start-up process due to unfavourable propellant injection conditions. Such unstable operation can be of great detriment to hardware longevity and overall thrust chamber performance.

The near injector field has been examined during injector coupled instability triggered during the start-up process. The flame and flow field have been seen to simultaneously oscillate strongly in the axial direction at frequencies between approximately 40 and 100Hz. The oscillating flow field creates pressure waves which move upstream and effectively modulate propellant flow into the chamber. The oscillation frequency changes with time due to the continual change in propellant injection conditions (i.e. propellant injection temperature, density and velocity). The unstable mode of operation was quickly damped in all cases where instability was observed during thrust chamber start-up. The damping appears to coincide with an increase in thrust chamber pressure near the thermodynamic critical pressure of oxygen ($P_{crit} \sim 50.4$bar).

A second start-up case was examined with an increase in propellant velocity ratio, with a slightly lower propellant flow rate (and thus a marginal decrease in injector pressure differential) resulting in a similar start-up process. In this particular instance of start-up however, the flame front appeared to momentarily oscillate in the axial direction at a frequency corresponding to the first longitudinal mode of the chamber (i.e. $f \sim 1700$Hz). During the axial oscillation of the flame, the emission intensity was observed to correlate strongly with flame front position. Dynamic pressure data did not indicate excessive pressure amplitudes at this point.

Injection with liquid oxidiser results in a significant increase in relative propellant velocity which typically results in enhanced atomisation and increased combustion efficiency. A draw-

back however is a significant reduction in pressure difference across the oxidiser side of the injector during the highly transient, unsteady start up period. Secondly, with the introduction of two phase flow, the evaporatio rate of the liquid oxygen may play an important role in the start-up process. In the ignition test case where liquid oxygen was injected, the flame appears to ignite approximately 80msec later than previous start-up tests at $t \sim 1.25$ seconds with $R_v \sim$ 120-145. The flame appears to extinguish after approximately 0.002 seconds before re-igniting some 0.01 seconds later. This observation may be attributed to the high strain rates at the propellant interface, low injection temperature and/or unsatisfactory localised mixing. Having undertaken only a single test at such conditions, it is difficult to clearly define the influential parameters.

Flame emission spectra have been recorded during thrust chamber start-up transients also. Spectral peaks correspond well with those previously assigned (Gaydon (1974)) and intensity increases with axial position. The intensity at $x/d = 17.5$ is approximately 2-3 times greater than that at $x/d = 5$ which is indicative of the relative level of mixing and reaction at the respective positions.

Whilst only a small number of thrust chamber start-up tests were performed, a series of important observations have been highlighted which may assist in the better understanding of the complex processes taking place in the near injector field of a liquid rocket motor.

9.5 Steady State Combustion

9.5.1. Background

The near injector combustion zone has been investigated in a coaxially injected liquid propellant rocket engine thrust chamber at steady state, high-pressure operating conditions - representative of modern day LPRE's. Despite the regular progress in low pressure combustion research and non-reacting high pressure studies, results can not be directly extrapolated to transcritical or supercritical reacting conditions. The influence of propellant injection velocity ratio R_V on atomisation has not been verified for combustion at conditions near to, or in excess of the critical point of the injected propellants. Results also highlight that reduced pressure (P_r) has a significant influence on propellant flow field evolution and the entire combustion process in a LPRE thrust chamber.

9.5.2. Subcritical Pressure Operation

Analysis of measurement system data indicates a significant difference exists between thrust chamber operation at pressures below, near and above the thermodynamic critical pressure of oxygen. The combustion efficiency estimation (Section 7.2.3) and the peak to-peak dynamic pressure data analysis (Section 7.2.1) consistently highlight dissimilarities between sub- and supercritical pressure regimes. An inherent unsteadiness at reduced pressure levels less than unity is frequently observed through examination of the flow-field and combustion zone images and measurement data over a broad range of test conditions. The liquid oxygen core typically exhibits an increase in local surface perturbations and flow oscillations at a reduced pressure of $P_r < 1$ which coincides with observations construed from the measurement data.

Classical atomisation and mixing regimes tend to dominate sub-critical injection, which is evidently dissimilar to high-pressure phenomenon as illustrated by Mayer and Tamura (1996) and Mayer and Smith (2004). Ligament formation and droplet detachment govern core flow

break-up at $P_r < 1$ which, when combined with highly perturbed flow oscillation, results in increased reaction due to greater interfacial propellant surface area and enhanced mixing. The outcome is an improvement in combustion efficiency, which appears to be comparatively insensitive to relative propellant velocities ranging from R_V =5 - 60. Despite this, data presented here indicate that enhanced flow field fluctuations experienced at $P_r < 1$ results in an increased likelihood of rough or unstable combustion. Frequency spectra constructed from flame emission centroid data do not indicate any interaction between the near injector flame and the acoustic modes of the chamber under any steady state operating conditions examined here.

9.5.3. Near Critical and Supercritical Pressure Operation

At elevated pressure, an entirely different cascade of events takes place. The propellant flow-field is highly insensitive to pressure disturbances over the broad range of injection conditions examined here. Isothermal compressibility k_T is relatively high (especially near the critical point) and thus flow field or pressure disturbances experienced downstream are easily damped and attenuated and are not transmitted upstream.

In general, flame emission intensity appears to move axially downstream with reduced velocity ratio, which is common to all pressure regimes. At $P_r > 1$ however, near injector emission intensity appears to be relatively low in comparison to $P_r \sim 1$, independent of propellant injection temperature. Further downstream in the heavy mixing and combustion zone (x/d>15), emission intensity is typically greatest at $P_r > 1$.

At $P_r \sim 1$ and $P_r > 1$, the combustion process appears to be extremely sensitive to injection velocity ratios of $R_v < 10$ and $R_v < 20$ respectively. Under such low R_v conditions, combustion efficiency diminishes dramatically and the intense regions of flame emission appear to shift further downstream with reduced R_v.

9.5.4. Influence of Propellant Injection Temperature

At $P_r > 1$, H_2 injection temperature has a negative impact on combustion efficiency. This observation is not obvious at near critical or subcritical pressure conditions. Furthermore, the H_2 injection temperature appears to have a significant impact on flame and flow field evolution in the near injector region at conditions where $P_r > 1$. The temperature of oxygen plays less of a role as density is relatively insensitive to changes in temperature at such pressure levels. With $T_{H2} < 80$K, optical clarity is lost and a strong cloud of combustion products appears to shroud the near injector zone resulting in scattered flame emission.

9.5.5. Summary

Application of high-speed, time resolved optical diagnostics has provided quantitative and qualitative evidence of dissimilar combustion behaviour at various reduced pressure levels through visualisation and analysis of flow-field and flame emission data. The results obtained using optical diagnostics highlight trends which correspond to those observed through analysis of the measurement system data. The observations realised with 2D imaging methods have been confirmed with spectroscopic techniques. It must be emphasised that all four independent analysis techniques have exhibited a strong influence of injection velocity ratio R_V (and also J) on the overall combustion behaviour and localised, near injector flame behaviour. All techniques concur that reduced pressure also plays a critical role and further influences the effect that relative propellant velocity has on mixing, atomisation and flow field evolution. Examination of the near injector field has proven to be an effective method of evaluating the global performance of a liquid rocket engine thrust chamber.

Such observations and results highlight the importance of further experimental investigations to provide additional fundamental information and enhance the current understanding of high-pressure, steady state, liquid rocket engine combustion.

9.6 LF Instability

9.6.1. Background

Combustion Instability in liquid rocket engines remains one of the most critical design and development issues facing engine manufacturers of today and tomorrow. The physical mechanism of combustion instability in liquid rocket engines is a coupling between the combustion process and the acoustic modes of the chamber or propellant feed system. Low frequency dominated combustion instability has been observed with the hardware employed here and is primarily attributed to the pressure differential across the injector element. A pressure drop across the H_2 side of the injector equivalent to 12-15% of chamber pressure P_{ch} has resulted in combustion instability with a LF dominance ($f \sim$ 40Hz-100Hz) at subcritical chamber pressure.

9.6.2. LF Instability Visualisation

High speed shadowgraph images recorded during unstable combustion showed strong modulation of the propellants. At the most brutal point of unstable operation, manifold dynamic data illustrated a coupling effect which assists in sustaining the excessive peak to peak pressures in the chamber. Emission images show a significant emission intensity increase with elongation of the flame before it retreats as the pressure waves propagate through the chamber. The flame was observed to entirely fill the optical path at times with the flame momentarily shrouding the entire face plate. Image processing techniques have shown that flame emission intensity fluctuates in a low frequency range in unison with chamber pressure oscillations.

9.6.3. Reduced Pressure Effects

Interesting to note from the test conditions examined, is that stability thresholds vary significantly based on reduced pressure. A typical steady state pressure differential equal to 12-15% of chamber pressure typically results in unstable combustion at subcritical pressure conditions. However injector pressure differentials as low as 6.6% and 8.9% of chamber pressure have not

resulted in unstable combustion whatsoever at nearcritical and supercritical pressure conditions respectively. In fact, under all test conditions investigated, no instability could be triggered whilst operating above or near to the critical pressure of oxygen.

A unique operating sequence was developed in an attempt to identify a stability threshold. The chamber pressure was ramped down steadily from $P_r > 1$ to $P_r < 1$ through propellant flow rate regulation at constant R_{OF}. This test sequence illustrates precisely where the transition from a stable to an unstable combustion mode occurs.

It was observed that as chamber pressure falls below the critical pressure of oxygen ($P_r = 1$), unstable operation follows which could be triggered with a H_2 injector pressure differential as high as 15% of chamber pressure. During negative and positive ramping of the chamber pressure, the peak-to-peak pressure values reached a minimum as reduced pressure approached unity. This was observed over a number of tests with different injection conditions. During pressure ramping tests, unstable operation was not experienced at reduced pressure equal to, or greater than unity.

9.6.4. Summary

Unstable combustion triggered at $P_r < 1$ could not be replicated at a P_r equal to, or greater than unity under near identical injection conditions. Unstable operation could not be triggered whatsoever with LOx/H_2 propellants at near critical or supercritical pressure conditions, irrespective of very low pressure differential across the injector. These consistent observations further add to the evidence that reduced pressure plays a critical role in combustion stability with LOx/H_2 propellants. Similar, independent observations have been made recently with a high-pressure heptane gas turbine combustor by Lal and Oljaca et al. (2004). The combustor operated at low-pressure exhibited unstable combustion, which appeared to stabilise as the critical pressure was exceeded. This further vindicates that the strong influence of reduced pressure may not only be associated with LOx/H_2 propellants.

9.7 Future Work

As a result of the work undertaken, it is suggested that further examination into the effect of reduced pressure on combustion stability is undertaken. Alternative fuels such as Methane or Kerosene could be used. To further validate findings, it would be of significant interest to undertake a similar study using a thrust chamber with geometries which would be more likely to trigger HF instability modes (i.e. radial, tangential and combined modes).

Another point of interest would be to extend the parametric study to examine the global effects of very low H_2 injection temperatures at near critical and supercritical pressure conditions. Verification with another thrust chamber with different geometries would be highly beneficial in validating findings presented here.

References

Aldén, M., Bengtsson, P.-E., and Edner, H., (1986) Rotational CARS Generation through a Multiple Four-Color Interaction. *Applied Optics* Vol. 25, pp. 4493-4500

Andrews, T. (1875) The Bakerian Lecture - On the Gaseous State of Matter. *Proc. Roy. Soc.*, (London). 24:455

Anon (1976) *Liquid Rocket Engine Injectors*. NASA SP-8089

Arianespace [online], Available from: <http://www.arianespace.com/index1.htm>, [access date: July 2001]

Barensky, S. (2001) Aestus Completes Ignition Tests. *e-space* [online], No. 169. Available from: http://www.arianespace.com/site/news/espace/e.space169.ang.pdf

Bazarov, V.G. (1993) A New Class of Porous Injectors for Combustion Chambers and Gas Generators. *AIAA/SAE/ASME/ASEE Joint Propulsion Conference and Exhibit*, Monterey, CA, June 28-30

Bellan, J., Supercritical (and Subcritical) Fluid Behaviour and Modeling: Drops, Streams, Shear and Mixing Layers, Jets and Sprays. *Progress in Energy and Combustion Science,* Vol. 26, No. 4-6, 2000, pp. 329-366

Bendat J. S., and Piersol, A. G. (1980) *Engineering Applications of Correlation and Spectral Analysis*. John Wiley & Sons, USA

Borghi, R., (1988) Turbulent Combustion Modelling. *Prog. Energy Combust.* Sci. Vol. 14, pp. 245-292

Braeunig, R., A. *Rocket & Space Technology* [online]. Available from: <http:// users.commkey.net/Braeunig/space/> [last update 2001]

Branam, R., and Mayer, W. (2003) Characterization of Cryogenic Injection at Supercriticl Pressure. *Journal of Propulsion and Power*, Vol. 19, No.3, pp. 342-355

Brown, C. D. (1996). *Spacecraft Propulsion*. Washington D.C., American Institute of Aeronautics and Astronautics

Burrows, M. C. and Povinelli, L. A. (1964) Emission Spectra from High Pressure Hydrogen-Oxygen Combustion. NASA TN-D-1305

Cagniard de la Tour, (1822) *C. Ann. Chim. Phys.* , 22, 127

Candel, S., Herding, G., Snyder, Scouflaire, P., Rolon, C., Vingert, L., Habiballah, M., Grisch, F., Péalat, M., Bouchardy, P., Stepowski, D., Cessou, A., Colin, P. (1998) Experimental Investigation of Shear Coaxial Cryogenic Jet Flames. *Journal of Propulsion and Power*, Vol. 14, No.5, pp. 826-834

Carreau, J. L., Le Visage, D., Monote, G., Gicquel, P., Roger, F., (1994) Characterization of the Near Injector Region of Coaxial Jets. *ICLASS-94 Proceedings*, Rouen, France

Chan, W.T., and Ko, N.W.M. (1978) Coherent Structures in the Outer Mixing Region of Annular Jets. *Journal of Fluid Mechanics*, Vol. 89, pp. 515-583

Chehroudi, B., Davis, D., and Talley, D. (2003) Initial Results from a cryogenic coaxial injector in an acoustic field. AIAA 2003-1339, *41st AIAA Aerospace Sciences Meeting and Exhibit*, Reno, NV

Chehroudi, B., Cohn, R., Talley, D., and Badakhshan, A. (2000) Raman Scattering Measurements in the Initial Region of Sub- and Supercritical Jets. AIAA 2000-3392, *36th AIAA/SAE/ASME/ ASEE Joint Propulsion Conference and Exhibit*, Huntsville, AL

Chehroudi, B., and Talley, D. (2002) Interaction of Acoustic Waves with a Cryogenic Nitrogen Jet at Sub- and Supercritical Pressures. AIAA 2002-0342, *40th AIAA Aerospace Sciences Meeting and Exhibit*, Reno, Nevada, USA

Chehroudi, B., and Talley, D. (2004) Fractal Geometry of a Cryogenic Nitrogen Round Jet Injected into Sub- and Supercritical Conditions. *Atomization and Sprays*, Vol. 14, pp. 81-91

Chehroudi, B., Talley, D., and Coy, E. (2002) Visual Characteristics and Initial Growth Rates of Round Cryogenic Jets at Subcritical and Supercritical Pressures. *Physics of Fluids,* Vol. 14, No. 2, pp. 850-861.

Clauss, W., Il'ukhin, A.A., Kozlov, D.N., Smirnov, V.V., Stel'makh, O.M., WVereschagin, K.A. (1995) Two Wavelength-CARS Thermometry of Hydrogen. *App. Physics B,* Vol. 62, No. 3, pp. 279-285

Clauss, W., Klimenko, D. N., Oschwald, M., Vereschagin, K. A., Smirnov V. V., Fabelinsky V. I., Stelmakh O. V. (2002) CARS Investigation of Hydrogen Q-Branch Linewidths at High Temperatures in a High-Pressure H2-O2 Pulsed Burner. *Journal of Raman Spectr.* 33, pp. 906-911

Clauss, W., Kozlov, D. N., Pykhov, R. L., Smirnov, V. V., Stel'makh O. M., and Vereschagin K. A. (1997) The Analysis of the Precision of Single Shot 2λ-CARS Temperature Measurements in Hydrogen. *Appl. Phys.* B65 pp. 619-624

Correia, D. P., Ferrao, P., and Caldeira-Pires, A., (2001) Advanced 3D Emission Tomography Flame Temperature Sensor. *Combustion Science and Technology,* Vol. 163, pp. 1-24

Culick., F. and Yang., V. (1995) Overview of Combustion Instabilities in Liquid Propellant Rocket Engines. In: Yang, V. and Anderson, W., (eds.), *Liquid Rocket Engine Combustion Instability*, AIAA, Washington D.C., Vol. 169, pp 3-38

Davis, D. and Chehroudi, B. (2004) The Effects of Pressure and Acoustic Field on a Cryogenic Coaxial Jet. AIAA-2004-1330, *42nd AIAA Aerospace Sciences Meeting and Exhibit*, Reno, Nevada, USA

Delplanque, J.-P., and Sirignano, W.A. (1993) Numerical Study of the Transient Vaporization of an Oxygen Droplet at Sub- and Supercritical Conditions. *Int. J. Heat Mass Transfer,* Vol. 36, pp. 303-314

Druet, S.A.J., Taran, J.P., (1981) CARS Spectroscopy. *Prog. Quant. Electr.* Vol.7, pp. 1-72

Eckbreth, A. C. (1996) *Laser Diagnostics for Combustion Temperature and Species*. CRC

Eckbreth, A.C., and Anderson, T.J., (1986) Simultaneous Rotational Coherent Anti-Stokes Raman Spectroscopy and Coherent Stokes Raman Spectroscopy with Arbitrary Pump-Stokes Spectral Separation. *Opt. Lett.* Vol. 11, pp. 496–498

Fabelinsky, V.I., Kozlov, D.N., Smirnov, V.V., Stelmakh, O.M., Vereschagin, K.A., and Clauss, W. (1999) Dual-broadband CARS thermometry in a H2/O2 atmospheric preessure diffusion flame. *Proc. SPIE*, Vol. 3732, pp. 32-37

Farago, Z., Chigier, N. (1992) Morphological Classification of Disintegration of Round Liquid Jets in a Coaxial Air Stream. *Atomization and Sprays*, Vol. 2, pp.137-153

Ferraro, M., Kujala, R.J., Thomas, J.L., Glogowski, M.J., Micci., M.M., (1996) Measurements of Shear Coaxial Injector Sprays: Cold Flow and Hot Fire Experiments. *32nd AIAA/ASME/SAE/ ASEE Joint Propulsion Conference*, Lake Buena Vista, FL, AIAA

Gaydon, A.G., (1974) *The Spectroscopy of Flames.* Chapman and Hall, 2nd edition.

German Aerospace Centre (DLR) [online], <http://www.dlr.de/DLR-Homepage/>, [last accessed: Oct 2001]

Gicquel, P., and Vingert, L. (2000) Flow Investigations of Cryogenic Sprays in Combustion at Sub and Supercritical Conditions. *ILASS-EUROPE-2000*, Darmstadt, Germany.

Gill, P. E. and Murray, W. (1978) Algorithms for the solution of the nonlinear least-squares problem. SIAM *J. Numer. Anal.* 15 [5] 977-992

Givler S.D., and Abraham, J. (1996) Supercritical Droplet Vaporization and Combustion Studies. *Prog. Energy and Combust. Sci.* 22 pp. 1-28

Glassman, I., (1977) *Combustion* New York, NY., Academic Press

Glogowski, M., (1994) Shear Coaxial Injector Instability Mechanisms. *30th AIAA/ASME/SAE/ ASEE Joint Propulsion Conference*, Indianapolis, IN, AIAA

Glogowski, M. and Micci., M.M., (1995) Shear Coaxial Injector Spray Characterization Near the LOX Post Tip Region. *31st AIAA/SAE/ASME/ASEE Joint Propulsion Conference*, July, San Diego, CA, AIAA

Gordon, S., and McBride, B. J. (1994). *Computer Program for Calculation of Complex Chemical Equilibrium Compositions and Applications*. NASA

Griffin, M.D. and French, J.R. (1991) *Space Vehicle Design.* Washington DC, AIAA

Habiballah M., and Dubois I. (1995) Numerical Analysis of Engine Instability. In: Yang, V. and Anderson, W., (eds.), *Liquid Rocket Engine Combustion Instability.* Washington DC, AIAA, Vol. 169, pp. 475-502

Habiballah M., Vingert, L., Duthoit, V., and Vuillermoz, P. (1997), Research as a Key in the Design Methodology of Liquid Propellant Combustion Devices. *Proceedings for the Third International Symposium on Space Propulsion*, Beijing, China, 3.1 pp. 1-23

Hancock, R.D., Bertagnolli, K.E., and Lucht, R.P., (1997) Nitrogen and Hydrogen CARS Temperature Measurements in a Near-Adiabatic, Surface-Mixing (Hencken) Burner. *Combustion and Flame*, Vol. 109, pp. 323-331

Hannay, J.B. and Hogarth, J. (1879) On the Solubility of Solids in Gases. *Proc. Roy. Soc.*, (London). 29:324

Harrje, D.J., and Reardon F.A., (eds.) (1972). *Liquid Propellant Rocket Combustion Instability.* NASA SP-194 Washington DC, NASA

Herding, G., Snyder, R., Rolon, C., and Candel, S., (1998) Investigation of Cryogenic Propellant Flames Using Computerized Tomography of Emission Images. *Journal of Propulsion and Power*, Vol. 14, No. 2, pp. 146-151

Hopfinger, E., and Lasheras, J. C. (1994) Breakup of a Water Jet in High Velocity Co-flowing Air. *Proceedings of the 6th International Conference on Liquid Atomization* Begell House, New York, pp. 110-117

Hulka, J., and Hutt, J.J,. (1994) Instability Phenomena in LOX/Hydrogen Propellant Rocket Engines. In: Yang, V. and Anderson, W. (eds.) *Liquid Rocket Engine Combustion Instability.* AIAA, Washington DC, Vol. 169, pp 39-72

Hulka, J., Makel, D. (1993). Liquid Oxygen/Hydrogen Testing of a Single Swirl Coaxial Injector Element in a Windowed Combustion Chamber. *AIAA/SAE/ASME/ASEE 29th Joint Propulsion Conference & Exhibit*, Monterey, CA., AIAA

Huzel, D. K., Huang, D. H. (1992) *Modern Engineering for Design of Liquid-Propellant Rocket Engines*. Washington DC, AIAA

Ivancic B., and Mayer, W. (2002) Time and Length Scales of Combustion in Liquid Rocket Thrust Chambers. *Journal of Propulsion and Power*, Vol. 18, No. 2, pp. 247-253

Jackson, I., (1995) Propellant Injection Sytems and Processes. *2nd International Symposium in Liquid Rocket Propulsion*, June 19-21, ONERA-Chatillon, France

Juniper, M., Tripathi, A., Scouflaire, P., Rolon, J.C., and Candel, S. (2000) Structure of Cryogenic Flames at Elevated Pressure. *Proceedings of the Combustion Institute*, 28: pp. 1103-1110

Kaltz, T., Glogowski, T., and Micci, M., (1993) Shear Coaxial Injector Instability Mechanisms. *AIAA Technical Report* Vol.2 pp 93-96

Kaminski, C.F., and Ewart, P. (1997) Multiplex coherent anti-Stokes Raman Spectroscopy of H2 Using a Modeless Laser. *Appl. Opt.*, Vol. 36, 731

Kanury, A.M., (1995) *Introduction to Combustion.* Vol. 2, 9th Edition, The Netherlands, Gordon and Breach Science Publishers

Kendrick, D., Herding, G., Scouflaire, P., Rolon, C., and Candel, S., (1999) Effects of Recess on Cryogenic Flame Stabilization. *Combustion and Flame*, No. 118 pp. 327-339

Kit, B. and Evered, D.S. (1960). *Rocket Propellant Handbook.* The Macmillan Company

Klimenko D.N., Clauss W., Oschwald M., Smith J.J., and Mayer W. (2002) CARS Temperature mapping in a cryogenic LOx-H2 rocket combustion chamber under Supercritical conditions. *J. Raman Spectrosc.* Vol. 33, pp. 900-905

Lal, M., Oljaca, M., Lubarsky, E,. Sheherbik, D., Bibik, A., and Menon, S. (2004) Controllable Injection for Supercritical Combustion. AIAA 2004-3383 *40th AIAA/ASME/SAEASEE Joint Propulsion Conference and Exhibit,* July 12-14, Fort Lauderdale, FL

Ledoux, M., Care, I., Micci, M., Glogowski, M., Vingert, L., Gicquel, P. (1995). Atomization of Coaxial-Jet Injectors. *2nd International Symposium on Liquid Rocket Propulsion,* June 19-21, ONERA-Chatillon, France

Lefebvre, A. (1988) *Atomization and Sprays.* Hemisphere Publishing Corporation, pp 37-58

Lide, D. R. (1997) *CRC Handbook of Chemistry and Physics* CRC Press

Man, J. (2000) *The Space Race*. London, Readers Digest

Maskrey, A., Puissant, C., Glogowski, M., and Micci, M. M. (1995) Shear Coaxial Injector Spray Combustion Experiments in a single Element Rocket Chamber. *31st AIAA/ASME/SAE/ASEE Joint Propulsion Conference*, July, San Diego, CA, AIAA

Mayer, W.O.H., (1998) Atomization and Breakup of Cryogenic Propellants Under High-Pressure Subcritical and Supercritical Conditions. *Journal of Propulsion and Power*, Vol. 14, no. 5, pp.835-842

Mayer, W. (1994) Coaxial atomization of a round liquid jet in a high speed gas stream: A phenomenological study. *Journal Experiments in Fluids*, Vol. 16, No. 6, pp. 401-410

Mayer, W., Ivancic, B., Schik, A., Hornung, U., (2001) Propellant Atomization and Ignition Phenomena in Liquid Oxygen/Gaseous Hydrogen Rocket Combustors. *AIAA Journal of Propulsion and Power,* Vol. 17, No. 4, pp. 794-799.

Mayer, W., Krulle, G. (1992) Rocket Engine Coaxial Injector Liquid/Gas Interface Flow Phenomena. *AIAA/SAE/ASME/ASEE 28th Joint Propulsion Conference & Exhibit*, Nashville, TN., AIAA

Mayer, W., and Krulle, G., (1994) Injection, Atomization and Mixing of Propellants in Liquid Rocket Engines Using Coaxial Injectors. *ICLASS-94 Proceedings*, Rouen, France

Mayer, W.O.H., Schik, A., and Schäffler, M. (2000) Injection and Mixing Processes in High Pressure Liquid Oxygen/Gaseous Hydrogen Rocket Combustors. *Journal of Propulsion and Power*, Vol. 16, No. 5, pp. 823-828

Mayer, W.O.H., Schik, A.H.A., Vielle, B., Chauveau, C., Gökalp, I., Talley., D.G. (1998) Atomization and Breakup of Cryogenic Propellants under High Pressure Subcritical and Supercritical Conditions. *Journal of Propulsion and Power*, Vol. 14, No.5, pp. 835-842

Mayer, W., and Smith, J. (2005) Fundamentals of Mixing and Combustion of Cryogenic Propellants. In: *Rocket Engine Thrust Chambers: Aspects of Modeling, Analysis, and Design.* AIAA Progress in Aeronautics and Astronautics

Mayer, W. and Tamura, H. (1996) Propellant Injection in a Liquid Oxygen/Gaseous Hydrogen Rocket Engine. *Journal of Propulsion and Power*, Vol. 12, No. 6, pp. 1137-1147.

Mayer, W., and Telaar, J., (2002) Investigation of Breakup of Turbulent Cryogenic Variable Density Jets. *Journal of Atomization and Sprays*, 12 (5) pp. 651-666

Mayer, W., Telaar, J., Branam, R., Schneider, G., and Hussong, J. (2003) Raman Measurements of Cryogenic Injection at Supercritical Pressure. *Heat and Mass Transfer*, 39, pp. 709-719

Micci, M.M., (1995) *Liquid Motor Combustion Stability Using Coaxial Injectors.* Washington DC, US Air Force Office of Scientific Research

Micci, M.M. (1997) *Contributions of Shear Coaxial Injectors to Liquid Rocket Motor Combustion Instabilities*. NASA

Michaut X., Berger J-P., Saint-Loup R, Chaussard F., and Berger H. (2001) Theoretical and experimental studies of H_2 vibraional lines in high pressure and high temperature mixtures II - Determination of the collisional broadening for Q-branch lines in H2-H2O mixture from 600 up to 1800K. In: *Combustion dans les Moteurs Fusees*. pp. 321–331

Miller, S., and Bellan, J. (2002) Direct Numerical Simulations of Supercritical Fluid Mixing Layers Applied to Heptane-Nitrogen. *J. Fluid Mech.* 436, pp. 1-34

Moser, M. D., Merenich, J. J., Pal, S., and Santoro, R. J. (1993) OH-Radical Imaging and Velocity Field Measurements in a Gaseous Hydrogen/Gaseous Oxygen Rocket. AIAA 93-1882, *29th AIAA/SAE/ASME/ASEE Joint Propulsion Conference and Exhibit*, Monterey, CA

Muss, J.A., (1995) Instability Phenomenon in Liquid Oxygen/Hydrocarbon Rocket Engines. In: Yang, V. and Anderson, W., (eds.) *Liquid Rocket Engine Combustion Instability.* AIAA, Washington DC, Vol. 169, pp. 73-88

Newman, J. A., and Brzustowski, T. A. (1971) Behaviour of a Liquid Jet Near the Critical Region. *AIAA Journal*, Vol. 9, No. 8, August, pp. 1595-1602

Nicoli, C., Haldenwang, P., Daou, J., (1996) Substitute Mixtures for LOX droplet Vaporization Study. *Combustion Science and Technology*, Vol. 12, pp55-74

Oefelein, J. (2003) LES of Supercritical LOX/H2 Injection and Combustion in a Shear-Coaxial Uni-Element Rocket. AIAA 2003-0479, *AIAA 41st Aerospace Sciences Meeting and Exhibit*, Reno, NV

Oefelein, J. (2004) Thermophysical Characteristics of Shear-Coaxial LOX–H2 Flames at Supercritical Pressure. *Proc. Combust. Symp.* Chicago

Oefelein J., and Yang, V. (1993) Comprehensive Review of Liquid-Propellant Combustion Instabilities in F-1 Engines. Journal of *Propulsion and Power,* Vol. 9, No.5, pp. 657-686

Oefelein, J.C., Yang, V. (1998) Modeling High Pressure Mixing and Combustion Processes in Liquid Rocket Engines. *Journal of Propulsion and Power*, Vol. 14, No.5, pp. 843-860

Okongo, N., and Bellan, J. (2000) Entropy Production of Emerging Turbulent Scales in a Temporal Supercritical n-Heptane/Nitrogen Three Dimensional Mixing Layer. *Proc. Combust. Inst.* Vol. 28, Pt. 1, pp. 497-504

Okongo, N., Harstad, K.G., and Bellan, J. (2002) Direct Numerical Simulations of O2/H2 Temporal Mixing Layers Under Supercritical Conditions. *AIAA Journal* 40(5), pp. 914-926

Oschwald, M., and Schik, A. (1999) Supercritical Nitrogen Free Jet Investigated by Spontaneous Raman Scattering. *Experiments in Fluids*, 27, 497-506

Oschwald, M., Schik, A., Klar, M., and Mayer, W. (1999) Investigation of Coaxial LN2-GH2 Injection at Supercritical Pressure by Spontatneous Raman Scattering. AIAA 99-2887, *35th AIAA/SAE/ASME/ASEE Joint Propulsion Conference*, Los Angeles, CA

Oschwald, M, Smith, J. J., Branam, R., Hussong, J., Schik, A., Chehroudi, B., and Talley, D. (2006) Injection of Fluids into Supercritical Environments. *Combust. Sci. and Tech.* Vol. 178, No. 1-3, pp. 49-100

Ostrovski, I., Butusov, I. I., and Ostrovska, G. V. (1977) Gologrаfiqeska Interferometri. *Izdatelstvo*, Moskow No. 44, p. 150

Pal, S., Moser, M. D. Ryan, H. M., Foust, M. J. and Santoro R. J. (1996) Shear Coaxial Injector Atomization Phenomena for Combusting and Non-Combusting Conditions. *Atomization and Sprays*, Vol. 6, pp. 227-244

Preclik, D., and Spagna, P. (1988) "Low DFrequency and High Frequency Combustion Oscillation Inside a Rocket Combustion Chamber Fed by Liquid or Gaseous Propellants," AGARD CP-450, pp. 6.1 - 6.18

Puissant, C., Glogowski, M., Micci, M. M. (1994). "Experimental Characterization of Shear Coaxial Injectors Using Liquid/Gaseous Nitrogen," *ICLASS-94 Proceedings,* Rouen, France

Pungor, E. and Cornides, L. (1969) Emission Problems of Unsalted Flames. In: Dean J. A., and Rains, T. C. *Flame Emission and Absorption Spectrometry.* Vol. 1, Dekker, London.

Rahman, S. A., Cramer, J. M., Pal, S., Santoro, R. J. (1995) Coaxial Swirl Injector Studies at High O/F Ratios. *32nd JANNAF Combustion Subcommittee Meeting and Propulsion Engineering Research Center 7th Annual Symposium*, pp. 31-42

Rahn L. A., Farrow R. L., Rosasco G. J. (1991) Measurement of the self-broadening of the H2 Q(0-5) Raman Transitions from 295 to 1000K. *Phys. Rev. A* Vol. 43, pp. 6075

Rehab, H., Villermaux, E., Hopfinger, E.J. (1997) Flow Regimes of Large-Velocity-Ratio Coaxial Jets. *Journal of Fluid Mechanics,* Vol. 345, pp. 357-381

Sasaki, M., Sakamoto, H., Takahashi, M., Tomita, T., Tamura, H., (1998) Experimental Study on Combustion Stability Characteristics of Non-Swirl and Swirl Coaxial Injectors. *34th AIAA/ ASME/SAE/ASEE Joint Propulsion Conference & Exhibit*, Cleveland, OH, AIAA

Schmidt, V., Sender, J., and Haidn, O.J., (1999) Droplet Tracking Velocimetry in a Burning LOx/ GH2 Spray. *Proceedings of the Third International Workshop on PIV*, Santa Barbara, USA, pp. 189-193

Schmidt, V., Sender, J., and Oschwald, M. (2001) Simultaneous Observation of Liquid Phase Distribution and Flame Front Evolution During the Ignition Transient of a LOx/GH_2 -Combustor. *Journal of Visualization*, Vol. 4, No. 4, pp. 365-372

Schmidt, R., and Wagner, W. (1985) A New Form of the Equation of State for Pure Substances and its Application to Oxygen. *Fluid Phase Equilibria* Vol. 19, pp. 175-200

Schoeyer, H.F.R. (ed). (1993) *Combustion Instability in Liquid Rocket Engines.* esa WPP-062, pp 6.0-6.36

Settles, G. S. (2006) *Schlieren & Shadowgraph Techniques.* 1st Edition, Springer

Singla, G., Scouflaire, P., Rolon, C., and Candel, S. (2004) Transcritical oxygen/transcritical or supercritical methane combustion. *Proc. Combust. Inst.* Chicago

Smith, J.J., Klimenko, D., Clauss, W., and Mayer, W. (2002) Supercritical LOx/Hydrogen Rocket Combustion Investigations Using Optical Diagnostics. *38th AIAA/ASME/SAE/ASEE Joint Propulsion Conference and Exhibit*, IN, USA, AIAA

Smith J.J., Suslov, D., Langener, T., Oschwald, M., Mayer, W., and Schneider, G. (2003) Hot Fire Testing of a LOx/H2 Porous Injector Head at High Pressure Conditions with Optical Diagnostics. *SPACE-2003*, Moscow-Kaluga, Russia

Snyder, R., Herding, G., Rolon, J.C., and Candel, S. (1997) Analysis of Flame Patterns in Cryogenic Propellant Combustion. *Combust. Sci. and Tech.* Vol. 124, pp. 331-370

space.com [online], Available from: <http://www.space.com/>, [access date: August 2001]

Street, W. B., Calado, J. C. G. (1978) Liquid-Vapor Equilibrium for Hydrogen and Nitrogen at Temperatures from 63 to 100 K and pressures to 57 Mpa. *J. Chem. Therm.*, Vol. 10, pp. 1089-1100

Stricker, W., Woyde, M., Lückerath, R., and Bergmann, V. (1993) Temperature Measurements in High Pressure Combustion. *Ber. Bunsenges. Phys. Chem.* Vol. 97, pp.1608-1618

Suslov, D., Kopp, W., Oschwald, M. (2003) Zur Temperaturmessungen mit Hilfe von Thermoelementen im Tieftemperaturbereich. *PTB-GMA Fachtagung TEMPERATUR 2003*, 8-9 September, Berlin

Tamura, H., Sakamoto, H., Sasaki, M., Takahashi, M., Tomita, T., and Mayer, W. (1995) An Experimental Study on the Stability Characteristics of the LOX/Methane Rocket Combustor. *31st AIAA/ASME/SAE/ASEE Joint Propulsion Conference and Exhibit*, July, San Diego, CA, AIAA

Tully, DeVaney, Rhodes, (1970) Phase Equilibria of the Helium- Nitrogen System from 122 to 126 K. *Advanced Cryogenic Engineering* Vol. 16 pp. 88-95, Bureau of Mines, Helium Research Center, Amarillo, Texas

Vereschagin, K. A., Vereschagin, A. K., Clauss, W., Klimenko, D. N., Oschwald, M., Smirnov, V. V., Stel'makh, O. M., and Fabelinsky, V. I. (2006) High Resolution Line-Shape Spectroscopy During a Laser Pulse Based on Dual Broad-Band CARS Interferometry, *Quantum Electronics*, Vol. 36, No. 7, pp. 687-690

Vingert, L., Gicquel, P., Lourme, D., and Ménoret, L. (1994) *Coaxial Injector Atomization.* Progress in Astronautics and Aeronautics, AIAA, Vol. 169, pp.145-189

Vingert, L., Gicquel, P., and Lourme, D. (1995) Coaxial Injector Atomisation. In: Yang, V. and Anderson, W. (eds.), *Liquid Rocket Engine Combustion Instability.* AIAA, Washington DC, Vol. 169, pp. 145-190

Vogel, A. (1994) Investigation on Atomization of a Coaxial H2/LOx Jet under Hot-Fire Conditions. *ICLASS 94 Conference Proceedings,* 6th International Conference on Liquid Atomization and Spray Systems, Rouen, France

Wade, M. (1999). Mark Wade's Encyclopedia Astronautica [online], Available from: <http:// www.friends-partners.org/mwade/spaceflt.htm> [last update 31 October, 2002]

Wanhainen, J. P., Parish, H. C., and Conrad, W. E. (1966) Effect of Propellant Injection Velocity on Screech in 20000 lb Hydrogen-Oxyen Rocket Engines. TN D-3373, Washington DC, NASA

Woodward, R.D., Pal, S., Farhangi, S., and Santoro, R.J. (2006) LOx/GH2 Shear Coaxial Injector Atomization Studies at Large Momentum Flux Ratios. *42nd AIAA/ASME/SAE/ASEE Joint Propulsion Conference & Exhibit*, 9-12 July, Sacramento, CA

Woodward, R. D., Pal, S., Santoro, R. J., and Kuo, K. (1996) Measurement of Core Structure of Coaxial Jets Under Colf-Flow and Hot-Fire Conditions. In: Kuo, K. (ed.) *Recent Advances in Spray Combustion: Spray Atomization and Drop Burning Phenomena Volume 1.* Progress in Aeronautics and Astronautics, Vol. 166, AIAA, Reston, VA

Woodward, R.D., and Talley, D.G. (1996) Raman Imaging of Transcritical Cryogenic Propellants. AIAA 96-0468, *34th Aerospace Sciences meeting and Exhibit,* Jan 15-19 Reno, NV

Yang, V. (2000) Modelling of Supercritical Vaporization, Mixing, and Combustion Processes in Liquid-Fueled Propulsion Systems. *Proc. Comb. Inst.* Vol. 28, pp. 925-942

Yang, V., and Anderson, W. (1995) *Liquid Rocket Combustion Instability.* American Institute of Aeronautics and Astronautics, AIAA Progress Series, Vol. 169, Washington DC

Yang, V., Hsiao, G. C., Shuen, J. S., and Hsieh K. C. (1995) Droplet Behaviour at Supercritical Conditions. In: Kuo, K. (ed.) *Recent Advances in Spray Combustion Vol. 1*, Progress in Aeronautics and Astronautics, Vol. 166, pp. 413-437

Younglove, B.A., (1982) Thermophysical Properties of Fluids. 1. Argon, Ethylene, para-Hydrogen, Nitrogen, Nitrogen Trifluoride and Oxygen. National Bureau of Standards, Volume II, Supplement No. 1

Zong, N., Wang, S.W., and Yang, V. (2003) A Numerical Study of Fluid Jet Dynamics at Supercritical Conditions. TSFP3-278, *3rd International Symposium on Turbulence and Shear Flow Phenomena*, Sendai, Japan

Zong, N., and Yang, V. (2003) Cryogenic Fluid Injection and Mixing at Supercritical Conditions. AIAA 2003-0480, *41st AIAA Aerospace Sciences Meeting and Exhibit*, Reno, NV

Appendix

A. Coefficients for EMG Curves

Table A1 EMG coefficients for x/d = 20 (80mm)

Radial Position	a	b	c	d	e
2mm	8165	0.9197109	0.8960965	1.5493123	51.547478
4mm	8165	0.9809868	0.9691035	1.6110958	116.08877
6mm (curve 1)	3330	0.9999959	0.9999835	0.04202725	81031.306
6mm (curve 2)	3330	0.7900699	0.6701098	1.1916546	10.035971
8mm (curve 1)	8165	0.9998366	0.9991829	0.1829939	1529.543
8mm (curve 2)	8165	0.901535	0.839994	1.183268	20.60075
10mm	8165	0.9921237	0.9855601	1.0031923	220.43481

B. Publications Originating from this Thesis

This sections lists the publications and international presentations that have directly resulted from the work undertaken to complete this thesis.

B.1 Book Chapter

1. Mayer W.O.H. and Smith J.J. **2005** Fundamentals of Supercritical Mixing and Combustion of Cryogenic Propellants. In: *Rocket Engine Thrust Chambers*, AIAA Progress in Aeronautics and Astronautics Series

B.2 International Journals

1. Smith, J.J., Schneider, G.M., Suslov, D., Oschwald, M., Haidn, O. **2007** Steady-State, High Pressure LOx/H_2 Rocket Engine Combustion. *Journal of Aerospace Science and Technology*, Elsevier Vol. 11 pp. 39-47
2. Oschwald, M, Smith, J.J., Branam, R., Hussong, J., Schik, A., Chehroudi, B., and Talley, D. **2006** Injection of Fluids into Supercritical Environments. *Journal of Combustion Science & Technology*, Vol. 178 pp. 49-100
3. Klimenko D.N., Clauss W., Oschwald M., Smith J.J. and Mayer W. **2002** CARS Temperature mapping in a cryogenic LOx-H_2 rocket combustion chamber under Supercritical conditions. *Journal of Raman Spectroscopy.* Vol. 33, pp. 900-905

B.3 International Conferences

1. Smith, J.J., Schneider, G.M., Suslov, D., Oschwald, M., Haidn, O. **2005** Steady-State, High Pressure LOx/H_2 Rocket Engine Combustion. *1st European Conference for Aerospace Sciences*, Moscow, 4 - 7 July

2. Klimenko, D.N., Clauss, W., Smith, J.J., and Oschwald, M. **2004** CARS Spectroscopy at High Pressure in a Cryogenic LOx/H_2 Rocket Combustion Chamber. *International Symposium on Space Technology and Science*, Miyazaki, Japan, 30 May - 6 June

3. Smith J.J., Bechle, M., Suslov, D., Oschwald, M., Haidn, O.J., Schneider, G.M. **2004** High Pressure LOx/H_2 Combustion and Flame Dynamics. *40th AIAA/ASME/SAE/ ASEE Joint Propulsion Conference and Exhibit*, Fort Lauderdale, USA, 11-14 July

4. Clauss, W., Klimenko, D., Oschwald, M., Mayer, W., and Smith, J. **2003** CARS Temperaturmessung am H2 Molekül in einer kryogenen LOX/H_2 Raketenbrennkammer unter überkritischen bedingungen. *DGLR Deutscher Luft und Raumfahrtkongress*, München, 17- 20 Nov.

5. Chehroudi, B., Talley, D., Mayer, W., Branam, R., Smith, J.J., Schik, A., and Oschwald, M. **2003** Understanding Injection Into High Pressure Supercritical Environments. *5th International Conference on Liquid Rocket Propulsion*, Chattanooga, USA. 27-30 Oct.

6. Smith J.J., Klimenko, D.N., Clauss, W., Mayer, W., Oschwald, M. **2003** Optical Diagnostics and Instrumentation for Supercritical Combustion Studies in a LOx/H2 Rocket Engine Combustion Chamber. *20th International Congress on Instrumentation in Aerospace Simulation Facilities*, Göttingen, Germany

7. Smith J.J., D. Suslov, T. Langener, M. Oschwald, W. Mayer, G. Schneider **2003** Hot-Fire testing of a LOx/H_2 porous injector head at high pressure conditions with optical diagnostics. *Space Challenge in 21st Century*, Moscow-Kaluga, Russia

8. Smith J.J., Klimenko D., Clauss W., Mayer W. **2002** Supercritical LOX/Hydrogen Rocket Combustion Investigations Using Optical Diagnostics. *38th AIAA/ASME/ SAE/ASEE Joint Propulsion Conference and Exhibit*, Indianapolis, USA